

DTIC QUALITY INSPECTED 3

**NUMERICAL ANALYSIS OF
TWO AND THREE DIMENSIONAL
RECESSED FLAME HOLDERS
FOR SCRAMJET APPLICATIONS**

DISSERTATION

Douglas L. Davis
Civilian

DISTRIBUTION STATEMENT A

Approved for public release;
Distribution Unlimited

DEPARTMENT OF THE AIR FORCE
AIR UNIVERSITY
AIR FORCE INSTITUTE OF TECHNOLOGY

Wright-Patterson Air Force Base, Ohio

19970501 168

AFIT/DS/ENY/96-12

**NUMERICAL ANALYSIS OF
TWO AND THREE DIMENSIONAL
RECESSED FLAME HOLDERS
FOR SCRAMJET APPLICATIONS**

DISSERTATION

Douglas L. Davis
Civilian

Approved for public release, distribution unlimited

The views expressed in this dissertation are those of the author and do not reflect the official policy or position of the Department of Defense or the U. S. Government.

AFIT/DS/ENY/96-12

**NUMERICAL ANALYSIS OF TWO AND
THREE DIMENSIONAL RECESSED
FLAME HOLDERS FOR SCRAMJET APPLICATIONS**

DISSERTATION

Presented to the Faculty of the School of Engineering
of the Air Force Institute of Technology
Air University in Partial Fulfillment of the
Requirements for the Degree of
Doctor of Philosophy

Douglas L. Davis
Civilian

September 1996

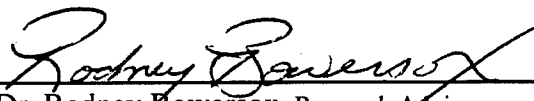
Approved for public release; distribution unlimited

**NUMERICAL ANALYSIS OF TWO AND
THREE DIMENSIONAL RECESSED
FLAME HOLDERS FOR SCRAMJET APPLICATIONS**

Douglas L. Davis

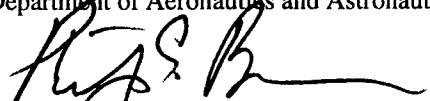
Civilian

Approved :




Dr. Rodney Bowersox, Research Advisor
Assistant Professor of Aerospace Engineering
Department of Aeronautics and Astronautics

Sept. 18, 1996
Date




Dr. Philip Beran, Committee Member
Associate Professor of Aerospace Engineering
Department of Aeronautics and Astronautics

Sept 20, 1996
Date




Major Thomas Buter, Committee Member
Assistant Professor of Aerospace Engineering
Department of Aeronautics and Astronautics

Sept 18, 1996
Date



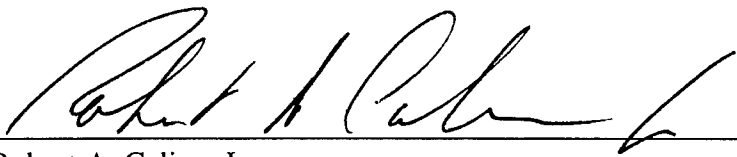
Dr. Aihua Shaker, Committee Member
Assistant Professor of Mathematics
Department of Mathematics and Statistics

Sept. 18, 1996
Date



Major Michael C. Roggemann, Dean's Representative
Associate Professor of Engineering Physics
Department of Engineering Physics

18 Sept 1996
Date



Robert A. Calico, Jr.
Dean, School of Engineering

Preface

This research was an investigation into the flame holding properties of wall cavities in supersonic flow. The revived interest in high speed flight has lead to investigations into hydrocarbon scramjet propulsion systems. Hydrocarbon fuels are more difficult to ignite than hydrogen fuels. In this research, recessed cavity flame holders were shown to provide adequate flame holding for hydrocarbon fuels. Based in part on the current research, cavity flame holders are being tested for application in the Hytec program.

The author would like to acknowledge the support of many individuals and organizations. A special thanks for their support goes to Dr. E.T. Curran, Maj. John Doty, W. Lee Bian III, and Lt. Col. Rich Moore and other personnel of the Advanced Propulsion Division of the Aeropropulsion and Power Directorate. All of the professors at AFIT have helped by building a foundation for research. The financial support of the Dayton Area Graduate Schools Institute, DAGSI, is also acknowledged. Computational support from the Department of Defense High Performance Computing initiative organizations at Naval Oceanographic Office and Army Research Laboratory was greatly appreciated. The guidance provided by my advisor and dissertation committee was appreciated. I greatly appreciated the patience and support of my wife and family.

Table of Contents

	Page
Preface	ii
Table of Contents	iii
List of Figures	vii
List of Tables	xiii
List of Symbols	xv
List of Terms and Acronyms	xviii
Abstract	xx
1. Introduction	1
1.1. Problem Statement	1
1.2. Scope of Research	3
1.3. Approach	4
1.4. Key Results	6
1.5. Overview of Dissertation	7
2. Background	8
2.1. Scramjet Overview	8
2.2. Hydrocarbon Scramjets	10
2.3. General Chemical Reaction Progression	13
2.4. Flame Propagation	14
2.5. Flame Holders	16
2.6. Flame Holding Analysis	19
2.7. Cavity Flame Holders	22
2.8. Cavity Flows	25
2.8.1 Cavity Classification	26

2.8.2 Cavity Instability Cycle	26
2.8.3 Cavity CFD Simulations	28
2.8.4 Three Dimensional Cavity Effects	29
2.8.5 Compressible Shear Layer Studies	30
2.8.6 Cavity Drag	31
2.9. Summary	32
3. Methodology	33
3.1. Chemical Reaction Rates	33
3.2. Perfectly Stirred Reactor Modeling	38
3.2.1 Time Dependent Perfectly Stirred Reactor Model	39
3.2.2 Steady State Perfectly Stirred Reactor Model	41
3.2.3 Simplified PSR Model	42
3.2.4 Estimate of Cavity Residence Time	44
3.2.5 Cavity Heat Loss Model	48
3.2.6 Reaction Rate Sets	49
3.3. Multi-Dimensional Modeling	50
3.3.1 Physical Models	51
3.3.2 Species Properties	55
3.3.3 Turbulence Modeling	58
3.3.4 Numerical Method	64
3.3.5 Boundary Conditions	65
3.3.6 Numerical Smoothing	65
3.3.7 Calibration Data	66
3.3.8 Residence Time Calculations	67
3.3.9 Multi-Dimensional Simulations	69
4. Perfectly Stirred Reactor Results	71
4.1. Simple Analytical PSR Results	71
4.2. PSR Code Development	74
4.2.1 PSR Code Calibration	75
4.2.2 Calculation of Limiting Residence Times	76
4.3. Chemical Kinetics Analysis	77
4.3.1 H-O Reaction Set Comparison	77
4.3.2 Reduced H-O Reaction Sets	79
4.3.3 Global Hydrogen Rate Equation	81
4.3.4 Hydrocarbon Results	84

4.3.5 Global Propane Reaction Rate	86
4.4. Flame Holder Analysis	87
4.4.1 Initial and Inflow Temperature Effect on Hydrogen Combustion	87
4.4.2 Initial and Inflow Temperature Effect on Hydrocarbon Combustion	91
4.4.3 Fuel to Air Ratio Effect	92
4.4.4 Mixing Simulation Results.	98
4.4.5 Heat Loss Effects	100
4.5. Perfectly Stirred Reactor Summary	102
5. Two-Dimensional Results	104
5.1. Numerical Quality Assessment	105
5.1.1 Two-Dimensional Validation Results	105
5.1.2 Grid Convergence	110
5.1.3 Effects of Added Artificial Viscosity	114
5.1.4 Temporal Convergence	115
5.1.5 Verification of Turbulence Model	117
5.2. Two-Dimensional Analysis of Cavity Flame Holders	119
5.2.1 Important Flow Features.	119
5.2.2 Variations in Fuel to Air Ratio	121
5.2.3 Transonic Effects at High Fuel to Air Ratios	124
5.2.4 Two-Dimensional Analysis and Perfectly Stirred Reactor Comparisons	127
5.2.5 Small Cavity	128
5.2.6 Free Stream Mach Number Effect.	130
5.2.7 Heat Transfer Effect.	131
5.2.8 Variations to the Turbulence Model	133
5.2.9 Boundary Layer Effects	141
5.2.10 Flow Stability.	142
5.2.11 Full H-O Kinetic Set	144
5.2.12 Hydrocarbon Results.	148
5.3. Summary of Two-Dimensional Results	150
6. Three-Dimensional Results	153
6.1. Three-Dimensional Code Validation	153
6.1.1 Comparison with Two-Dimensional Code Results.	153

6.1.2 Grid Refinement Results	155
6.2. Three-Dimensional Simulation Results	156
6.2.1 Swept Cavity Results	156
6.2.2 Variable Aspect Ratio Swept Cavity	160
6.2.3 Three-Dimensional Reacting Flow Simulations	161
6.3. Summary of Three-Dimensional Results	163
7. Conclusions	164
7.1. Perfectly Stirred Reactor Results	164
7.2. Multi-Dimensional Results	166
7.3. Recommendations	168
Appendix A. Numerical Integration Methods for Perfectly Stirred Reactor Model. ...	169
A.1. Arbitrary Order Runge-Kutta.	169
A.2. Third Order Adams-Moulton Method.	172
A.3. Euler Implicit Method.	175
A.4. Comparison of Methods	178
Appendix B. Summary of Reaction Rate Sets.	180
References	206
Vita	213

List of Figures

Figure	Page
Figure 1. Baseline Cavity Dimensions in cm.	5
Figure 2 Propulsion Performance for Various Systems as Flight Speed Increases. (4:402)	9
Figure 3. Vortices Lifting from a Wall Boundary Layer (15:820)	11
Figure 4. Hydrocarbon Scramjet Tested at Central Institute for Aviation Motors (17:5)	11
Figure 5. Species Mass Fractions for a Hydrogen Oxygen Reaction Progressing in Time as Calculated by a Time Dependent Perfectly Stirred Reactor Code.	13
Figure 6. Flame Propagation Types.	14
Figure 7 Various Types of Flame Holders	17
Figure 8. Typical Blowout Limits for Ignition Time Concept.	20
Figure 9. Typical Blowout Limits for Stirred Reactor Experiments.	21
Figure 10. Comparison of 90 degree V-Gutter (37.5% Blockage) with the Baseline Cavity Flame Holder, No. 2 (2:34)	22
Figure 11. Effect of Cavity Depth on Blowout Velocity.	23
Figure 12. Divided Strut Flame Holder	24
Figure 13 Film of an Unstable Flow in a Cavity Combustor (55:4).	28
Figure 14. Triangular Cavity Geometry.	30
Figure 15. Perfectly Stirred Reactor Model Used in this Analysis.	38

Figure 16. Illustration of a Perfectly Stirred Reactor Simulation of a Mixing Shear Layer	41
Figure 17. Cavity Dimensions for Residence Time Estimate	45
Figure 18. Comparison of Species Enthalpy Curves.	57
Figure 19. Viscosity Curves for Propane.	57
Figure 20. Calibration and Baseline Cavity Geometries	68
Figure 21. The Effect of Temperature Rise Parameter on the Degree of Reaction with Residence Time.	72
Figure 22. The Effect of Activation Energy on the Relation between Degree of Reaction and Residence Time.	73
Figure 23. Water Mass Fraction Comparison with Different H-O Reaction Rate Sets for Ignition Delay Simulations.	78
Figure 24. Temperature from Lower Residence Time Calculation with Different H-O Reaction Rate Sets.	79
Figure 25. Ignition Delay Calculation with the Full Radhakrishnan H-O Reaction Set.	80
Figure 26. Calculations using the tuned global hydrogen chemical kinetics model. ...	83
Figure 27. Comparison of Tuned Global Reaction Rate with Full Propane Reaction Rate Set for $\phi=1.0$	86
Figure 28. Temperature Variation with Time for a Constant Pressure Reaction at Different Initial Temperatures for hydrogen combustion in air.	88
Figure 29. Effect of Initial or Inflow Temperature on Ignition Delay, Upper Residence, and Lower Residence Times for Hydrogen Air Combustion.	89
Figure 30. Free Stream Mach Number Effect on Water Mass Fraction for Lower Residence Time Calculation.	90

Figure 31. Ignition Delay Calculations with the Full Propane Reaction Set.	91
Figure 32. Ignition Delay, Upper and Lower Residence Times from Propane Perfectly Stirred Reactor Simulations.	92
Figure 33. Water Mass for Lower Residence Time Calculations with Lean Fuel to Air Ratios Using the Global Water Reaction.	93
Figure 34. Water Mass for Lower Residence Time Calculations with Lean Fuel to Air Ratios Using a Full Water Rate Set.	94
Figure 35. Water Mass for Lower Residence Time Calculations for Rich Fuel to Air Ratios Using the Global Water Reaction.	95
Figure 36. Water Mass for Lower Residence Time Calculations for Rich Fuel to Air Ratios Using a Full Water Reaction Set.	96
Figure 37. Lower Residence Time Variation with ϕ for Several Chemical Kinetic Rate Models.	97
Figure 38. Mixing Layer Simulations with Various Product Percentages.	98
Figure 39. PSR Shear Layer Simulations with Various Reactant / Product Temperatures.	99
Figure 40. OH Concentration Change with Time for Various Mixing Cases.	100
Figure 41. Comparison of Velocity Results with Experimental Data.	107
Figure 42. Comparison of Shear Stress from Experiment and SPARK Simulation. ...	108
Figure 43. Decay of "Cavity Air" Mass Indicating the Residence Time for Several Turbulence Approximations.	109
Figure 44. Coarse Grid for Baseline Geometry.	110
Figure 45. The effect of grid refinement on the calculated mean velocities.	111
Figure 46. Water Production Rate Contours for Three Grid Refinement Levels.	112

Figure 47. Water Mass Fraction Contours for the Three Grid Levels at $\phi = 0.45$	113
Figure 48. Water Production Rate Contours with Different Amounts of Added Numerical Smoothing. $\phi=0.45$, 51 X 51 Grid	114
Figure 49. Unsteady Pressure for Different Amounts of Added Numerical Smoothing.	115
Figure 50. Initial Condition for Baseline Cavity Simulation.	116
Figure 51. Temporal Convergence Parameters for a Cavity Flame Holder Simulation.	117
Figure 52. Velocity Vectors and Water Contours for a Condition Near Blowout and a Reactive Condition.	120
Figure 53. Typical Pressure Contours for Reactive and Near Blowout Conditions. . .	121
Figure 54. Progression of Integrated Water Mass within the Cavity.	122
Figure 55. Integrated Water Mass Fraction Within the Cavity for Converged Solutions.	122
Figure 56. Water Production Rate Contours for Lean Fuel to Air Ratios.	123
Figure 57. Water Production Rate Contour Variation for Rich Fuel to Air Ratios. . .	125
Figure 58. Transonic Mach Number Contours for Different Reaction Levels.	126
Figure 59. Comparison of Cavity Water Mass Fraction from Perfectly Stirred Reactor and Two-dimensional Simulations.	127
Figure 60. Cavity Water Mass Variation with Time for Small Cavity Simulations. . .	129
Figure 61. Water Mass Fraction Comparison Between the Small Cavity CFD Results and the Perfectly Stirred Reactor Results @ 0.1 msec.	130

Figure 62. Water Production Near the Cavity Wall for the Small Cavity Simulation.	130
Figure 63. Effect of Free Stream Mach Number on Water and Temperature Contours.	131
Figure 64. Effect of Heat Loss on Cavity Water Mass.	132
Figure 65. Temperature Contours as Heat Transfer Rate was Increased.	133
Figure 66. The Density Residual Reduction for Various Turbulence Models.	135
Figure 67. Pressure Oscillations for Turbulence Modifications.	135
Figure 68. Convergence of the Integrated Cavity Water Mass for Different Turbulence Models.	136
Figure 69 Axial Velocity Contours for Several Turbulence Variations.	137
Figure 70 Shear Stress Contours for Several Turbulence Variations.	138
Figure 71 Water Production Variation with Turbulence Model.	140
Figure 72. The effect of boundary layer thickness on velocity and water production rate.	143
Figure 73. Unsteady Pressure Variation with Fuel to Air Ratio.	144
Figure 74. Comparison of Temperature Contours for Full and Global Hydrogen Kinetics Models.	145
Figure 75. Water Production Rate Contours using the Full Kinetics Rate Set.	146
Figure 76. Comparison of Water, Hydrogen, Oxygen, and Hydroxyl Mass Fractions from PSR and CFD.	147
Figure 77. Comparison of Remaining Mass Fractions from PSR and CFD.	148

Figure 78. Comparison of Adjusted Water Production Contours for Global Hydrogen and Global Propane Reactions.	150
Figure 79. Comparison of Water Production Contours from the Two-dimensional and Three-dimensional CFD Codes.	154
Figure 80. Comparison of Normal Velocity Contours on Two Grid Refinement Levels.	155
Figure 81. Three-dimensional Cavity Geometries. Dimensions in cm.	156
Figure 82. 18 Degree Swept Cavity Configuration.	157
Figure 83. Axial Vorticity Generated by the Swept Cavity.	158
Figure 84. Axial Velocity Contours for the Symmetry Planes.	159
Figure 85. Velocity Vectors Off the Cavity Surface for the Swept Cavity Configuration.	160
Figure 86. Axial Velocities on the Symmetry Planes of the Variable Aspect Ratio Cavity Using a 51 X 51 X 53 Grid.	161
Figure 87. Time History of Integrated Cavity Water Mass for Three Dimensional Calculation.	162
Figure 88. Cross Plane Velocity Vectors and Water Mass Fraction Contours at the Domain Exit.	163
Figure 89. Operator Magnitude for Fourth Order Runge-Kutta Integration for Complex Values of $a\Delta t$	172
Figure 90. Largest Operator Magnitude for Third Order Adams-Moulton Predictor Corrector Method.	175
Figure 91. Operator Magnitude for Euler Implicit Method.	178
Figure 92. Comparison of Integration Methods for a Full Set H-O Ignition Calculation on an Expanded Scale.	179

List of Tables

Table	Page
Table 1. Flame Speeds in Air at Standard Temperature and Pressure.	16
Table 2. Reaction Rate Set for Hydrogen Oxygen Reaction Excluding HO ₂ and H ₂ O ₂	36
Table 3. Catalytic Efficiencies for Common Combustion Species.	37
Table 4. Perfectly Stirred Reactor Simulation Comparison for H-O Reaction	75
Table 5. Propane Perfectly Stirred Reactor Simulation Comparison.	76
Table 6. Ignition Time Variations with Elimination of Trace Species. (Time in milliseconds)	81
Table 7. CPU Times for Ignition Delay Simulations in Seconds.	84
Table 8. Lower Residence Times Calculated For Different Hydrocarbons, Including Reduced Rate Set Results.	85
Table 9. Increase in Lower Residence Time Due to Heat Loss.	101
Table 10. Heat Loss from the Heat Transfer Models for 1000 K / 500 K Walls.	102
Table 11. Computational Time Factors for Various Simulation Changes.	113
Table 12 Comparison of Baldwin Lomax Turbulent Viscosity with Shear Layer Mixing Length Model for $\phi = 0.2$ Case.	118
Table 13. Inflow Mach Number Change with Stoichiometric Ratio.	125
Table 14. Temperature Variation with Turbulence Model.	141
Table 15. Inflow Boundary Layer Temperature Effect on Water Production.	142

Table 16. Rate Set Input File Format.	181
--	-----

List of Symbols

a	Speed of Sound
A, B	General Reactant and Product Species
A_b, A_f	Backward and Forward Reaction Rate Constants
Ar	Cavity Aspect Ratio. L/D
C	Time Step Control Constant
C_D	Drag Coefficient
C_f	Skin Friction Coefficient
C_p	Specific Heat at Constant Pressure
D	Cavity Depth, Species Diffusion Coefficient
E	Activation Energy for Reaction Rate
E, F, G	Flux Vectors
F_i	Mass of Species i in the Perfectly Stirred Reactor
frr	Molar Forward Reaction Rate
ΔG^0	Gibb's Free Energy Change Across Reaction
h	Specific Enthalpy
H	Source Vector
ΔH_f	Reaction Heat Release
k	Stage of Integration for Each Time Step, Heat Transfer Coefficient
k_b	Reverse Reaction Rate Coefficient
k_c	Concentration Equilibrium Constant
k_f	Forward Reaction Rate Coefficient
$\ln()$	Natural Logarithm
L	Cavity Length
l_{mix}	Turbulent Mixing Length
M	Mach Number, Reaction Third Body Species
\dot{M}	Mass Flow Rate
M_c	Convective Mach Number
Mw_i	Molecular Weight of Species i
M_t	Total Gas Mass in the Perfectly Stirred Reactor
n	Time Step Number, Oscillation Mode Number
Δn	Difference in the Number of Moles of Gas on Each Side of a Reaction
$order$	Order of the Time Integration.
p	Temperature Exponent for Reaction Rate, Gas Pressure
Pr	Prandtl Number
Q	Residence Time Scale Factor
\dot{Q}	Heat Loss Rate from the Perfectly Stirred Reactor

R	Gas Constant
Re	Reynolds Number
R_u	Universal Gas Constant
rr_j	Molar Reaction Rate for Reaction j
S_i	Entropy of Species i per Unit Mass, Viscosity Coefficient
s_i	Chemical Species i
S_l	Laminar Flame Speed
S_t	Turbulent Flame Speed
$[s_i]$	Molar Concentration of Species i
T	Temperature
T_o	Viscosity Coefficient
T_f	Reference Reaction Flame Temperature
t	Time
Δt	Time Step
u, v, w	Velocity Components
$\tilde{u}, \tilde{v}, \tilde{w}$	Species Diffusion Velocity Components
U	Velocity Magnitude
\mathbf{U}	Conservation Vector
u'	Fluctuation Component of Turbulent Velocity
u_{cv}	Contravariant Velocity, Velocity in the Grid Line Direction.
V_{ol}	Volume of the Perfectly Stirred Reactor
Wa	"Cavity Air" Mass
x, y, z	Physical Coordinates
X	Distance Around Cavity
Y_i	Mass Fraction of Species i
Y_{oi}	Mass Fraction of Species i in the Flow Entering the Perfectly Stirred Reactor
α	Low Pass Filter Coefficient, Numerical Smoothing Coefficient
γ	Specific Heat Ratio
ϵ	Numerical Smoothing Coefficient
ζ	Nuzzelt Number
η, ξ, ζ	Computational Coordinates
Θ	Total Enthalpy of the Perfectly Stirred Reactor
μ	Viscosity
μ_0	Species Viscosity Coefficient
v'_i	Reactant Coefficient for Species i
v''_i	Product Coefficient for Species i
π	3.14159...
ρ	Mass Density

τ_r	Residence Time
$\tau_{xx}, \tau_{xy} \dots$	Stress Components
ϕ	Stoichiometric Value
Φ, Ψ	General Scalars
ϕ', ϕ''	Scalar Fluctuation Components
ω	Vorticity

Subscripts

i	Species Index, Grid Index
in	Flow into the Perfectly Stirred Reactor
j	Chemical Reaction Index, Grid Index
out	Flow Out of the Perfectly Stirred Reactor
t	Total or Stagnation
1	Above Shear Layer
2	Below Shear Layer
∞	Free Stream Condition

List of Terms and Acronyms

Term	Definition
CFD	Computational Fluid Dynamics - The field of numerical simulation of fluid flow.
Characteristic Time	The cavity length divided by the free stream velocity.
Equivalence Ratio	Stoichiometric Ratio.
Ignition	The rapid temperature rise phase of a combustion reaction.
Ignition Delay Time	The time required for ignition to occur starting with no intermediate species or product species.
Lower Residence Time	The lowest residence time where a perfectly stirred reactor can sustain a high degree of chemical reaction.
LDV	Laser Doppler Velocimetry - The use of laser interference fringe patterns to measure particle velocities.
Monotonic	Either a nondecreasing or nonincreasing function.
Perfectly Stirred Reactor	A chemically reacting volume where the contents are mixed uniformly throughout the volume.
PSR	Perfectly Stirred Reactor.
Residence Time	The mean time that a molecule remains inside a stirred reactor or flame holder.
Stationary	Wide sense stationary - The time mean is constant and the autocorrelation function is independent of time.
Stoichiometric	Pertaining to the balance point of the fuel and oxidizer that would completely consume both if complete combustion occurred.

Stoichiometric Ratio	The actual fuel to air ratio, divided by the stoichiometric fuel-to-air ratio.
Upper Residence Time	The lowest residence time where a perfectly stirred reactor must sustain a high level of reaction.
VLES	Very Large Eddy Simulation - Any CFD simulation where the larger scales of the turbulent fluctuations are numerically resolved.

Abstract

Scramjet combustor technology is currently under development by the Air Force and a key component of scramjet combustors is the flame holder. This study investigated the flame holding properties of recessed cavities in supersonic flow using numerical analysis techniques. The numerical models developed for this analysis included several perfectly stirred reactor models. A simplified analytical model indicated that an important property for flame holding was the lower residence time. This model also showed that under certain conditions, the solution for combustion systems was not unique. It was found, that the ignition delay time and lower residence times varied by orders of magnitude with reaction mechanism. The perfectly stirred reactor model also indicated that trace species diffusion should increase flame spreading rate, and that heat loss reduces flame holding limits. Reduced mechanisms for hydrocarbons were also shown to have orders of magnitude variation in lower residence times. After nonreacting calibration, two-dimensional simulations confirmed the perfectly stirred reactor results for blowout limits. Also, the effect of trace species diffusion on flame spreading was shown to be negligible, and the reduced flammability with heat loss was confirmed. Lowering the temperature of the inflow boundary layer was shown to reduce the flammability limits. Cavity sweep and cavity sweep with variable aspect ratio were shown to generate axial vorticity. The variable aspect ratio cavity was demonstrated to slightly enhance flame spreading. The methodology developed in this research provides a design guide for the size of cavity required to provide flame holding for a scramjet combustor. Also, reduction of heat losses was shown to be a method to improve flame holding performance without increasing the cavity size.

NUMERICAL ANALYSIS OF TWO AND THREE DIMENSIONAL RECESSED FLAME HOLDERS FOR SCRAMJET APPLICATIONS

1. Introduction

The US Air Force has realized that for applications utilizing the efficiency of scramjet propulsion systems with storable fuels, the propulsion technology base must first be expanded. The Wright Laboratory HyTech program was established to develop the technology required to build a hydrocarbon fueled scramjet propulsion system. According to D. Bushnell, Chief Scientist at NASA Langley Research Center, "ignition and flameholding [are] a first order issue" for endothermic hydrocarbon scramjet applications(1). The characteristics of recessed cavity flame holders for scramjet applications were investigated in this research.

1.1. Problem Statement

As flight speeds increase, the performance of air breathing propulsion systems is increasingly adversely affected by losses in all flow components. Due to the complexity of the physics and the difficulty in testing these systems, the physical characteristics of many of the propulsion system components are not well understood. In order to make a rational design choice for the type of flame holder to use in a supersonic combustion ramjet (scramjet), the physics of many types of flame holders must be characterized.

order to make a rational design choice for the type of flame holder to use in a supersonic combustion ramjet (scramjet), the physics of many types of flame holders must be characterized.

Recessed flame holders, because of their low total pressure losses and wide flammability limits, as demonstrated in low speed flows (2), show potential for scramjet propulsion systems. In order to apply cavity flame holders, some guidelines on the size and type of flame holder to use are needed. A better understanding of the flow and combustion characteristics of recessed flame holders in supersonic flow would help in the design of scramjet systems. Hence, the potential advantages of recessed flame holders could be exploited to give superior scramjet propulsion system performance. Two problems associated with recessed flame holders in low speed flow are the low flame spreading angle, and the high heat fluxes within the cavities (3). Hence, a portion of this research was to investigate if cavity sweep or variable aspect ratio could be used to generate axial vorticity. The actively cooled, high-temperature technology available today has the potential to withstand the high cavity heat-flux loads.

As mentioned above, hydrocarbon scramjet propulsion technology is currently under development under the HyTech program. The HyTech program aims to develop the technology required to build a hydrocarbon scramjet propulsion system. A part of the technology required in order to design a scramjet propulsion system is an efficient method of flame holding. The current program examined the flame holding properties of recessed cavity flame holders in supersonic flow. The test condition was based on the contention that the lower speed operating range of the scramjet propulsion system is believed to be the most difficult design point for flame holding.

1.2. Scope of Research

An objective of this research was to investigate recessed cavities as flame holders for scramjet applications. The key characteristic for a flame holder is how well it holds a flame. This research focused on determining the flammability limits of cavity flame holders in supersonic flow using numerical analysis methods. The determination of the size of flame holder required to provide flame stabilization, and what conditions effect the flammability limits, were important parts of this research. The other major part of scramjet combustor design, fuel mixing, was not a part of the current research, therefore, the fuel was considered premixed for these flameholding studies. Also, evaluating the validity and usefulness of current combustion models was a part of this research.

Perfectly stirred reactor (PSR) models were developed for global flame holding analysis. An analytical model was developed that showed that the lower residence time was a flame holding limit, and not an optimal condition as indicated by Glassman (3). A method for calculating the flame holding limit using detailed chemical kinetic rate sets was also developed. The PSR models were used to analyze the effects of inflow temperature, heat loss, trace species diffusion, chemical kinetics rate set variations, fuel-to-air ratio, and fuel type. The PSR model was applied to determine global rate equations for use in the multi-dimensional simulations. The global rate equations significantly reduced the computational requirements so that many cavity variations could be investigated.

A unique part of this research was that it combined multi-dimensional computational fluid dynamics (CFD) analysis with the global PSR analysis. The combined approach yielded an accurate assessment of the level of detail required for

design of cavity flame holders. With two-dimensional CFD analysis; the effects of fuel-to-air ratio, residence time, free stream Mach number, viscosity, inflow boundary layer thickness, upstream wall temperature, fuel type, and chemical kinetics models were investigated. Three-dimensional CFD analysis was required to investigate the effects of cavity sweep and cavity sweep with variable aspect ratio.

The results of this research apply directly to the current programs for scramjet technology. The design guidelines and methods developed in this research are being applied to hydrocarbon scramjet combustor designs currently planned for testing.

1.3. Approach

This research was conducted with the aim of providing valid and useful design tools and guidelines. The approach of combining several levels of analysis provided design guidelines and an assessment of the level of complexity required in the design tools. The results of the lower complexity tools were systematically validated with the more complex tools. Each tool was validated before it was applied in this research.

The first step in the analysis was to develop perfectly stirred reactor models. A simplified perfectly stirred reactor model was used to analyze flammability and residence time characteristics. A method for determining the flammability limit of a perfectly stirred reactor, the lower residence time, was developed. Combustion reaction mechanisms and reduced kinetics sets were compared using perfectly stirred reactor models. The model was further used to calibrate a global reaction model for multi-dimensional simulations, to find ignition delay and residence time characteristics, and to analyze the effect of fuel-to-air ratio variation with full and reduced mechanisms. Lastly,

the model was used to simulate shear layer reactions and for estimating the effects of heat loss.

In order to verify the perfectly stirred assumption and to conduct further investigations into the flame holding properties of cavity flame holders, two and three dimensional simulations of a cavity flame holder were performed. First, the reacting computational fluid dynamics (CFD) codes, SPARK and GASP, were validated with non-reacting data. Several turbulence models, chemical kinetics models, and boundary conditions were incorporated into the SPARK code for this research. The CFD results were compared with the perfectly stirred reactor results. A method was developed for determining the residence time of a cavity. The effects of turbulence modeling, fuel-to-air ratio, cavity size, free stream Mach number, full and global reaction sets, and propane fuel were investigated. The baseline case was for a Mach 4.0 free stream, where flame holding should be more difficult due to the lower temperatures. The baseline geometry (Figure 1) was chosen to be similar to one that was experimentally shown to be effective in subsonic flow (2).

Three dimensional simulations were also performed. The objective of these simulations were to determine if cavity sweep could generate axial vorticity to enhance

Static Pressure = 42058 Pa
Static Temperature = 480 K
Velocity = 969.75 m/s
Boundary Layer Thickness = .13 cm

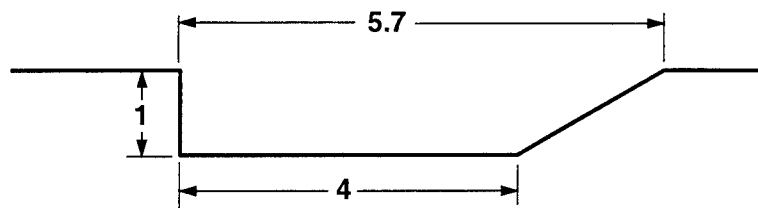


Figure 1. Baseline Cavity Dimensions in cm.

downstream mixing. Cavity sweep and variable aspect ratio were investigated as means to redirect the cavity vorticity. Both non-reacting and reacting simulations were performed.

1.4. Key Results

The research presented in this dissertation represents several contributions to the state-of-the-art in scramjet and combustion technology. The use of the PSR model to determine the blowout limits of a flame holder was developed and validated in this research. A methodology for evaluating and tuning reduced kinetic rate sets to give accurate blowout limits was also developed. The inflow temperature and heat loss were shown to effect flame holder performance using the PSR model. Also, detailed chemical kinetics models were shown to have significant variations of ignition delay and lower residence time in the pressure and temperature range of interest in scramjet combustors.

The CFD simulations validated the PSR model for flame holding, with the chemical kinetics the same in both cases. The CFD methods showed that heat loss from the cavity or upstream of the cavity, reduces the flame holding effectiveness of a cavity flame holder. A smaller cavity was also shown to reduce flame holding effectiveness. Chemical kinetic variations were shown to follow the same trends given from the PSR model. Turbulence variations and inflow boundary layer thickness were shown to have little effect on flame holding. An efficient method for averaging the numerically resolved Reynolds averaged turbulent flow quantities was also applied in this research. The progression of the flame front as conditions approached blowout was illustrated. The unsteady flow oscillations associated with cavity flows were shown not to be enhanced by the chemical reactions. Flame holding with hydrocarbon fuel was also demonstrated.

Three dimensional cavity geometries were also shown to slightly enhance flame spreading downstream of the cavity.

This research was responsible for two configurations being tested at the United Technologies Research Corporation under the Hydrocarbon Scramjet Technology Program. The results of the research will apply directly to the combustor design for the Hypersonic Technology Program of the Propulsion Directorate. The methodology developed in this program for flame holder analysis also applies to other combustion systems.

1.5. Overview of Dissertation

Chapter 1 provides a brief description of this research. Chapter 2 summarizes background information on scramjets and flame holders. A description of the methodology is given in Chapter 3. The results from the perfectly stirred reactor analysis are presented in Chapter 4. Chapter 5 covers results from the two-dimensional analysis, while the three-dimensional results are presented in Chapter 6. Chapter 7 summarizes this research, and recommendations are given in Chapter 8.

2. Background

In this chapter a brief background is given. First, an overview of scramjet propulsion systems is presented including hydrocarbon scramjets. Then, a brief review of chemical reaction and flame propagation demonstrates the purpose of a flame holder. Different types of flame holders are then summarized. Previous methodologies for analyzing flame holders is also presented. Finally, the prior research on cavity flame holders and related cavity flows is discussed.

2.1. Scramjet Overview

A ramjet engine is a jet propulsion system where the incoming air is compressed by the forward momentum of the engine. The pressure of the air is increased by decreasing the velocity of the incoming air to low subsonic velocities (relative to the engine). Heat is then added to the air by combustion of a fuel. The velocity of the air is then increased by expanding it through a nozzle, to greater than the inflow velocity. A supersonic combustion ramjet, scramjet, is a ramjet where the air flow through the combustor remains supersonic, instead of being compressed to subsonic velocities.

Scramjet propulsion systems have the potential to exceed the propulsive efficiency of other propulsion systems at high speeds as illustrated by the thrust specific impulse (ISP) curves shown on Figure 2. The ISP of a propulsion system is the net thrust normalized by the fuel flow rate. Since air-breathing systems do not carry their own oxidizer, they typically have much greater ISP values than rocket systems. Conventional rocket systems have a maximum ISP of about 470 seconds.

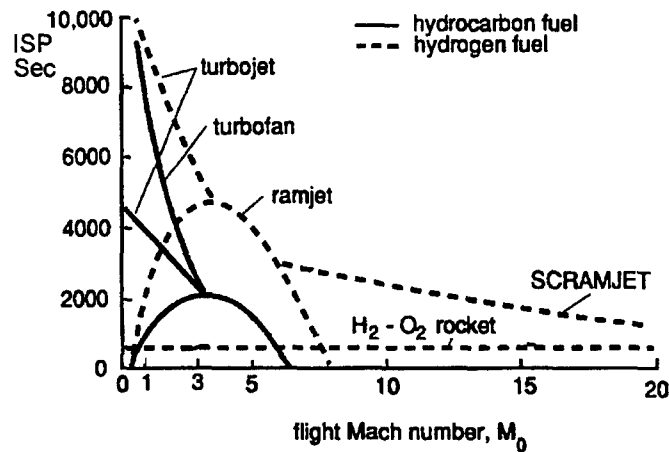


Figure 2 Propulsion Performance for Various Systems as Flight Speed Increases. (4:402)

The excessive flow temperatures, associated with high-speed flight, limit the propulsive efficiency of conventional turbojet and ramjet systems (4). Uncooled solid objects in contact with the high speed flow have surface temperatures near the stagnation temperature of the free stream flow. The high-speed flight performance of turbojets is limited by the rotating machinery material limits and the energy removed from the flow by the turbine to compress the incoming air. The ramjets are limited by the ability of fuels to react in a manner that will release energy at very high temperatures. This is a result of the chemical equilibrium state tending toward the small free radicals at high temperature, which reduces the energy available for propulsion (see Sect. 4.4.1 and 4.4.2 for examples). The scramjet circumvents these limitations by removing the requirement of decelerating the incoming air to subsonic velocities within the engine. Thus, the core temperatures and pressures in scramjet systems are much lower than other air-breathing systems at high speeds. Moreover, as the flight speed continues to increase, the net propulsive thrust becomes a smaller fraction of the gross air stream thrust entering or

leaving the engine. The small fraction of net thrust makes the performance of scramjet systems very susceptible to drag losses in the inlet, combustor and nozzle. The drag of conventional flame holders may greatly reduce available thrust of high-speed propulsion systems. Also, the extreme thermal environment in a scramjet combustor would most likely destroy conventional protrusive flame holders.

Another major issue with scramjet propulsion systems is the fuel and air mixing process. The fuel and air must be mixed and reacted before it leaves the combustor, which may be only a few milliseconds. This fuel and air mixing must also be accomplished without large total pressure losses. One proposed method to accomplish this mixing is by introducing axial vorticity near the fuel and air interface. This vorticity then stretches the interface, thus increasing the contact area between fuel and air, resulting in more rapid mixing. Due to the high momentum of the air stream, it is difficult to get the fuel into the core flow. A pair of axial vortices with the proper orientation will lift out of the boundary layer into the core of the air stream. Figure 3 illustrates this lifting of vortices in a boundary layer flow. Several researchers have demonstrated the applicability of using axial vorticity increase mixing in scramjet combustors (5-14). Swept cavities were investigated in the current research to examine the possibility of inducing axial vorticity to enhance mixing.

2.2. Hydrocarbon Scramjets

Hydrocarbon fuels ignite much slower than hydrogen, and must be vaporized in order to react. Both of these phenomena make supersonic combustion of hydrocarbon fuels very difficult. Researchers in Russia (16-18) have demonstrated supersonic combustion of hydrocarbon fuel, kerosene, using recessed flame holders. This

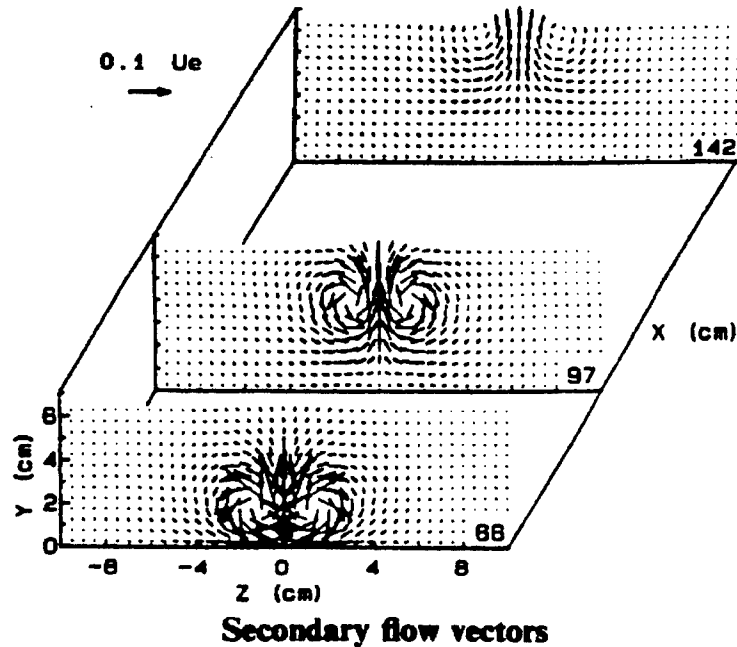
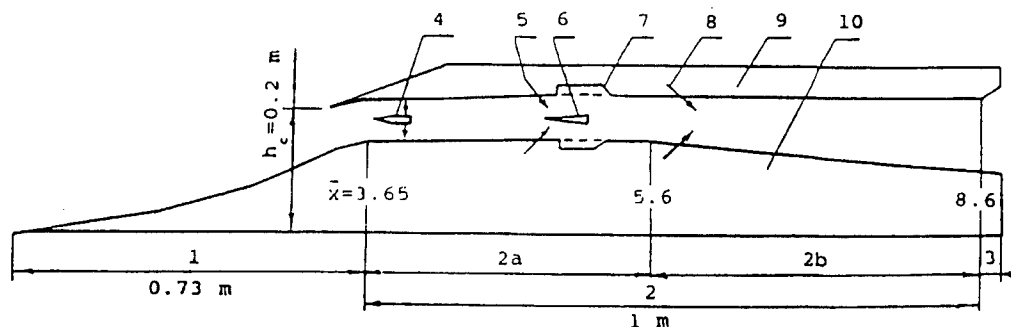


Figure 3. Vortices Lifting from a Wall Boundary Layer
(15:820)

demonstration in most cases, required the injection of additional gaseous hydrogen into the recess to maintain combustion (Figure 4). Also fuel vaporization was enhanced by the addition of hydrogen gas bubbles to the fuel before it was injected. These bubbles rapidly expand after the fuel is injected into the lower pressure air flow thereby shattering the liquid into small droplets, that vaporize quickly.



Scheme of the investigated 2-D
scramjet
1-inlet, 2-combustor (2a-constant area
section, 2b-expanding section), 3 -

nozzle, 4-kerosene injector, 5, 8- H_2
injectors, 6-hydrogen strut-stabili-
zator, 7-cavity flameholders, 8-cowl
(upper wall), 9-bottom wall

Figure 4. Hydrocarbon Scramjet Tested at Central Institute for Aviation Motors (17:5)

For high free stream Mach numbers, a cavity used in conjunction with a ramp fuel injector has been shown to improve flammability limits (19) over those of the ramp alone. Facility total temperatures were representative of Mach 6 to 8 free stream conditions. Both hydrogen and ethylene fuels were shown to sustain combustion. In many cases both fuels autoignited with the combination ramp and cavity.

Researchers at the Johns Hopkins University, Applied Physics Laboratory (JHU/APL) proposed a hydrocarbon scramjet design called the dual combustor scramjet (20). In this design, a portion of the inlet air was diverted into a subsonic combustor. The high temperature, radical rich reaction products from this combustor are then injected into the supersonic stream to initiate the supersonic combustion. A variation of this design using smaller dump combustors, known as pilot fuel injectors, was tested at United Technologies Research Center (21). The inflow conditions for this research were from the conditions used to test the pilot fuel injector. The most difficult condition for sustaining combustion was reported to be the Mach 4 free stream case, which was chosen as the baseline case for this research. However, other Mach number cases were also simulated in this research.

For typical scramjet flows, the static pressure is high enough to support combustion of hydrocarbon fuels and the temperature in the boundary layer is heated by viscous forces to relatively high levels. The combination of these effects may support hydrocarbon ignition in a recessed flame holder. The use of a recessed flame holder in place of the pilot fuel injector would eliminate additional flow losses associated with the subsonic combustor and inlet. Also, the cooling requirement for a recess should be less than for a pilot injector because of the reduced area in contact with the hot gasses.

2.3. General Chemical Reaction Progression

Figure 5 shows a typical hydrogen oxygen reaction as it progresses in time. First, the molecules decompose into free radicals; O, H and OH. Then, when the concentration of free radicals reaches a critical value they rapidly combine to form the final product species, H_2O . The initial phase, where energy is absorbed to form free radicals, is the induction phase. When sufficient concentrations of free radicals are formed, the formation of final products releases enough energy to raise the temperature. The temperature rise in turn causes the formation of more radicals, leading to a very rapid reaction and heat release. Finally, the concentration of reactants diminishes and the reaction exponentially converges to equilibrium concentrations. Intermediate species often exceed their equilibrium concentration near the ignition phase of the reaction. The

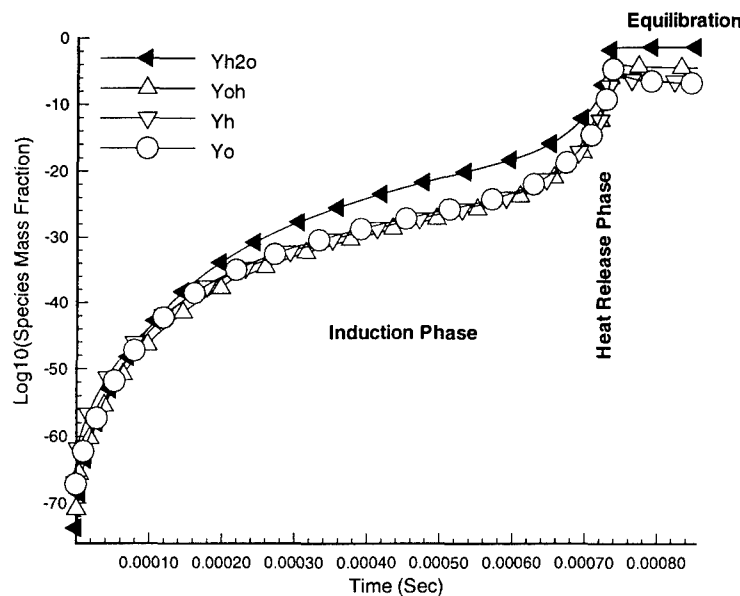


Figure 5. Species Mass Fractions for a Hydrogen Oxygen Reaction Progressing in Time as Calculated by a Time Dependent Perfectly Stirred Reactor Code.

important phase for flame holding studies is the induction phase. The induction phase is also the most difficult to study or model, since it involves the competition of several individual reactions that form and consume trace amounts of free radical species. The mass fractions of these species are very low, which makes them difficult to be measured and calculated.

2.4. Flame Propagation

Premixed and diffusion flames are the two main model reactions typically used for analyzing combustion reactions. The flame is the location where the high heat release rate occurs. A premixed flame is where the reactants are premixed and the flame front propagates through the mixture. The flame propagates due to diffusion of the trace species and thermal conduction, initiating the rapid reaction phase. Figure 6 illustrates a premixed flame and a diffusion flame. The one-dimensional speed of propagation of a premixed flame in a laminar flow is called the laminar flame speed. The other type of

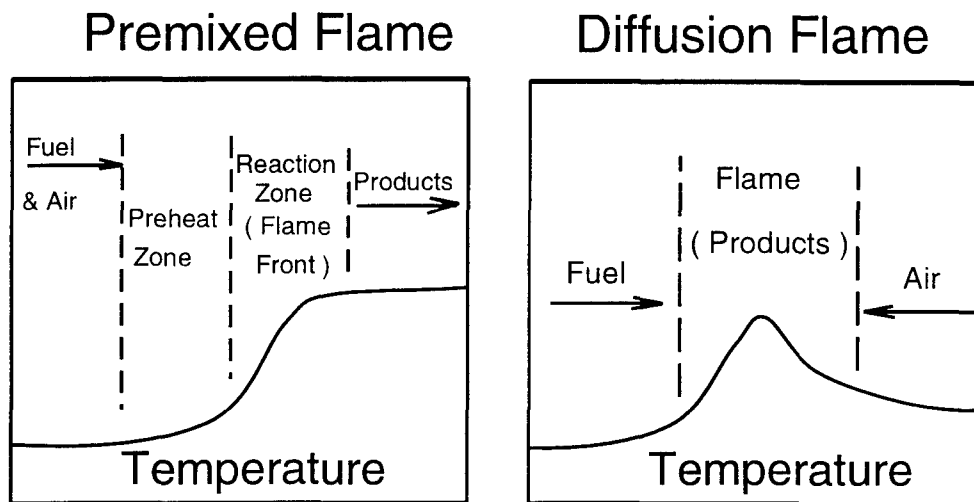


Figure 6. Flame Propagation Types.

flame is the diffusion flame where the reactants are not premixed, and the diffusion of reactants controls the progression of the reaction. The diffusion flame illustrated in Figure 6 shows that the propagation for the flame is dependent on the difference between the fuel and air diffusion velocities. Typically, diffusion flames do not propagate but only grow wider. Both types of flame propagation are similar since they are both controlled by diffusive processes.

In turbulent flow, the diffusion of heat and species is increased, and the effective flame area is increased due to the distortion of the flame front. Both of these phenomena tend to increase the flame speed relative to laminar flames. A correlation for the relation between laminar and turbulent flame speed (3:178) is given by

$$S_t = S_l \sqrt{1.0 + \frac{\overline{u'^2}}{S_l^2}}$$

where S_l is the laminar flame speed, S_t is the turbulent flame speed and u' is the turbulent fluctuation velocity component. Laminar flame speeds for several fuels in air at standard temperature and pressure are summarized in Table II (22:12). Common flow velocities in combustors are 50 meters per second for turbojets, 100 meters per second for ramjets, and 800 to 8,000 meters per second for scramjets. Also shown in Table II are turbulent flame speeds from the above correlation, with an assumed free stream turbulence intensity of 10%. Clearly, a one dimensional flame could not be sustained in practical propulsion combustion systems, since the flame propagation speed is significantly lower than the flow speed through the combustor.

Table 1. Flame Speeds in Air at Standard Temperature and Pressure.

	S_f (m/s)	S_f (m/s) U= 50 m/s	S_f (m/s) U= 100 m/s	S_f For Large U
Hydrogen	2.83	5.8	10.4	$\approx 0.1 \times U$
Acetylene, C_2H_2	2.67	5.7	10.4	
Butane, commercial	0.87	5.1	10.0	
Propane, commercial	0.85	5.1	10.0	
Ethylene, C_2H_4	0.77	5.1	10.0	
Ethane, C_2H_6	0.48	5.0	10.0	
Propane, C_3H_8	0.46	5.0	10.0	
Methane, CH_4	0.45	5.0	10.0	
Butane, n- C_4H_{10}	0.40	5.0	10.0	
Natural Gas	0.30	5.0	10.0	

2.5. Flame Holders

In order to maintain a flame in a jet engine combustor, some ignition source is required to start the reaction. Then, the flame can propagate, normal to the flow velocity, to fill the combustor. Some ignition sources are illustrated in Figure 7. Important parameters for flame holders are the flow velocities where a flame is no longer held and the drag or total pressure loss as a result of the device. Even though heated plates, lasers, and electric arcs induce minimal pressure loss they require a large external power source thus making them impractical. The storage and handling of highly reactive chemicals is dangerous, so operational constraints usually eliminate them from further consideration. The other methods shown all involve the establishment of recirculation zones where

some hot reaction products are carried upstream in a separated flow region to ignite the oncoming stream. The choice of flame holding method depends largely on a balance between combustor size and weight, pressure loss, and flammability limits. Also affecting the choice of flame holder type are material temperature and structural limitations.

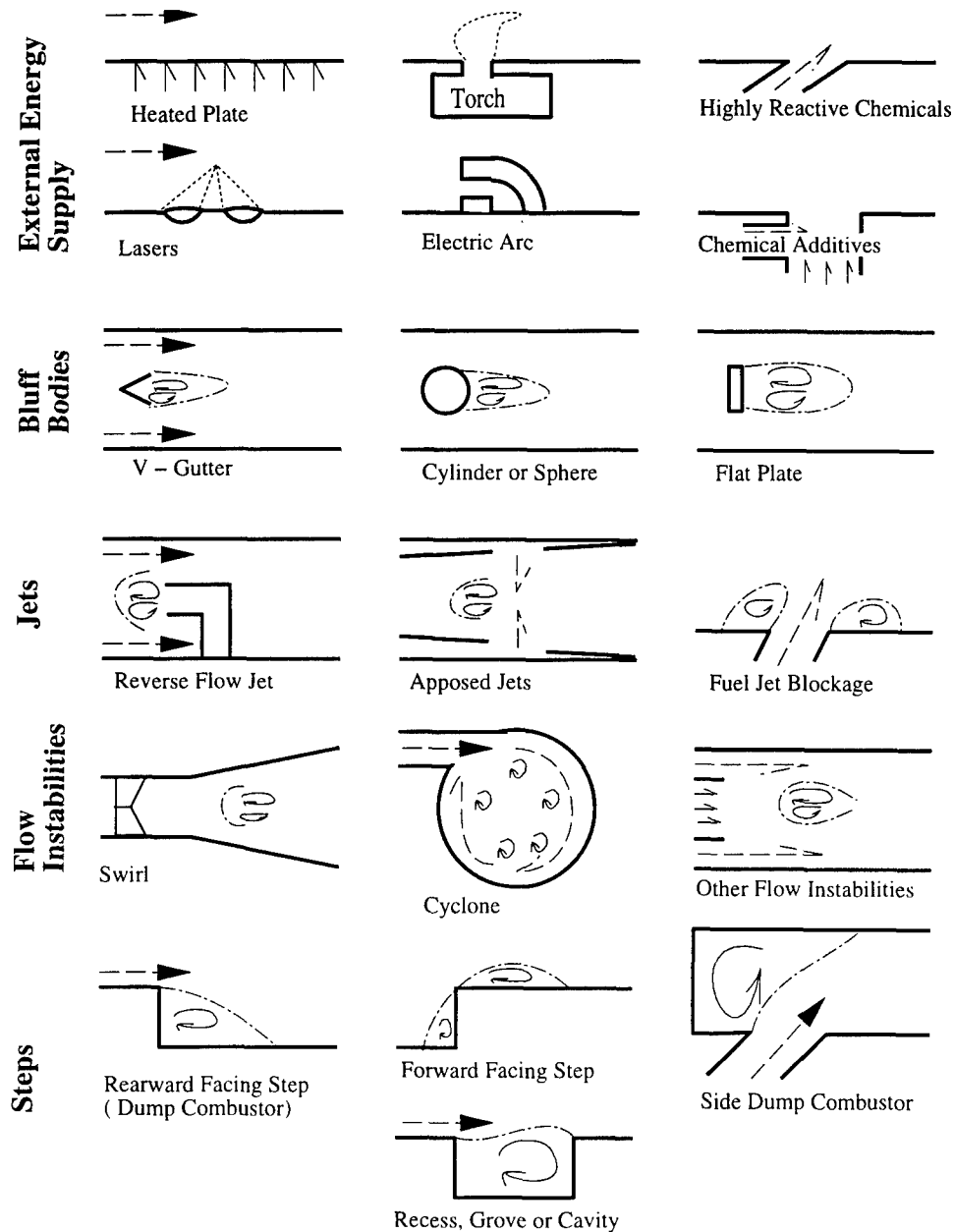


Figure 7 Various Types of Flame Holders

With bluff bodies, jets and vortex breakdown flame holders, the flame can be anchored to multiple points in the interior of the flow so that the transverse distance the flame must spread to fill the combustor is reduced. Also, these flame holders generate turbulence that increases the lateral flame spreading rate. Both of these phenomena allow a shorter combustor length, which could result in lighter weight systems. However, the turbulence generation causes a total pressure loss that decreases the available thrust from a propulsion system. Increasing the number of flame holders decreases the required combustor length, but induces larger total pressure losses. Hence, combustor design depends largely on balancing the losses, efficiency and the combustor size.

For a given drag coefficient, the drag force increases as the flow velocity increases. Therefore the higher drag methods tend to be more suitable for lower speed flows. Typical turbojet main combustors use opposed jet flame holders that generate high turbulence levels, while afterburner combustors use V-gutter flame holders to reduce total pressure losses in the higher velocity flows. For ramjet combustors in missile applications, the reward facing step is the most common flame holding method. With a step flame holder, the hot reaction products are next to the wall, resulting in high wall heat fluxes. However, the typical short mission length of missiles makes the thermal protection problem much simpler.

A recessed flame holder is a modification of a step flame holder, where the recirculation zone is contained in a cavity. This type of flame holder has the potential to have very low total pressure losses due to the pressure forces on the downstream and downstream faces being nearly equal. For open cavities in supersonic flow, the shear layer spans the cavity so that shock losses are also relatively small. Generally, the disadvantages with this class of flame holders are they do not generate high turbulence

levels and they must be located on walls resulting in high wall heat fluxes. In a recent scramjet test (23:7) with recessed flame holders, the cavity wall temperature was 1100 °C, while the combustor wall temperatures were less than 700 °C. The low turbulence levels make the flame spreading rate slower, thus requiring longer combustors for the same combustion efficiency with this type of flame holder.

2.6. Flame Holding Analysis

There are two main techniques used for the analysis of flammability limits as summarized by Curran (24). Zukoski and Marble (25) proposed using the length of the recirculation zone and the free stream velocity to correlate an ignition time. The other major approach is to approximate the recirculation region as a perfectly stirred reactor (24).

In the ignition time concept, the time that the unreacted fluid is in contact with the hot recirculation zone products is proposed to govern ignition. In order to avoid confusion with the ignition delay time, this time will be referred to as contact time for the remainder of this report. The idea is that the free stream reactants require a minimum time in contact with the products before they can ignite. The time that the reactants are in contact with the products is estimated as the recirculation zone length divided by the free stream velocity. This concept is applied by experimentally measuring the recirculation zone length, fuel to air ratio and velocity at blowout for fixed inflow temperature and pressure. A typical experimental correlation is of the form shown in Figure 8. The stoichiometric ratio (ϕ) is the fuel-to-air ratio normalized by the ideal fuel-to-air ratio. The ideal fuel-to-air ratio is the fuel-to-air ratio that would result in complete

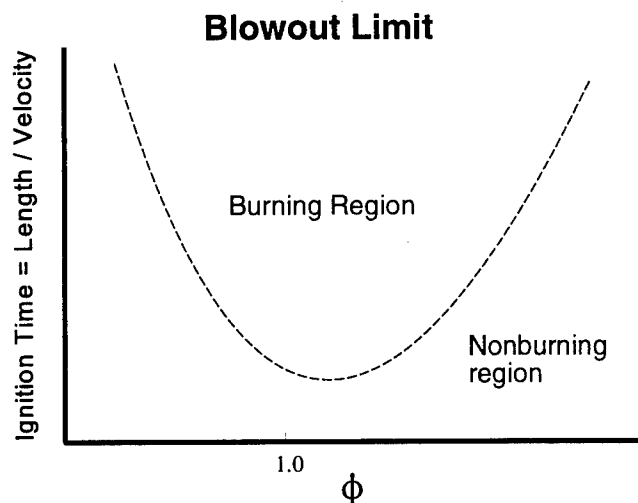


Figure 8. Typical Blowout Limits for Ignition Time Concept.

consumption of both fuel and oxygen if the chemical reaction were to progress to completion.

The other major concept is the stirred reactor concept, where the recirculation zone is considered to be approximated by a perfectly stirred reactor. From experimental studies using highly turbulent reacting spheres, a blowout correlation of the form shown in Figure 9 is obtained. The correlating parameter of $\dot{M} / (Vol \cdot p^n)$ can be expressed as a residence time function by using the ideal gas law

$$\frac{\dot{M}}{Vol \cdot p^n} = \frac{\dot{M}}{Vol \cdot \rho} \cdot \frac{\rho}{p^n} = \frac{1}{\tau_r \cdot \rho^{n-1} \cdot R^n \cdot T^n}$$

where \dot{M} is the mass flow rate through the reactor; Vol is the volume of the reactor; p is the pressure; ρ is the gas density; R is the gas constant, and T is the static temperature.

The residence time correlation then separates the flow field effects, τ_r , from the chemical

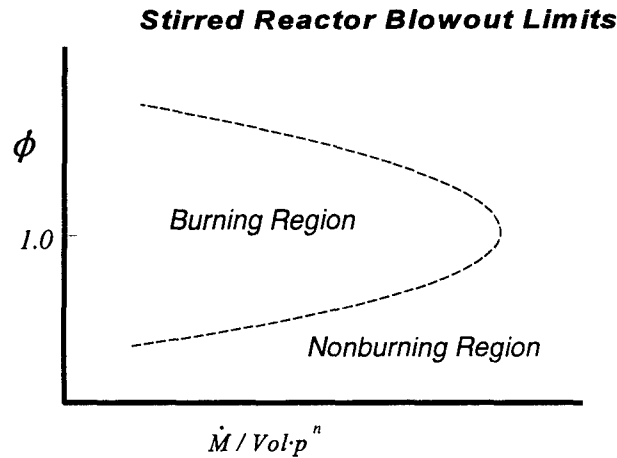


Figure 9. Typical Blowout Limits for Stirred Reactor Experiments.

kinetic effects. In addition, the prior correlation parameter was popular because the quantities in the parameter are easily measured.

For a combustor, the lean flammability limits are often correlated by $U^\alpha / (Ls^\gamma \cdot p^\beta \cdot T^\delta)$, where α , β , γ and δ are experimentally determined constants (24,26), and Ls is a length scale. In this approach, the residence time is considered to be proportional to Ls^γ / U^α if the total temperature is used for T . Ls could be any physical characteristic dimension of the flame holder. For bluff bodies, Ls is often taken as the diameter, while for a backward step, the step height is a common length scale (26).

As discussed further in Sect 3.2.4, the recirculation zone length divided by the velocity should be proportional to the reciprocal residence time. Therefore, because experimental data was used to obtain the correlation curves, the correlation was independent of the blowout limit analysis method.

2.7. Cavity Flame Holders

The flammability limits for several cavity shapes were investigated by Huellmantel et al. (2). They used premixed propane air at velocities below 110 m/sec and atmospheric pressures. The floor of the baseline cavity was 2.54 cm long, followed by a 30 degree ramp. The depth of the baseline cavity was 0.63 cm. The blowout data of many of the geometries tested were plotted around one curve, the curve is labeled cavity number 2 in Figure 10. Holding the depth, D , constant and varying the length, L , they changed the contact time without changing the residence time. Very short cavities ($L/D \approx 1$) did not stabilize a flame. A slightly longer cavity ($L/D \approx 2$) had flammability limits near those of the baseline geometry.

It was demonstrated that cavity flame holders had better flame holding characteristics with lower total pressure loss than a V-gutter flame holder (Figure 10).

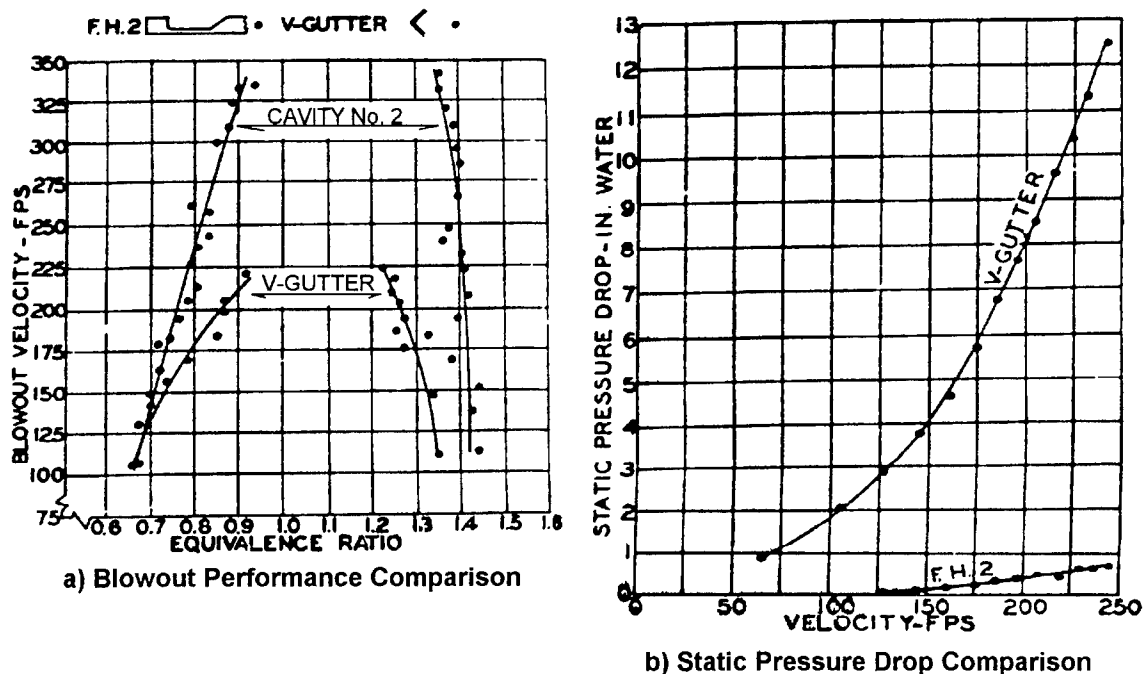


Figure 10. Comparison of 90 degree V-Gutter (37.5% Blockage) with the Baseline Cavity Flame Holder, No. 2 (2:34)

Other findings included that the cavity needed to have sufficient volume to provide adequate flame holding, and that the upstream corner had to be sharp enough to cause separation. The baseline geometry for the current research was chosen to correspond to the flame holder number two shown here.

The depth of one cavity was reduced, while the length was maintained the same. Ideally, this would separate the effects of contact time and residence time by reducing the residence time with a constant contact time. The cavity exhibited greatly reduced flammability limits as the depth and hence residence time (Sect. 3.2.4) was reduced (Figure 11). Later Povinelli (27) successfully applied the ignition delay concept to the reduced depth cavities. However, he used a length of 5 times the depth, instead of the cavity length as the recirculation zone length. The methodology he used to determine the length was not described.

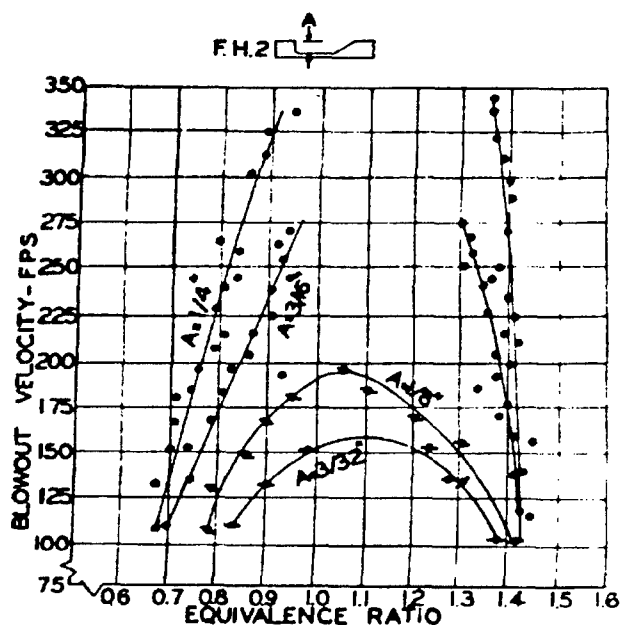


Figure 11. Effect of Cavity Depth on Blowout Velocity.

An axi-symmetric cavity similar to the drag reduction device of Little and Whipkey (66) was tested by Hsu et al. (28). The maximum velocity was only 42 m/sec and fuel and air were injected on the downstream cavity face. This combustor design showed very wide flammability limits with low pressure losses.

A flame stabilization device similar to a cavity was tested in supersonic flow by Niioka et al. (29). The divided strut flame holder tested is illustrated in Figure 12 with dimensions in millimeters. The fuel was hydrogen gas at room temperature. The test section pressure was "a bit below atmospheric." The blowout plots of total temperature versus hydrogen flow rate are difficult to interpret because at fixed Mach number reducing the total temperature reduces the chemical kinetic rate, the residence time and the contact time. As the separation distance (L) was increased, two stable combustion regions were observed. This was explained as an effect of residence time, and LDV data was used to estimate the residence time. They defined the residence time as the separation distance divided by the average velocity on the centerline. The LDV data however showed that the flowfield was dominated by the fuel injection when the interval distance was small. On the other hand, the fuel injection had less impact when the

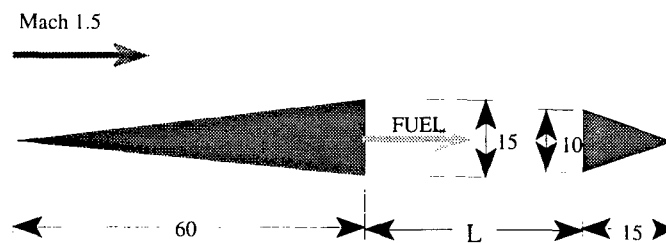


Figure 12. Divided Strut Flame Holder

interval was long. The effect of fuel injection on the flow field could have caused the dual stability range. This study was not used for validation in this research because of the effect of the fuel injection.

Results for a cavity in conjunction with a ramp fuel injector were presented after much of the current research was completed(19). They showed that the small (3 by 3 mm) cavity enhanced flame holding and combustion efficiency. They also reported that for some conditions, reaction occurred in the cavity that did not spread to the free stream flow. Similar findings are reported in Chapter 5 of this document.

The mixed results of past research indicated that the fluid dynamics and chemical kinetics associated with cavity flame holders are very complex and not well understood or characterized. This lack of understanding was one of the motivating factors in defining the present study. The present research has helped to aid in the understanding of cavities for use as flame holders in supersonic flows.

2.8. Cavity Flows

Cavity flows have been the subject of many investigations. On aircraft, cavity type geometries are present as landing gear bays and bomb bays. The inherent unsteadiness of cavity flows can lead to adverse effects from structural loading and induced drag. Due to the adverse effects of the unsteady flow within cavities, they have been the focus of much research. There have been at least four review articles on cavity flows (30-33). Computational fluid dynamics (CFD) methods have proven to be an important tool in the analysis of unsteady cavity flows (34-52).

2.8.1 Cavity Classification. Rockwell (31) classified cavity flows by the type of instability of the unsteady flow. His classification divides the instabilities into three classes. A fluid-dynamic class where the shear layer instabilities interact with the cavity to produce pressure oscillations. A fluid resonant class that is further divided into shallow ($L/D > 1$) and deep ($L/D < 1$) cavities. This class oscillates at an acoustic mode of the cavity. Rockwell also includes Helmholtz resonators in this class. The final class is fluid-elastic, where displacements of the solid surfaces play a part in the oscillation cycle.

Another classification for shallow cavities is by the flow field. The cavity is called an open cavity when the shear layer spans the opening of the cavity. A closed cavity is where the shear layer attaches to the floor of the cavity dividing the cavity into a back facing step followed by a forward facing step. For a rectangular cavity, the flow is generally open for $L/D < 10$ and closed for $L/D > 13$.

The cavity flame holders studied in this investigation are of the open cavity type. The open cavity provides for a long contact time for the cavity flow to interact with the core flow and a large volume giving a long residence time for the reaction.

2.8.2 Cavity Instability Cycle. The dominant fluid-dynamic instability for open cavities consists primarily of a shear layer oscillation caused by unsteady pressure at the cavity leading edge (34,30). This shear layer oscillation then impinges on the downstream edge of the cavity generating a pressure wave as the shear layer moves down into the cavity. This pressure wave moves upstream to the cavity leading edge to complete the cycle. Heller and Bliss (30) used an unsteady potential analysis of a pressure matched thin shear layer above the cavity to show that a downstream moving pressure wave is amplified by the shear layer displacement while an upstream traveling

wave is damped. The amplification of the downstream moving wave explains why almost all cavity flows are unsteady. This instability cycle has been shown to be two-dimensional in nature both experimentally and computationally (39).

Many methods have been shown to reduce the oscillation amplitude (30,41,53,54). Successful methods for reducing the dominant oscillation include sloping the downstream wall, placing a fence or vortex generators near the upstream edge, using a porous wall with a cavity behind it, placing an object in the shear layer, mass injection into the cavity and inflow boundary layer modification. However, the broadband noise level often increases with the reduction in the dominant tone amplitude.

For determining the frequency of oscillation, a semi-empirical equation derived by Rossiter, with a modification by Heller et al. (30), has been fairly successful, generally within 20%, (30-33). The modification accounted for a recovery factor of one to determine the temperature within the cavity. The recovery factor is the fraction of kinetic energy that results in a temperature rise on a boundary wall. The equation with modification is

$$f_n = \frac{U_\infty}{L} \cdot (n - 0.25) \cdot \left[\frac{M}{\left(1 + \frac{\gamma - 1}{2} \cdot M^2\right)^{1/2}} + \frac{1}{0.56} \right]^{-1}$$

where n is an integer for the oscillation mode number. This formula has been shown to be accurate for Mach numbers from 0.5 to 3.0 (51).

Unstable premixed propane flames in a cavity have been recorded as shown in Figure 13(55). These instabilities were later found to be coupled to the acoustics of the air feed system.

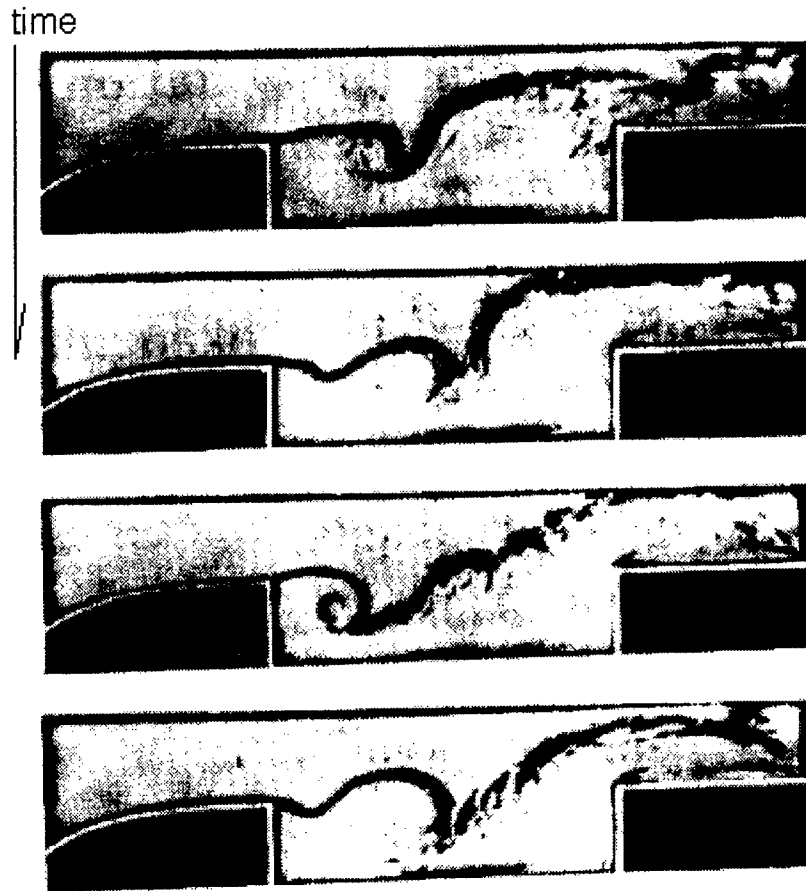


Figure 13 Film of an Unstable Flow in a Cavity Combustor (55:4).

2.8.3 Cavity CFD Simulations. As mentioned earlier, CFD has been used extensively to characterize cavity flows (35-52). Nearly all of the reported CFD studies used a Baldwin Lomax turbulence model, usually with some sort of modification. The modifications include elimination of the turbulent viscosity in the shear layer (37), accounting for the front and/or back cavity faces (36), Goldberg backflow model (40), Degani-Schiff condition (52) and axial relaxation of turbulent viscosity near the upstream lip (34). When comparisons were made between turbulence models and laminar simulations, the flow field was always similar. The method used in this research was similar to past research on supersonic cavity flows.

The primary concern for most of the cavity simulations has been the suppression of oscillations or reduced drag. However, for the study of flame holding properties, Giovannini (56) used a random vortex method to simulate a cavity and a backward facing step. The CFD method was limited to laminar, two-dimensional simulations. He calculated the residence time from the decay rate of particles initially within the flame holder. A similar method of calculating the residence time was used in this research.

2.8.4 Three-Dimensional Cavity Effects. Maull and East (57) reported three-dimensional instabilities for rectangular cavities. They used a water tunnel with rectangular and cylindrical cavities along a wall. They varied the cavity width and observed flow cells within the cavity at various width-to-length ratios. When the cellular structure was present, the flow was steady, while without a cellular structure the flow was unsteady. The cellular structure appeared only for narrow ranges of preferred widths. These preferred widths correspond to an integer number of cells within the cavity. This would partially explain the two-dimensional flow obtained by Settles et al. (58), while Petrie et al. (59) showed oil flow patterns of a cellular structure on the reattachment ramp in compressible flow studies.

Torda and Patel (60) conducted flow visualization studies of triangular cavities. The flow was from the apex of equilateral triangles as illustrated in Figure 14. Apex angles of 30 and 60 degrees were tested. The flow had a strong downwash along the triangular base. They also observed vortical structures in the axial direction. For some conditions small vortices formed at downstream base and convected upstream through the cavity. For deep cavities, the instability frequency was approximately $1.88 \cdot U/L$, where U was the free stream velocity and L was the cavity length. For

Triangular Cavity

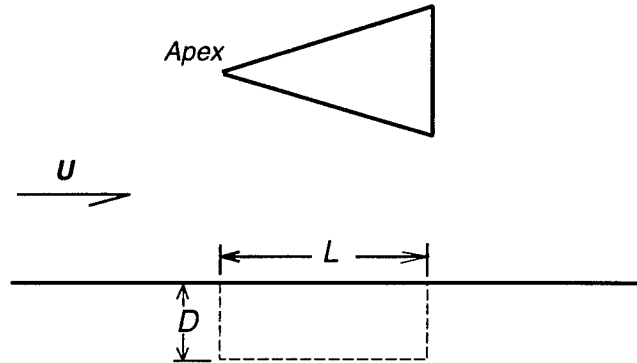


Figure 14. Triangular Cavity Geometry.

shallow cavities no single frequency was predominant. These tests were conducted for low (0.1 - 0.2) Mach number flow.

2.8.5 Compressible Shear Layer Studies. More recently researchers have used cavity configurations for the study of reattaching compressible shear layers. By adjusting the angle of the downstream cavity wall, a pressure matched compressible shear layer could be obtained. Petrie et al. (59) and Samimy et al. (61) used this configuration to study compressible the shear layer growth with laser Doppler velocimetry (LDV). This data was used to calibrate the CFD code used in this study, and is discussed further in Sect. 3.3.7. Hayakawa et al. (62) conducted hot wire measurements on a similar configuration with Mach 2.9 free stream flow. They observed that the turbulence intensity increased dramatically near the reattachment point. Horstman et al. (63) simulated these experiments using a Wilcox-Rubesin $k-\omega$ turbulence model and obtained

fair agreement in the free shear layer. The reattachment profiles were poorly matched until the boundary layer length scale was multiplied by an ad-hoc factor of three.

A similar configuration was also used by King et al. (64) for the study of turbulent transition in a compressible free shear layer. The Mach number for these experiments, conducted in the NASA Langley Research Center quiet tunnel, was 3.5. They used a cavity with a length-to-depth ratio of over 30 and still maintained an open flow structure. The transition was unaffected by free stream noise level possibly due to the noise feedback through the subsonic cavity. They also measured initial instability frequencies of 10 - 40 KHz using hot wire anemometry. Frequencies on the order of 40 KHz were observed in the current research for Mach 1.91 flow over a smaller cavity than that used in the King et al. research.

2.8.6 Cavity Drag. McGregor and White (65) developed a drag model for steady rectangular cavities of

$$C_D = \left(\frac{1}{4 \cdot \sigma^3} \right) \cdot \left(\frac{\rho_{cavity}}{\rho_{\infty}} \right) \cdot \left(\frac{a_1 \cdot L}{u_{\infty}} \right)$$

where σ is the boundary layer spreading parameter, a_1 includes the effects of the initial boundary layer profile, and L is the cavity length. They noted however that the drag increased by up to 250% when the flow was unsteady. Heller and Bliss (30) did not observe an increase in drag due to resonance effects. They reported that cavity drag was less than four times the drag of a flat plate without the cavity. Little and Whipkey (66) used a cavity created by a disk behind a missile afterbody to reduce base drag by up to 25%. The base pressurization was found by Tanner (67) to reduce at angles of attack

greater than 3 degrees. These studies indicate that cavity drag should be small relative to blunt body flame holder drag.

2.9. Summary

In this chapter it is shown that scramjet propulsion systems are more efficient than other propulsion systems for high speed flight. The need for some type of flame holder is discussed. The two main models of flame holding are summarized. Also, experimental investigations of cavity flame holders in low speed flow are reviewed.

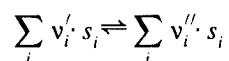
The flow structure and oscillation frequency of non-reacting flow over configurations similar to the proposed cavity flame holder are reviewed. One issue for the current research was whether the oscillation was enhanced by chemical kinetics. Three-dimensional effects have been shown to reduce oscillation amplitude. Three-dimensional effects were proposed in this research for mixing enhancement.

3. Methodology

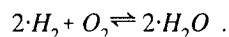
This chapter describes the numerical methods and physical models used in this research. First, a chemical kinetics review is given. Then, detailed chemical kinetics models are applied to time dependent and steady state perfectly stirred reactor analysis. Further, a simplified analytical perfectly stirred reactor model is derived. Finally, the multi-dimensional physical and numerical models are described.

3.1. Chemical Reaction Rates

A general chemical reaction between gas species is represented in the form



where s_i represents molecules of species i , and the coefficients, v_i' and v_i'' , represent the number of each type of molecule in the reaction. The v_i must maintain an atomic balance of all elements on both sides of the reaction by the law of mass action. The v_i represent the number of molecules that must collide, so that for true molecular reactions the coefficients are integers. For other reaction types, the coefficients may be set to be non integers in order to match the experimental reaction rate change with pressure. For example, the formation of water from hydrogen and oxygen molecules could be represented by the single reaction equation



Gas molecules repel each other as they approach due to their electron clouds

having like charges. Therefore in order for molecules to react, they must collide with sufficient velocity to overcome the repulsive force. From a statistical gas dynamics perspective, temperature is a measure of the average velocity of the gas molecules. As the average velocity increases, a higher fraction of the molecules have enough velocity to overcome the repulsive forces and can therefore react. Also influencing the reaction rate is the concentration of gas molecules. The probability of a collision between molecules increases as the number of molecules in a given volume increases. To account for both temperature and concentration effects, the forward molar reaction rate, frr , has been curve fit to the form

$$frr = \left(\prod_i [s_i]^{v'_i} \right) \cdot A \cdot T^p \cdot \exp \left(\frac{-E}{R_u \cdot T} \right)$$

where A , p , and E are constants for each reaction, R_u is the universal gas constant, T is the temperature, and $[s_i]$ indicates the molar concentration per unit volume of species i . The temperature dependent terms are typically grouped together into a forward reaction rate coefficient, k_f , defined by

$$k_f = A \cdot T^p \cdot \exp \left(\frac{-E}{R_u \cdot T} \right) .$$

Also, particularly at high temperatures, the molecular collisions can impart enough energy into a molecule to break the chemical bonds holding it together and cause the molecule to decompose into other species. This effect causes a balance to form for each reaction between the forward and reverse reaction rates, given sufficient time. The reverse rate is often indicated by a constant similar to the forward rate constant. When the forward and

reverse rates are equal the reaction is in chemical equilibrium. From thermodynamic considerations, the concentrations of the species in equilibrium are related by the concentration equilibrium coefficient, which is defined as

$$k_c = (R_u \cdot T)^{\Delta n} \cdot \exp\left(\frac{-\Delta G^0}{R_u \cdot T}\right) = \frac{\prod_i [s_i]^{v_i''}}{\prod_i [s_i]^{v_i'}}$$

where $\Delta n = \sum_i (v_i' - v_i'')$ and ΔG^0 is Gibb's free energy change for the reaction. The Gibb's free energy change is given by

$$\Delta G_j^0 = \sum_i Mw_i \cdot (v_{i,j}'' - v_{i,j}') \cdot (h_i - T \cdot S_i)$$

where

h_i = Enthalpy of Species i at Temperature T

S_i = Entropy of Species i at T and Standard Pressure

Mw_i = Molecular Weight of Species i

With this definition, the reverse reaction rate can be calculated as $k_b = k_f / k_c$. In some cases, the reverse rate coefficient is defined with an equation similar to the forward rate coefficient. By assuming that the Gibb's free energy does not change with temperature, then substitution for the forward and equilibrium coefficients into the reverse rate coefficient expression gives

$$k_b = \frac{A \cdot T^p \cdot \exp\left(\frac{-E}{R_u \cdot T}\right)}{(R_u \cdot T)^{\Delta n} \cdot \exp\left(\frac{-\Delta G^0}{R_u \cdot T}\right)} = \frac{A}{R_u^{\Delta n}} \cdot T^{p-\Delta n} \cdot \exp\left(\frac{\Delta G^0 - E}{R_u \cdot T}\right) .$$

A general chemical reaction is modeled as a set of reactions that all occur simultaneously. For example, Table 2 shows a set of reactions that represents the combustion of hydrogen and oxygen to form water (68:336). In this reaction set, both forward and reverse rate constants are specified. The net change in species concentration is then the sum over all of the reactions of the amount of each species formed as products minus the amount consumed as reactants. Note that reactions 5 to 8 have a species that are the same on both sides of the reaction. Such species are called catalyst.

Table 2. Reaction Rate Set for Hydrogen Oxygen Reaction Excluding HO₂ and H₂O₂

Reaction	$k_f = A \cdot T^p \cdot \exp\left(\frac{E}{R_u \cdot T}\right)$			$k_b = A \cdot T^p \cdot \exp\left(\frac{E}{R_u \cdot T}\right)$		
	A	p	E	A	p	E
1 $H + O_2 \rightleftharpoons OH + O$	1.2×10^{17}	-91	69.1	1.8×10^{13}	0	0
2 $O + H_2 \rightleftharpoons OH + H$	1.5×10^7	2.0	31.6	-----	---	---
3 $OH + H_2 \rightleftharpoons H_2O + H$	1.0×10^8	1.6	13.8	4.6×10^8	1.6	77.7
4 $OH + OH \rightleftharpoons H_2O + O$	1.5×10^9	1.14	0	1.5×10^{10}	1.14	72.2
5 $H + H + Ar \rightleftharpoons H_2 + Ar$	6.4×10^{17}	-1.0	0	2.2×10^{14}	0	402
6 $H + H + H_2 \rightleftharpoons H_2 + H_2$	9.7×10^{16}	-0.6	0	8.8×10^{14}	0	402
7 $H + OH + H_2O \rightleftharpoons H_2O + H_2O$	1.4×10^{23}	-2.0	0	1.6×10^{17}	0	478
8 $O + O + Ar \rightleftharpoons O_2 + Ar$	1.0×10^{17}	-1.0	0	1.2×10^{14}	0	451

$$k_b = \frac{A \cdot T^p \cdot \exp\left(\frac{-E}{R_u \cdot T}\right)}{(R_u \cdot T)^{\Delta n} \cdot \exp\left(\frac{-\Delta G^0}{R_u \cdot T}\right)} = \frac{A}{R_u^{\Delta n}} \cdot T^{p-\Delta n} \cdot \exp\left(\frac{\Delta G^0 - E}{R_u \cdot T}\right) \cdot$$

A general chemical reaction is modeled as a set of reactions that all occur simultaneously. For example, Table 2 shows a set of reactions that represents the combustion of hydrogen and oxygen to form water (68:336). In this reaction set, both forward and reverse rate constants are specified. The net change in species concentration is then the sum over all of the reactions of the amount of each species formed as products minus the amount consumed as reactants. Note that reactions 5 to 8 have a species that are the same on both sides of the reaction. Such species are called catalyst.

Table 2. Reaction Rate Set for Hydrogen Oxygen Reaction Excluding HO₂ and H₂O₂

Reaction	$k_f = A \cdot T^p \cdot \exp\left(\frac{E}{R_u \cdot T}\right)$			$k_b = A \cdot T^p \cdot \exp\left(\frac{E}{R_u \cdot T}\right)$		
	A	p	E	A	p	E
1 $H + O_2 \rightleftharpoons OH + O$	1.2×10^{17}	-0.91	69.1	1.8×10^{13}	0	0
2 $O + H_2 \rightleftharpoons OH + H$	1.5×10^7	2.0	31.6	-----	---	---
3 $OH + H_2 \rightleftharpoons H_2O + H$	1.0×10^8	1.6	13.8	4.6×10^8	1.6	77.7
4 $OH + OH \rightleftharpoons H_2O + O$	1.5×10^9	1.14	0	1.5×10^{10}	1.14	72.2
5 $H + H + Ar \rightleftharpoons H_2 + Ar$	6.4×10^{17}	-1.0	0	2.2×10^{14}	0	402
6 $H + H + H_2 \rightleftharpoons H_2 + H_2$	9.7×10^{16}	-0.6	0	8.8×10^{14}	0	402
7 $H + OH + H_2O \rightleftharpoons H_2O + H_2O$	1.4×10^{23}	-2.0	0	1.6×10^{17}	0	478
8 $O + O + Ar \rightleftharpoons O_2 + Ar$	1.0×10^{17}	-1.0	0	1.2×10^{14}	0	451

A catalyst is any chemical species that increases the reaction rate but does not chemically change itself. In the gas phase, a catalyst works by absorbing energy so that the energy of the product is low enough for it to remain bonded. The catalyst is often taken as a weighted sum of all of the species present which would combine reactions like 5 and 6 from Table 2 into one reaction. Table 3 summarizes the catalytic weights for common species in a combustion reaction as recommended by Warnatz (68:199). Using these weights, the total third body, i.e. the catalyst, concentration would be

$$[M] = 0.4[O_2] + 0.4[N_2] + 6.5[H_2O] + 0.75[CO] + 1.5[CO_2] \\ + 6.5[CH_4] + 0.35[Ar] + 0.35[He] + \sum [All\ Other\ Species] \quad .$$

Then, reactions 5 and 6 would be combined as $H + H + M \rightleftharpoons H_2 + M$.

Table 3. Catalytic Efficiencies for Common Combustion Species.

H ₂	O ₂	N ₂	H ₂ O	CO	CO ₂	CH ₄	Ar	He
1.0	0.4	0.4	6.5	0.75	1.5	6.5	0.35	0.35

In order to determine the equilibrium constant and the thermodynamic state as the reaction proceeds, thermodynamic data for each species must be known. The most common methods for determining thermodynamic values are based on the Joint Army, Navy, NASA, and Air Force (JANNAF) thermodynamic tables. Either a table look up or a curve fit of the data is commonly used to determine the required data. Usually, this data is incorporated into an equation-of-state subroutine, where given the species mass fractions and two thermodynamic values, the remaining thermodynamic values can be

determined. The thermodynamic values are pressure, temperature, entropy, enthalpy, and density.

3.2. Perfectly Stirred Reactor Modeling

For analysis purposes, the recirculation region of a combustor is often modeled as a perfectly stirred reactor (24:13-23,3:178-182). A perfectly stirred reactor is where a volume is assumed to have uniform species and temperature distributions. The reactants enter and instantly mix throughout the volume, and the exit flow has the same temperature and species concentration as the reactor volume. The model used for this research is illustrated in Figure 15. A heat loss rate may also be included in the model. A key parameter for determining the reactor chemical state is the residence time. The residence time is defined as the mean time that a molecule remains in the reactor. The residence time equals the reactor mass divided by the mass flow rate.

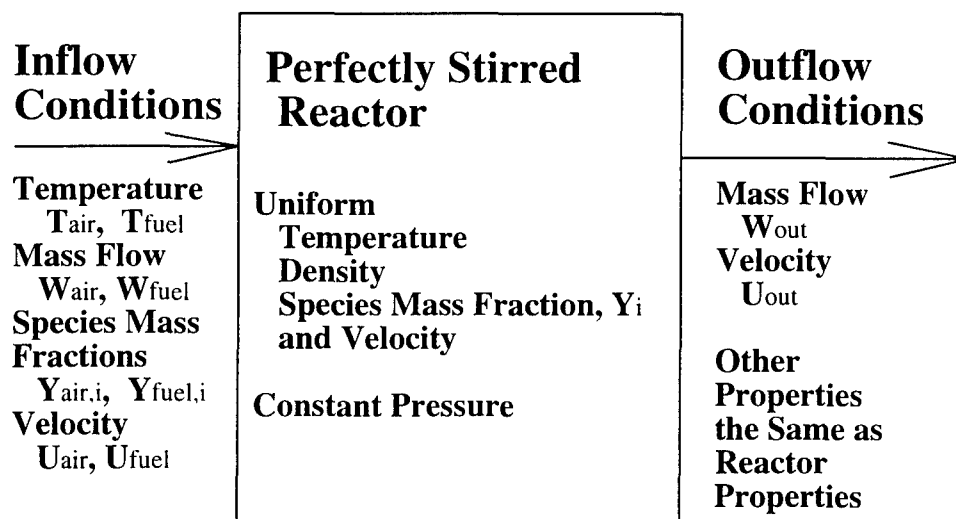


Figure 15. Perfectly Stirred Reactor Model Used in this Analysis.

3.2.1 Time-Dependent Perfectly Stirred Reactor Model. The time rate of change of each species mass is solved from the species mass conservation equations,

$$\frac{\partial F_i}{\partial t} = \dot{M}_{in} \cdot Y_{0_i} - \dot{M}_{out} \cdot Y_i - \left(\sum_j (v'_{i,j} - v''_{i,j}) \cdot rr_j \right) \cdot Mw_i \cdot V_{ol} \quad (1)$$

where F_i is the mass of species i in the reactor; \dot{M}_{in} and \dot{M}_{out} are the mass flow rates into and out of the reactor; Y_{0_i} is the mass fraction of species i in the inflow gas; Y_i is the mass fraction of species i in the reactor and outflow gas; $v'_{i,j}$ and $v''_{i,j}$ are the stoichiometric coefficients of species i for the reactants and products, respectively in the j^{th} equation; Mw_i is the molecular weight of species i ; V_{ol} is the volume of the reactor, and rr_j is the molar reaction rate per unit volume for the j^{th} chemical kinetics equation. rr_j is defined as

$$rr_j = \left(\prod_i [s_i]^{v'_{i,j}} \right) \cdot k_{f_j} - \left(\prod_i [s_i]^{v''_{i,j}} \right) \cdot k_{b_j} \quad (2)$$

with

$$[s_i] = \left(\frac{\rho \cdot Y_i}{Mw_i} \right)$$

$$k_{f_j} = A_j \cdot T^{p_j} \cdot \exp \left(\frac{-E_j}{R_u \cdot T} \right)$$

$$k_{b_j} = \frac{k_{f_j}}{k_{c_j}} = k_{f_j} \cdot (R_u \cdot T)^{\Delta n_j} \cdot \exp \left(\frac{\Delta G_j}{R_u \cdot T} \right) .$$

An integrated form of the conservation of energy equation can be expressed as

$$\frac{\partial H}{\partial t} = \frac{\partial (\rho \cdot V_{ol} \cdot (h + \frac{1}{2} \cdot u^2))}{\partial t} = \dot{M}_{in} \cdot \left(h_{in} + \frac{1}{2} \cdot u_{in}^2 \right) - \dot{M}_{out} \cdot \left(h_{out} + \frac{1}{2} \cdot u_{out}^2 \right) - \dot{Q} \quad (3)$$

where H is the enthalpy in the reactor, h , h_{in} and h_{out} are the specific enthalpies within the reactor and of the reactor inflow and outflow gasses, respectively; u , u_{in} and u_{out} are the velocities within the reactor and for the reactor inflow and outflow, respectively, and \dot{Q} is the heat loss rate from the reactor.

Equations (1) and (3) can be numerically integrated in time using various methods including arbitrary order Runge-Kutta, third order Adams-Moulton, or Euler Implicit methods. The numerical integration methods used in this research are described in Appendix A. The different integration methods all gave virtually identical results due to the small time step limitation for stability.

The time step, Δt , is determined so that no species would be reduced by more than some fraction of its current value,

$$\Delta t = \min_{i \mid \frac{\partial F_i}{\partial t} < 0} \left(C \cdot \frac{-F_i}{(\partial F_i / \partial t)} \right)$$

where C is a constant value that is adjusted to give stable results in a reasonable number of time steps.

An advantage of the time dependent perfectly stirred reactor model is that an ignition delay simulation, a mixing layer simulation or a steady state result can be achieved by varying the inflow and outflow rates. For an ignition delay simulation, the inflow and outflow rates and the initial concentration of product and intermediate species are set to zero. For a steady state cavity flame holder, the inflow and outflow mass flow rates are equal. To approximate a convecting portion of a mixing layer, flow enters the

reactor from above and below the shear layer with no flow out of the reactor, as shown in Figure 16. The flow above the reactor consist of reactants while the flow below the reactor is assumed to be reaction equilibrium products. Note that with this model, the reactor volume increases in time thus simulating the spatial growth of the shear layer. A limitation of this model is that the ratio of products to reactants entering a shear layer is, in general, unknown.

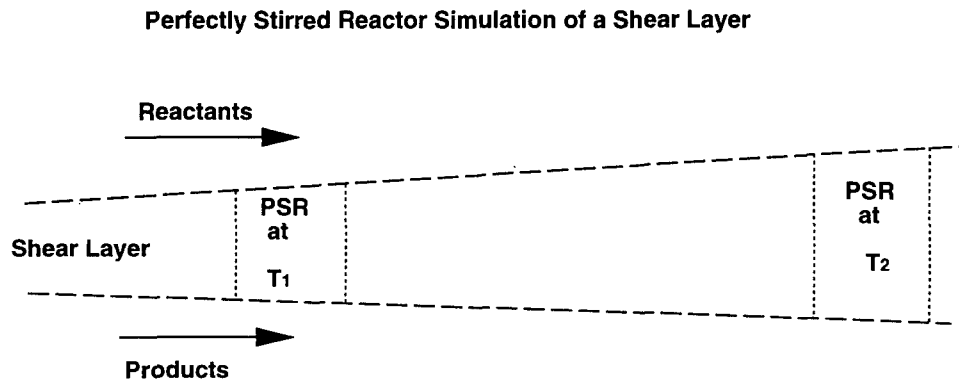


Figure 16. Illustration of a Perfectly Stirred Reactor Simulation of a Mixing Shear Layer.

3.2.2 Steady-State Perfectly Stirred Reactor Model. The steady-state model assumed that the time rate of change of all values was zero, and that the mass flow rate into the reactor equaled the mass flow rate out of the reactor, $\dot{M} = \dot{M}_{inflow} = \dot{M}_{out}$. The conservation of species and energy equations then reduced to

$$\dot{M} \cdot (Y_i - Y_{0_i}) = \left(\sum_j (v''_{ij} - v'_{ij}) \cdot r r_j \right) \cdot M_{w_i} \cdot V_{ol}$$

$$(h_{out} + \frac{1}{2} \cdot u_{out}^2) = (h_{in} + \frac{1}{2} \cdot u_{in}^2) - \dot{Q} / \dot{M}$$

Substitution for the reaction rates, rr_j , defined in Equation (2), gives a nonlinear system of equations that can be solved by several methods.

A Newton iteration was used to solve steady state equations rewritten as

$$0 = Y_i - Y_{0_i} - \left(\sum_j (v''_{ij} - v'_{ij}) \cdot rr_j \right) \cdot Mw_i \cdot \tau_r$$

$$0 = h - h_{in} + \frac{1}{2} \cdot (u_{out}^2 - u_{in}^2) + \frac{\dot{Q}}{\dot{M}}$$

The independent variables were species mass fractions and temperature. The mixture gas density, third body concentration, heat transfer rate, and reaction rate coefficients were treated as constants across each iteration.

3.2.3 Simplified PSR Model. In order to clarify some of the results from more complex reactions, a simplified steady state stirred reactor model was developed as part of the current research. This model assumed a simple forward reaction, $A \rightarrow B$, with a forward reaction rate of

$$rr = [A]^n \cdot A_f \cdot \exp\left(\frac{-E}{R \cdot T}\right),$$

where $[A]$ is the concentration of reactant species which includes fuel and air; A_f is a forward reaction rate constant, and E is the activation energy required for reaction to occur. The reaction order, n , was taken as 1.8, which is the recommended value for hydrocarbon reactions (3:181). Further, the specific heat, Cp , was assumed constant for both reactant and product. Also, the mass fraction of species A was 1.0 for the inflow. Finally, in order to be consistent with the reaction equation, the molecular weights of the

reactant and product species were equal. With these assumptions, the mass conservation of reactant species gives

$$\dot{M} - rr \cdot Vol \cdot Mw - Y_A \cdot \dot{M} = Mass_{In} - Mass_{Consumed\ In\ Reaction} - Mass_{Out} = 0 \quad (4)$$

With $\tau_r = Vol / \dot{M}$, equation (4) simplifies to

$$1.0 - Y_A = W_\tau \quad (5)$$

where $W_\tau \equiv rr \cdot \tau_r \cdot Mw$. With the molar heat of reaction defined as

$\Delta H_f = (T_f - T_{in}) \cdot Cp / Mw$ and Cp held constant, the energy conservation equation can be

written as

$$Cp \cdot T_{in} \cdot \dot{M} + (T_f - T_{in}) \cdot Cp \cdot Mw \cdot Vol - Cp \cdot T \cdot \dot{M} = Energy_{in} + Energy_{Produced} - Energy_{out} = 0 \quad ,$$

which simplifies to

$$\frac{T}{T_{in}} = 1 + \frac{T_f - T_{in}}{T_{in}} \cdot W_\tau \quad (6)$$

In the reaction rate equation, substitution for the concentration of reactant species,

$[A] = \frac{P}{Ru \cdot T} \cdot Y_A$, gives

$$rr = A_f \cdot \left(\frac{P}{Ru \cdot T} \cdot Y_A \right)^n \cdot \exp \left(\frac{-E}{R \cdot T_{in}} \cdot \frac{T_{in}}{T} \right) \quad .$$

Substitution for Y_A and T/T_{in} from equations (5) and (6), gives

$$rr \cdot Mw = Q \cdot (1 - W_\tau)^n \cdot \exp\left(\frac{-\Theta}{1 + \Psi \cdot W_\tau}\right)$$

where

$$Q = Mw \cdot A_f \cdot (Ru \cdot T_{in} / P)^n$$

$$\Theta = E / (Ru \cdot T_{in})$$

$$\Psi = (T_f - T_{in}) / T_{in}$$

Q is a lumped constant that scales the residence time. Θ is a non-dimensional activation energy and represents how strongly the reaction rate varies with temperature. The non-dimensional heat release parameter, Ψ , indicates the reaction temperature rise.

Multiplying both sides of equation (6) by the residence time and rearranging to give τ_r as a function of W_τ yields

$$\tau_r \cdot Q = \frac{W_\tau}{(1 - W_\tau)^n} \cdot e^{\Theta / (1 + \Psi \cdot W_\tau)} \quad (7)$$

From the mass conservation equation, $Y_A \in [0, 1]$, therefor W_τ is between 0.0 and 1.0.

3.2.4 Estimate of Cavity Residence Time. The PSR residence time is the mass in the reactor divided by the mass flow rate through the reactor. For a cavity as shown in Figure 17, the residence time can be estimated by assuming the mass flow rate in and out of the cavity is dominated by the free shear layer. For an incompressible mixing layer the velocity profile has been estimated to be

$$\frac{\bar{u} - U_2}{U_1 - U_2} = \frac{1}{2} \cdot \left(1 + \operatorname{erf} \left(\frac{\sigma \cdot y}{x} \right) \right)$$

where $\sigma \approx 13.5$, \bar{u} is the local velocity; U_1 and U_2 are the velocities above and below the shear layer. The above equation has also been used for high speed shear layers, where σ varies from 13 to 30 depending on the convective Mach number (69:476).

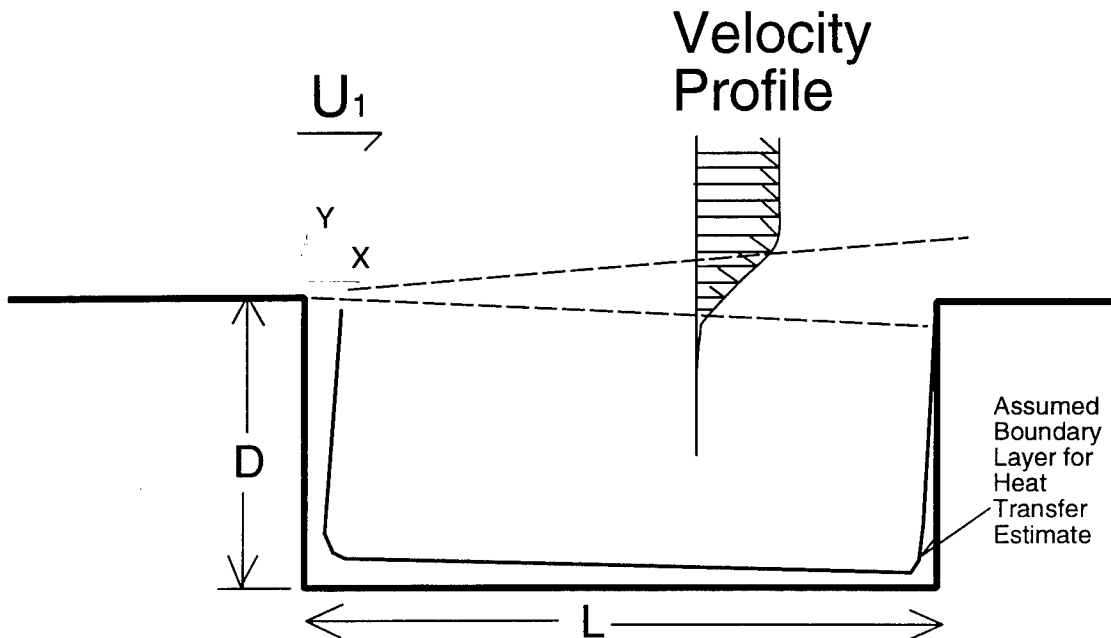


Figure 17. Cavity Dimensions for Residence Time Estimate

The convective Mach number is defined as

$$M_c = \frac{U_1 - U_2}{a_1 + a_2} .$$

At convective Mach numbers greater than one, disturbances on the low-speed side of the shear layer cannot travel upstream on the high speed side of the shear layer. This decouples the two sides of the shear layer in terms of instability growth. Experimentally, the shear layer growth rate decreases as the convective Mach number increases from 0.2 to 1.0. Assuming the cavity velocity to be negligible, $U_2 \approx 0$, the convective Mach number for the shear layer becomes

$$M_c = \frac{M_1}{1 + \sqrt{1 + \frac{\gamma - 1}{2} \cdot M_1^2}} .$$

Also as the cavity temperature rises from combustion, a_2 increases, resulting in a decrease in the convective Mach number.

Again, assuming the cavity internal velocity to be zero, then the mass flow into the cavity can be estimated as the mass flow below $y=0$ at the cavity downstream edge. Heller and Bliss (30) point out that for steady state flow, the mass flow into the cavity must equal the mass flow out of the cavity, which is satisfied for $y=0$ with no initial boundary layer. Assuming constant species density within the shear layer, the mass flow rate into the cavity becomes

$$\dot{M} = \rho \cdot U_1 \cdot \int_{-\infty}^0 \frac{1}{2} \cdot \left(1 + \operatorname{erf} \left(\frac{\sigma \cdot y}{x} \right) \right) dy$$

With a change of variables ($z = \sigma \cdot y / x$) this reduces to

$$\dot{M} = \frac{\rho \cdot U_1 \cdot x}{2 \cdot \sigma} \cdot \int_{-\infty}^0 \left(1 + \operatorname{erf}(z) \right) dz = \frac{\rho \cdot U_1 \cdot x}{2 \cdot \sigma \cdot \sqrt{\pi}}$$

For a rectangular cavity, the mass in the cavity is $\rho_{Cavity} \cdot D \cdot L$ with the density, ρ_{Cavity} , in the cavity being adjusted for the cavity temperature. The temperature in the cavity without reaction approaches the total temperature of the free stream flow (30), so that the density is reduced by a factor of

$$\frac{\rho_{Cavity}}{\rho} = \frac{T}{T_{total}} = \frac{1}{1 + \frac{\gamma - 1}{2} \cdot (M_1)^2},$$

which gives the residence time as

$$\tau_r = \frac{\rho_{Cavity} \cdot D \cdot L}{\left(\frac{\rho \cdot U_1 \cdot L}{2 \cdot \sigma \cdot \sqrt{\pi}} \right)} = \frac{2 \cdot \sigma \cdot \sqrt{\pi}}{1 + \frac{\gamma - 1}{2} \cdot M_1^2} \cdot \frac{D}{U_1} \quad (8)$$

When the Mach number is low ($M_1 < 0.2$), the shear layer growth parameter, σ , is a constant value of 13.5 giving a residence time of $\tau_r = 48 \cdot D / U_1$. Because σ increases as the Mach number increases, (69) the net effect on residence time is small. For example, at $M_1 = 2$, $\sigma \approx 27$ giving $\tau_r = 53 \cdot D / U_1$.

Several effects are not accounted for in this very simple model for approximating the residence time of a cavity. The temperature or species within the cavity may further change the density. Also, density and species variations within the shear layer are not included. Another effect not accounted for is the bulk unsteady exchange of mass at the

cavity trailing edge which could decrease the residence time. In addition, the initial boundary layer could change the effective center of the velocity profile. This model, however was used for the further development of a heat transfer model and shows that the residence time should scale as the cavity depth and reciprocal velocity.

3.2.5 Cavity Heat Loss Model. For first-order estimation of the convective heat loss within a cavity, a turbulent boundary layer was assumed to start at the trailing edge and wrap around the cavity to the leading edge (Figure 17). The boundary layer was assumed to be turbulent because of the turbulent shear layer reattaching at its starting point. The length of the boundary layer based on dimensions of Figure 17 is $L + 2 \cdot D$. Given a free stream velocity and Mach number, equation (8) can be used to determine L . Then with a given cavity aspect ratio, Ar , the boundary layer length becomes $X = \tau_r \cdot U_1 \cdot (Ar + 2) / 48$. Assuming the average velocity near the cavity wall to be one tenth of the free stream velocity, then the Reynolds number becomes $Re_X = \rho \cdot (0.1 \cdot U_1) \cdot X / \mu$. The following integral turbulent boundary layer correlations from White (69)

$$\frac{\zeta \cdot X}{k} = C_h \cdot Re_X \cdot Pr$$

$$C_f \approx \frac{0.455}{\ln^2(0.06 \cdot Re_X)}$$

$$C_h \approx \frac{C_f / 2}{1 + 13 \cdot (Pr^{2/3} - 1) \cdot (C_f / 2)^{1/2}}$$

were used to estimate the mean heat transfer per unit area as

$$q_w = \frac{C_f \cdot (T_1 - T_0) \cdot \rho \cdot (0.1 \cdot U_1) \cdot C_p}{2}$$

with Pr assumed equal to 1.0. The Prandtl number and Nusselt numbers are defined as $Pr \equiv \mu \cdot C_p / k$ and $\zeta \equiv q_w / (T_1 - T_0)$. The area can be determined from the volume, length and aspect ratio as

$$area = \frac{(2 + Ar)^2}{Ar} \cdot \frac{Vol}{L}$$

so that the total heat transfer becomes $q_w \cdot area$.

If a significant amount of soot formed within the cavity, then there would also be radiation heat loss from the cavity. In order to determine if radiation may reduce flammability limits, an estimate of the maximum possible radiation loss was made. The maximum radiation possible would be associated with black-body radiation. To estimate this heat transfer rate, the gas was assumed to radiate to the wall with an emissivity of one and an area equal to that of the cavity wall. From Plank's law of radiation, the heat transfer becomes

$$\dot{Q}_{loss} = \sigma \cdot (T_{\infty}^4 - T_{wall}^4) \cdot area$$

3.2.6 Reaction Rate Sets. Four detailed reaction rate sets were compared for a hydrogen-oxygen reaction. The reaction sets are referred to as Glassman (3:448,449) Warnatz(68:336,337), Radhakrishnan(70:82-84), and Drummond (71:374). For the

hydrogen-oxygen reaction set, only reactions involving O_2 , H_2 , H_2O , O , H , OH , HO_2 and H_2O_2 were used.

For the Warnatz reaction set, reaction rates were given with specific third-body gasses. The third-body gasses given were Argon, H_2 , N_2 , or H_2O . Warnatz also recommended general third body efficiencies for some species (Sect. 3.1). To convert the rates given with specific third body species to rates using the recommended third body efficiencies, the given rates were divided by the recommended efficiency of the species given. For example, if a rate was given with argon as a third body, the rate constant, A , was divided by 0.35 (see Table 3), then the general third body weights were used. When multiple third body reactions were given, the Argon rate was used. Also, some of the reactions had both forward and reverse reaction rates. If both forward and reverse rates were given, both were used. If only a forward rate was given the reverse rate was calculated from thermodynamic curve fits using Gibb's energy minimization as described in Sect 3.1.

For the remaining rate sets, the third body efficiencies of all species were set to one (1.0) unless otherwise specified, and reverse reaction rates were all calculated from thermodynamic curve fits. The NASA Lewis thermodynamic curve fits were used, see Sect. 3.3.2 except for the Drummond set, where the thermodynamic properties were curve fit over a single temperature range.

3.3. Multi-Dimensional Modeling

Two different computer codes were compared for use in the cavity simulations, GASP (72) and SPARK (73). The majority of the work was performed using the SPARK code. The SPARK code was used to obtain time-accurate simulations. For the SPARK

code, Smagorinsky sub-grid and Baldwin Lomax turbulence models were included as part of this research.

3.3.1 Physical Models. The species continuity, conservation of energy and Navier Stokes equations were used to model the flow field. The species formation rates were treated as source terms to the species equations. A density and $n-1$ species continuity equations were solved. In Cartesian vector form, the equations solved were

$$\frac{\partial \mathbf{U}}{\partial t} + \frac{\partial \mathbf{E}}{\partial x} + \frac{\partial \mathbf{F}}{\partial y} + \frac{\partial \mathbf{G}}{\partial z} = \mathbf{H} \quad (9)$$

where

$$\mathbf{U} = \begin{pmatrix} \rho \\ \rho \cdot u \\ \rho \cdot v \\ \rho \cdot w \\ \rho \cdot E \\ \rho \cdot Y_1 \\ \rho \cdot Y_2 \\ \vdots \\ \vdots \\ \rho \cdot Y_{n-1} \end{pmatrix}, \quad \mathbf{E} = \begin{pmatrix} \rho \cdot u \\ \rho \cdot u^2 - \tau_{xx} \\ \rho \cdot u \cdot v - \tau_{xy} \\ \rho \cdot u \cdot w - \tau_{xw} \\ \rho \cdot u \cdot E - \tau_{xx} \cdot u - \tau_{xy} \cdot v - \tau_{xz} \cdot w + q_x + \sum_{i=1}^n h_i \cdot \tilde{u}_i \\ \rho(u + \tilde{u}_1)Y_1 \\ \rho(u + \tilde{u}_2)Y_2 \\ \vdots \\ \vdots \\ \rho(u + \tilde{u}_{n-1})Y_{n-1} \end{pmatrix},$$

$$\mathbf{F} = \begin{pmatrix} \rho \cdot v \\ \rho \cdot u \cdot v - \tau_{xy} \\ \rho \cdot v^2 - \tau_{yy} \\ \rho \cdot v \cdot w - \tau_{yz} \\ \rho \cdot v \cdot E - \tau_{xy} \cdot u - \tau_{yy} \cdot v - \tau_{yz} \cdot w + q_y + \sum_{i=1}^n h_i \cdot \tilde{v}_i \\ \rho(v + \tilde{v}_1)Y_1 \\ \rho(v + \tilde{v}_2)Y_2 \\ \vdots \\ \rho(v + \tilde{v}_{n-1})Y_{n-1} \end{pmatrix},$$

$$\mathbf{G} = \begin{pmatrix} \rho \cdot w \\ \rho \cdot u \cdot w - \tau_{xz} \\ \rho \cdot v \cdot w - \tau_{yz} \\ \rho \cdot w \cdot w - \tau_{zz} \\ \rho \cdot w \cdot E - \tau_{xz} \cdot u - \tau_{yz} \cdot v - \tau_{zz} \cdot w + q_z + \sum_{i=1}^n h_i \cdot \tilde{w}_i \\ \rho(w + \tilde{w}_1)Y_1 \\ \rho(w + \tilde{w}_2)Y_2 \\ \vdots \\ \rho(w + \tilde{w}_{n-1})Y_{n-1} \end{pmatrix}, \quad \mathbf{H} = \begin{pmatrix} 0 \\ 0 \\ 0 \\ 0 \\ 0 \\ \dot{w}_1 \\ \dot{w}_2 \\ \vdots \\ \vdots \\ \dot{w}_{n-1} \end{pmatrix},$$

and ρ is the gas density; u , v and w are the velocity components; τ_{ij} is the stress tensor; h_i is the enthalpy of species i ; E is the energy ($e + \frac{1}{2}(u^2 + v^2 + w^2)$) where e is the internal energy of the gas); \tilde{u}_i , \tilde{v}_i and \tilde{w}_i are species diffusion velocities; q_x , q_y and q_z are the thermal conductivity components, and Y_i is the mass fraction of species i .

The diffusive coefficients were treated as the sum of a molecular part (subscript *lam*) and a turbulent part (subscript *turb*). The molecular diffusive coefficients were

properties of the statistical molecular interactions, while the turbulent diffusive coefficients were properties of the fine scale unsteadiness of the flow. The components of the shear-stress tensor, heat-flux vector and species diffusion are as follows:

$$\tau_{xx} = \frac{2}{3}(\mu_{lam} + \mu_{turb}) \cdot \left(2 \cdot \frac{\partial u}{\partial x} - \frac{\partial v}{\partial y} - \frac{\partial w}{\partial z} \right) - p$$

$$\tau_{yy} = \frac{2}{3}(\mu_{lam} + \mu_{turb}) \cdot \left(2 \cdot \frac{\partial v}{\partial y} - \frac{\partial u}{\partial x} - \frac{\partial w}{\partial z} \right) - p$$

$$\tau_{zz} = \frac{2}{3}(\mu_{lam} + \mu_{turb}) \cdot \left(2 \cdot \frac{\partial w}{\partial z} - \frac{\partial u}{\partial x} - \frac{\partial v}{\partial y} \right) - p$$

$$\tau_{xy} = (\mu_{lam} + \mu_{turb}) \cdot \left(\frac{\partial u}{\partial y} + \frac{\partial v}{\partial x} \right)$$

$$\tau_{xz} = (\mu_{lam} + \mu_{turb}) \cdot \left(\frac{\partial w}{\partial x} + \frac{\partial u}{\partial z} \right)$$

$$\tau_{yz} = (\mu_{lam} + \mu_{turb}) \cdot \left(\frac{\partial v}{\partial z} + \frac{\partial w}{\partial y} \right)$$

and

$$q_x = -k \cdot \frac{\partial T}{\partial x}$$

$$\tilde{u}_i = -\frac{D}{Y_i} \cdot \frac{\partial Y_i}{\partial x}$$

$$q_y = -k \cdot \frac{\partial T}{\partial y}$$

$$\tilde{v}_i = -\frac{D}{Y_i} \cdot \frac{\partial Y_i}{\partial y}$$

$$q_z = -k \cdot \frac{\partial T}{\partial z}$$

$$\tilde{w}_i = -\frac{D}{Y_i} \cdot \frac{\partial Y_i}{\partial z}$$

The mixture molecular viscosity, thermal conductivity and species diffusion coefficients were calculated as follows. First Wilke's law of mixture viscosity was used as

$$\mu_{lam} = \sum_{i=1}^n \frac{Y_i \cdot \mu_i}{Mw_i \cdot \left(\sum_{j=1}^n \frac{Y_j}{Mw_j} \cdot \phi_{ij} \right)}$$

where

$$\phi_{ij} = \frac{\left[1 + \left(\frac{\mu_i \cdot Y_j}{\mu_j \cdot Y_i} \right)^{0.5} \cdot \left(\frac{Mw_i}{Mw_j} \right)^{0.25} \right]^2}{\left(8 + 8 \cdot \frac{Mw_i}{Mw_j} \right)^{0.5}}$$

and Sutherland's law was used for the species viscosity as

$$\mu_i = \mu_{0_i} \cdot \left(\frac{T}{T_{0_i}} \right)^{1.5} \cdot \left(\frac{T_{0_i} + S_i}{T + S_i} \right)$$

The laminar thermal conductivity (k_{lam}) and laminar species diffusivity (D_{lam}) were calculated assuming constant Prandtl and Schmidt numbers:

$$k_{lam} = \frac{C_p \cdot \mu_{lam}}{Pr} \quad D_{lam} = \frac{\mu_{lam}}{\rho \cdot Sc}$$

where the Prandtl number (Pr) and Schmidt number (Sc) were taken to be 0.7 and 0.22, respectively. The turbulent diffusion coefficients were also based on turbulent Prandtl and Schmidt numbers. Thus, the total or effective thermal diffusivity and species diffusion coefficients were given by:

$$k = k_{lam} + k_{turb} = C_p \cdot \left(\frac{\mu_{lam}}{Pr} + \frac{\mu_{turb}}{Pr_{turb}} \right)$$

$$D = D_{lam} + D_{turb} = \frac{1}{\rho} \cdot \left(\frac{\mu_{lam}}{Sc} + \frac{\mu_{turb}}{Sc_{turb}} \right)$$

where Pr_{turb} and Sc_{turb} were assumed to be one.

3.3.2 Species Properties. The thermodynamic properties of each species were determined from polynomial curve fits. The constant pressure specific heat coefficient for most species changes value at about 1000 K. This is due to the increased activation of the vibrational states of the molecule at higher temperatures. There is another change in slope at about 5000 K due to rotational energy, but this is outside the range of interest for most combustion problems. In order to accurately fit the curves with a change in slope, the polynomial fits were split into separate temperature ranges of 200 -1000 K, 1000 - 5000 K and 5000 - 30,000 K (74). However, the temperature range for scramjet combustion problems is from 400 K to 3000 K, and the temperature split cost computational effort and can create oscillations at the switching temperatures. Therefore, one curve fit was used for the temperature range of interest. The polynomials used were

$$\frac{Cp_i}{R} = A_i + B_i \cdot T + C_i \cdot T^2 + D_i \cdot T^3 + E_i \cdot T^4$$

$$h_i = h_{0_i} + R \cdot \left[A_i \cdot T + \left(\frac{B_i}{2} \right) \cdot T^2 + \left(\frac{C_i}{3} \right) \cdot T^3 + \left(\frac{D_i}{4} \right) \cdot T^4 + \left(\frac{E_i}{5} \right) \cdot T^5 \right]$$

$$\frac{h_i - s_i \cdot T}{R} = A_i \cdot T \cdot (1 - \ln(T)) + \left(\frac{B_i}{2} \right) T^2 + \left(\frac{C_i}{6} \right) T^3 + \left(\frac{D_i}{12} \right) T^4 + \left(\frac{E_i}{20} \right) T^5 + F_i - G_i \cdot T$$

where the coefficients for each species are A_i , B_i , C_i , D_i , E_i , F_i , G_i , and h_{0i} .

The coefficients for hydrogen, oxygen and nitrogen species were previously coded in the SPARK code. However, new coefficients were needed for propane and carbon dioxide in order to perform the propane reaction simulations. To determine coefficients for propane and carbon dioxide, a least squares fit to the split range curves of McBride, (Lewis curves) over the temperature range of 400 to 3000 K was used. Figure 18 compares the new curves and the original curves for propane and carbon dioxide. The new curves were on top of the dashed line for the Lewis curves. The maximum difference between the enthalpies over there valid ranges was 25.3 J/Kg for propane and 7.7 J/Kg for carbon dioxide. For the global reaction the enthalpy coefficient, h_{0i} of carbon dioxide was adjusted to give the same equilibrium temperature as the full reaction.

Sutherland coefficients were available for all species used except propane. A split temperature viscosity fit from McBride et al. (74) was used to graphically fit new Sutherland coefficients for propane. The viscosity curves used by McBride et al. were of the form:

$$\ln(\mu_i) = A_i \cdot \ln(T) + (B_i / T) + (C_i / T^2) + D_i$$

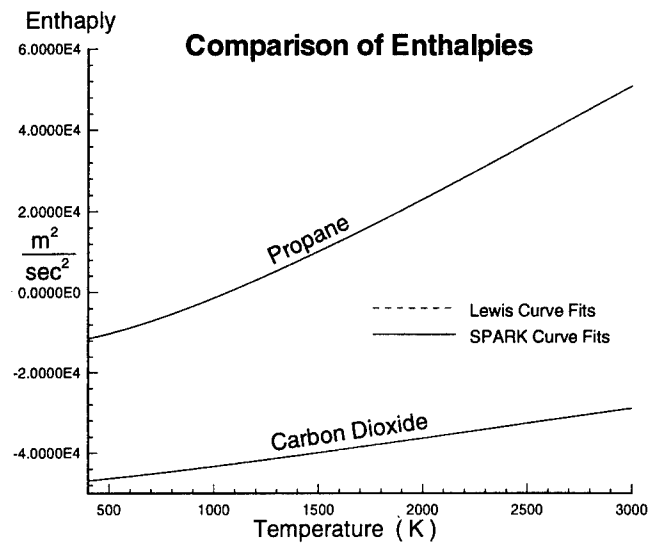


Figure 18. Comparison of Species Enthalpy Curves.

where A_p , B_p , C_i and D_i were constant over specified temperature ranges. Shown in Figure 19 are the new viscosity curve (SPARK) as well as the multi-temperature range curve (Lewis) and a curve fit from Andrussov (75) valid to 1000 K (ASME).

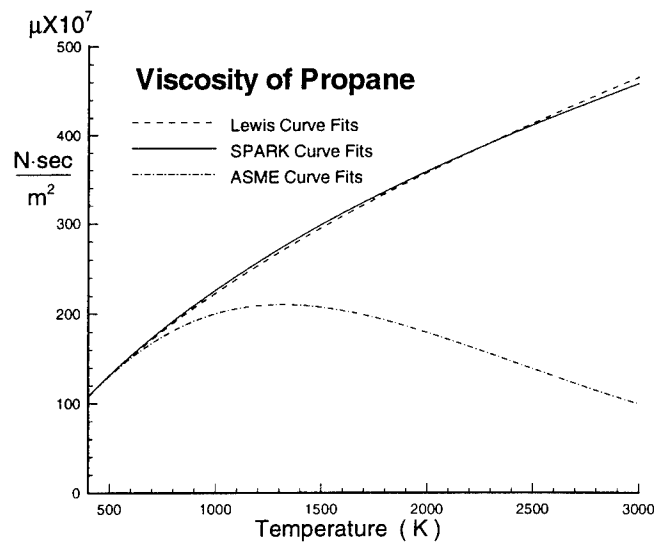


Figure 19. Viscosity Curves for Propane.

3.3.3 Turbulence Modeling. With the Kolmogorov length scale given as

$\eta_K \sim l_{mix} \cdot Re_T^{-\frac{3}{4}}$ (76) where l_{mix} is the turbulent mixing length and Re_T is the turbulent

Reynolds number ($Re_T \equiv \mu_{turb} / \mu_{lam}$). For a free shear layer, $l_{mix} \approx \alpha \cdot \delta$, where $\alpha = 0.071$ and δ is the shear layer thickness. Assuming a negligible velocity on one side of the shear layer, the turbulent viscosity becomes

$$\mu_{turb} \approx \rho \cdot l_{mix}^2 \cdot \left| \frac{dU}{dy} \right| \approx \rho \cdot \alpha^2 \cdot \delta \cdot U$$

Using values representative of the calibration case $\rho = 1 \text{ Kg/m}^3$, $U = 500 \text{ m/sec}$, $\delta = 0.005 \text{ m}$ and $\mu_{lam} = 0.00002 \text{ N}\cdot\text{sec/m}$, the Kolmogorov length scale becomes $\eta_K \sim 0.000003 \text{ m}$. This would require over 1500 grid points across the shear layer to resolve the turbulence in the normal direction. With current computers this scale of resolution is not practical. Therefore, a model of the fine scale motion was required. The models were obtained by averaging the Navier-Stokes equations over time to obtain the Reynolds or Favre averaged Navier-Stokes equations.

In the Reynolds averaged Navier-Stokes equations, apparent stress terms arise from the averaging of second and higher order terms. For example the time average of the product of two scalar terms becomes the product of the averages of the two terms plus an additional term. The following sequence of equations illustrates the source of the additional term with

$$\begin{aligned}\Phi &= \bar{\Phi} + \phi' \\ \Psi &= \bar{\Psi} + \psi'\end{aligned}$$

where Φ and Ψ are scalar variables and $\bar{\Phi}$ and $\bar{\Psi}$ are the time average of the scalar variables,

$$\bar{\Phi} = \lim_{T \rightarrow \infty} \frac{1}{T} \cdot \int_0^T \Phi dt.$$

Also, the average of ϕ' , the fluctuating component of Φ , is zero by the definitions of Φ and $\bar{\Phi}$.

The average of the product of Φ and Ψ becomes

$$\begin{aligned} \overline{\Phi \cdot \Psi} &= \lim_{T \rightarrow \infty} \frac{1}{T} \cdot \int_0^T \Phi \cdot \Psi dt \\ &= \lim_{T \rightarrow \infty} \frac{1}{T} \cdot \int_0^T (\bar{\Phi} + \phi') \cdot (\bar{\Psi} + \psi') dt \\ &= \lim_{T \rightarrow \infty} \frac{1}{T} \cdot \int_0^T (\bar{\Phi} \cdot \bar{\Psi} + \bar{\Phi} \cdot \psi' + \phi' \cdot \bar{\Psi} + \phi' \cdot \psi') dt \\ &= \bar{\Phi} \cdot \bar{\Psi} + \bar{\Phi} \cdot 0 + 0 \cdot \bar{\Psi} + \lim_{T \rightarrow \infty} \frac{1}{T} \cdot \int_0^T \phi' \cdot \psi' dt \\ \overline{\Phi \cdot \Psi} &= \bar{\Phi} \cdot \bar{\Psi} + \overline{\phi' \cdot \psi'} \end{aligned} \quad (10)$$

If the scalar variables are further split into a numerically resolved part, ϕ' , and an unresolved part, ϕ'' , and the time average of both parts is assumed to be zero, then the above sequence of equations yields

$$\begin{aligned} \overline{\Phi \cdot \Psi} &= \lim_{T \rightarrow \infty} \frac{1}{T} \cdot \int_0^T (\bar{\Phi} + \phi' + \phi'') \cdot (\bar{\Psi} + \psi' + \psi'') dt \\ \overline{\Phi \cdot \Psi} &= \bar{\Phi} \cdot \bar{\Psi} + \overline{\phi' \cdot \psi'} + \overline{\phi' \cdot \psi''} + \overline{\phi'' \cdot \psi'} + \overline{\phi'' \cdot \psi''} \end{aligned} \quad (11)$$

The last three Reynolds stress like terms of equation (11) are the turbulent terms that need to be modeled. Assuming the numerically resolved scalar values are

$$\begin{aligned}\widehat{\Phi} &= \bar{\Phi} + \phi' \\ \widehat{\Psi} &= \bar{\Psi} + \psi' \quad ,\end{aligned}$$

then the time average of the product of resolved scalar values becomes

$$\overline{\widehat{\Phi} \cdot \widehat{\Psi}} = \lim_{T \rightarrow \infty} \frac{1}{T} \cdot \int_0^T (\bar{\Phi} + \phi') \cdot (\bar{\Psi} + \psi') dt = \bar{\Phi} \cdot \bar{\Psi} + \overline{\phi' \cdot \psi'} \quad . \quad (12)$$

In Large Eddy Simulations (LES), additional terms are added to the Navier-Stokes equations so that the averages of equation (12) will yield the same results for the nonlinear Reynolds stress terms corresponding to the last three terms of equation (11). The additional stress terms can be modeled by averaging the Navier-Stokes equations over a small time interval. This average, defined as

$$\bar{\Phi}(t) = \frac{1}{\Delta T} \cdot \int_t^{t+\Delta T} \Phi d\tau \quad ,$$

gives

$$\Phi \cdot \Psi = \bar{\Phi} \cdot \bar{\Psi} + \phi'' \cdot \widetilde{\psi''}$$

for the cross terms of the Navier-Stokes equations, which is an identical form to the Reynolds averaged Navier-Stokes equations. The sub-grid scale stress terms are then

modeled in a manner similar to the Reynolds stress terms. This however leads to some inconsistency, because the terms modeled as shear stresses will tend to damp out the resolved fluctuations, while the true high frequency oscillations will excite the lower frequency resolved oscillations.

The Smagorinsky model (76) used for the shear stress terms was

$$\begin{aligned}\tau_{i,j} &= 2 \cdot \mu_T \cdot S_{i,j} \\ S_{i,j} &= \frac{1}{2} \cdot \left(\frac{\partial \tilde{u}_i}{\partial x_j} + \frac{\partial \tilde{u}_j}{\partial x_i} \right) \\ \mu_T &= \rho \cdot (C_S \cdot \Delta)^2 \cdot \sqrt{S_{i,j} \cdot S_{i,j}}\end{aligned}\tag{13}$$

where Δ is the grid spacing. Δ was taken to be geometric mean of the grid spacing in each direction, $\Delta = (\Delta\eta \cdot \Delta\xi)^{\frac{1}{2}}$, with $\Delta\xi = ((x_{i+1,j} - x_{i-1,j})^2 + (y_{i+1,j} - y_{i-1,j})^2)^{1/2}$ and $\Delta\eta = ((x_{i,j+1} - x_{i,j-1})^2 + (y_{i,j+1} - y_{i,j-1})^2)^{1/2}$. The constant C_S was set to the highest recommended value of 0.24 (76:326) for these simulations.

The time resolved Reynolds stress was calculated as

$$\tau_{i,j} = \rho \cdot \langle u'_i \cdot u'_j \rangle + \mu \cdot S_{i,j} = \rho \cdot (\langle u_i \cdot u_j \rangle - \langle u_i \rangle \cdot \langle u_j \rangle) + \mu \cdot S_{i,j}$$

with $\langle \rangle$ indicating a low pass filter to approximate a time average. The low pass filter was

$$\frac{1}{T} \cdot \int_0^T \Phi dt \doteq \langle \Phi \rangle^k = (1 - \alpha) \langle \Phi \rangle^{k-1} + \alpha \cdot \Phi^k$$

where $T=k \cdot \Delta T$, k indicates the solution time level and $\alpha=\min(0.0003,1/k)$. Note that for $k < 33,333$, this sequence gives the ensemble average, $\langle \Phi \rangle^k = \frac{1}{k} \cdot \sum_{i=1}^k \Phi^i$. For larger

k , the early solution values become less significant, thus mitigating the effects of any initial transients. This averaging procedure uses very little additional memory because the only the filtered values need to be stored. Another advantage of this method is that the averaged values are available for every time step.

The averaging above was used to account for the apparent stress of the resolved unsteady flow with all turbulence models. The grid resolution was not sufficient to resolve a significant amount of the turbulent fluctuations for a realistic simulation. The turbulence variations were used to gain some qualitative insight into chemical kinetic interactions with the flow.

For the laminar and Smagorinski SGS simulations, the inflow was forced with velocity oscillations. The oscillation amplitude and phase were set to approximate the amplitude and phase of the incompressible boundary layer data of Klebanov (69). The oscillation frequency was taken as the axial velocity divided by the outer layer turbulent mixing length. The resulting forcing functions were:

$$\eta = y/\delta$$

$$\omega = 69.81 \cdot (u \cdot t/\delta + \eta)$$

$$u' = U_{\infty} \cdot (0.113 - 0.11 \cdot \eta) \cdot \sin(\omega)$$

$$v' = U_{\infty} \cdot (0.113 - 0.11 \cdot \eta) \cdot (0.62 + 0.38 \cdot \eta) \cdot \sin(\omega + 1.62)$$

where δ is the boundary layer thickness, y is the height, u is the local velocity, and t is time.

For most of this research a more global model of the turbulent diffusive components was applied. The Baldwin Lomax turbulence model (77) was the primary turbulence model for this research. The Baldwin Lomax algebraic turbulence model simulates turbulence in two layers. The inner layer is a layer near a wall that is dominated by the wall shear force. The outer layer is mainly influenced by the wake from the upstream forces.

The inner region is modeled using a Prandtl-Van Driest formulation as

$$(\mu_{turb})_{inner} = \rho \cdot l_{mix}^2 |\omega|$$

where

$$l_{mix} = \kappa \cdot y \cdot \left[1 - \exp\left(\frac{-y^+}{A^+}\right) \right]$$

$$|\omega| = \sqrt{\left(\frac{\partial u}{\partial y} - \frac{\partial v}{\partial x}\right)^2 + \left(\frac{\partial v}{\partial z} - \frac{\partial w}{\partial y}\right)^2 + \left(\frac{\partial w}{\partial x} - \frac{\partial u}{\partial z}\right)^2}$$

$$y^+ = \frac{y \cdot \sqrt{\rho_w \cdot \tau_w}}{\mu_w} ,$$

the subscript w indicates the value at the wall, $A^+ = 26$ and $\kappa = 0.4$.

The outer region is modeled as a wake where upstream drag leaves a velocity deficit in the flow. The model is

$$(\mu_{turb})_{outer} = K \cdot C_{CP} \cdot \rho \cdot F_{WAKE} \cdot F_{KLEB}(y)$$

where $K = 0.0168$ and $C_{CP} = 1.6$. Also,

$$F_{WAKE} = \min \left[\left(y_{MAX} \cdot F_{MAX} \right), \left(\frac{C_{WK} \cdot y_{MAX} \cdot u_{DIF}^2}{F_{MAX}} \right) \right]$$

$$F_{KLEB}(y) = \left[1 + 5.5 \cdot \left(\frac{C_{KLEB} \cdot y}{y_{MAX}} \right)^6 \right]^{-1}$$

where $C_{WK} = 0.25$ and $C_{KLEB} = 0.3$. u_{DIF} is the maximum difference in the magnitude of the velocity at each streamwise location. F_{MAX} and y_{MAX} are determined from the function

$$F(y) = y \cdot |\omega| \cdot \left[1 - \exp\left(\frac{-y}{A}\right) \right]$$

F_{MAX} is the maximum value of $F(y)$ at each streamwise location while y_{MAX} is the y location of F_{MAX} .

The Degani-Schiff modification to the Baldwin Lomax model is where the search for F_{MAX} is stopped when the value of $F(y)$ falls below 0.9 time the current value of F_{MAX} . This limits the F_{MAX} to the local maximum in $F(y)$ nearest the wall. The Degani-Schiff modification was applied only where stated.

3.3.4 Numerical Method. The algorithm used in the SPARK code was the unsplit MacCormac method (78, 79). A generalized coordinate transformation in weak conservation law form was used to transform the equations from the nonuniform physical grid to a uniform computational grid. Pressure and temperature based artificial viscosity terms were added to reduce the order of the solution near discontinuities. The convective fluxes were differenced in a forward-backward, backward-forward sequence over two time steps to avoid biasing from the MacCormac method. For more details on the code

see Carpenter (73). For details on the GASP code numerical methods see Walters et al. (72)

3.3.5 Boundary Conditions. All boundary conditions were either first-order computational space extrapolations from the interior or fixed. The inflow boundary was fixed with the boundary layer profile set to a power law profile. For the calibration case an experimental fit gave 0.166 as the power law exponent, which was used for all calculations. Within the inflow boundary layer, the stagnation enthalpy was held constant and the static temperature was approximated as

$$T = T_{\infty} + \frac{1}{2 \cdot C_p} \cdot (u_{\infty}^2 - u^2) \quad .$$

Outflow boundary values were extrapolated from the interior with constant extrapolation. For the wall boundaries, the velocities were all set to zero; the remaining values (p, e, Y_i) were set equal to the first grid point off the wall unless otherwise specified. For adiabatic boundary condition the static temperature at the boundary was set equal to the static temperature at the first interior point.

For the calibration case, the top boundary was a physical wall. The effects of the viscosity on the upper wall were far removed from the area of interest so a slip condition ($v=0$) was applied on that boundary. For the reacting cases the far field boundary was unknown so a constant extrapolation was used on the top boundary.

3.3.6 Numerical Smoothing. In order to prevent oscillations caused by numerical truncation error near discontinuities, numerical smoothing was added to the fluxes in each direction. The smoothing was applied based on the second derivatives of pressure and

temperature, as recommended by MacCormack and Baldwin (78, 79), with an added term in the two dimensional code. The flux in each direction; E , F and G of Equation (9); has a term added to it based on the following weight, ω_p , from

$$\omega_p = \alpha \cdot \frac{|p_{i+1} - 2 \cdot p_i - p_{i-1}|}{(1-\epsilon) \cdot (|p_{i+1} - p_i| + |p_i - p_{i-1}|) + \epsilon \cdot |p_{i+1} + 2 \cdot p_i + p_{i-1}|} \quad (14)$$

where i is the index for the computational direction and α and ϵ are user defined constants. An identical term based on the temperature was added to this term to get the total dissipation weight, ω . To implement the smoothing, the flux in each direction has a vector added to it of the form

$$\mathbf{T} = \omega \cdot (u_{cv} + a) \cdot (\mathbf{U}_{i+1} - \mathbf{U}_i)$$

where u_{cv} is the contravariant velocity in the flux direction, a is the speed of sound, and \mathbf{U} is the conservation vector. The indexing on \mathbf{U} is the same as for viscous terms so that the net effect of the smoothing is to add a second-order dissipation proportional to the convective flux in each direction. For the three-dimensional code, the first term in the weight equation, (14), denominator was eliminated, which was equivalent to $\epsilon = 1.0$. Unless otherwise specified the dissipation weights were $\omega_p = \omega_T = 0.2$ and $\epsilon = 0.4$. As shown in Sect. 5.1.3, these values were the lowest dissipation where solutions were stable and higher dissipation did not effect the solution.

3.3.7 Validation Data. Detailed flow measurements for geometries similar to a flame holder cavity without reaction have been taken with both Laser Doppler Velocimetry (LDV) and hot-wire probes (58-64). These geometries were used to obtain a pressure balanced compressible shear layer or for studying the shear layer growth or the

reattachment of a supersonic shear layer. The flow within the cavity was usually not studied in detail because it was of secondary interest, and measurements were very difficult. In addition, the measurements were challenging due to the uncertain flow direction and the difficulty of seeding the cavity flow. Because it included measurements within the cavity and its similarity to proposed flame holder designs, the data of Samimy et al.(61) was used as the primary calibration case.

Figure 20 summarizes the geometry used for both the calibration case and the baseline reacting flow simulation. The figure also shows the inflow conditions for both cases. The baseline geometry was chosen to be similar to the geometries tested in low speed, with the inflow conditions selected to approximate a Mach 4 free stream condition and the boundary layer thickness scaled from the validation case. The Mach 4 free stream condition was selected because it was anticipated to be the most difficult for flame holding.

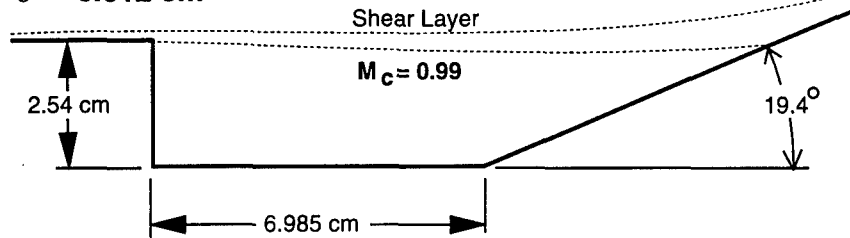
3.3.8 Residence Time Calculations. The residence time is the characteristic time of the decay in mass of the fluid initially within the cavity. For a perfectly stirred reactor with an initial species (wa) within the reactor and no additional source of wa , the time rate of change of wa within the reactor is $-Y_{wa} \cdot \dot{W}$. The amount of wa within the reactor is given by $Y_{wa} \cdot \rho \cdot Vol$, then

$$\frac{d(Y_{wa})}{dt} = -Y_{wa} \cdot \frac{\dot{W}}{\rho \cdot Vol} = -\tau_r^{-1} \cdot Y_{wa} \quad .$$

which can be integrated to give $Y_{wa} = Y_{wa_0} \cdot e^{-t/\tau_r}$, where Y_{wa_0} is the initial mass fraction of wa .

Mach 2.46

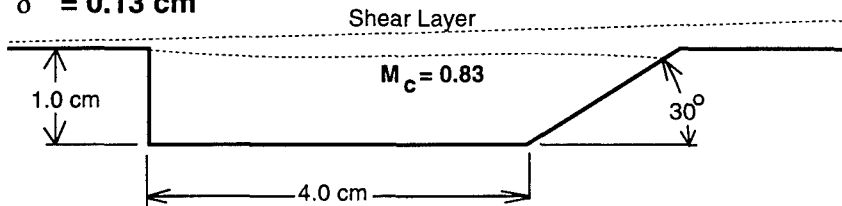
$Re = 5.01 \times 10^7/m$
 $Pt = 528.1 \text{ kPa}$
 $Tt = 297 \text{ K}$
 $\delta = 0.312 \text{ cm}$



a) Calibration Case

Mach 1.91

$Re = 8.47 \times 10^6/m$
 $Pt = 286.6 \text{ kPa}$
 $Tt = 830.6 \text{ K}$
 $\delta = 0.13 \text{ cm}$



b) Baseline Reacting Case

Figure 20. Calibration and Baseline Cavity Geometries

In order to determine the residence time from the numerical simulations two different "air" species were used in the SPARK code. One of the air species consisted of a mixture of oxygen and nitrogen with mass fractions of 0.2314 and 0.7686 respectively, and a new cavity air species. The thermo-chemical data for the cavity air species was calculated to have the same properties as the averaged mixture. The fluid within the cavity was reset to be "cavity air". The remaining flow properties were set as the results

of a prior calculation so that the flow would physically represent a realistic state. By integrating the "cavity air" remaining in the cavity ($y < 0$) as physical time progressed, the residence time was determined from the decay rate of the integrated cavity air mass as

$$\tau_r = \frac{-dt}{d(\ln(wa))} \approx \frac{t_2 - t_1}{\ln(wa_1/wa_2)}$$

where wa_2 and wa_1 were the integrated mass of cavity air within the cavity at times t_2 and t_1 , respectively. For the reacting cavity, the residence time was determined in the same manner but using water mass in the cavity with the chemical reaction turned off as the indicator. The initial conditions were set from a reacting simulation.

3.3.9 Multi-Dimensional Simulations. In order to assure realistic simulations, the CFD codes were calibrated with experimental LDV data. The configuration and flow conditions were similar to the proposed baseline geometry. Variations in turbulence models were compared with the data and a code was selected for further use. For further code assessment, the number of grid points was doubled and solutions were recomputed and compared with the coarse grid solution. An additional doubling of the number of grid points was also evaluated. Simulations with variations of the numerical viscosity coefficients were used to evaluate the effect of artificial viscosity. Temporal convergence was assured by examining the time rate of change of the integrated water mass within the cavity. The calculated turbulent viscosity for the shear layer was evaluated by comparison with Prandtl's mixing length model.

In order to determine the flammability limits of the baseline geometry, the cavity was simulated with decreasing and increasing stoichiometric ratios. At conditions near blowout, these simulations were repeated on finer grids to further assess grid convergence

of the solution. The water mass fraction from the CFD simulations and PSR calculations for several fuel to air ratios were compared to validate the perfectly stirred reactor assumption. Other two-dimensional simulations for the verification of the perfectly stirred reactor assumption included a very small cavity, full H-O kinetic rate set, variations of the turbulence model and a global propane rate.

Other inflow effects investigated included variations in free stream Mach number, boundary layer thickness, and boundary layer temperature. Also the effect of cavity heat loss was evaluated by decreasing the cavity wall temperature.

Three dimensional simulations were performed on a three dimensional cavity geometry. First, a three dimensional simulation of the two dimensional cavity was performed for verification of the three dimensional code. Then, a swept cavity was simulated without chemical kinetics. Finally, three dimensional reacting simulations were performed on a swept cavity with variable aspect ratio.

4. Perfectly Stirred Reactor Results

Results from all three types of perfectly stirred reactor analysis are presented in this chapter. The results for the simple analytical model (Sect. 3.2.3) are presented first to illustrate some of the phenomena observed in later results. Next, results showing the characteristics of different chemical kinetics models are presented, using the more complex methods (Sect 3.2.1 and 3.2.2). Analysis of flame holding properties comparing the effects of inflow temperature, initial temperature, fuel-to-air ratio and heat loss are presented. Then, mixing layer simulation results are presented. Perfectly stirred reactor results using hydrogen and hydrocarbon kinetics models are included.

4.1. Simple Analytical PSR Results

In order to investigate the characteristics of a perfectly stirred reactor, a simplified global reaction PSR analysis was developed (Sect. 3.2.3). This analysis provides a clear illustration of the flammability limits associated with a perfectly stirred reactor. The analysis also gives a range of residence times where multiple solution states are possible. The residence time bounds on the multiple solution range indicate residence times with important physical meaning, which are discussed below.

Assuming an equilibrium flame temperature, T_f , of 3000 K, then for inflow temperatures of 3000, 1000, 750, and 600 K the temperature rise parameter, $\Psi = (T_f - T_{in}) / T_{in}$, would be 0, 2, 3 and 4 respectively. This represents the range of values that may be anticipated for a scramjet engine based on total temperature. Lowering the inflow temperature increases the temperature rise parameter. Figure 21

shows how the degree of reaction parameter, W_τ , varies with the residence time, τ_r , for different Ψ values.

There were three values of W_τ for some residence times ($\tau_r \cdot Q$). This gave a residence time range where the degree of reaction could be nearly complete or nearly zero. This range was brought about by the sensitivity of the reaction rate to temperature rise. If the reaction was progressing at a high degree of reaction, then the heat release kept the temperature high, thereby maintaining the high reaction rates. However at lower temperatures, the reaction rates are too slow to provide the heat necessary to sustain the combustion process. For the purpose of flame holding, the multiple solution residence time represents a range where the reactor may or may not be ignited. This range of values was bounded by a lower residence time and an upper residence time. The upper residence

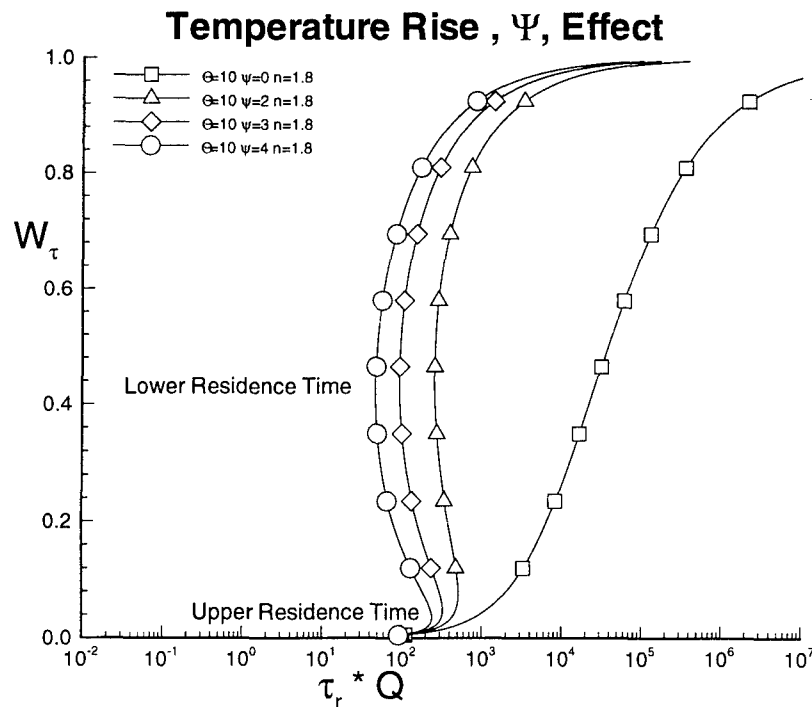


Figure 21. The Effect of Temperature Rise Parameter on the Degree of Reaction with Residence Time.

time indicates the lowest residence time where the reactor would auto ignite. The lower residence time is the minimum residence time required for the reactor to sustain combustion. The lower residence time gives an indication of the size of flame holder required to sustain combustion through the residence time estimation model (Sect. 3.2.4).

The activation energy parameter, $\Theta = E / (R \cdot T_{in})$, indicates the sensitivity of the reaction rate to temperature changes. Figure 22 shows curves for different values of the activation energy parameter, Θ , with the temperature rise parameter fixed at $\Psi = 3$. The upper and lower residence times are also indicated. For high Θ values, the high temperature produced by the reaction can serve to support the reaction at residence times below the auto ignition residence times. Thus again there exist a range of residence times where multiple solutions are possible. Glassman shows a PSR curve similar to those of

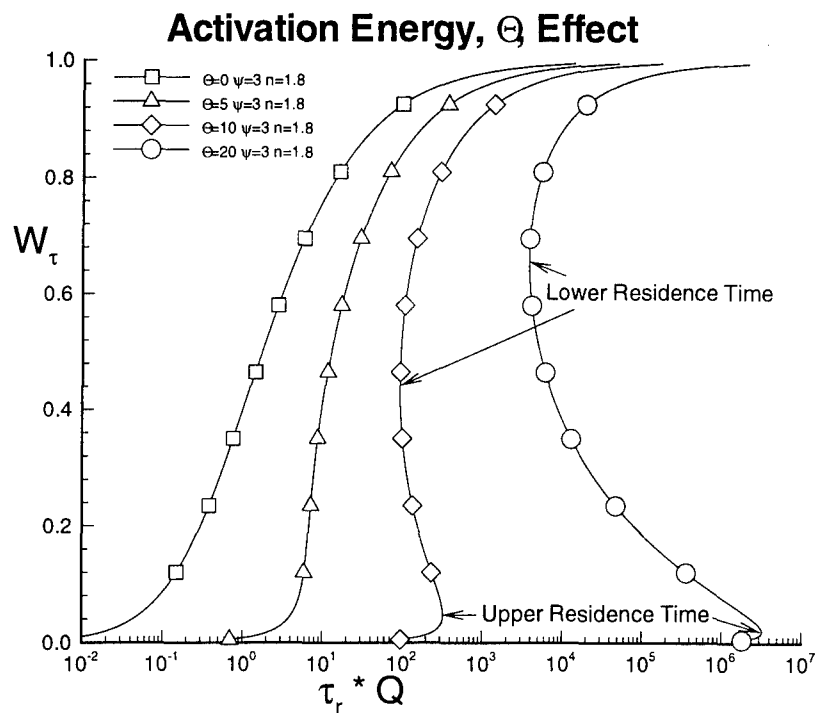


Figure 22. The Effect of Activation Energy on the Relation between Degree of Reaction and Residence Time.

Figure 21 and Figure 22 (3:181) and provides an argument for eliminating the middle solution as unstable. He also states that the lower reaction state "cannot exist physically since the mixture could not be ignited at temperatures this low." However, the lower state is possible but it is not ignited.

The significance of the multiple solution range is that for residence times in this range, either the reacting or essentially non reacting solutions are possible. If the reacting solution was an initial condition, it may be reasonable to assume that the reactor state would not jump to the non-reacting solution. Also, oscillation between solutions may be a driver in combustion instabilities especially near the lower limit of the multiple solution range. Near the lower limit for multiple solutions, the degree of reaction is very sensitive to small changes in residence time because $\partial \omega_r / \partial \tau_r = \infty$, possibly leading to high amplification of oscillations. If the solution state remains constant, the lower residence time would be the most significant for flame holding estimation.

This simplified analysis also illustrates why some ignition source or igniter is required for most combustion systems. At the low temperatures of most combustion systems, the required volume to assure auto-ignition is impractical. The exception is diesel internal combustion engines where the gas is compression heated to high temperatures where the upper residence time is much shorter.

4.2. PSR Code Development

In this section the verification and use of the perfectly stirred reactor code are described. The code was verified by comparing results of the present code to previously

reported perfectly stirred reactor code data. The methodology for calculating the limiting residence times is also reported.

4.2.1 PSR Code Calibration. In order to calibrate the present PSR code, results were compared with LSENS code results (?) in perfectly stirred reactor mode. Two cases were compared, one with a hydrogen oxygen reaction set including 8 species and 18 reactions, and the other a more complex propane reaction with 42 species and 136 reactions and heat loss. For the first case, (Table IV) the mass fractions agreed to within 10^{-5} and the temperature difference was 0.6 K (0.04%). For the propane reaction, the mass fractions differed by less than 2.0×10^{-3} , with a temperature difference of 6.7 K

Table IV. Perfectly Stirred Reactor Simulation Comparison for H-O Reaction

Case 1. H-O Reaction		
Pressure = 1 atm.		Inlet Temperature = 298 K
$\tau_r = 3.0 \times 10^5$		Stoichiometric Fuel - Air Mixture
Species Mole Fraction	PSR Code	LSENS Report
N ₂ (Inert)	0.629	0.629
H ₂ O	0.203	0.203
H ₂	0.0643	0.0643
H	0.0503	0.0503
O ₂	0.0392	0.0392
O	0.00795	0.00795
OH	0.00602	0.00603
H ₂ O ₂	2.69×10^{-5}	2.71×10^{-5}
HO ₂	1.81×10^{-5}	1.85×10^{-5}
Temperature (K)	1398.23	1398.81
Density (Kg / m ³)	2.00×10^{-4}	2.00×10^{-4}

Table V. Propane Perfectly Stirred Reactor Simulation Comparison.

Case 2. Propane Reaction		Inflow Mass Fractions	
Heat Transfer (J/sec) = $-42.88 + 0.05 T$		C3H8	0.0873262
Pressure = 5 atm.		N2	0.6892887
Inflow Temperature = 614 K		O2	0.21232
$\tau_r = 0.13801875$ msec		Ar	0.011737
Stoichiometric Ratio = 1.5		CO2	0.0004162
Mass Fraction Results	PSR Code	LSENS Report	
N ₂	0.6892	0.6892	
CO	0.1085	0.1073	
H ₂ O	0.0995	0.1014	
CO ₂	0.07858	0.07710	
H ₂	0.003954	0.003674	
O ₂	0.002207	0.002705	
C ₂ H ₂	0.001589	0.002671	
CH ₃	0.000977	0.001006	
Temperature (K)	2142.0	2148.7	
Density (Kg / m ³)	7.362 X 10 ⁻⁴	7.361 X 10 ⁻⁴	

(0.31%), see Table V. The slightly larger differences in the propane results are most likely due to slight differences in the thermodynamic curve fits.

4.2.2 Calculation of Limiting Residence Times. Since the simplified analysis (Sect. 4.1) indicated that the lower residence time is a critical parameter, further analyses were performed using more complete reaction sets. The more detailed analysis used the same perfectly stirred assumption but with more realistic chemical kinetics (Sect. 3.2.1 and 3.2.2). In order to determine the lower residence time using the perfectly stirred reactor model, a steady state calculation was performed at a long residence time (1 sec),

then successively shorter residence times were calculated using the last solution as an initial guess. This was continued until negative species mass fractions were obtained or the unreacted level was obtained. The negative species were obtained because no physical solution exist close to the initial guess from the last solution and the derivatives are close to zero giving singular behavior to the Newton iteration. The upper residence time was obtained in a similar manner. Starting with a nonreacting short residence time, the solutions were calculated with successively longer residence times until the reacting solution was obtained or negative species mass fractions were obtained. When oscillations occurred near the limit, time dependent calculations with fixed residence times were performed to verify the limit. Time dependent calculations were also performed to calculate ignition delay time and mixing shear layer simulations.

4.3. Chemical Kinetics Analysis

In this section, a comparison of various chemical kinetic rate sets is reported. Results from full and reduced kinetic rate sets for hydrogen and hydrocarbon rate sets are presented. Also, the calibrations of global reaction rate equations for hydrogen and propane are presented.

4.3.1 H-O Reaction Set Comparison. Ignition delay and lower residence time calculation results for the hydrogen oxygen reaction rate set models described in Appendix B are shown in Figure 23 and Figure 24. The conditions for the calculations were based on the anticipated cavity fluid properties from nonreacting simulations. The ignition delay time varies by about two orders of magnitude with the different rate sets.

The lower residence times also vary by about an order of magnitude for these conditions. The relatively low temperatures and low pressure make this case sensitive to the kinetic mechanism model. The lower residence time was less sensitive to reaction set because of the higher temperatures in the reactor.

Calculations at a higher pressure of 101 kPa had longer ignition delay times (0.2 to 1.6 sec) and longer lower residence times (10^{-5} to 3×10^{-4}). The higher pressure for these conditions apparently reduces the net formation of free radicals by increasing the three body reaction rates, e.g. $H+H+M \rightarrow H_2 + M$. With fixed mass fractions, the forward rate of this reaction was proportional to the pressure cubed while the reverse reaction was proportional to the pressure squared, so as the pressure increased more free radicals were consumed. These three body reactions consumed free radicals so that a sufficient quantity of radicals was not available for ignition.

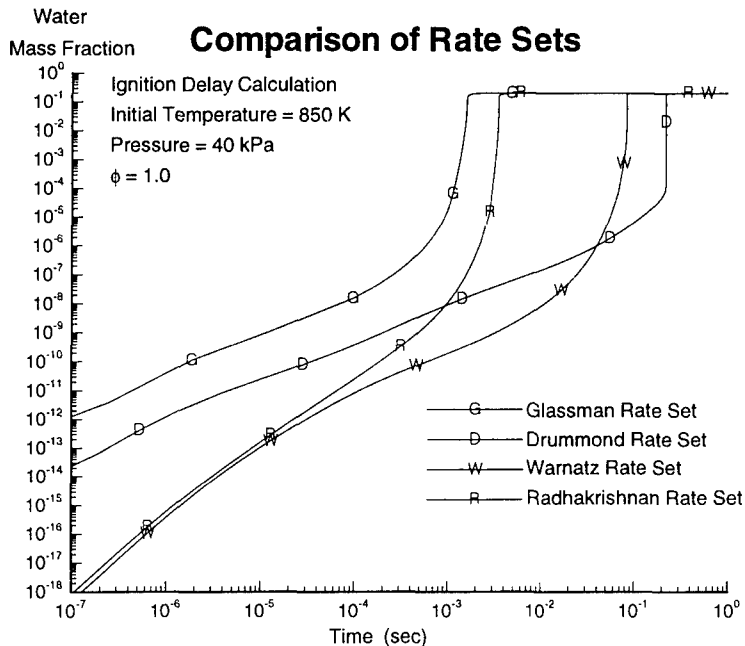


Figure 23. Water Mass Fraction Comparison with Different H-O Reaction Rate Sets for Ignition Delay Simulations.

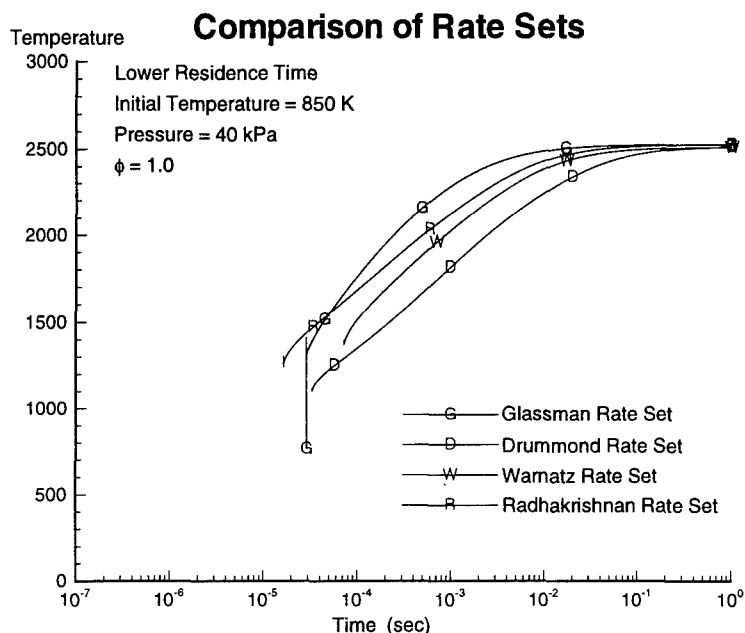


Figure 24. Temperature from Lower Residence Time Calculation with Different H-O Reaction Rate Sets.

4.3.2 Reduced H-O Reaction Sets. Since for each chemical species, a new partial differential equation must be solved, elimination of trace species would significantly improve the computational efficiency of multi-dimensional simulations. Ignition delay simulations were calculated with the time-dependent perfectly stirred reactor model using the H-O reaction set of Radhakrishnan. The effects of deleting the reactions involving H_2O_2 and HO_2 were investigated.

The formation of hydrogen peroxide (H_2O_2) can reduce the concentration of free radicals available for water formation. The hydrogen peroxide decomposes slowly consuming hydrogen and oxygen molecules. This can be seen as the long time where hydroxyl radical concentration does not increase in 79. Reactions that delay ignition by consuming free radicals are called chain terminators while reaction that produce free

radicals are called chain branching reactions. For example, the reaction

$OH + OH + M \rightleftharpoons H_2O_2 + M$ consumes two hydroxyl molecules, thus slowing water formation through reactions like $OH + H + M \rightleftharpoons H_2O + M$.

At temperatures from 800 to 900 K, the trace species have a major effect (4 orders of magnitude) on ignition delay times as shown in Table 6. Pressure also has an effect on how the ignition delay time was changed by the inclusion of the additional species reactions. These slight changes in reaction set also demonstrated the dramatic sensitivity of the ignition delay calculations to what would normally be considered small changes. This sensitivity makes the determination of a reaction set very difficult for a wide range of conditions. No consistent trends were observed for the effect of elimination of species, on ignition delay time.

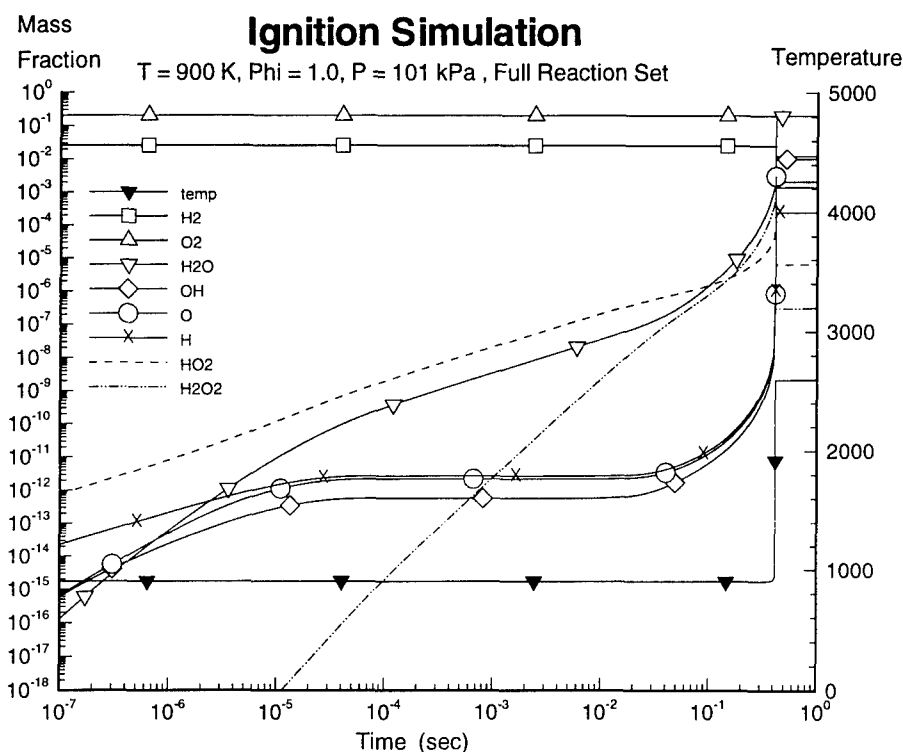


Figure 25. Ignition Delay Calculation with the Full Radhakrishnan H-O Reaction Set.

Table 6. Ignition Time Variations with Elimination of Trace Species.
(Time in milliseconds)

Pressure (Pa)	Temperature (K)	Full Rate Set	Delete H ₂ O ₂	Delete H ₂ O ₂ & HO ₂
40000	800	5095.	30406.	4.47
	850	3.54	2.58	2.46
	900	1.05	.98	1.46
	950	0.55	.54	.91
60000	800	58,887.	*	2.98
	850	22.29	9.42	1.64
	900	0.95	0.81	0.97
	950	0.41	0.39	0.61
	1000	0.23	0.23	0.40
101325 (1 atm.)	800	4660.	*	1604.
	850	4790.	10,263.	0.98
	900	3.07	1.21	0.57
	950	0.33	0.29	0.36
	1000	0.16	0.15	0.23

* Ignition time greater than 100,000 milliseconds.

4.3.3 Global Hydrogen Rate Equation. The relatively large variation of ignition delay and lower residence time with different chemical kinetics models at these conditions serves to justify the use of a much simpler tuned global kinetics model. This approach will facilitate more complicated CFD analysis by reducing the computational

cost, while providing reasonable estimates of the combustion processes. The global reaction rate coefficients were based on the results of the Radhakrishnan, which was better defined and the most current. To determine the global reaction rate, the heat of formation of water was increased to give the same equilibrium temperature as the other rate sets. Secondly, the Arrhenius rate coefficients were both adjusted to give the ignition delay time and lower residence time equal to those of the above simulations with the Radhakrishnan rate set. Figure 26 shows ignition delay and lower residence time simulations with the global reaction set as

$$\dot{W} = [O_2] \cdot [H_2]^2 \cdot (1 \cdot 10^{22}) \cdot \exp(-18000/T)$$

to approximate the Radhakrishnan results shown in Figure 23 and Figure 24. The reaction rate for the higher pressure calculations was

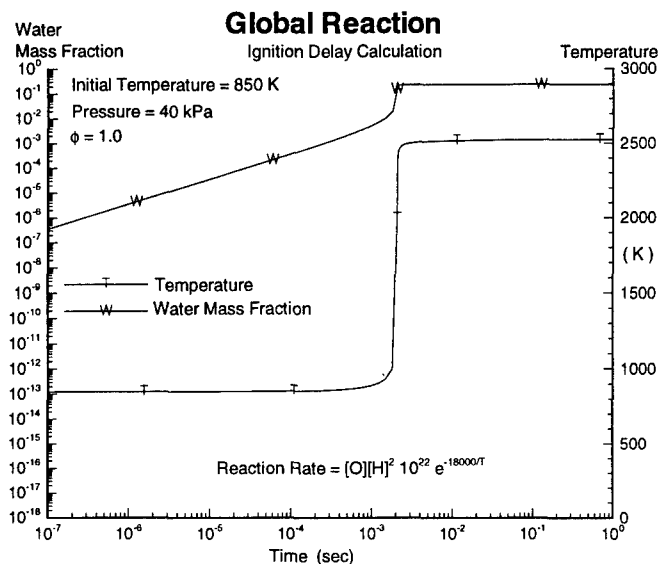
$$\dot{W} = [O_2] \cdot [H_2]^2 \cdot (2 \cdot 10^{21}) \cdot \exp(-23000/T) .$$

In addition a global rate equation tuned to the Drummond rate set was determined as

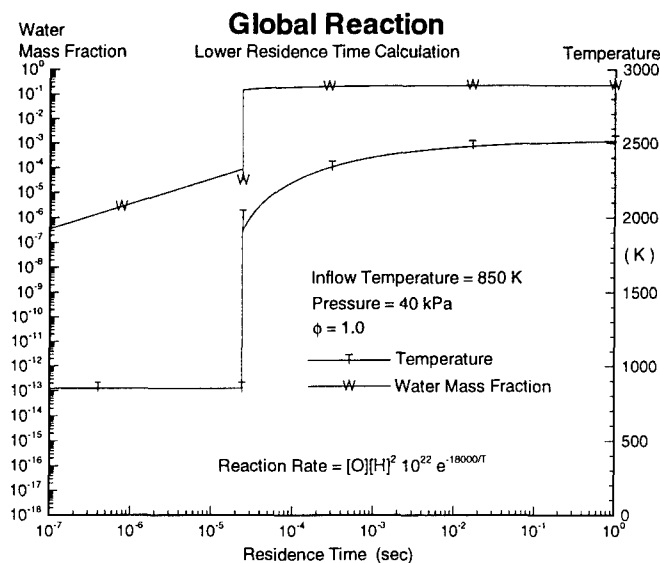
$$\dot{W} = [O_2] \cdot [H_2]^2 \cdot (7.5 \cdot 10^{23}) \cdot \exp(-28300/T) .$$

Table 7 shows the computer time for several ignition delay simulations using different chemical kinetics rate sets. This table also shows that a global reaction takes significantly less computer time than any of the more complex reaction sets. The global reaction was simulated for 10 second in order to obtain a measurable cpu time. After adjustment for the simulated time, the global reaction required 5 orders of magnitude less computer cpu time than the other reaction mechanisms. The explicit methods time step decreased significantly at the ignition time and remained small at the high temperatures, while the Euler implicit simulations time step increased again after the ignition time. The

ignition time was 0.3 msec for the hydrogen reactions and 0.4 msec for the propane reaction.



a) Ignition Delay Calculation



b) Lower Residence Time Simulation

Figure 26. Calculations using the tuned global hydrogen chemical kinetics model.

Table 7. CPU Times for Ignition Delay Simulations in Seconds.

	1 st order Runge- Kutta	4 th order Runge- Kutta	3 rd order Adams- Moulton	2 nd order Adams- Moulton Predictor	1 st order Euler Implicit
Global @ 10 sec	0.7	1.4	1.7	1.7	0.5
Radhakrisn an H-O @ 1 msec	17.4	Unstable	85.0	29.5	13.4
Radhakrisn an H-O-N @ 1 msec	284.7	1161.7	Unstable	501.5	85.1
Drummond @ 1 msec	7.2	Unstable	Unstable	11.9	8.6
Full Propane @ 1 msec	700,000 estimated from 0.53 msec calculation	No Time Calculated	No Time Calculated	No Time Calculated	9179.2

4.3.4 Hydrocarbon Results. For hydrocarbon combustion, the fuel molecule has more decomposition steps to go through before products can form. The ignition delay time is increased because of the extra decomposition steps and the initial decrease in temperature due to the energy absorbed in the decomposition process. The energy absorbed in the fuel decomposition could be used to cool the engine structure if the decomposition could occur at lower temperatures. The process of using fuel decomposition to increase the cooling capacity of the fuel is called endothermic fuels.

Lower residence time calculations for some common hydrocarbons were calculated with the baseline inflow conditions. The lower residence time from these calculations are summarized in Table 8. The full rate sets for ethylene and methane were obtained by eliminating reactions involving heavier hydrocarbons from the full propane reaction set. The reduced set reactions are listed in Appendix B. These results are consistent with the relative flame speeds for hydrocarbons. As shown in Sect. 2.4, methane has the slowest flame speed and acetylene has the highest flame speed with other hydrocarbons having about the same flame speed. The lower residence time for methane indicates that a larger cavity may be required for methane as a fuel. None of the reduced reaction rate sets gave lower residence times close to the full set results.

Table 8. Lower Residence Times Calculated For Different Hydrocarbons, Including Reduced Rate Set Results.

Fuel	Rate Set	ϕ	Lower Residence Time (msec)
Propane	Full	0.5	0.50
		1.0	0.08
		2.0	0.04
		3.0	0.05
	2 Step	1.0	31.7
Ethylene	Full	1.0	0.03
	Reduced Eth.	1.0	1.7
Methane	Full	1.0	0.8
	Reduced Meth.	1.0	0.03

4.3.5 Global Propane Reaction Rate. A global reaction rate for propane was calibrated from the full set results. The water enthalpy was held the same as in the global water reaction and the carbon dioxide heat of formation was first adjusted to give the equilibrium temperature. The Arrhenius rate coefficients were then set to give the same ignition delay time and lower residence time as the full rate set. The ignition delay time calculated using the full propane reaction set was 632 seconds. The comparison between the full and global rate sets is shown in Figure 27.

As shown in Table 7 of Sect. 4.3.3, the computer time for the full reaction rate set was substantially (10 orders of magnitude) more than a global reaction equation. The extra computer time was due to the stiffness of the reaction set. The stiffness of a

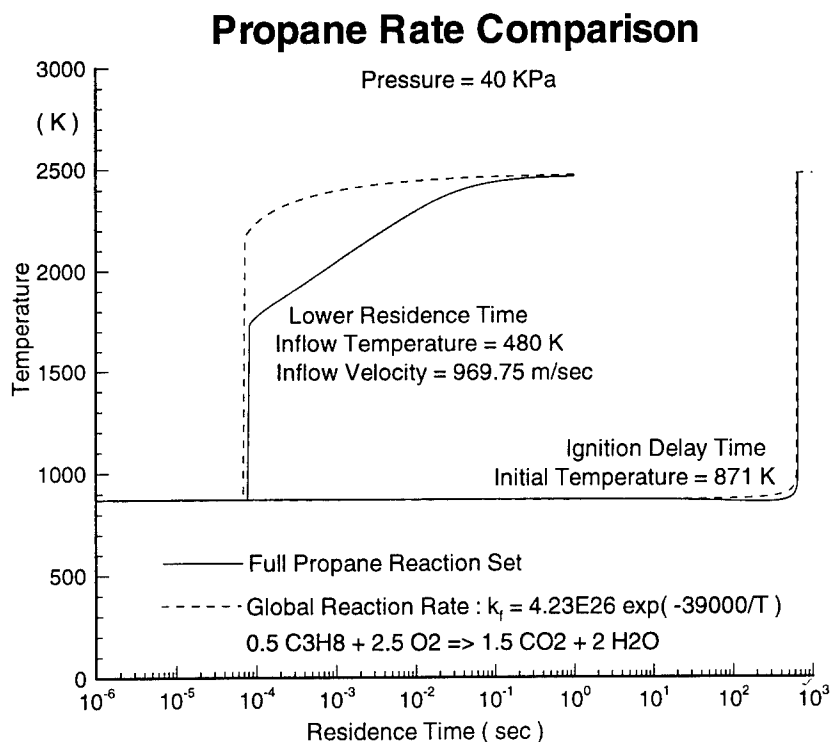


Figure 27. Comparison of Tuned Global Reaction Rate with Full Propane Reaction Rate Set for $\phi=1.0$.

reaction set was the result of the size of the eigenvalues differing by several orders of magnitude. The time step for stability and accuracy is limited by the largest eigenvalue while the characteristic time is governed by the smallest eigenvalues. A multi-dimensional simulation also requires the additional calculation of species diffusion so that a single CFD simulation with a full chemical kinetic rate set for propane is impractical.

Some of the reduced rate sets had an exponent on the fuel concentration of 0.1. This reduced exponent value gave numerical problems in the perfectly stirred reactor model because as the fuel concentration approached zero, the reaction rate approached zero at a lower order. This caused the reaction to try to consume more fuel than was available for reaction. For these reduced rates, the lower residence time calculation had to be started at a shorter residence time in order to have a high enough fuel concentration for stability. These types of problems need to be considered when reduced kinetics reaction sets are developed for fluid flow simulations.

4.4. Flame Holder Analysis

In this section, the results of perfectly stirred reactor analysis of the characteristics of flame holders are presented. The effects of temperature, fuel to air ratio and heat loss were analyzed. Also, presented are mixing layer simulation results from the perfectly stirred reactor analysis.

4.4.1 Initial and Inflow Temperature Effect on Hydrogen Combustion. The effects of changing the initial temperature, using the Radhakrishnan hydrogen-oxygen rate set, on the ignition process were illustrated in Figure 28. The rapid rise in

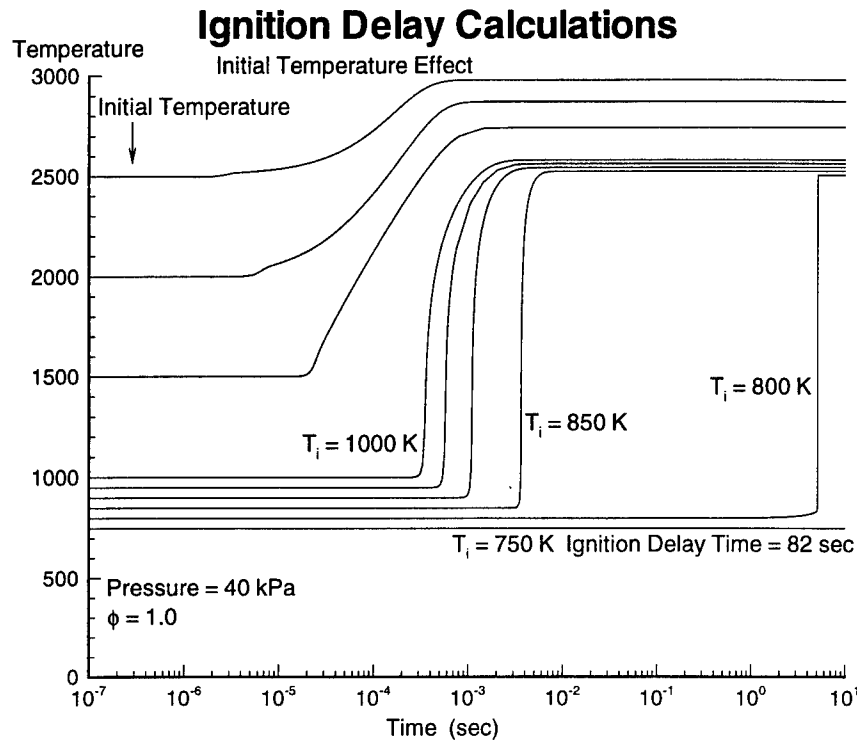


Figure 28. Temperature Variation with Time for a Constant Pressure Reaction at Different Initial Temperatures for hydrogen combustion in air.

temperature indicated the ignition delay time. At initial temperatures above 1500 K, the temperature rise was not as rapid, so the initial rise in temperature was taken as the ignition time. The equilibrium or final temperature did not increase as much as the initial temperature. Due to equilibrium constraints, the maximum temperature was about 3000 K and higher initial temperatures only produced more free radicals that absorbed the energy. Recall that this was a primary reason for considering a scramjet at high flight speeds, where the static temperatures in the combustor were maintained low enough for combustion to add thermal energy to the flow. For initial temperatures below 800 K, the

ignition delay times increased significantly, 4 orders of magnitude for 50 K temperature difference.

Figure 29 shows the ignition delay times of Figure 28, as well as the upper and lower residence times for different inflow temperatures. The upper residence time follows the same trends as the ignition delay times. Compared to the ignition delay and upper residence times, the lower residence time was not as significantly affected by the inflow temperature. This was because the heat release kept the reactor temperature high enough to sustain the reaction even at low inflow temperatures. The lower residence times at low temperatures illustrate the flame holding effectiveness of stirred reactors. As the initial temperature is increased, the heating value and activation energy parameters of

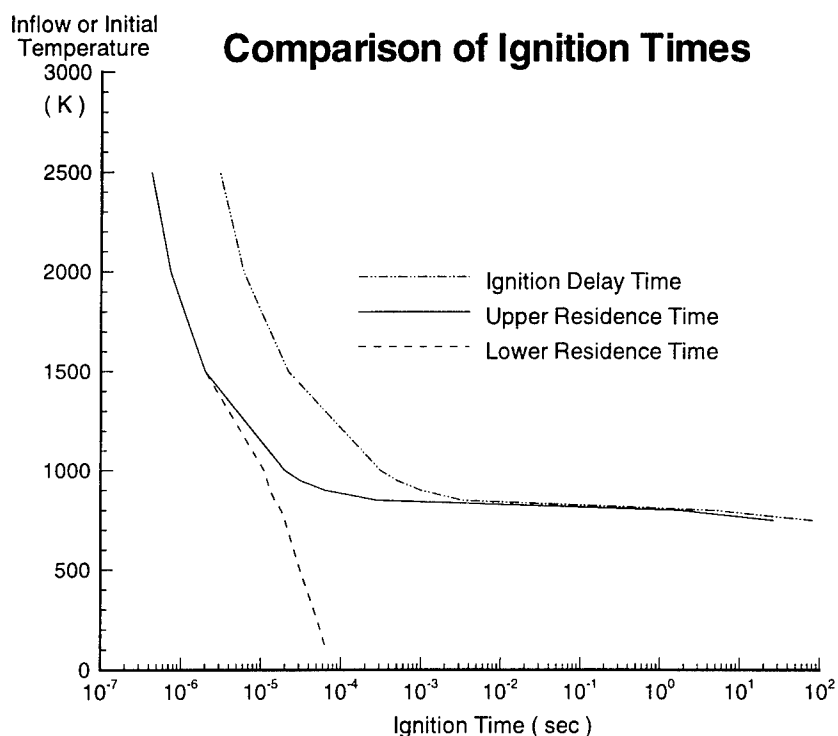


Figure 29. Effect of Initial or Inflow Temperature on Ignition Delay, Upper Residence, and Lower Residence Times for Hydrogen Air Combustion.

the simplified analysis both decrease moving the reaction into the single solution range. As discussed below, the residence times for the calibration and baseline cavities were about 5 and 1 milliseconds, respectively, which were above the lower residence time required for sustained combustion at these conditions.

For the flight Mach number conditions under evaluation, the temperature increases with Mach number and for the higher Mach numbers the static pressure is lower. The results of lower residence time calculations using the global hydrogen chemical kinetic rate are shown in Figure 30. These results show that the lower residence time decreases with Mach number, confirming the expected result that the lower Mach number case is the most difficult for flame holding. Also shown in Figure 30 is that the water mass fraction decreases as free stream Mach number increases due to the shifting equilibrium at high temperatures as discussed in Sect. 4.4.1. The equilibrium temperatures were 2275, 2472, and 2716 K for free stream Mach numbers of 4.0, 5.6, and 7.0, respectively.

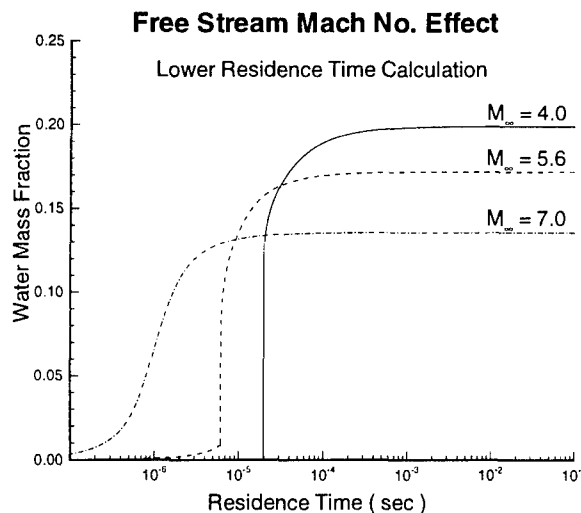


Figure 30. Free Stream Mach Number Effect on Water Mass Fraction for Lower Residence Time Calculation.

4.4.2 Initial and Inflow Temperature Effect on Hydrocarbon Combustion.

Figure 31 shows ignition delay calculations using the full propane reaction rate set. For the higher initial temperatures, the temperature decreases significantly before ignition. At an initial temperature of 2500 K, the temperature drops 500 K during the decomposition process. This illustrates the amount of energy absorbed during propane fuel decomposition.

The lower residence time, upper residence time and ignition delay time for propane at a stoichiometric ratio of 1.5 were calculated at various initial and inflow temperatures. The results were plotted in Figure 32. The full propane reaction set was used for these calculations. The ignition delay time and upper residence time each

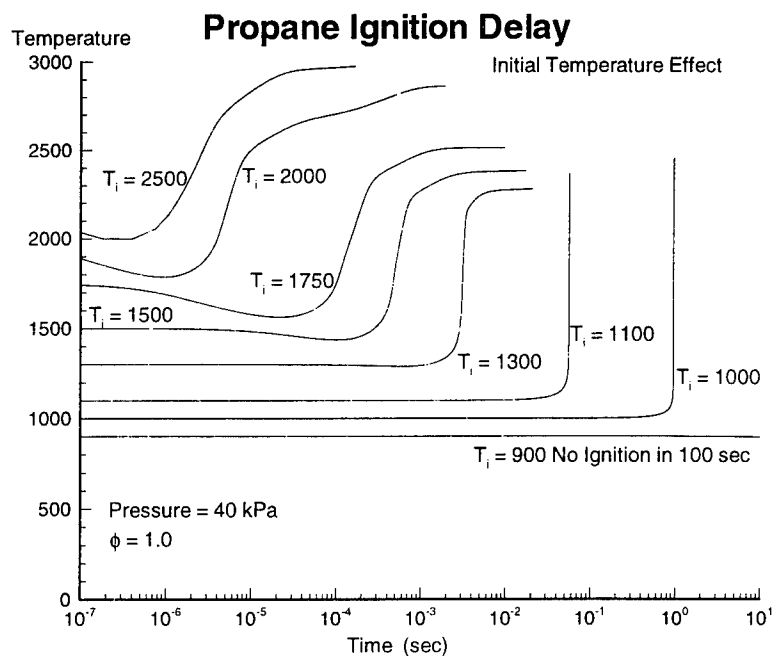


Figure 31. Ignition Delay Calculations with the Full Propane Reaction Set.

increase significantly as the temperature drops below 1100 K. The times were determined from the perfectly stirred reactor simulation plots. At high temperatures (>1800 K), the ignition temperature rise is not clearly discernable as shown in Figure 31, which resulted in the apparent irregularities in the ignition delay time at high temperatures in Figure 32.

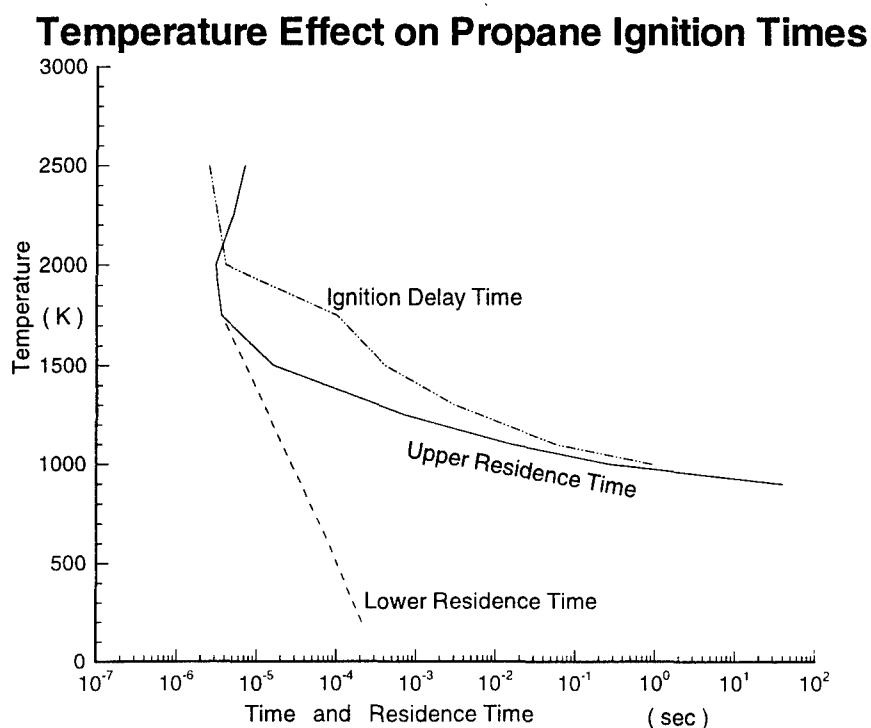


Figure 32. Ignition Delay, Upper and Lower Residence Times from Propane Perfectly Stirred Reactor Simulations.

4.4.3 Fuel to Air Ratio Effect. Lower residence time simulation results using the global reaction rate for lean fuel to air ratios were shown in Figure 33. As the fuel to air ratio was decreased below the optimal stoichiometric value, $\phi = 1$, the heat release per reactant mass decreases. The decrease in heat release makes the temperature lower so that the reaction rates were lowered, making the lower residence time higher. Also at lower ϕ values, the concentration of hydrogen was reduced making the reaction rate slower, again increasing the lower residence time.

Lower residence time simulations were also computed using the complete eight species, eighteen reaction set of Drummond (71:374) as shown in Figure 34. The Drummond rate set was used here for future comparisons with the multi-dimensional

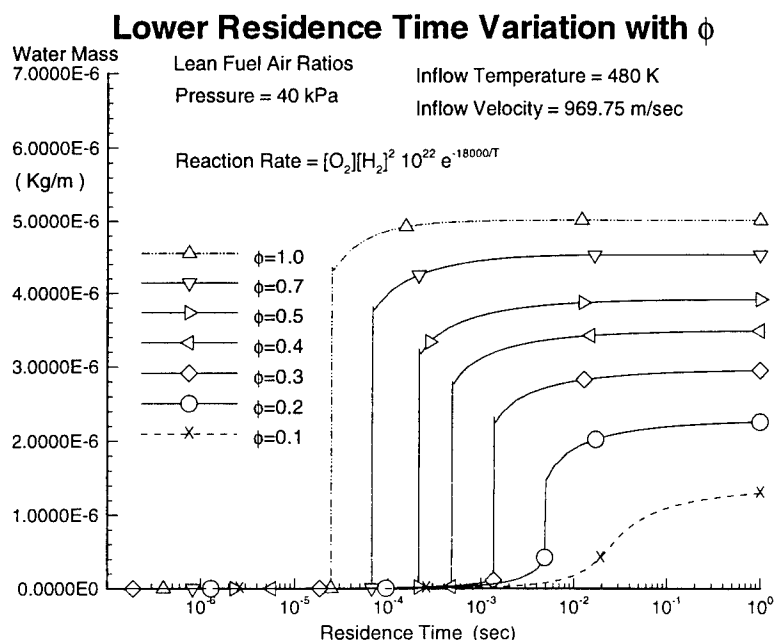


Figure 33. Water Mass for Lower Residence Time Calculations with Lean Fuel to Air Ratios Using the Global Water Reaction.

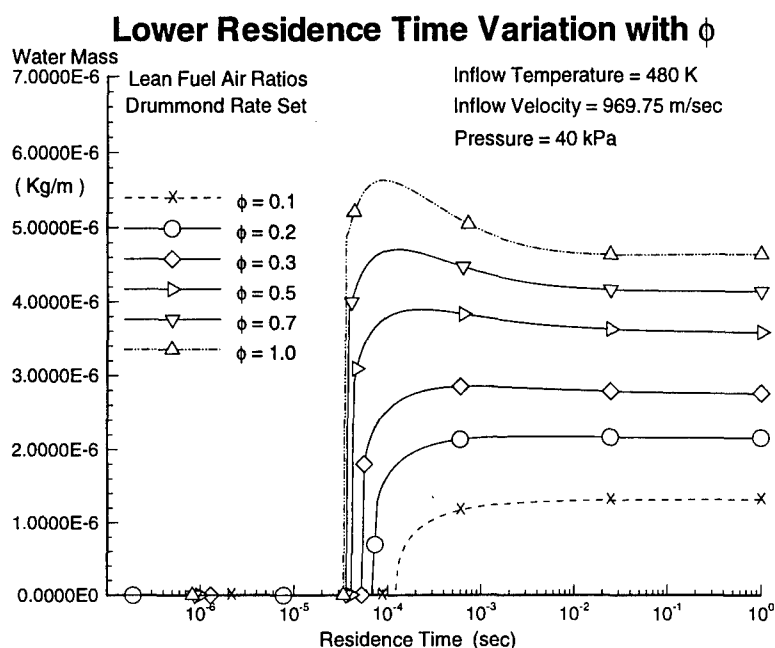


Figure 34. Water Mass for Lower Residence Time Calculations with Lean Fuel to Air Ratios Using a Full Water Rate Set.

simulations using the Drummond rate set. The lower residence times did not increase with ϕ as much as the global reaction. The mixing of trace species helped to sustain combustion at the low fuel to air ratios. These simulations showed that the lower residence time remained below one millisecond for ϕ values as low as 0.1.

Lower residence time simulations were also calculated for rich fuel to air ratios with the global reaction rate set as shown in Figure 35. The shortest lower residence time and greatest water mass was calculated for $\phi = 2.0$. The water mass fraction was also higher for this fuel to air ratio. For the global reaction, the additional hydrogen increased the equilibrium water concentration. This increased the temperature which in turn increased the reaction rate, thereby reducing the lower residence time. The exponent of two on the hydrogen concentration in the global reaction rate, $[H_2]^2 \cdot [O_2] \cdot k_f$

makes the rate more sensitive to hydrogen concentration. Excess hydrogen increases the reaction rate more than low oxygen decreases the rate. However, at even higher ϕ values, the low oxygen level slows the reaction rate.

The fuel rich, lower residence time results shown in Figure 36 were computed using the Drummond reaction set. These results showed a lower increase in residence time than the global reaction. Also the shortest residence time was for a stoichiometric fuel to air mixture. The sensitivity of the full rate set reaction to excess hydrogen was less than the global rates concentration squared term. The rise in water mass for ϕ near two was caused by the temperature decrease near the lower residence time. The temperature decrease resulted in a density increase because the pressure was fixed. The

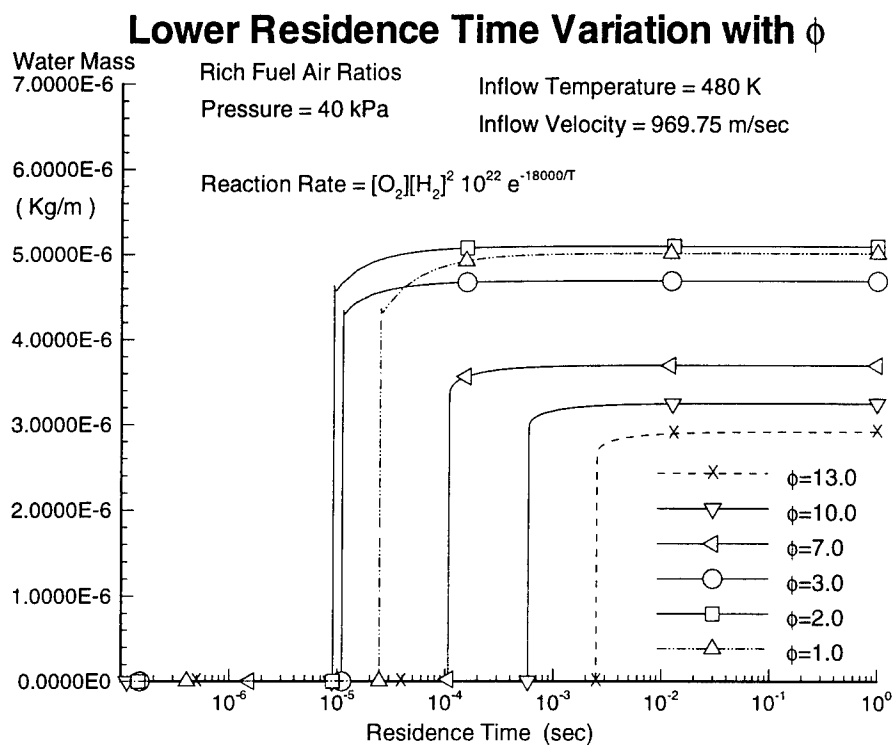


Figure 35. Water Mass for Lower Residence Time Calculations for Rich Fuel to Air Ratios Using the Global Water Reaction.

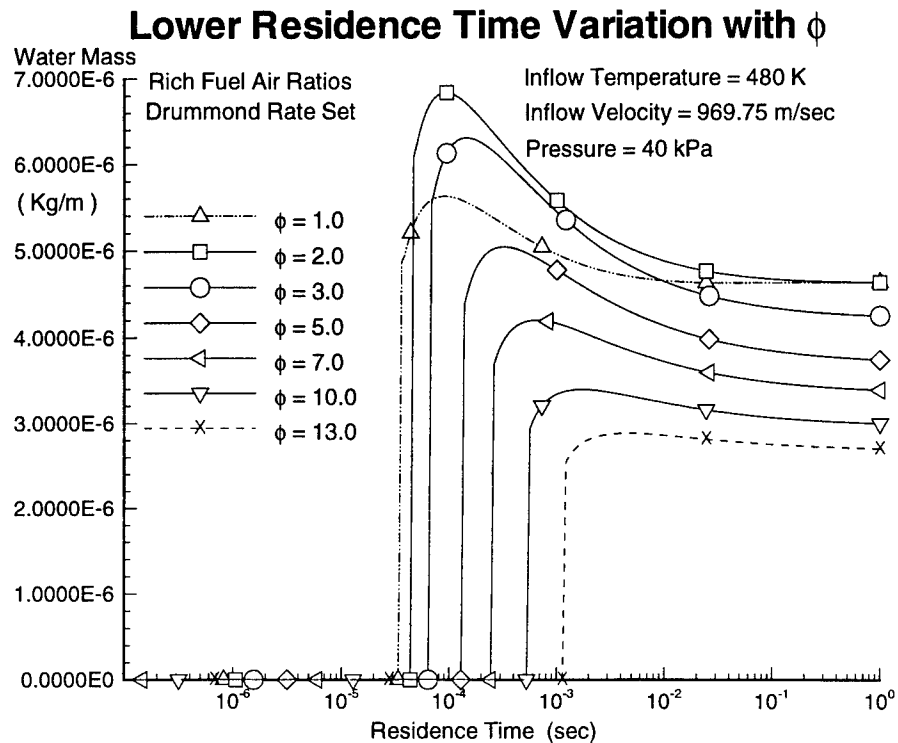


Figure 36. Water Mass for Lower Residence Time Calculations for Rich Fuel to Air Ratios Using a Full Water Reaction Set.

density increase caused an increase in the water mass for the fixed volume. However, the water mass fraction decreased monotonically with residence time for all cases.

The lower residence time variation with fuel-to-air ratio for several combustion models is shown in Figure 37. For a fixed fuel-to-air ratio, if the residence time was above the curves, then combustion could be supported by the flame holder. Also if a flame holder residence time was known, then the fuel-to-air ratios that could support combustion would fall between the curves as indicated by the dashed line. The global models were tuned at a stoichiometric ratio of one so at that point, the lower residence times are about the same.

The difference between the global and complex reaction sets indicate that the global reaction rate equation gives the same results as a complex reaction only over a narrow range. The use of a global reaction rate was not valid over a broad operating conditions. However, the efficiency of the global reaction makes it a good candidate for multi-dimensional simulation. It is shown in Sect. 5.2.11 that the phenomena associated with blowout does not change significantly by using a global model.

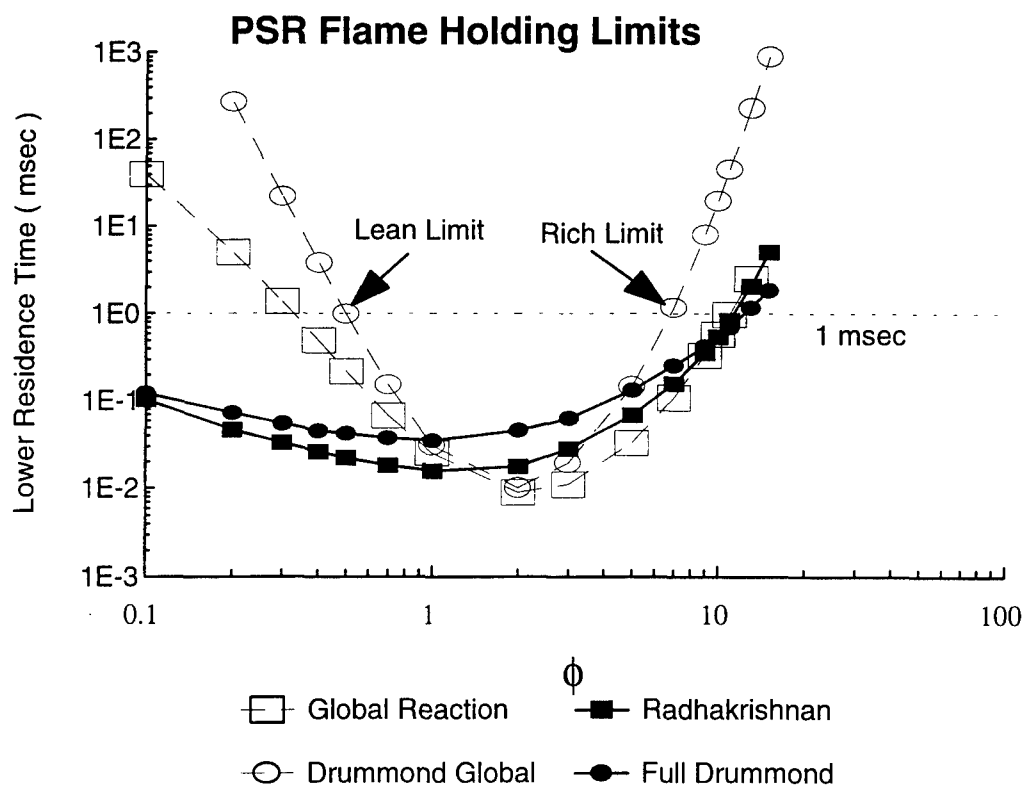
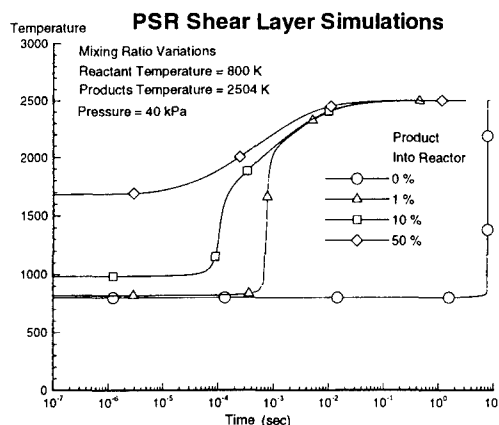


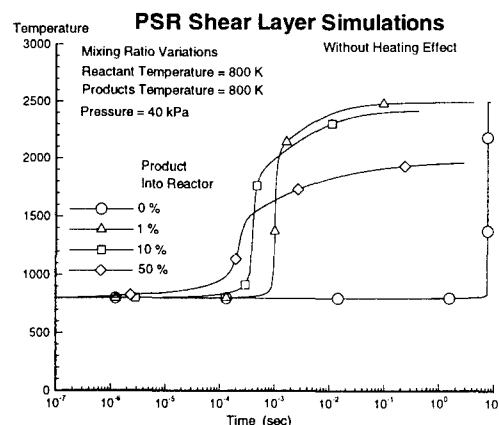
Figure 37. Lower Residence Time Variation with ϕ for Several Chemical Kinetic Rate Models.

4.4.4 Mixing Simulation Results. In order to evaluate the relative importance of thermal and trace species diffusion on the flame spreading in a shear layer, mixing shear layers were simulated with and without thermal effects. The analysis procedure is described in Sect. 3.2.1. The calculation results shown in Figure 38 a) show that with the products at the equilibrium temperature, a modest 1% product mixing with the reactants greatly reduces the ignition delay times.

The change in ignition delay time may have been caused by the high temperature of the products. Comparison of Figure 38 a) with Figure 28 at 1000 K where the 0% ignition delay time was 3×10^{-4} which was very close to the 10% mixing simulation ignition time. Further simulations were conducted using cold products entering the shear layer. These results are shown in Figure 38 b). Without the heating effect of thermal diffusion, the ignition delay time is still substantially reduced giving an indication that trace species diffusion is significant in the shear layer flame spreading process. The concentrations of free radical species in the products are above



a) Equilibrium Temperature Products



b) Low Temperature Products

Figure 38. Mixing Layer Simulations with Various Product Percentages.

the critical concentrations required for ignition, thus any mixing significantly reduces the ignition delay time, at this temperature. However due to the wide temperature difference, 2300 K, across the shear layer, the effects of thermal diffusion should dominate the flame spreading process. Also, the ignition delay calculations in Sect. 4.4.1 showed that ignition times were very sensitive to temperature in the 800 K range.

Figure 39 shows the results of calculations with various reactant and product temperatures at a 10% mixture ratio. These results showed that at mixture temperatures below 700 K (\square), the ignition delay time was substantial. For all 10% product calculations, the initial mass fraction of hydroxyl (OH) initially decreased below the unreacted mixture values, and then increased near ignition as shown in Figure 40. For the cold case, the hydroxyl mass fraction continues to decrease to seven orders of magnitude below the unreacted mixture value indicating that ignition is not eminent. These results

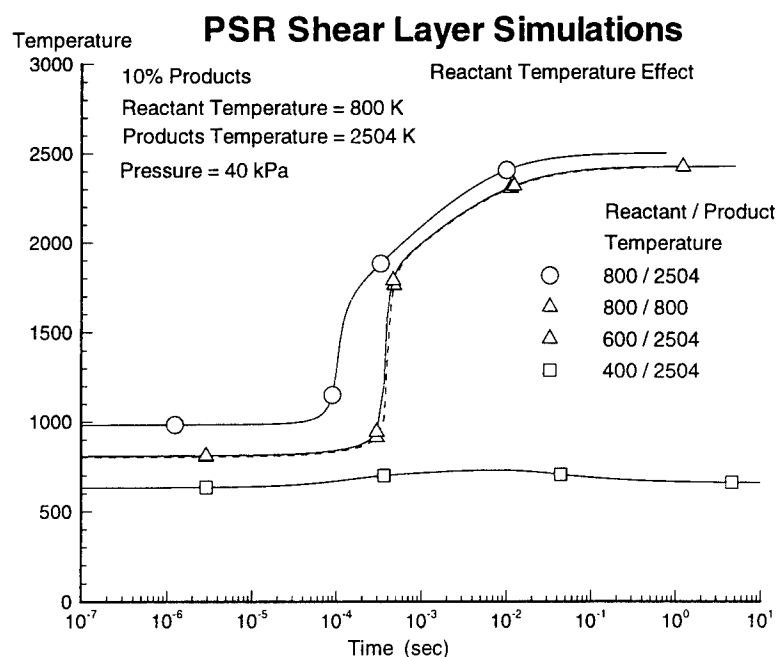


Figure 39. PSR Shear Layer Simulations with Various Reactant / Product Temperatures.

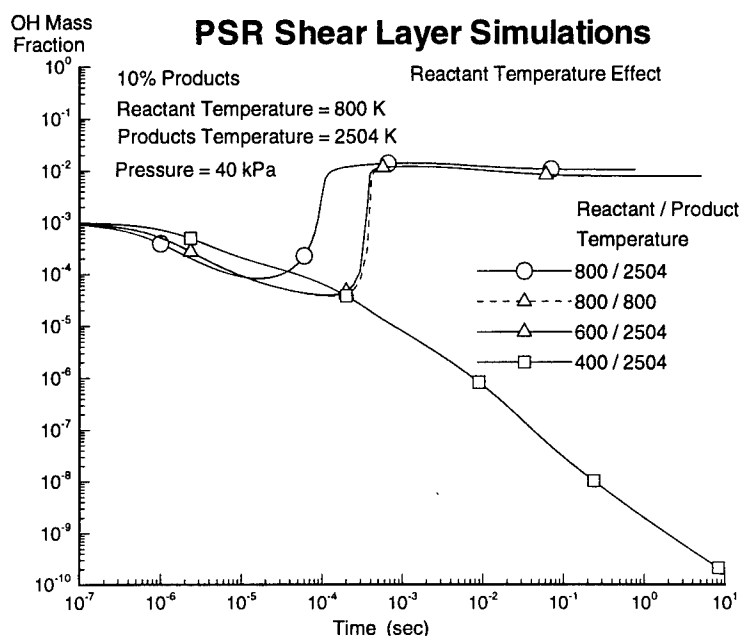


Figure 40. OH Concentration Change with Time for Various Mixing Cases.

indicate that at low reactant temperatures (<700 K), thermal diffusion may dominate the ignition process in shear layers, while at higher reactant temperatures (800 - 1000 K) radical diffusion becomes important.

The contact time (cavity length / free stream velocity) for the calibration case was 1.7×10^{-4} seconds, and for the baseline case it was 5.8×10^{-5} seconds. These contact times are similar to the those required for a temperature rise to occur, indicating that the contact time may be the limiting factor for flame propagation out of the cavity and into the free stream.

4.4.5 Heat Loss Effects. The heat loss approximation model (Sect. 3.2.5) was applied in lower residence time calculations. The effect of heat loss on lower residence time is summarized in Table 9. This table indicates that heat loss may increase the lower residence time; i.e., reduce the flammability range for cavity flame holders. This reduction was similar to the experimental values obtained comparing steel and cooled aluminum walls for a reversed step flame holder (24:57). Also, the effect on lower residence time of the maximum possible radiation loss was on the order of the convection loss.

Table 9. Increase in Lower Residence Time Due to Heat Loss.

		Lower Residence Time (msec)			
ϕ	Wall Temperature (K)	Adiabatic	Convective Heat Loss Estimate	5* Convective Heat Loss Estimate	Convective + Radiative Heat Loss
0.4	1000 K	0.48	0.52	0.69	0.83
	500 K	0.48	0.63	1.35	1.18
1.0	1000 K	0.025	0.035	0.086	0.203

The heat transfer per unit mass increases as the residence time decreases for these models. As the residence time decreases the cavity size decreases. The wall area decreases linearly with residence time and the volume decreases quadratically, per unit depth. This leads to an increase in the heat loss per unit mass as the residence time decreases. For the convective heat transfer model, as the length decreases, the Reynolds number decreases leading to an increase in the averaged heat transfer. Table 10 summarizes the unit heat transfer from the models for various residence times. The radiative heat transfer estimate was larger than the convective heat transfer estimate.

Also, as the residence time decreases the convective heat transfer makes up a larger fraction of the combined heat transfer. The radiation heat loss increases less with reduced wall temperatures.

Table 10. Heat Loss from the Heat Transfer Models for 1000 K / 500 K Walls.

Residence Time (msec)	Convective Heat Loss Model (MJ / Kg)		Convective + Radiative Heat Loss Model (MJ / Kg)	
	$\phi = 0.4$	$\phi = 1.0$	$\phi = 0.4$	$\phi = 1.0$
0.1	0.12 / 0.24	0.34 / 0.52	2.0 / 2.4	8.5 / 8.8
0.01	1.78 / 3.52	5.33 / 7.97	18.8 / 22.35	83.0 / 86.5
0.001	23.97 / 50.62	92.81 / 136.0	111.9 / 26.6 *	747.2 / 783.1

* - No Combustion

4.5. Perfectly Stirred Reactor Summary

The perfectly stirred reactor analysis indicated several results. First, the ad hoc elimination of species for reducing chemical kinetic rate sets is not accurate. Also, orders of magnitude variations in ignition delay time and lower residence times was obtained for the variety of chemical kinetic rate sets compared. The model also showed that ignition delay times of well over 1.0 second could be expected for temperatures below 800 K with hydrogen and below 1000 K with propane. Moreover, lower residence times were fractions of a millisecond, even for low inflow temperatures. This implies that small flame holders could sustain a flame at low inflow temperatures. The lower

residence time variation with fuel-to-air ratio was shown for several chemical kinetics models. Heat loss was shown to increase the lower residence time. A preliminary investigation into flame spreading within the shear layer using a full kinetics models showed that trace species diffusion may impact flame spreading, if thermal diffusion does not dominate the spreading process. The perfectly stirred reactor model was also used to calibrate global reaction models for use in multi-dimensional analysis.

In this chapter, the lower residence time has been identified as an important flame holding parameter. For a stirred reactor the lower residence time represents the minimum residence time required to sustain a flame. If the perfectly stirred reactor assumption is valid and the residence time approximation model is reasonable, the size of cavity flame holder can be determined. As will be shown in Chapter 5, the perfectly stirred reactor and residence time approximation model give good results on flammability limits. The analysis presented in this chapter is sufficient for determining the minimum size of cavity flame holder required to sustain a flame.

5. Two-Dimensional Results

In order to further assess the blowout mechanism for a cavity in supersonic flow, two dimensional simulations were performed. The results of these simulations are presented in this chapter. First, the accuracy of the computational method was assessed. A comparison of the results from two CFD codes with experimental data on a configuration similar to the proposed cavity is discussed. The results of a grid resolution study are presented next. Also, the results of the assessment of the effect of numerical smoothing, and a verification of the simulated turbulent shear stress within the shear layer are presented.

The important flow features of the cavity flame holder are shown to be that the shear layer spans the cavity opening and the large vortex within the cavity. The fuel-to-air ratio blowout limits for the baseline cavity flame holder are presented. Next, the perfectly stirred assumption was validated by comparing the combustion performance from the two-dimensional simulations and the perfectly stirred reactor results for several fuel-to-air ratios. To further validate the perfectly stirred reactor model, simulations of an order of magnitude smaller cavity are shown. Also, flame holding was shown to be more difficult at the low free stream Mach number, as expected. It was confirmed that heat loss reduced the flammability limits. The results of several turbulence modifications illustrated the generality of the PSR flame holding limits. The inflow boundary layer thickness was shown to have negligible impact. Lower temperatures upstream of the cavity were shown to reduce the cavity flame holding ability. The full hydrogen rate set results showed that trace species diffusion did not enhance the flame spreading rate. The PSR flammability limits were shown to agree for a full hydrogen rate set. Finally, verification of flame holding with propane as a fuel was shown.

5.1. Numerical Quality Assessment

The validation of the numerical method to sufficiently resolve the flow for this study is presented in this section. First, a comparison of solutions with experimental data is shown. Then the results of the grid refinement and artificial viscosity studies are presented. Finally, temporal convergence and a check of the turbulence model are shown.

5.1.1 Two-Dimensional Validation Results. The laser Doppler velocimetry data, described in Sect 3.3.7, was used to calibrate the computational fluid dynamics codes. Figure 41 a) shows the averaged axial velocity measurements of Samimy et al. (61) for comparison with the calculated simulations. Velocity profiles from the GASP code using the Baldwin Lomax and K- ϵ turbulence models and from the SPARK code using the Baldwin Lomax turbulence model are compared with the experimental data.

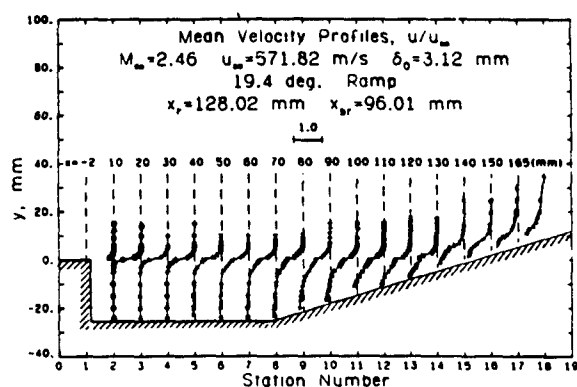
The velocity profiles from the GASP code simulation with the Baldwin Lomax turbulence model (Figure 41 b)) exhibit poor agreement with the data. The high vorticity of the shear layer far from the cavity wall artificially increased the turbulent viscosity within the shear layer. Because of the high shear layer spreading, the pressure within the cavity was also reduced. A thick shear layer caused a smaller portion of the shear layer flow to be diverted upstream into the cavity thereby reducing the cavity pressure. Hence, a slight expansion and recompression above the cavity was simulated.

The velocity profiles from the GASP K- ϵ turbulence model simulation using the Lam-Bremhorst near wall model shown in Figure 41 c) agreed better within the shear layer. However, the velocities within the cavity were above the experimental values and a secondary vortex was located in the upstream portion of the cavity. Also there were two non-physical slip lines that could not be removed with any of the flux limiters or by a

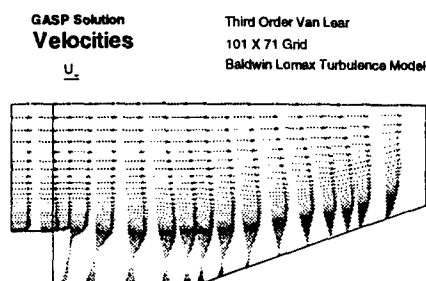
reduction in CFL by two orders of magnitude. One slip line was through the main cavity vortex center and the other was at the initial shear layer formation. The K- ϵ simulations could only be converged an order of magnitude, while the Baldwin Lomax solution residual reduced by three orders of magnitude. However there was no noticeable change in the K- ϵ solution for several thousand iterations at a CFL of 0.5. The inherent unsteadiness of the flow may be the reason for the lack of convergence with the K- ϵ simulation. Because of the relatively poor comparison with data and the unphysical slip lines the GASP code was not used further in this research.

The standard Baldwin Lomax turbulence model (Sect. 3.3.3) was adapted to this problem in the SPARK code. With this form of the model, the velocities computed with the SPARK code (Figure 41 d)) compare reasonably well with the experimental data of Samimy (Figure 41 a)). The backflow velocities at the ramp corner were about twice the experimental values and a small secondary vortex was located in the upstream portion of the cavity. The remaining velocities and the shear layer spreading were in good agreement with the experimental values as shown in Figure 41 d). The only known differences between the Baldwin Lomax model in the two codes are that the GASP code used the Degani-Schiff condition and the SPARK code switches to the outer layer permanently after $\mu_{turb_{outer}} < \mu_{turb_{inner}}$ while the GASP code uses $\mu_{turb} = \min(\mu_{turb_{outer}}, \mu_{turb_{inner}})$. Hence, the model in the SPARK code is more consistent with the original Baldwin Lomax model developed for separated flow (78).

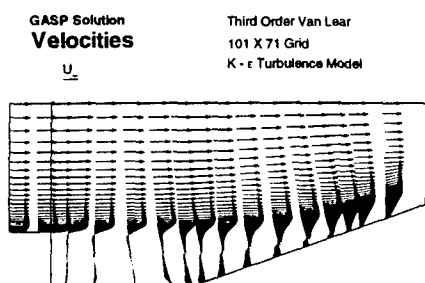
The measured and simulated shear stress values were also very close as shown in Figure 42. The simulation results were about 40% more than the experimental values for the first 4 cm of the shear layer and within the scatter in the data elsewhere. The LDV experimental values measure only the velocity cross correlation so the density cross terms (80) are not included.



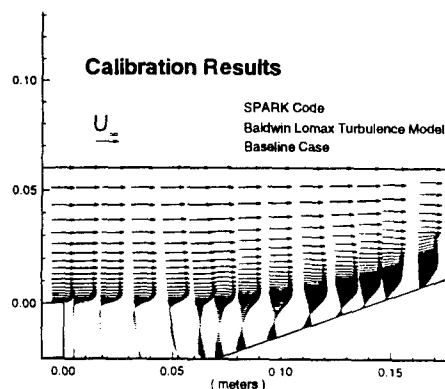
a) Experimental Axial Velocities



b) GASP with Baldwin Lomax Turbulence Model



c) GASP Results with K- ϵ Turbulence Model



d) SPARK Results with Baldwin Lomax Turbulence Model

Figure 41. Comparison of Velocity Results with Experimental Data.

Because of the good comparison with data and the time accurate simulation capability, the SPARK code was chosen for the remaining research. The time accuracy was important in order to determine a residence time and to indicate if the chemical reaction coupled with the flow instabilities.

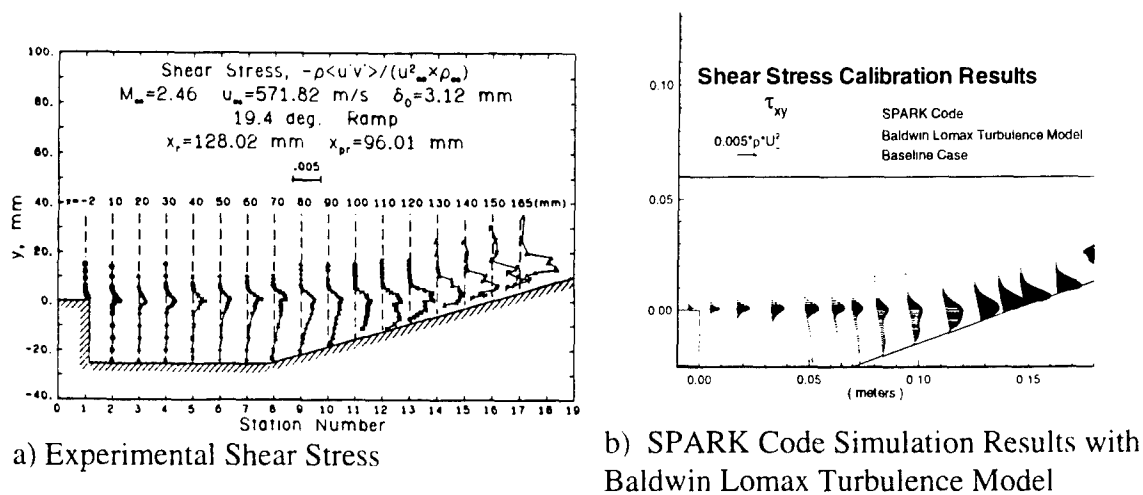


Figure 42. Comparison of Shear Stress from Experiment and SPARK Simulation.

The very large eddy simulation (VLES) results using both the Smagorinski SGS turbulence model and laminar viscosity gave poor results. The shear layer from the simulation was thinner than the experimental shear layer. The thinner shear layer separated upstream of the cavity leading edge and reattached at the aft end of the ramp. The thinner shear layer increased the cavity pressure by diverting more flow into the cavity. As pointed out in Sect. 3.3.3, it was not practical to resolve the fine scales of the turbulent fluctuations. The purpose of these simulations was to qualitatively examine the effects of the largest scale fluctuations by eliminating the damping effects of the Baldwin Lomax models turbulent viscosity and to provide a lower limit on viscosity to bound the error introduced by turbulence model approximation. Also Risha (81), matched compressible shear layer spreading rate measurements using the laminar VLES methodology.

The residence time was calculated by tagging the air initially within the cavity as described in Sect. 3.3.8 and integrating the tagged air within the cavity as the

calculation proceeded. The integrated, tagged air ("cavity air") mass decreased exponentially, where the residence time, τ_r , was the decay time constant or

$$\text{Cavity Air Mass} = \text{Initial Cavity Air Mass} \cdot e^{-t/\tau_r}$$

Figure 43 shows the decay of cavity air mass for different turbulence approximations. A straight line on the semi-log graph above shows that the solution is stationary. The slightly higher slope for the initial decay is due to the tagged mass near the shear layer being removed from the cavity at a rapid rate. The reduced effective viscosity of the laminar and Smagorinski simulations increased the residence time. As indicated on Figure 43, the variation of simulated residence time was about a factor of two, while the different chemical kinetic rate sets showed an order of magnitude deviation (Sect. 4.2.1). The residence time estimation model (Sect. 3.2.4) predicted about ½ the residence time of the Baldwin Lomax CFD results.

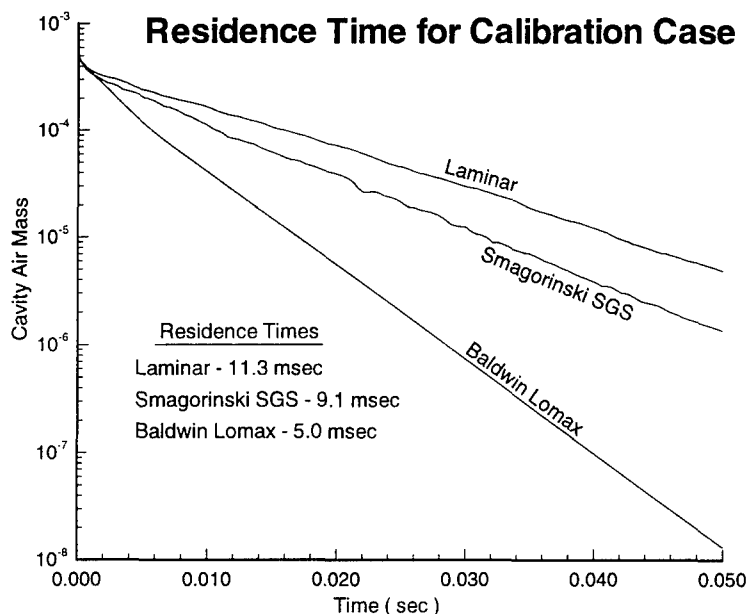


Figure 43. Decay of "Cavity Air" Mass Indicating the Residence Time for Several Turbulence Approximations.

5.1.2 Grid Convergence. Three grid refinement levels were used to determine the sensitivity of the blowout calculated with grid refinement. The number of grid points in each direction for the different grids were 51 by 51, 71 by 71 and 101 by 101 for the coarse, medium and fine grids, respectively. The coarse grid is illustrated in Figure 44. This approximately doubled the number of grid points for each grid refinement. The grids were uniformly refined over the domain. On the coarse grid several fuel to air ratios were calculated with premixed fuel. Each case was calculated for 20 milliseconds physical time to assure a converged solution. The inflow velocity profile, static temperature and static pressure were held constant. At selected fuel to air ratios near the blowouts, the finer grids were used to recalculate the flowfield. The refined grid solutions were initialized with converged coarse grid solution and calculated for 10 milliseconds physical time. The solution for initialization of the fine grids was at a fuel to air ratio near the blowout limit. Due to the unsteadiness of the flow, the residual did not reduce to machine zero. Temporal convergence is discussed in Sect. 5.1.4. As will

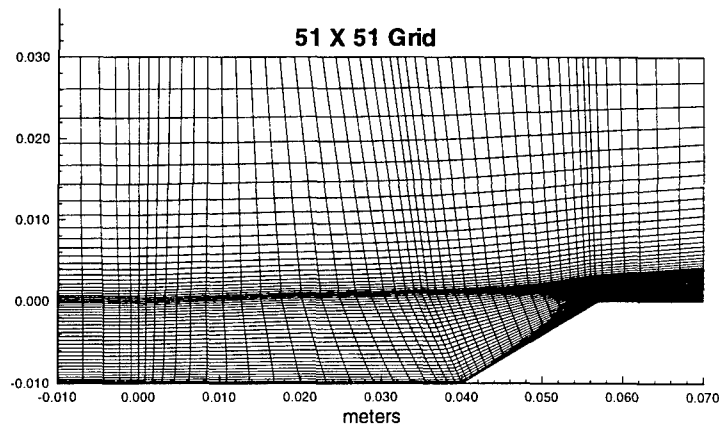


Figure 44. Coarse Grid for Baseline Geometry.

be described below, the agreement between the three grid levels was considered excellent, which indicated that all solutions were grid converged.

The mean axial velocity contours in Figure 45 show that all three grid levels gave nearly identical results. The cavity flow has a primary vortex at about four step heights from the upstream edge of the cavity. The velocities elsewhere in the cavity are at about five percent of the free stream velocity. This comparison was for a stoichiometric ratio of 0.45 which was near the lean blowout for the cavity. This condition was chosen because any sensitivity of the chemical kinetics to grid refinement would have been amplified near blow-out.

The water production rate is the most important parameter for flame holding. Figure 46 shows the water production rate contours for all three grid levels. Again, the agreement was considered excellent. These calculations were performed using the global reaction rate tuned for 40,000 Pascals. For all three grid levels, the water production rate was highest in the shear layer at the upstream part of the cavity. Also, a higher water

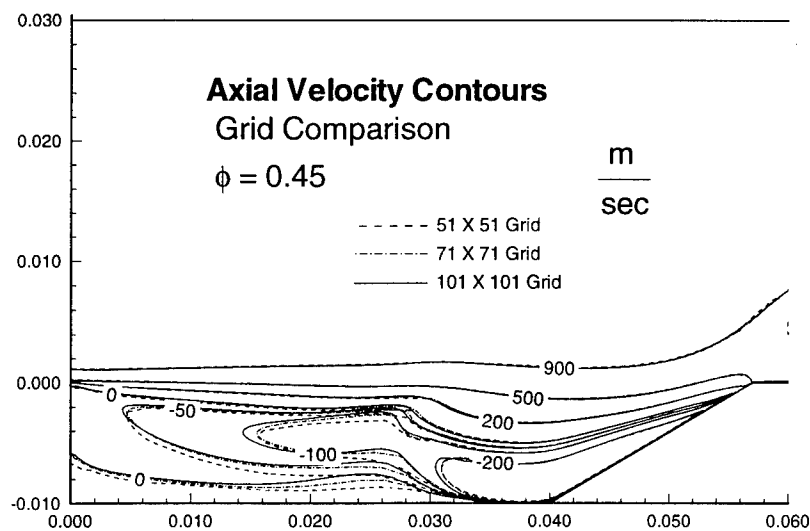


Figure 45. The effect of grid refinement on the calculated mean velocities.

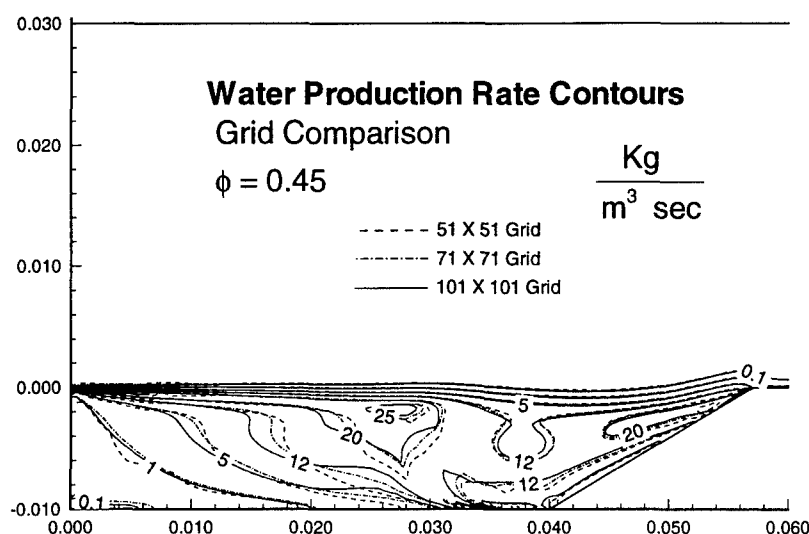


Figure 46. Water Production Rate Contours for Three Grid Refinement Levels.

production rate was located at the shear layer reattachment point. There is a low water production rate within the primary vortex because the water mass collects within the vortex, reducing the reactant concentration. The high water concentration can be seen in Figure 47 where the peak water concentration within the primary vortex is near the complete reaction value of 0.1 for the stoichiometric ratio of 0.45. Additional confirmation that the grid refinement level has negligible effect on the calculated flammability limits for the baseline cavity is given in Sect. 5.2.2.

The CPU time required for the fine grid solutions was substantially more than the coarse grid solutions. The solution time depended on the fuel-to-air ratio, with rich fuel-to-air ratios taking about 40% more CPU time. Table 11 summarizes the increases in CPU time for various cases. On the SGI Power Challenge computer, the baseline coarse grid, low ϕ simulations required 1.4 days of CPU time for a 20 millisecond simulation.

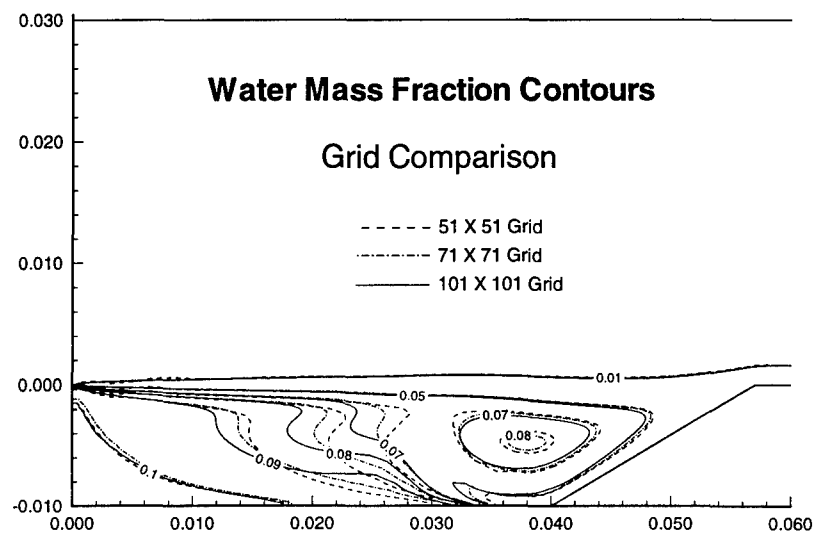


Figure 47. Water Mass Fraction Contours for the Three Grid Levels at $\phi = 0.45$.

Table 11. Computational Time Factors for Various Simulation Changes.

	CPU time factor
High Phi	1.4
71 X 71 Grid	2.5
101 X 101 Grid	8.2
Full H-O Kinetics	3.5

5.1.3 Effects of Added Artificial Viscosity. In order to obtain a solution with the SPARK code, numerical smoothing was applied, as described in Sect. 3.3.6. The minimum amount of smoothing required to consistently obtain a solution was applied. Without the additional smoothing, an odd/even decoupling grew out of control. The instability usually started near the cavity trailing edge. Unless otherwise stated the smoothing coefficients were set to $\alpha=0.2$ and $\epsilon=0.4$ in equation (14) of Sect.3.3.6. Increasing α or decreasing ϵ applies more numerical smoothing.

Figure 48 shows that increasing the amount of numerical smoothing had negligible effect on the water production rate. The range of coefficients investigated effectively doubled the amount of smoothing. As shown in Figure 48, varying the artificial viscosity had minimal effects on the water production. Contours of other properties showed smaller differences.

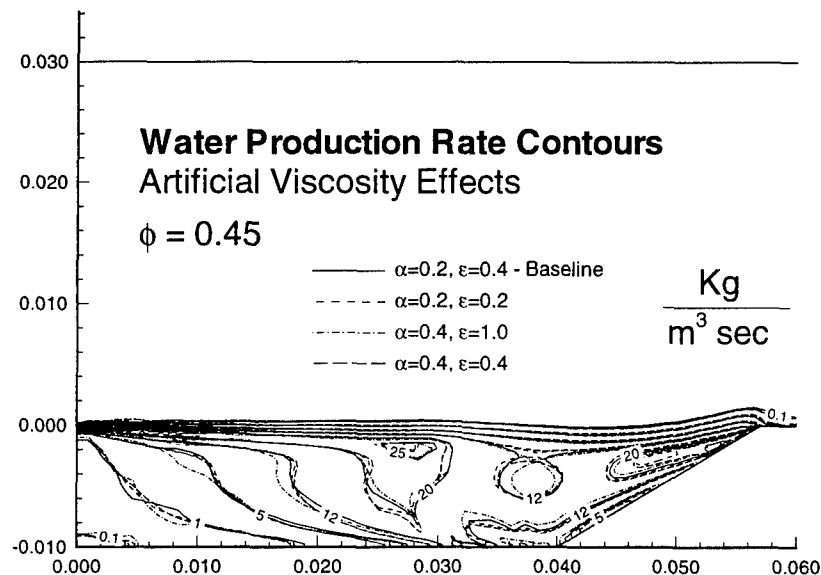


Figure 48. Water Production Rate Contours with Different Amounts of Added Numerical Smoothing. $\phi=0.45$, 51 X 51 Grid

The numerical smoothing was also shown to have negligible effect on the flow stability of the cavity. Figure 49 shows the unsteady pressure at two step heights downstream of the cavity lip. These oscillation amplitudes were all significantly less than the pressure oscillation amplitudes obtained in the laminar flow simulations shown in Sect. 5.2.8.

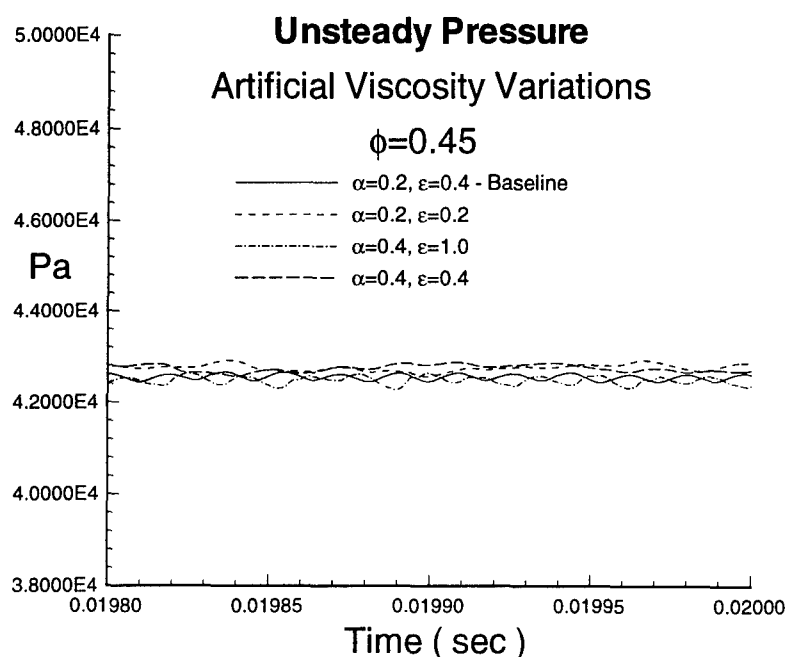


Figure 49. Unsteady Pressure for Different Amounts of Added Numerical Smoothing.

5.1.4 Temporal Convergence. Because nearly all simulations had oscillations due to the inherent unsteadiness for cavity flows described in Sect. 2.8.2, the residuals were not a measure of convergence. In order to evaluate temporal convergence, the integrated water mass within the cavity was used. When the integrated water mass was stationary, the solution was considered converged.

Figure 50 shows the progression of the integrated water mass and the density residual for a calculation starting initialized to the condition shown in Figure 51. The initial condition was for $\phi = 1.0$ with the inflow stoichiometric ratio fixed at a value of 0.5. The cavity was set to equilibrium values of temperature and species mass fraction; the axial velocity was set to a power law profile in y , and the normal velocity was set to zero. For the baseline geometry the water mass levels off before 5 milliseconds, but the calculations were continued for 20 milliseconds to assure that a stationary final state was obtained. This time corresponds to over 300 characteristic times. For most similar calculations of cavity flows, a stationary state was achieved in 6 characteristic times (35-42). The additional time for these calculations was required for species and thermal diffusion into the cavity. The diffusion processes occur on the order of the residence time, which is much longer than the characteristic time. The residence time for this configuration was 1.2 milliseconds while the characteristic time was 0.06 milliseconds. Temporal convergence results are presented throughout the remainder of this report.

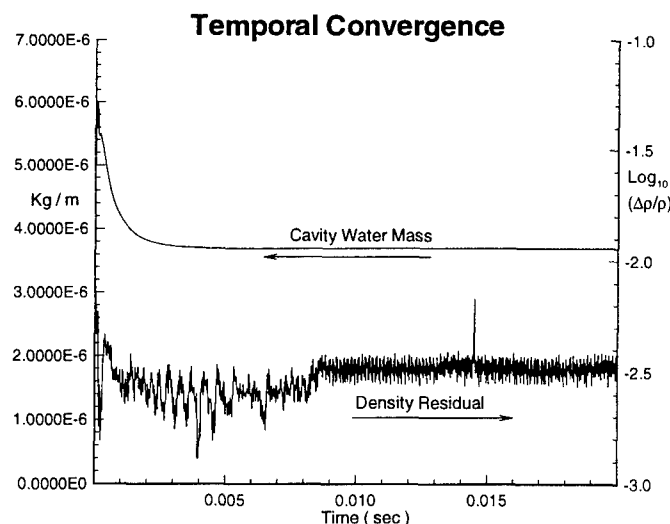


Figure 50. Temporal Convergence Parameters for a Cavity Flame Holder Simulation.

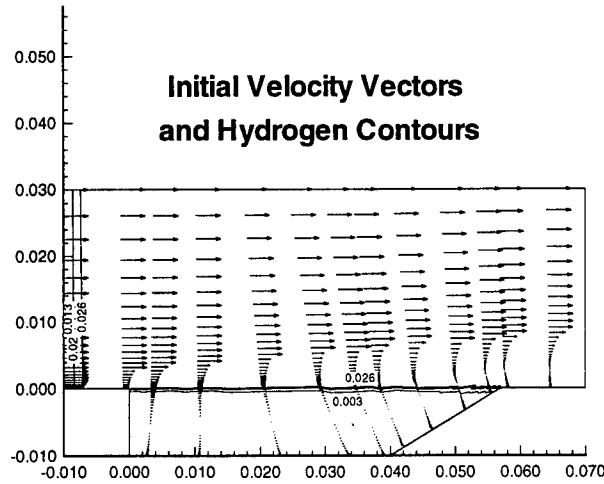


Figure 51. Initial Condition for Baseline Cavity Simulation.

5.1.5 Verification of Turbulence Model. The accuracy of the Baldwin Lomax turbulence model was qualitatively assessed, as described in Sect. 5.1.1. To further confirm the applicability of the Baldwin Lomax turbulence model for the flame holding cavity flow, a comparison of calculated turbulent viscosity with accepted turbulence viscosity for a free shear layer was performed. For a free shear layer, Prandtl's mixing length model for the turbulent viscosity is given by:

$$\mu_{turb} = \rho \cdot l_{mix}^2 \cdot \left| \frac{dU}{dy} \right|$$

where for a shear layer $l_{mix} = \alpha \cdot \delta(x)$, $\alpha = 0.071$, and $\delta(x)$ is the shear layer thickness. By selecting values of y and axial velocity from above and below the shear layer and density from the mid point the accepted turbulent viscosity could be estimated as

$$\mu_{turb} = \alpha^2 \cdot \rho_{mid\ point} \cdot (y_{above} - y_{below}) \cdot (\bar{u}_{above} - \bar{u}_{below}) . \quad (15)$$

Table 12 compares μ_{turb} values from CFD simulations to that calculated with equation (15). Due to the complexity of the flow, and the approximate nature of equation 16 only qualitative agreement was expected. However the comparisons are considered very good with a nominal difference of only 5-10% for the shear layer center.

Table 12 Comparison of Baldwin Lomax Turbulent Viscosity with Shear Layer Mixing Length Model for $\phi = 0.2$ Case.

	x location (mm)	y location (mm)	mean axial velocity (m / sec)	density (Kg / m ³)	μ_{turb}	μ_{turb} eq. 16
51 X 51 Grid	10.36	1.279	921.5	0.2437	0.00260	0.00153
	10.38	0.1051	520.2	0.1567	0.00167	
	10.47	-1.048	91.6	0.1409	0.00156	
	20.01	1.270	906.5	0.2362	0.00347	0.00222
	20.03	-0.156	502.6	0.1559	0.00227	
	20.83	-1.997	40.4	0.1409	0.00210	
71 X 71 Grid	10.25	1.170	912.5	0.2379	0.00250	0.00154
	10.23	0.05	493.2	0.1543	0.00161	
	10.29	-1.140	55.6	0.1413	0.00152	
	19.39	1.142	895.4	0.2295	0.00325	0.00212
	19.71	-0.361	411.9	0.1509	0.00215	
	20.07	-1.655	72.8	0.1408	0.00205	

5.2. Two-Dimensional Analysis of Cavity Flame Holders

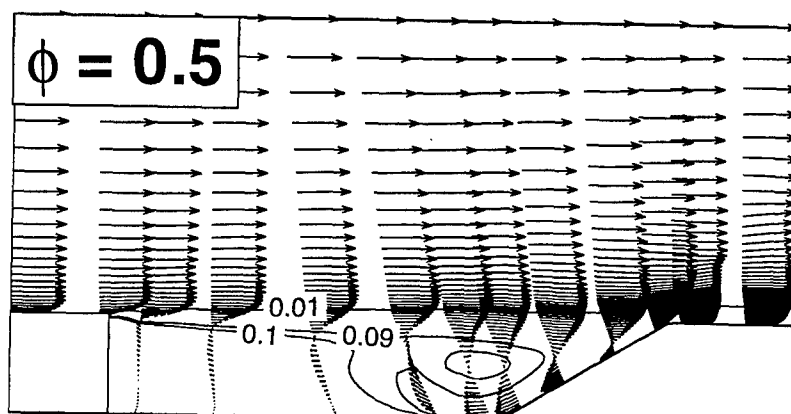
In this section, the results of the two-dimensional analysis of cavity flame holders are presented. Simulations with variations in fuel to air ratio, turbulence model, inflow boundary layer, free stream Mach number, heat loss, cavity size, and chemical kinetics are presented. Also, included are a discussion of the transonic effects at high fuel to air ratios and comparisons with perfectly stirred reactor results.

5.2.1 Important Flow Features. The cavity flow was dominated by a large vortex centered in the downstream part of the cavity as shown in Figure 52. This figure shows the results of calculations near lean blowout (Figure 52 a)) and well within the flammability limits (Figure 52 b)). For both cases, the high velocity downflow along the cavity ramp is evident. A small separation is also evident on the cavity floor. During the blowout process, the separation temporarily supports a flame front within the cavity, as described in Sect. 5.2.2 and 5.2.5. The lean case water contours show that partially reacted flow enters the cavity at the downstream edge. The flame front progresses higher into the flow for the reactive case. In the next section, it will be shown that at fuel to air ratios near blowout, most of the cavity reacts at the same rate, which validated the perfectly stirred reactor assumption. The shear layer spans the cavity opening, i.e., an open cavity flow was observed.

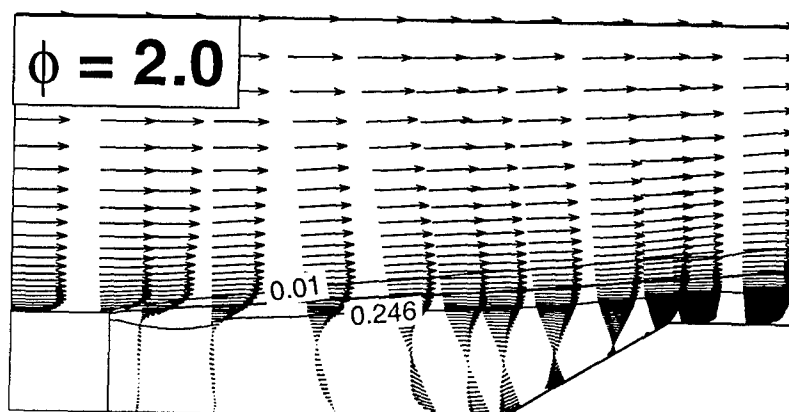
The shock structure well within the flammability limits differs from that near blowout. For the reactive case, an oblique shock forms at the cavity leading edge as shown in Figure 53. For the case near blowout the pressure contours show that a shock forms near the reattachment point. The reaction in the cavity acts to expand the gas, causing the shear layer to rise slightly, thus reducing the downstream shock strength for

the reactive case. For most cases, the pressure field had little impact on the water production. The exception is when the reaction was near blowout at transonic flow conditions, as described in Sect. 5.2.3.

Velocity Vectors and Water Mass Fraction Contours



a) Near Blowout



b) Reactive

Figure 52. Velocity Vectors and Water Contours for a Condition Near Blowout and a Reactive Condition.

Pressure Contours

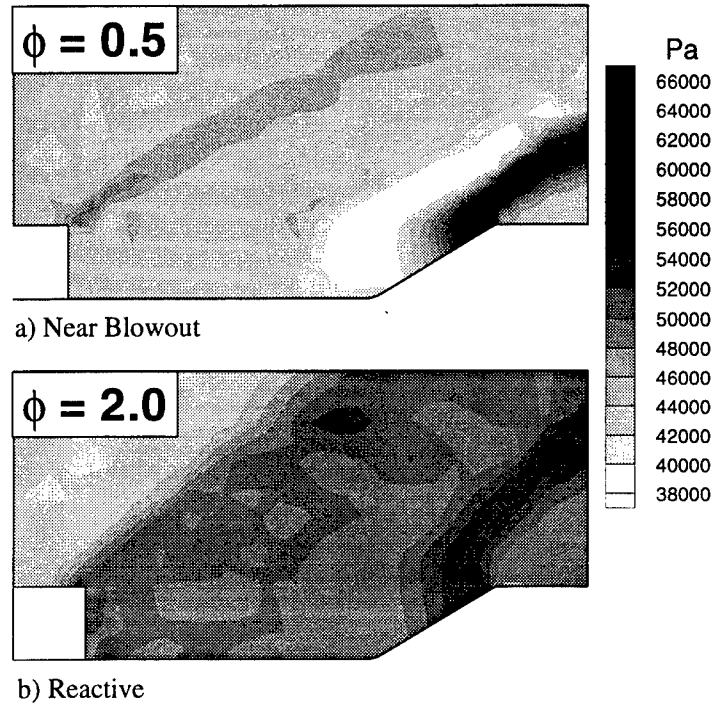


Figure 53. Typical Pressure Contours for Reactive and Near Blowout Conditions.

5.2.2 Variations in Fuel to Air Ratio. The integrated water mass within the cavity was used as an indication of the flame holder effectiveness. Figure 54 shows the time history of the water mass within the cavity for lean fuel to air ratios on the coarse grid. The integrated water mass levels off to show that the solution was stationary.

Integrated Cavity Water Mass Change with Time

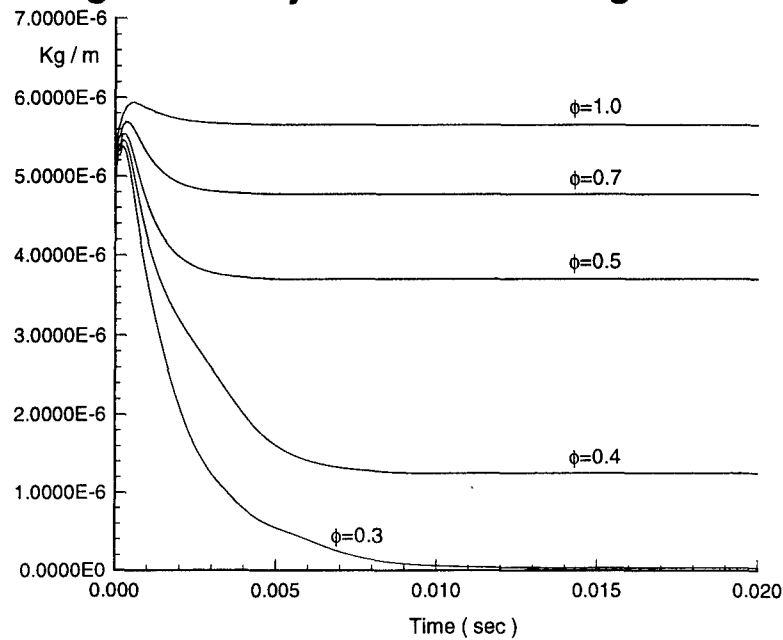


Figure 54. Progression of Integrated Water Mass within the Cavity.

To compare grid refinement levels effect on combustion, the water within the cavity was integrated for each calculation. Figure 55 shows the final water mass fraction for the three different grids over the variation in fuel to air ratio. At $\phi = 11$ the finer grid maintained the intermediate blowout profile. The different grid levels had negligible

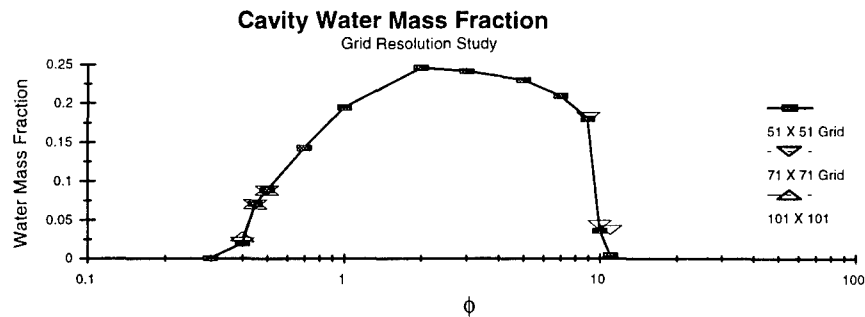


Figure 55. Integrated Water Mass Fraction Within the Cavity for Converged Solutions for Various Fuel-to-Air Ratios.

effect on the blowout fuel to air ratio. This again confirms the grid independence of the solution for blowout calculations. A slight difference was observed for the rich blowout limit where the finer grid maintained the flame at the stagnation point on the cavity wall better than the coarse grid. This effect was minimal because the flame was not propagating into the core flow at these conditions. The transonic effects, described in Sect. 5.2.3, limit the usefulness of the rich blowout condition.

Figure 56 shows the progression of water production as lean blowout was approached. At fuel to air ratios near stoichiometric, all of the water production occurs in the shear layer. As the fuel-to-air ratio is decreased, the flame front widens and moves

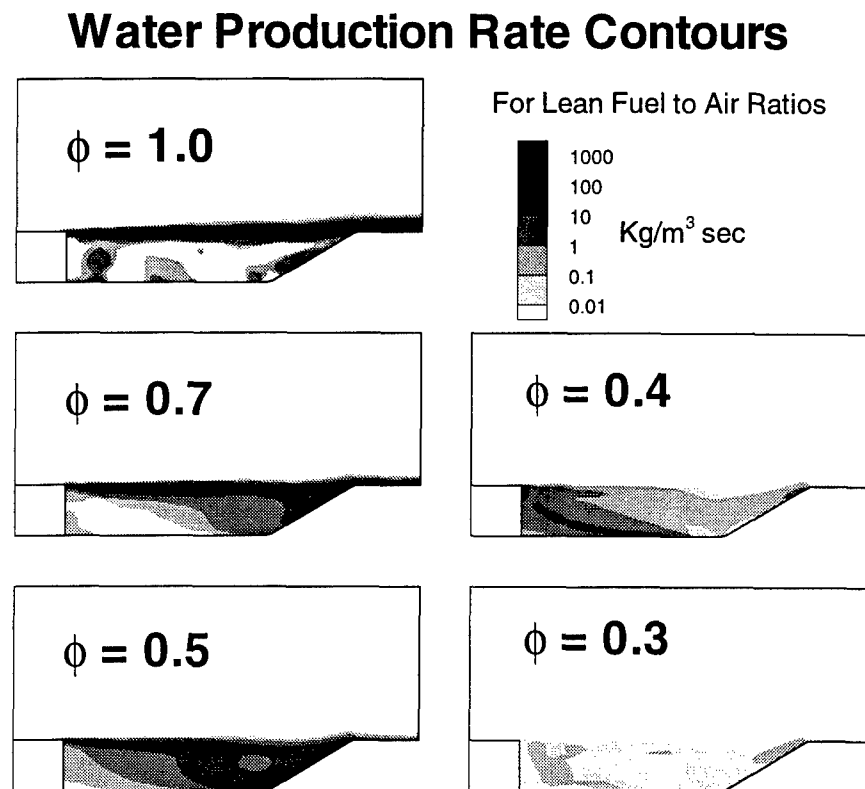


Figure 56. Water Production Rate Contours for Lean Fuel to Air Ratios.

within the cavity. At fuel to air ratios very near blowout, nearly the entire cavity was producing water at the same rate. This would indicate that residence time should dominate the cavity blowout process rather than contact time. However, near blowout, no reacting flow was leaving the cavity, which indicates that the core flow has not been ignited. This phenomenon, where the cavity was ignited, but failed to ignite the main flow, was also observed in recent scramjet experiments with a cavity following a ramp fuel injector (19). Therefore, contact time may be a factor in igniting the core flow. The water production rates for the $\phi = 0.3$ case are at an insignificant level for this fuel-to-air ratio indicating a non-combusting solution.

The trends as the rich blowout was approached were the same as those discussed for the lean blowout (see Figure 57). For the $\phi = 2.0$ case, the reaction progresses farther into the core flow. As the fuel to air ratio was increased, the water production location moves inside the cavity. Also, the water production becomes more uniform within the cavity. The instabilities in the shear layer are also more evident for the lower Mach number cases. The five humps in the shear layer for the $\phi = 9.0$ case indicate that the dominant oscillation mode was at least five. It is at least five to account for the added time of the pressure feedback through the cavity.

5.2.3 Transonic Effects at High Fuel to Air Ratios. With the velocity held fixed, in order to maintain a fixed residence time, variation in fuel to air ratio changed the Mach number. When the fuel to air ratio was increased, the low molecular weight of the hydrogen fuel increased the speed of sound, thereby decreasing the Mach number. At stoichiometric ratios near rich blowout the inflow Mach number was approaching one. Table 13 shows the variation of Mach number as the fuel to air ratio increased. Also listed in Table 13 are the total temperature calculated from the perfect gas relation and

Water Production Rate Contours

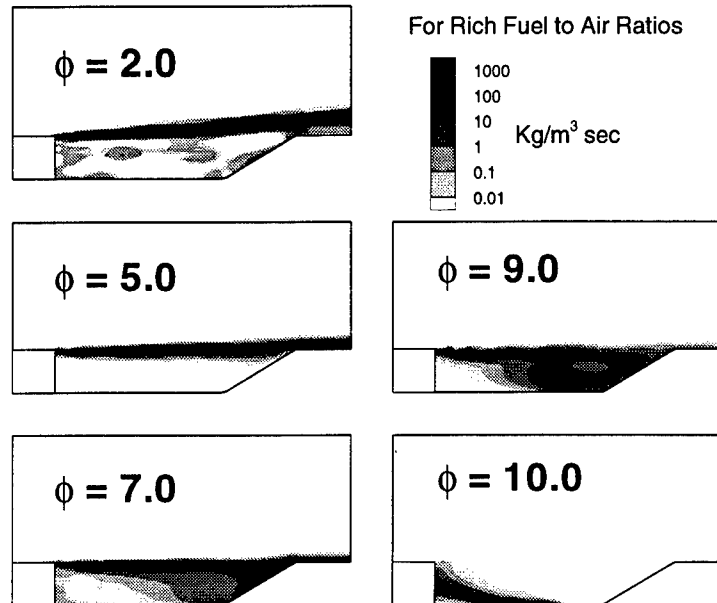


Figure 57. Water Production Rate Contour Variation for Rich Fuel to Air Ratios.

Table 13. Inflow Mach Number Change with Stoichiometric Ratio.

ϕ	Species Mass Fractions			Mach No.	$T(1+0.2M^2)$	T_i from PSR
	H ₂	O ₂	N ₂			
0.0	0.0	0.2318	0.7682	2.216	951.4	912.6
0.4	0.01025	0.2294	0.7603	2.078	894.5	865.1
1.0	0.02525	0.2259	0.7488	1.915	832.1	811.6
2.0	0.04925	0.2204	0.7304	1.718	763.3	751.1
5.0	0.1147	0.2052	0.6801	1.389	665.2	660.6
10.0	0.2057	0.1841	0.6102	1.141	605.0	603.2

from the perfectly stirred reactor code using the thermodynamic curve fits from the SPARK code.

The transonic Mach number created a condition where a normal shock was sometimes located upstream of the cavity. Figure 58 shows Mach number contours for the same fuel to air ratio where the cavity water mass was at the different levels. Often in simulations for the transonic high ϕ values, a shock propagated upstream to the computation boundary making the results unusable. To overcome the shock boundary problem, the solutions for high ϕ values were restarted from slightly lower ϕ value solutions without the shock present. Also, for scramjet combustors, the inflow Mach number cannot be close to one or thermal choking would unstart the inlet. Due to the difficulties with transonic flow, less emphasis was placed on the rich blowout calculations for the remainder of the research.

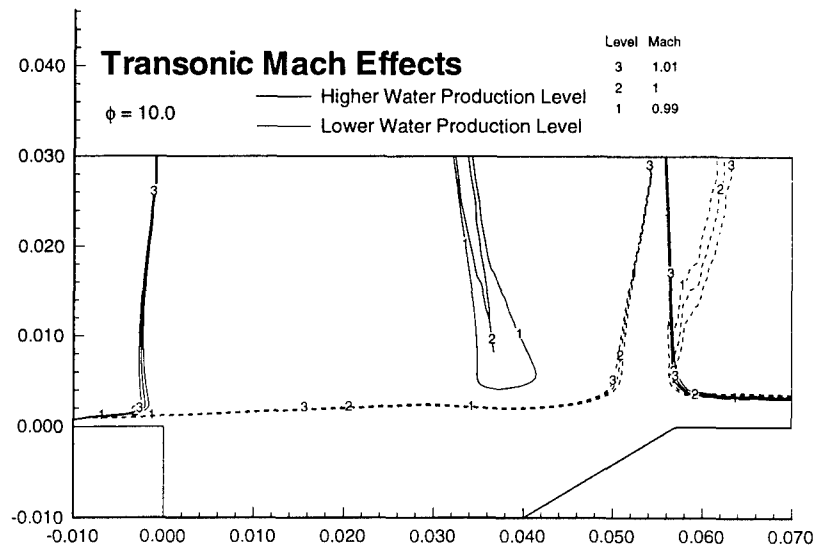


Figure 58. Transonic Mach Number Contours for Different Reaction Levels.

5.2.4 Two-Dimensional Analysis and Perfectly Stirred Reactor

Comparisons. In order to compare the two-dimensional results with the perfectly stirred reactor, a residence time for the two-dimensional cavity was needed. In order to calculate this residence time a converged solution was restarted with the reaction rates set to zero. The integrated water mass decay rate was used to determine the cavity residence time as described in Sect. 3.3.8. The resulting residence time was 1.2 milliseconds. The estimation using equation (8) of Sect. 3.2.4 gave 0.55 milliseconds. This was the same difference that was obtained for the validation geometry.

The cavity water mass fraction from the two-dimensional simulations and the perfectly stirred reactor calculations was shown in Figure 59. The same global chemical kinetics model was used in both the perfectly stirred reactor and two-dimensional simulations. This was a major advantage over experimental comparisons, where the

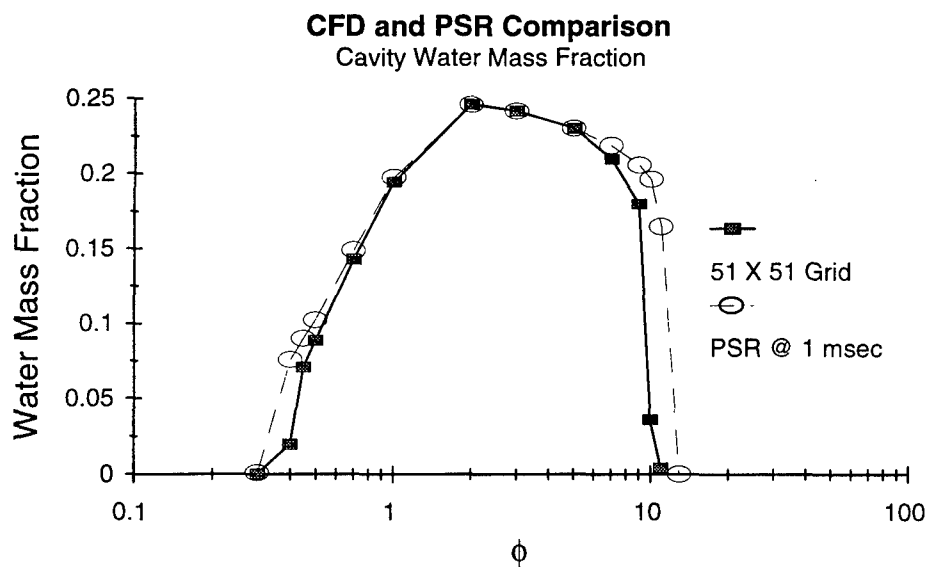


Figure 59. Comparison of Cavity Water Mass Fraction from Perfectly Stirred Reactor and Two-dimensional Simulations.

chemical kinetics were unknown. In this way, a comparison between the simple PSR model and multi-dimensional effects could be made. Also, the inflow velocity option of the perfectly stirred reactor was used to determine the inflow enthalpy. As the fuel to air ratio was increased, the Mach number decreased, leading to a reduced temperature within the cavity. This reduction in static temperature acted to slow the reaction rates at high fuel to air ratios. The perfectly stirred reactor results were for a pressure of 40,000 Pascals and a residence time of one millisecond. The blowout stoichiometric ratio from the perfectly stirred reactor analysis and the two-dimensional simulations agreed very well.

5.2.5 Small Cavity. The PSR lower residence time analysis (Sect. 4.4.3) showed that cavities with much lower residence times than the baseline cavity should support combustion. Hence, the baseline cavity size was reduced by a factor of ten to test this result. The inflow boundary layer was also reduced by a factor of ten so that the only major change would be the residence time. Figure 60 shows the time history of the water mass within the cavity. Convergence was obtained at an order of magnitude shorter time and the water mass remained stationary after 0.5 milliseconds. The calculations were stopped at a time of 2 milliseconds as compared to the large cavity calculations which were stopped at 20 milliseconds. The computational time step was smaller for the small cavity due to the decreased grid spacing therefor the CPU time was about the same.

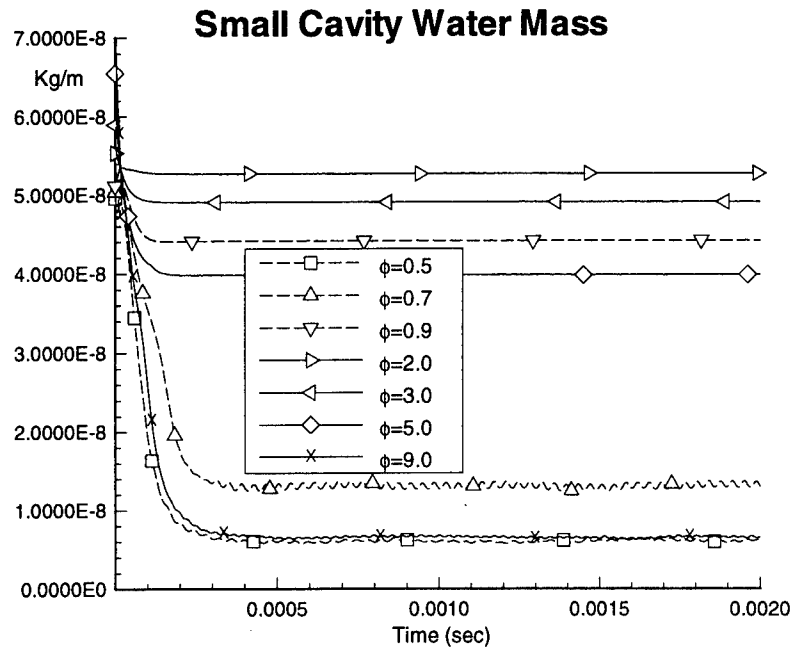


Figure 60. Cavity Water Mass Variation with Time for Small Cavity Simulations.

As indicated in Figure 61, the comparison between the perfectly stirred reactor analysis and the two-dimensional analysis was good. The combustion limits were not as sharp as the baseline cavity results (Figure 59) due to a reaction zone on the cavity wall. The reduced flammability limits of the small cavity compare well between the lower residence time and two-dimensional simulations.

The lower Reynolds number supported a reaction zone on the cavity floor after the main cavity reaction had stopped. Figure 62 shows this reaction zone for $\phi=0.5$. The smaller cavity had a larger fraction of the flow dominated by the laminar sublayer. The laminar sublayer with an adiabatic wall acted to support a flame front on the cavity floor. A similar type of flame stabilization on a flat plate was demonstrated in the heated plate experiments of Ziemer and Cambel (82).

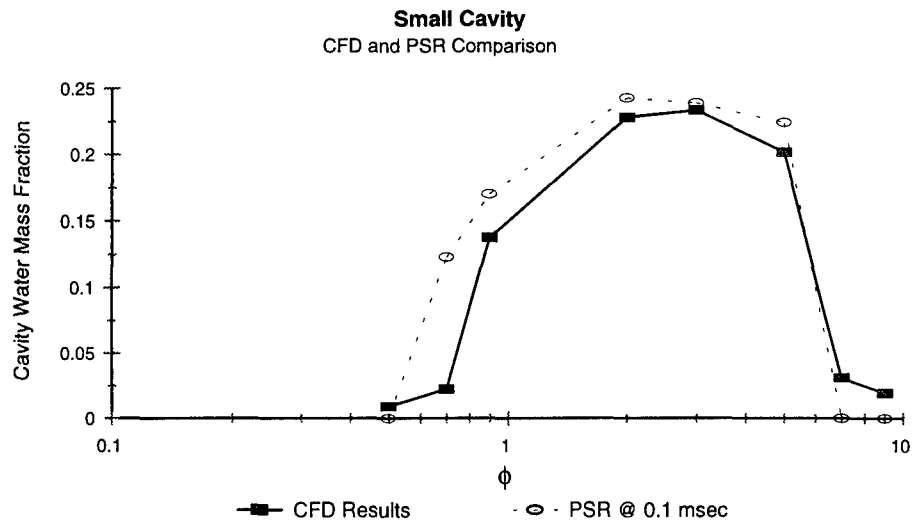


Figure 61. Water Mass Fraction Comparison Between the Small Cavity CFD Results and the Perfectly Stirred Reactor Results @ 0.1 msec.

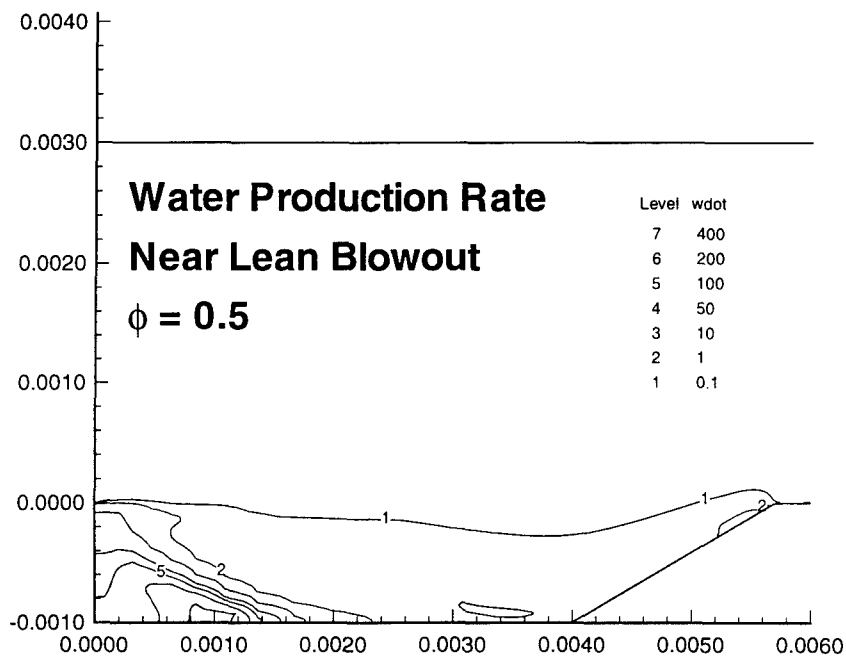


Figure 62. Water Production Near the Cavity Wall for the Small Cavity Simulation.

5.2.6 Free Stream Mach Number Effect. The combustor inflow conditions from Kay et al. (21) for flight Mach numbers of 5.6 and 7.0 were simulated at a ϕ value of one. The water and temperature contour results are shown in Figure 63. As anticipated, the higher static temperature enhance the flame holding. For the Mach 7.0 condition, the water production in the shear layer upstream of the cavity indicates that the boundary layer may be sufficient for flame holding for $Mach \geq 7$. The water mass fraction and temperature within the cavity closely match those calculated from the PSR analysis (Sect.4.4.1).

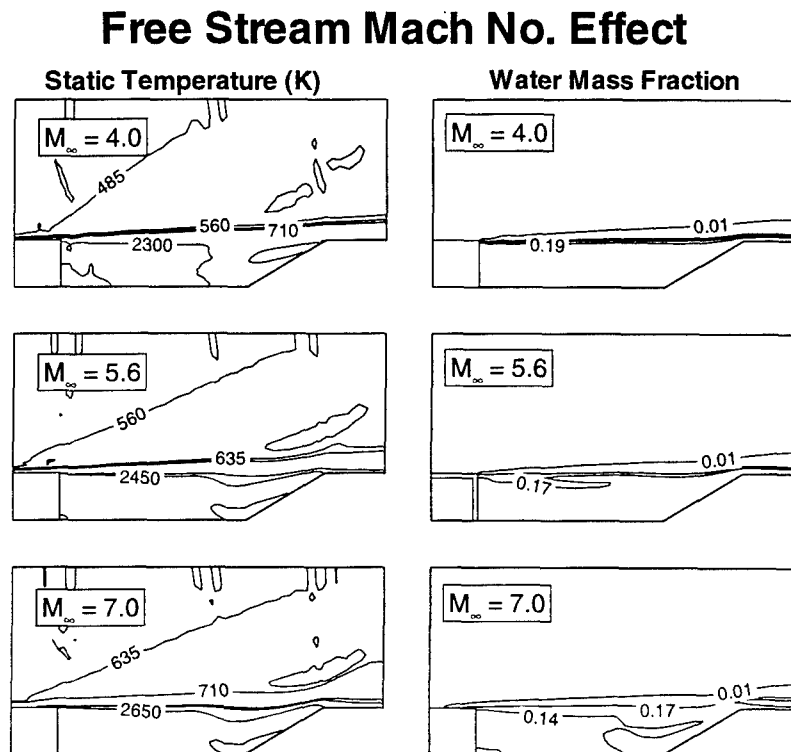


Figure 63. Effect of Free Stream Mach Number on Water and Temperature Contours.

5.2.7 Heat Transfer Effect. The perfectly stirred reactor model showed that the flammability limits are reduced by cavity heat loss (Sect. 4.4.5). To confirm these results two-dimensional simulations were performed with decreasing wall temperatures. In order to prevent heat transfer into the cavity, the specified wall temperature was applied only when it was lower than the adiabatic wall temperature.

The simulation was run at the lean stoichiometric ratio just before blowout. The simulation was started from a prior solution. The wall temperature was specified at 1500 K for 20 milliseconds. The solution was then restarted with successively lower wall temperatures until flame holding stopped. Figure 64 shows the integrated cavity water mass and the heat transfer rate for the calculations. The heat transfer rate was the wall heat transfer divided by the integrated mass within the cavity. The combustion stopped when the wall temperature was reduced to 1000 K. In order to confirm that the combustion stopped due to heat loss and not wall temperature, the final wall temperature

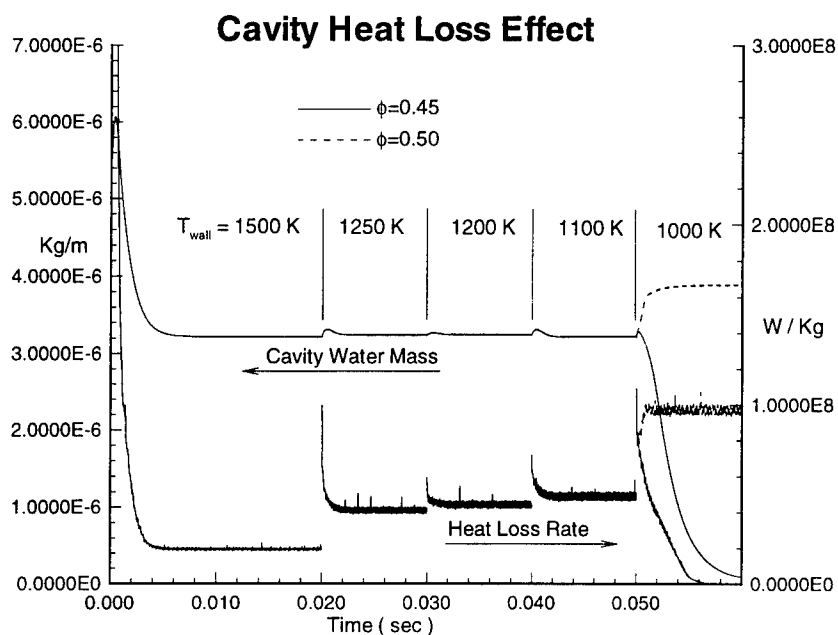


Figure 64. Effect of Heat Loss on Cavity Water Mass.

calculation was repeated with a slightly higher fuel to air ratio ($\phi=0.5$). There was no reduction in cavity water mass before flame holding stopped.

The temperature contours (Figure 65) also show little change as the wall temperature was decreased until blowout was reached. The temperature within the cavity gradually decreased until only a very small portion of the cavity gas was above 1600 K ($T_{\text{wall}}=1100$ K). Then the next increase in heat transfer extinguished the flame.

Heat Loss Effect

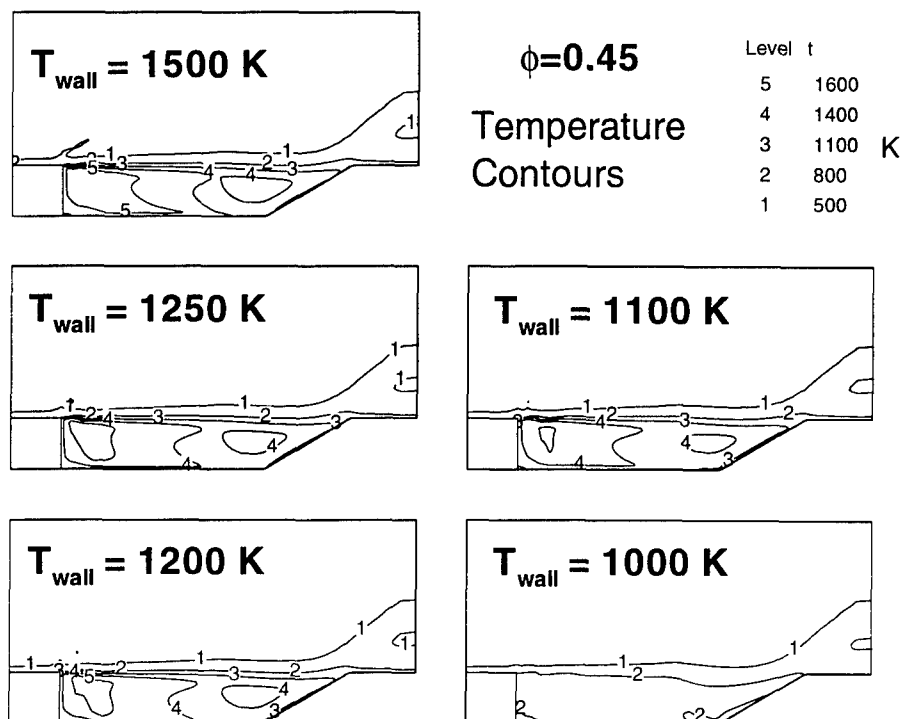


Figure 65. Temperature Contours as Heat Transfer Rate was Increased.

5.2.8 Variations to the Turbulence Model. The interactions of chemical kinetics and turbulence are not well understood. These are very complicated phenomena occurring at many scales. In an attempt to evaluate the impact of turbulence on the flame holding characteristics of the baseline cavity, some widely different turbulence models were compared. A fuel to air ratio near lean blowout ($\phi = 0.45$) was simulated on the coarse grid. The primary purpose of the turbulence variations was not for more accurate flow simulations but rather provide an assessment of the effects of viscosity variations. The turbulence models used are described in Sect. 3.3.3. In addition, a low viscosity limit of laminar and a high viscosity laminar multiplier model were applied.

As mentioned earlier, the residual did not reduce to machine zero for most calculations. For the SPARK code, the residual was calculated as $|\rho_t - \rho_{t-\Delta t}| / (2 \cdot stable \cdot \rho_t)$ where *stable* was the time step stability factor. The values shown in Figure 66 were the maximum value on the grid. The ad hoc laminar turbulence multiplication factor of 250 was chosen to give steady results, where residual reduction to machine zero levels was obtained. This reduction illustrated that the high residual levels were not caused by problems with the code. Instead, the limited reduction in residual was an indication of the flow unsteadiness.

For an unsteady flow, the residual is the driver for the time variation of the terms. For example, $\partial \rho / \partial t = \nabla \cdot (\rho Vel) = \rho \cdot Residual$. Because of this, the residual does not make a good indication of a converged solution for unsteady flow. Moreover, the residual did reduce to a stable value in a very short time. For the Baldwin Lomax turbulence model, a total reduction of close to three orders of magnitude was achieved.

The pressure fluctuations at a point two step heights downstream of the cavity leading edge, within the shear layer are shown in Figure 67. The dominant frequency of oscillation was about 40 kHz. This frequency corresponds to an oscillation mode number

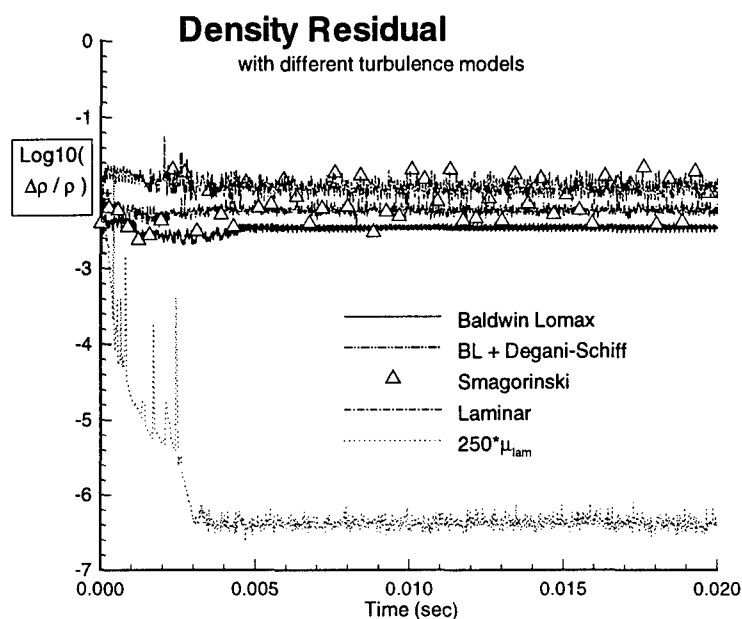


Figure 66. The Density Residual Reduction for Various Turbulence Models.

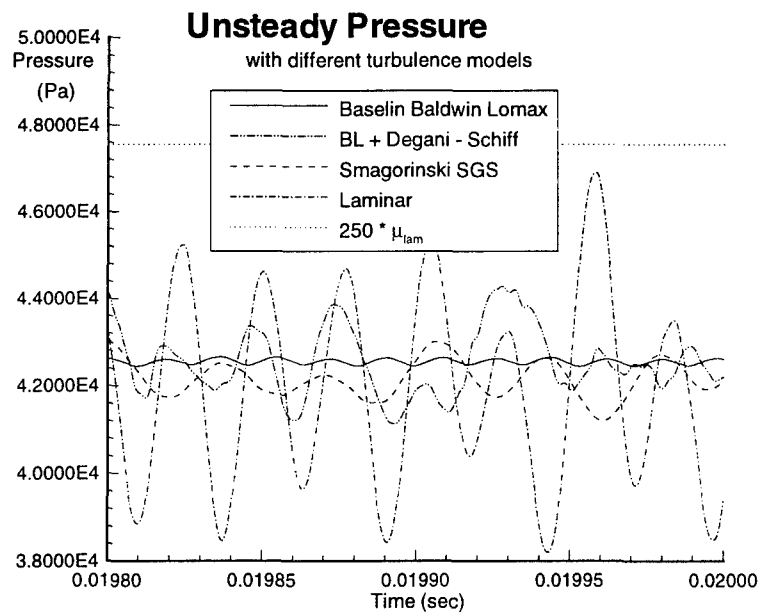


Figure 67. Pressure Oscillations for Turbulence Modifications.

of seven in the modified Rossiter's formula (Sect. 2.1.2). The frequency of oscillation was on the order of the frequencies observed by King et al.(64) in shear layer transition studies (Sect. 2.1.5). The amplitude of oscillation increased with decreasing turbulent viscosity. Comparison of Figure 67 and Figure 66 show that solutions with higher oscillation levels also had higher residual levels. The peak to peak pressure variation was 19% for laminar flow and 0.35% for the baseline Baldwin Lomax case.

As an indication of the convergence of the solutions, the integrated water mass was used. When the water mass was no longer drifting with time, the solution was considered stationary. Some solutions had an oscillation in the integrated water levels but they remained stationary. Figure 68 shows the integrated water mass for the different turbulence models. The convergence rate was slower for the lower viscosity models and highest for the laminar multiplier model. The convergence rate was also a qualitative indication of the residence time for the cavity. For the validation case, the residence time was shown to be substantially longer for the laminar and Smagorinski SGS turbulence

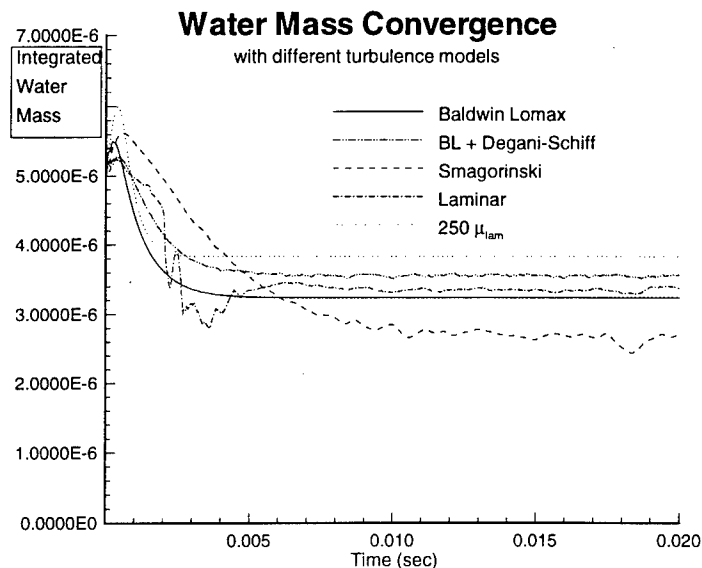


Figure 68. Convergence of the Integrated Cavity Water Mass for Different Turbulence Models.

approximations (Sect. 5.1.1). Also, the water mass for the viscosity multiplier model levels off at about the same time as the residual reaches machine zero (Compare with Figure 66). For the other models, the water mass levels off after the residual reduction stops. This implies that the integrated quantities can be a better indication of convergence than residual reduction.

For evaluation of the effect of turbulent viscosity on the solution, several turbulence variations were compared. Modifications to the Baldwin Lomax Model, including adding a wall function, basing the viscosity on time-averaged velocities, and holding the viscosity fixed after a number of iterations all gave nearly identical results.

Comparison of Turbulence Models

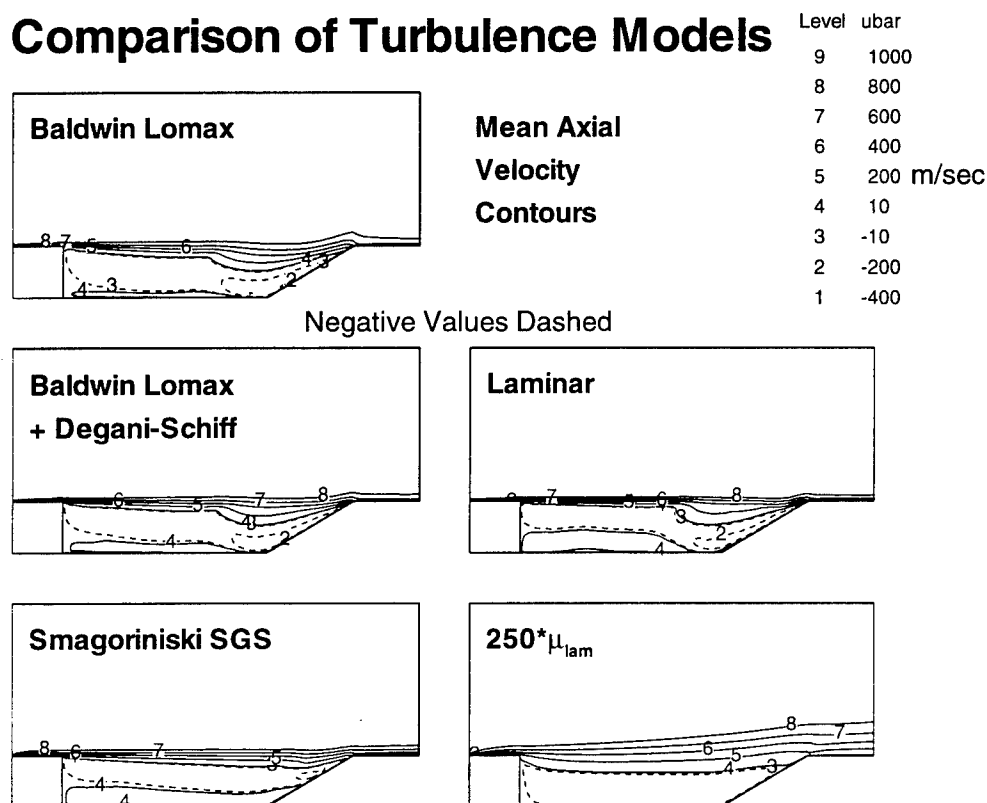


Figure 69 Axial Velocity Contours for Several Turbulence Variations.

Figure 69 shows the velocity contours from simulations using various turbulence models. The Smagorinski SGS model gave only slightly higher shear layer spreading than the laminar calculation. The laminar viscosity multiplier model was not physical and hence it was inaccurate.

The flow within the cavity was also altered by the turbulence models. The Smagorinski SGS model gave a long secondary vortex filling the lower half of the cavity. The viscosity multiplier model gave a single weak vortex in the cavity.

Figure 70 shows the variation in total shear stress

$(\tau_{xy} = \tau_{xy}^{resolved} + \tau_{xy}^{turb\ model} + \tau_{xy}^{lam})$ for different turbulence models. This shear stress

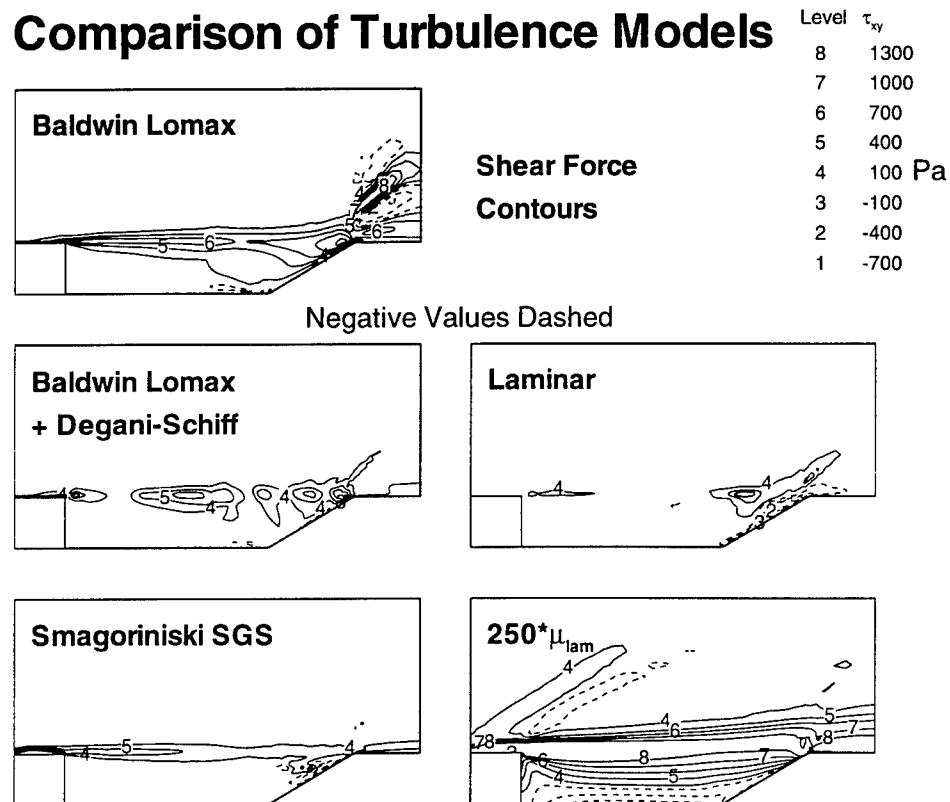


Figure 70 Shear Stress Contours for Several Turbulence Variations.

includes the time averaged, numerically resolved Reynolds stress

($\tau_{xy}^{resolved} = \rho \cdot \langle u' \cdot v' \rangle$) as described in Sect. 3.3.3, and the modeled turbulent viscosity based shear force. The Smagorinski SGS model gave very high shear stress in the boundary layer upstream of the cavity and low shear stress in the shear layer. The Degani-Schiff modification that selects the first peak in the vorticity function, F_{MAX} , bases the turbulent stress on a thinner boundary layer length scale yielding a lower shear stress than the baseline model. The baseline model seems to pick an appropriate length scales from the shear layer, even far from the wall.

The water production contours for different turbulence models are illustrated in Figure 71. For these calculations, the fuel to air ratio was near the lean blowout at a stoichiometric ratio of 0.45. The lower viscosity models (laminar, Degani-Schiff, and Smagorinski SGS) all had thin reaction zones. The laminar and Smagorinski SGS cases were shown to have higher residence times for the validation case (Sect. 5.1.1). The Smagorinski SGS turbulence model had lower integrated water mass as show in Figure 68. The water production contours of Figure 71 show that the flame front has moved inside the cavity for the Smagorinski SGS model. This indicates that under some conditions, the residence time may not be the only indicator for cavity flame holding performance. The wall temperature upstream of the cavity for the Smagorinski SGS turbulence model was lower than the other models as shown in Table 14. The wall temperatures in Table 14 were taken as the perfect gas total temperature of the first grid point off of the wall. The perfect gas total temperatures were calculated from

$T_{total} = T_{static} \cdot (1 + 0.2 \cdot M^2)$, the recover temperature was calculated from $T_{recovery} = T_{static} \cdot (1 + 0.2 \cdot M^2 \cdot P_{r_{lam}}^{1/3})$, and the estimated adiabatic wall temperature was calculated by multiplying the curve fit total temperature by the ratio of recovery to total temperature for the ideal gas. The curve fit total temperature was calculated using the

perfectly stirred reactor code. The lower wall temperature from the Smagorinski SGS turbulence model was as a result of the rapid growth of the boundary layer in the first grid plane, which gave a low upstream temperature.

Comparison of Turbulence Models

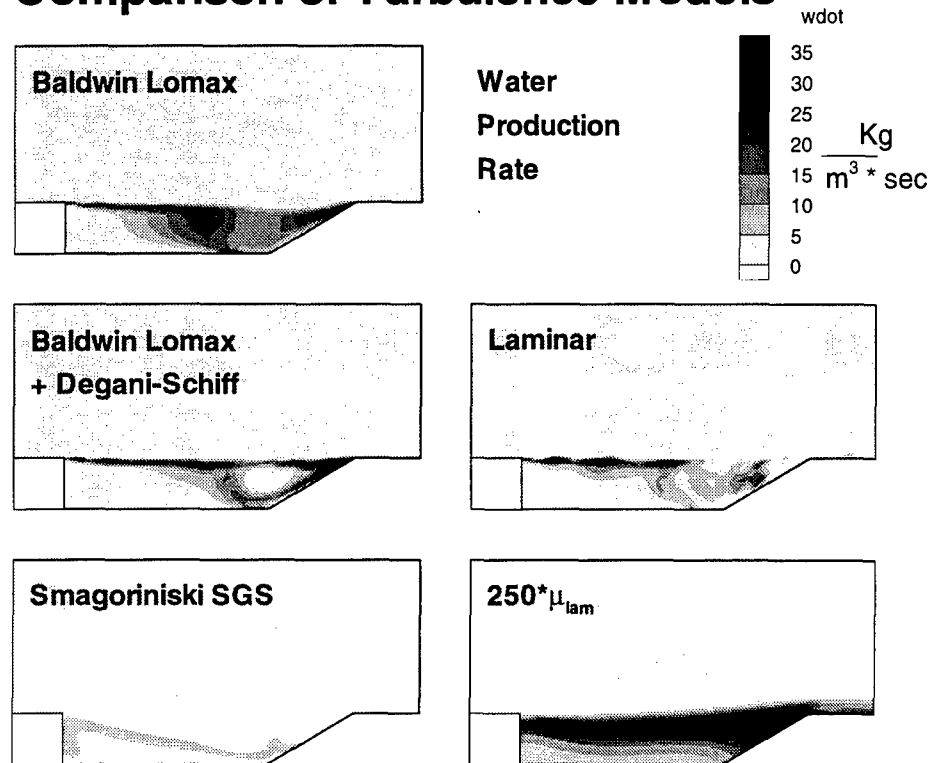


Figure 71 Water Production Variation with Turbulence Model.

Table 14. Temperature Variation with Turbulence Model.

	Temperature
Perfect Gas , Total	888
Perfect Gas, Recovery	842
Thermodynamic Curve Fits, Total	860
Estimate of Adiabatic Wall	815
Baldwin Lomax, Wall	802
Baldwin Lomax + Degani-Schiff, Wall	792
Smagorinski SGS, Wall	708
Laminar, Wall	829
250 μ_{lam} , Wall	806

5.2.9 Boundary Layer Effects. The boundary layer for the Smagorinski SGS turbulence model was thicker and had a lower temperature than the other turbulence models. By varying the temperature of the wall upstream of the cavity and the incoming boundary layer thickness, there effect on the chemical kinetics was determined. This section shows the results of lowering the upstream wall temperature and the results of increasing the boundary layer thickness.

As described in Sect. 5.2.8, the total temperature of the first point off the wall was lower for the Smagorinski SGS turbulence model. The reaction rate for the Smagorinski SGS turbulence model was much less than other models. By lowering the wall temperature upstream of the cavity to 550 K, nearly the same total temperature for the first point off the wall was obtained. Table 15 summarizes the upstream wall temperature effect.

Table 15. Inflow Boundary Layer Temperature Effect on Water Production.

	Temperature @ +1	Mach @+1	Total Temperature (K)	Cavity Water Mass	Water Mass Fraction
Baseline	742.6	.6317	802.	3.24	.071
$T_{\text{upstream}}=650$	745.2	.3723	766.	3.21	.070
$T_{\text{upstream}}=550$	674.7	.3413	690.	1.34	.021
Smagorinski SGS			708.	2.70	.046

The inflow boundary layer thickness was also investigated. By increasing the inflow boundary layer thickness by factors of 2, 5 and 10, the effect on water production was investigated. Figure 72 shows the velocity and water production contours for these simulations. Varying the boundary layer thicknesses had minor effects on the water production rate. The thickest boundary layer had a slightly thicker reaction zone leaving the cavity indicating the flame holding may be slightly better. Therefore, the reduced water production from the Smagorinski SGS turbulence model was due to the lower temperature of the inflow boundary layer.

5.2.10 Flow Stability. The unsteady pressures shown in Figure 73 indicate that combustion does not enhance the flow instability. As the fuel to air ratio was increased from lean blowout the pressure oscillation amplitude decreased due to the displacement of the shear layer. The mean static pressure increase gives an indication of the pressure oscillation level that could be supported if combustion enhanced the oscillations. At the stoichiometric fuel to air ratio, $\phi=1.0$, the oscillation amplitude was small with turbulent

burst causing most of the pressure fluctuation. The highest amplitude oscillation (4% peak-to-peak pressure oscillation) was observed for the $\phi = 7.0$ case.

Inflow Boundary Layer Affect

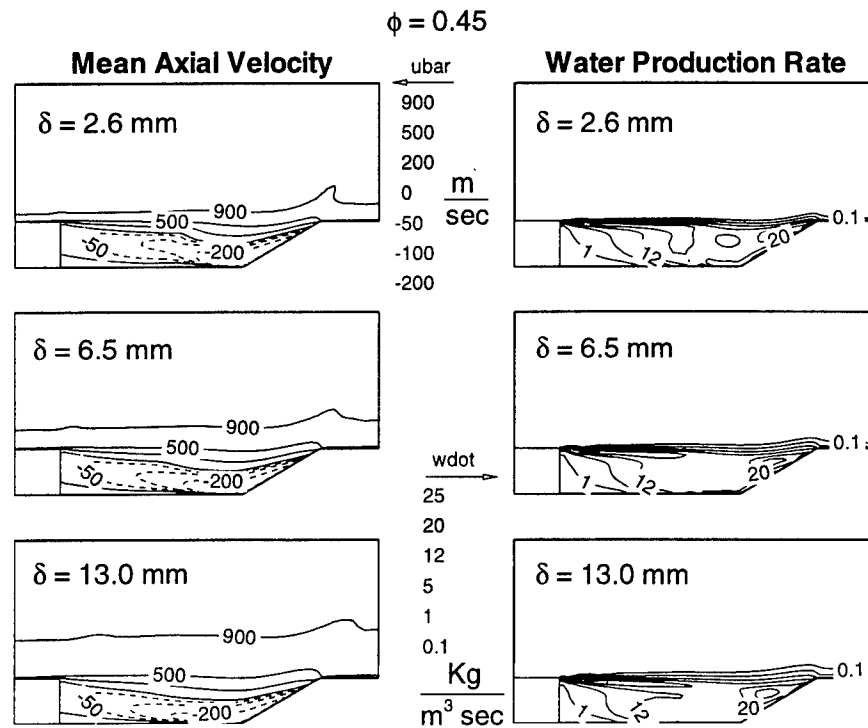


Figure 72. The effect of boundary layer thickness on velocity and water production rate.

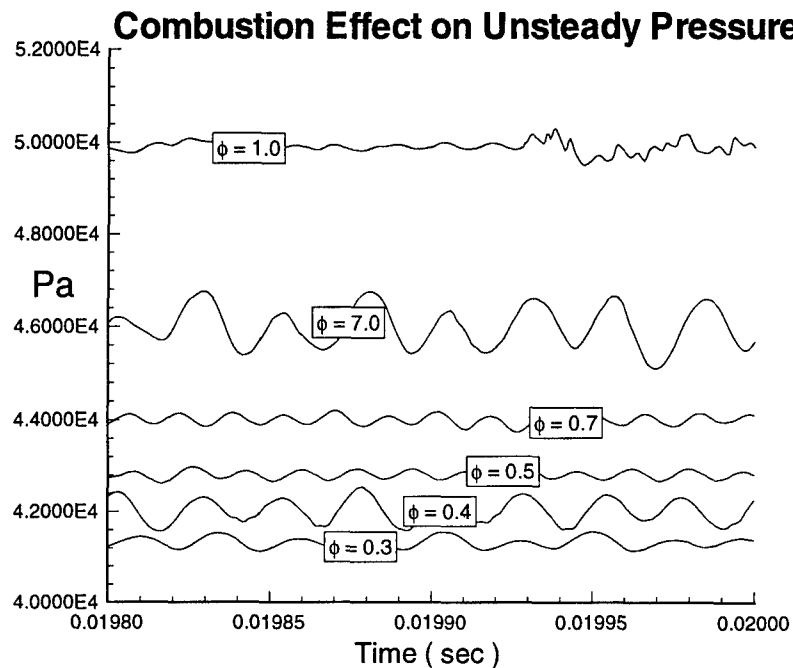


Figure 73. Unsteady Pressure Variation with Fuel to Air Ratio.

5.2.11 Full H-O Kinetic Set. The hydrogen oxygen reaction rate set of Drummond (71:374) was used for two dimensional full kinetic set simulations. The issues to resolve by two dimensional simulation were, whether trace species diffusion affected the flame propagation rate, and to confirm the predicted low fuel-to-air ratio operation. The perfectly stirred reactor model predicted that combustion would occur at a stoichiometric ratio of 0.1. Lower stoichiometric ratios are of no practical importance, because overall ratios of 0.4 are required for low thrust cruise, and the local cavity fuel air ratios would in general be higher than the overall fuel to air ratios.

Figure 74 shows that the temperature contours for the full kinetic set are more spread out than for the global reaction. However, the flame fronts of the two cases spread at the same rate; which indicated that trace species diffusion did not enhance the flame spreading. The flame spreading was not enhanced because the thermal diffusion rate was

lower for the full reaction set. The thermal diffusion rate was lower due to the reduced temperature gradient. This offset the trace species diffusion effect shown with the perfectly stirred reactor model in Sect. 4.4.4.

These calculations used the global reaction model, tuned to the Drummond rate set(Sect. 4.3.3) at $\phi=1.0$. As shown in Figure 74, the full rate set maintains a broader reaction front than the global rate, but other features in the flow field behave nearly identically. This indicates that the global reaction rate may yield small deviations in flow details, but the trends and sensitivities are modelled well. The global model however requires about $\frac{1}{4}$ of the computer time (Table 7) for a simulation, making it very effecient for determining the flame holding characteristics of cavity flame holders.

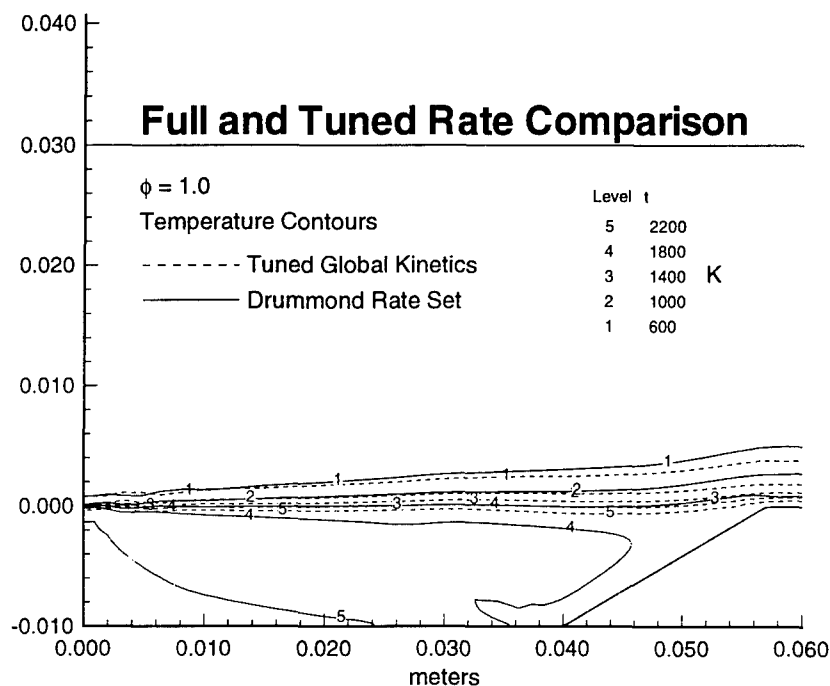


Figure 74. Comparison of Temperature Contours for Full and Global Hydrogen Kinetics Models.

Based on the perfectly stirred reactor analysis, two-dimensional simulations were computed for $\phi = 0.1, 0.4, 1.0, 2.0, 7.0, 11.0$ and 13.0 . From the perfectly stirred reactor analysis with a one millisecond residence time, the $\phi = 13$ case should not support combustion. The $\phi = 13$ two-dimensional simulation did not sustain combustion, while all other cases supported combustion as indicated by the perfectly stirred reactor model. The rich blowout comparison was good, even with the transonic difficulties discussed in Sect. 5.2.3.

Comparing the full kinetic rate set, water production contours of Figure 75 to those of Figure 56 and Figure 57 in Sect. 5.2.2, several observations were made. At $\phi = 1$,

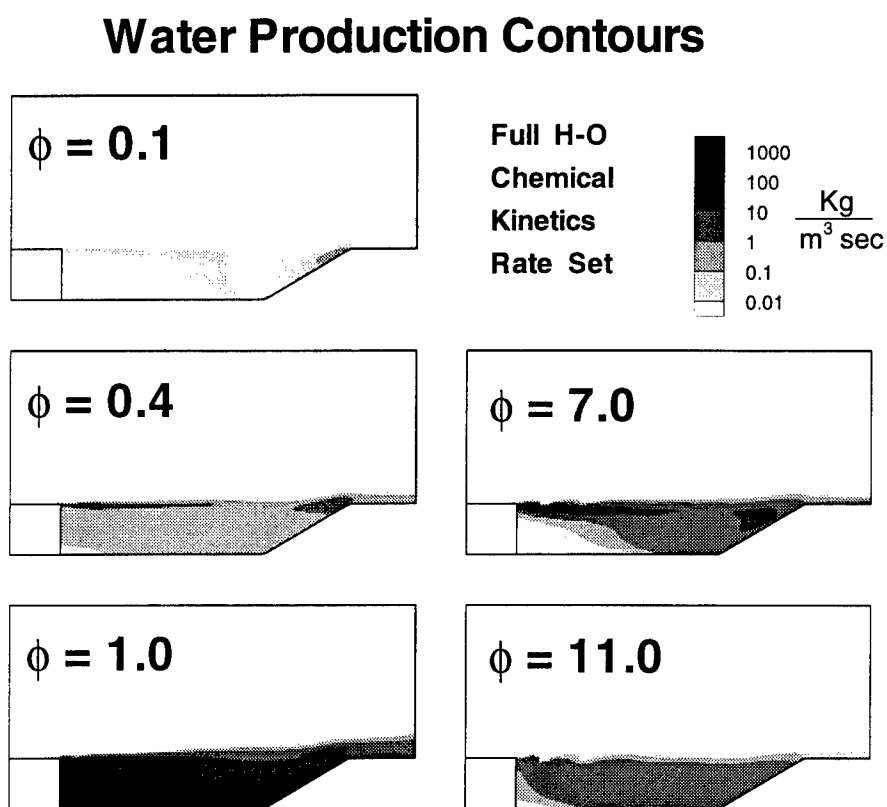


Figure 75. Water Production Rate Contours using the Full Kinetics Rate Set.

the peak production rate for the full set was lower than for the global reaction rate. The water production was more uniform within the cavity for the full rate set simulations. These contours with large reaction zones indicate that the perfectly stirred reactor assumptions may be better for the full kinetic set than for the global reaction rate. Also, the reaction rate within the cavity became more uniform as rich blowout was approached, supporting the perfectly stirred reactor model for predicting flame holding limits.

Figures 76 and 77 show the comparison of the perfectly stirred reactor model and the CFD model for all of the reacting species. All of the species agree very well, again supporting the use of the perfectly stirred reactor model for flame holding analysis.

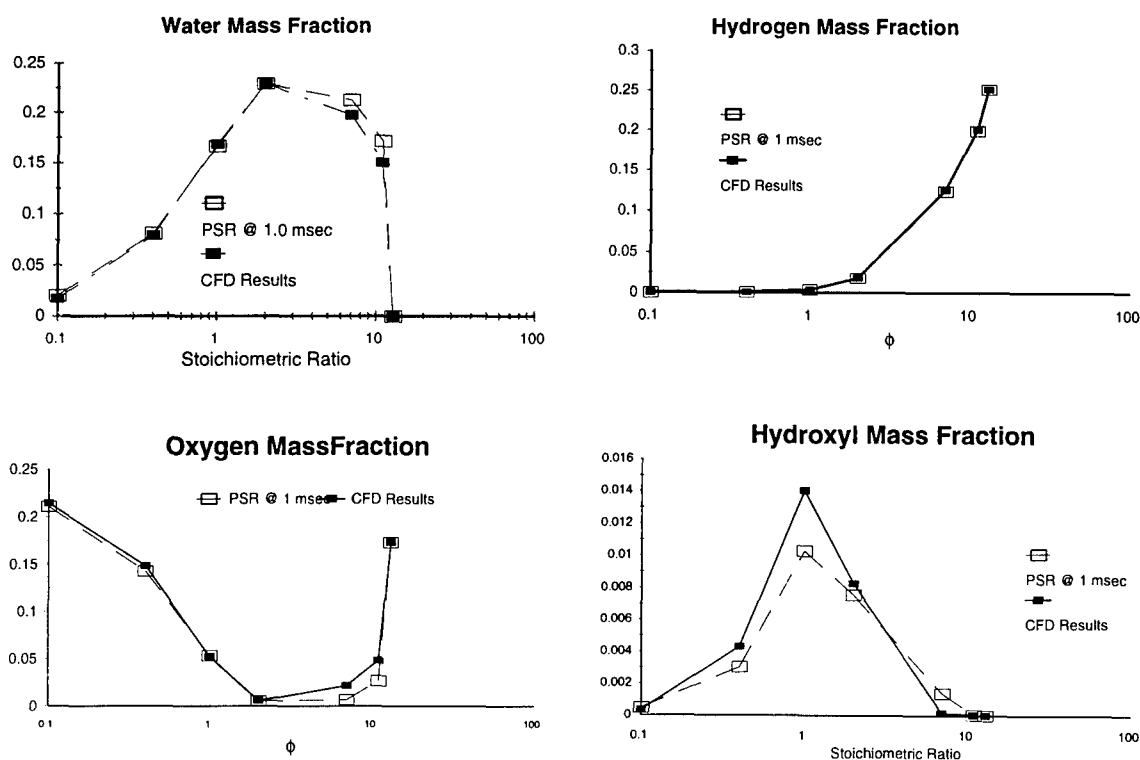


Figure 76. Comparison of Water, Hydrogen, Oxygen, and Hydroxyl Mass Fractions from PSR and CFD.

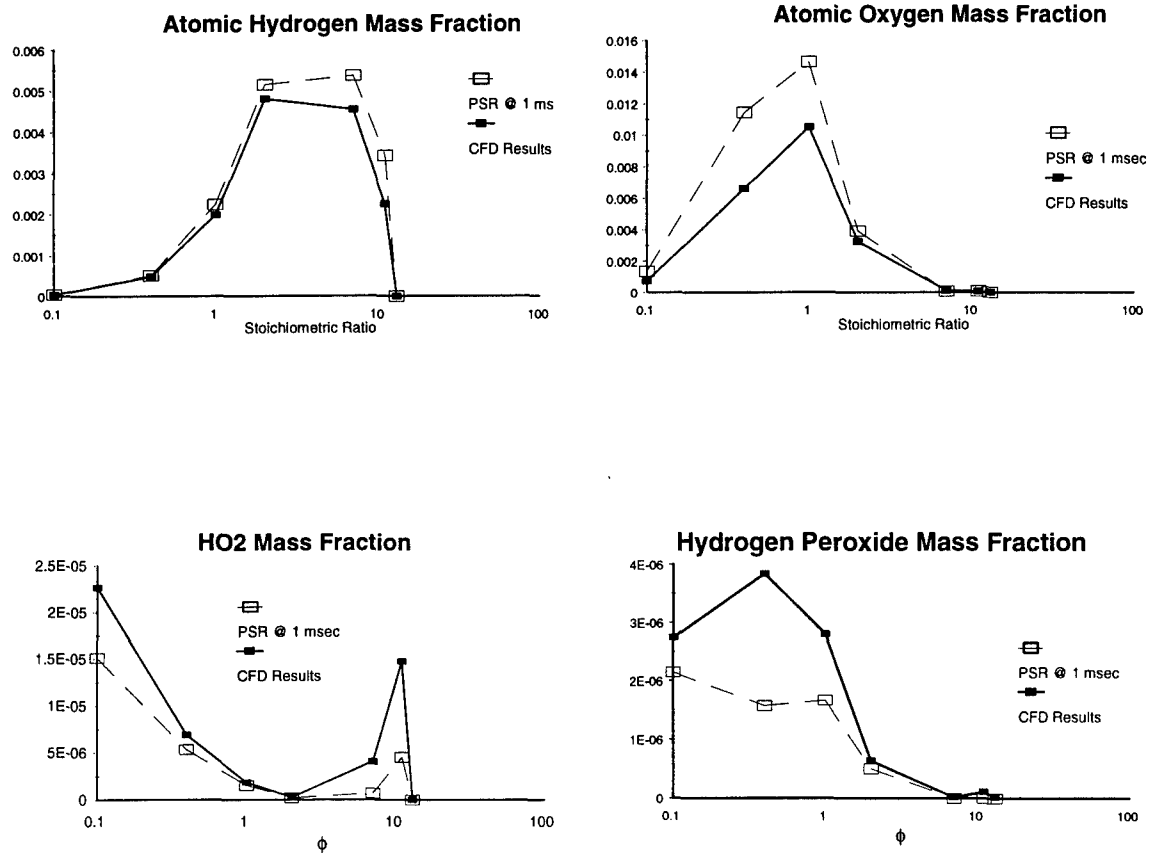
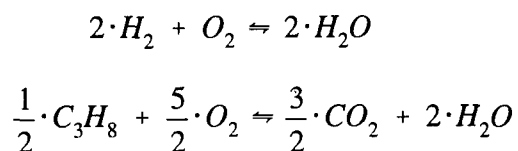


Figure 77. Comparison of Remaining Mass Fractions from PSR and CFD.

5.2.12 Hydrocarbon Results. The lower residence time for propane indicates that propane should sustain combustion for the baseline case. However the very long ignition delay time may reduce the flame spreading angle so that the flame would not propagate from the cavity. A two dimensional simulation for $\phi = 1.0$ was performed on the 51 by 51 grid using the tuned global propane chemical reaction model.

The scaled water production rate contours for the propane and hydrogen fueled calculations are shown in Figure 78. The water production rate for propane was multiplied by 5/2 to scale the rate based on oxygen consumption. The oxygen consumption is a comparison indicator of reaction rate when different fuels are combusted due to the formation of CO₂. The factor of 5/2 is from the law of mass action for hydrogen and propane combustion. The global rate equations, scaled to produce two moles of water, show the factor of 5/2 on oxygen consumption as



The flame spreading for the propane reaction was lower than for the similar hydrogen reaction. The flame front was thinner for the propane reaction and more reaction occurred within the cavity to compensate for the lower reaction within the shear layer. This again supports the lower residence time model for blowout of the cavity flame holder, and shows that hydrocarbon flame holding can be achieved with a relatively small cavity in supersonic flow.

A numerical round off problem was encountered during the initial propane calculations. When the low fuel concentrations were multiplied, the result was truncated to zero, giving a zero reaction rate for much of the domain. To overcome this problem, the species coefficients were cut in half and the calculations were performed in a different order. Reducing the reaction species coefficients reduced the reaction order to a value closer to the accepted experimental value of 1.8. For a global reaction, the reaction order was the sum of the reactant species coefficients.

Production Rate Contours

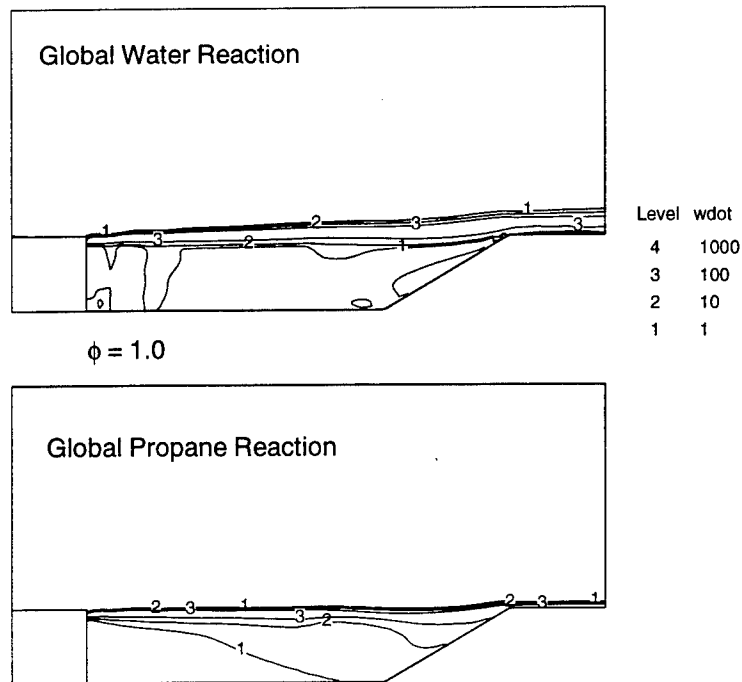


Figure 78. Comparison of Adjusted Water Production Contours for Global Hydrogen and Global Propane Reactions.

5.3. Summary of Two-Dimensional Results

This chapter presented results of several two-dimensional simulations of cavity flame holders. First, the simulation methodology was shown to yield acceptably accurate results. Then, simulations were performed to examine the flame holding process of recessed cavities in supersonic flow.

The accuracy of the numerical results were validated by several methods. Grid refinement studies showed that the flow field and blowout limits were essentially

unaffected by refining the grid. The added artificial viscosity was also shown to have an insignificant effect. Temporal convergence was shown by stationary integrated water mass results. For final assessment, the code results were shown to compare well with detailed flow field experimental measurements.

The flame holding process for cavities was shown by the results of several simulations at varying conditions. At conditions well within the flammability limits, most of the reaction occurred in a distinct flame front above the cavity. As blowout conditions were approached, the reaction moved into and filled the cavity. At blowout conditions, a weak flame front was sustained inside the cavity. This weak flame front did not act as a flame holder because the core flow was not ignited.

The combustion process did not enhance the flow oscillations. The expansion effect of the reaction process actively decreased the oscillation level by lifting the shear layer. With the shear layer lifted, the shear layer was decoupled from the cavity pressure.

Results presented throughout the chapter support the perfectly stirred reactor assumption. The PSR assumption was validated with flammability limit determinations. Other supporting results include simulations of a very small cavity flame holder, simulation using a full H-O rate set, and simulations with various turbulence models. The lower residence time limit validation led to a model for determining the required cavity depth to sustain a flame.

Heat loss was shown to reduce the flammability limits. Heat loss from the cavity and lower inflow boundary layer temperatures were both shown to reduce the flammability limits.

Other results shown illustrate various flame holder properties. The low Mach number case was shown to be the most difficult for flame holding. The baseline cavity was sufficient for propane flame holding. The boundary layer thickness had little effect.

For high fuel-to-air ratios with hydrogen fuel, the inflow conditions became transonic, which was undesirable.

6. Three-Dimensional Results

The flame spreading from the two-dimensional simulations was fairly low. Three-dimensional cavity geometries may be useful for enhancing the downstream flame spreading rate by producing secondary motion. Axial vorticity has been shown to enhance the downstream mixing and flame spreading rate (5-14) for scramjets.

In this chapter, the three-dimensional simulations are validated by comparison with two-dimensional simulations and by grid refinement in the new direction. The validated code was then used to investigate a swept cavity and a swept cavity with variable aspect ratio. In addition, the variable aspect ratio cavity was simulated with finite rate chemical kinetics.

6.1. Three-Dimensional Code Validation

The two-dimensional code was fully validated in Sect. 5.1. The three-dimensional code validation by comparison with two-dimensional results and by grid refinement in the new direction are presented first.

6.1.1 Comparison with Two-Dimensional Code Results. A three-dimensional simulation of the two-dimensional baseline cavity was calculated. The grid was generated by replicating the two-dimensional grid at equally spaced intervals in the transverse direction. Seven grid planes were generated spanning 10 cm. The water production rate contours for the two dimensional and three dimensional simulations are

compared in Figure 79. The three-dimensional simulation was started from a prior solution for the same fuel to air ratio and computed for a simulation time of 7.6 milliseconds to assure convergence. The two-dimensional simulation required about 1.5 CPU hours per msec of physical time while the three dimensional computation required 5.8 CPU hours per millisecond on a Silicon Graphics Inc., R8000 CPU. The water production contours compare very well. There was a slight variation in the three-dimensional simulations contours for different grid planes. The contours from all other grid planes of the three-dimensional simulation, more nearly matched the two-dimensional contours. Hence, the use of the three dimensional code was validated.

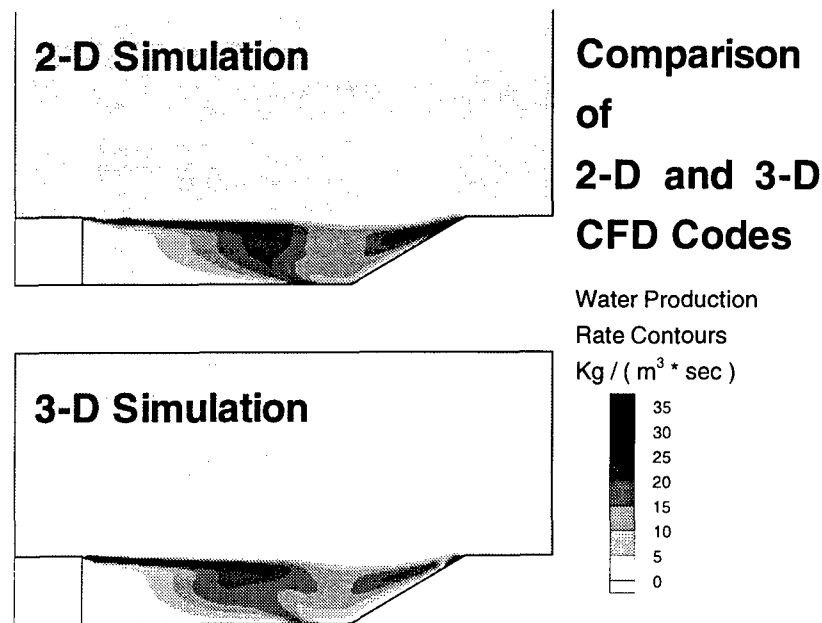


Figure 79. Comparison of Water Production Contours from the Two-Dimensional and Three-Dimensional CFD Codes.

6.1.2 Grid Refinement Results. For grid refinement, a single grid doubling was performed in the spanwise direction on the variable aspect ratio swept cavity (Figure 81). The fine grid had 105 points in the spanwise direction and the coarse grid had 53 points in the spanwise direction. The primary issue for grid refinement was the axial vortex strength leaving the cavity. In order to save computer time, the fine-grid solution was initialized from a partially converged coarse grid solution. The kinetic rate was changed to create a disturbance then both grids were computed until the integrated water within the cavity was stationary. Figure 80 shows the normal velocity contours for both grid resolutions. The comparison was considered very good with only slightly higher upward velocity near the centerline on the fine grid.

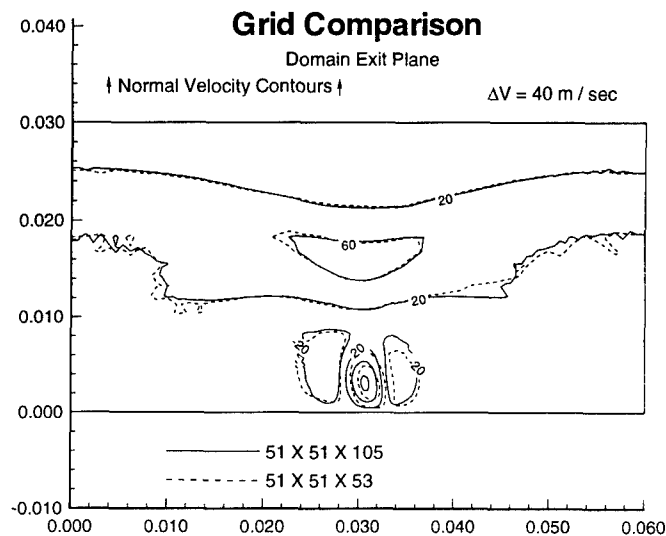


Figure 80. Comparison of Normal Velocity Contours on Two Grid Refinement Levels.

6.2. Three-Dimensional Simulation Results

The results of three dimensional cavity simulations are presented in this section. Two three dimensional geometries illustrated in Figure 81 were simulated at the Mach 4 flight condition with $\phi = 1.0$. The results show that some enhancement in flame spreading can be achieved by cavity geometry modification.

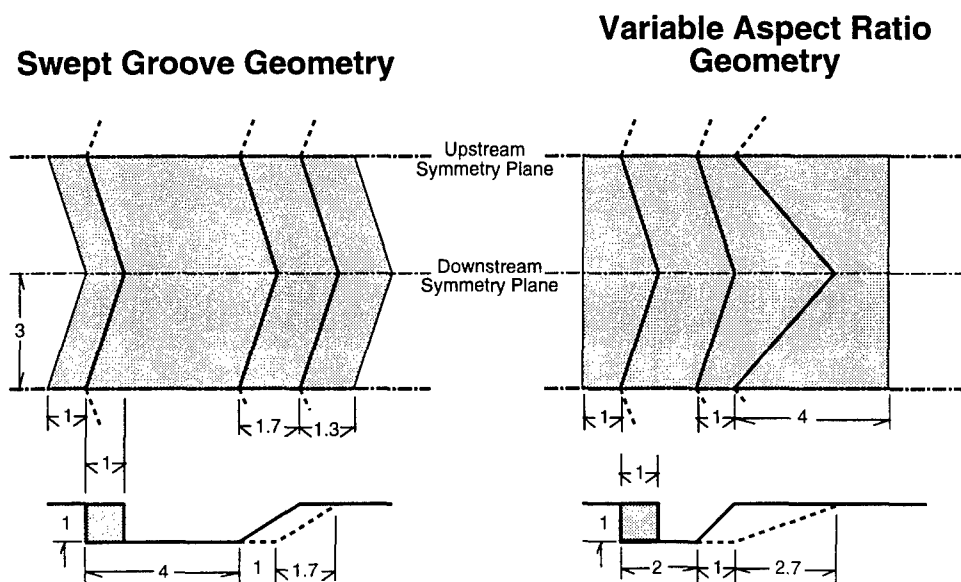


Figure 81. Three-dimensional Cavity Geometries. Dimensions in cm.

6.2.1 Swept Cavity Results. The baseline cavity grid was translated at an 18 degree angle to generate a swept groove configuration. The 18 degree sweep was an arbitrary choice to start the investigation. Figure 82 shows the configuration for two "V" grooves. The numerical solutions were obtained for one "V" with slip boundary conditions on the near and far sides to obtain a symmetry condition relative to the grid. Other boundary conditions were the same as for the two-dimensional baseline case (Sect. 3.3.5). Originally 27 grid planes were used in the lateral direction. Initial results

indicated that a finer grid would be required so the number of planes was doubled. The finer grid resolution was shown to resolve the flow features for the variable aspect ratio swept cavity in Sect. 6.1.2.

Figure 83 shows the axial vorticity on computational cross planes indicated in Figure 82. There was an organized pair of vortices leaving the center of the “V”. These vortices were much weaker than anticipated because most of the vorticity moved upstream within the cavity.

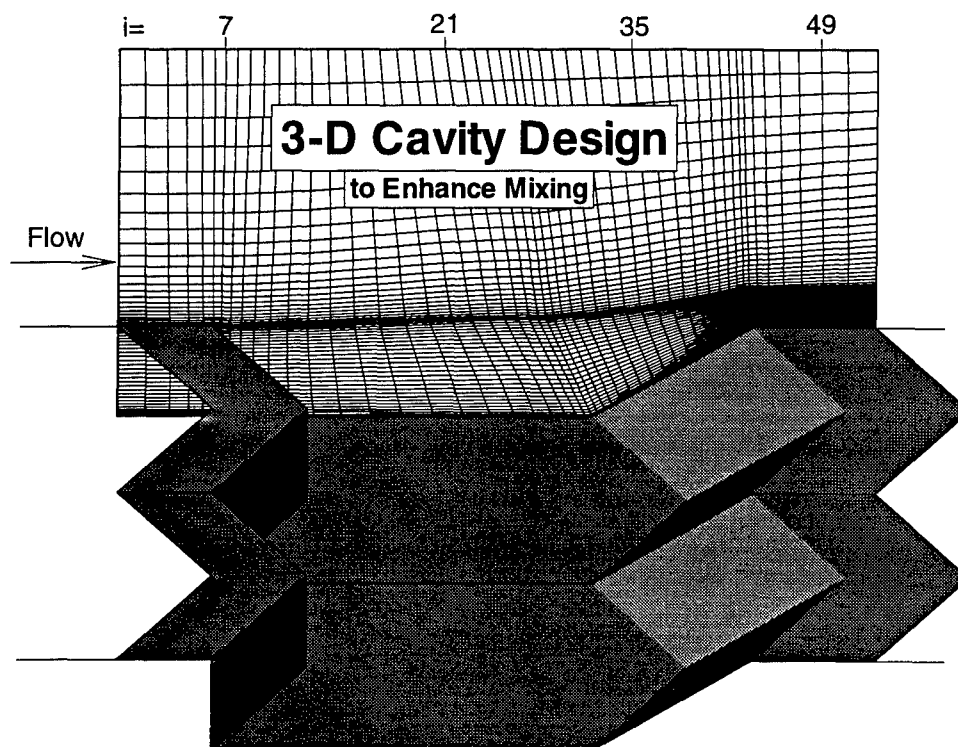
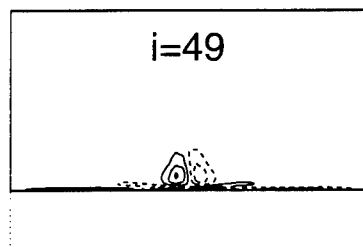
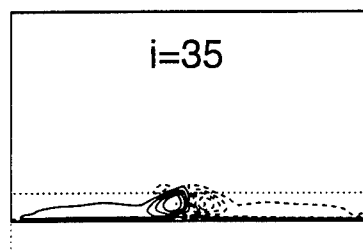
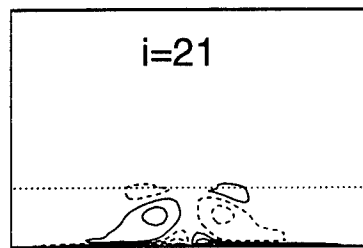
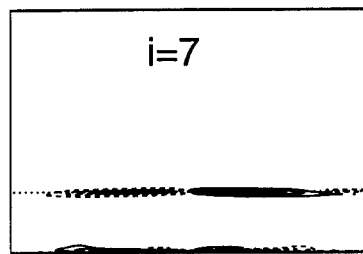


Figure 82. 18 Degree Swept Cavity Configuration.



Axial Vorticity

at Computational
Cross Planes

51 X 51 X 57 Grid

ω_{ave}

180000
140000
100000
60000
20000
-20000
-60000
-100000
-140000
-180000

--- Cavity

Figure 83. Axial Vorticity Generated by the Swept Cavity.

The velocity contours of Figure 84 show that the upstream symmetry plane had velocities similar to the two dimensional results. However, on the downstream symmetry plane, nearly the entire cavity had flow in the upstream direction. The cavity flow in the upstream direction was limited to a narrow region near the downstream symmetry plane as illustrated by the velocity vectors one point off the surface plotted in Figure 85. On the downstream symmetry plane, the shear layer was pushed upward a small amount. These features indicate that a large mass flow was entering the cavity at the downstream vertex. For improved flame propagation the flow was expected to exit

Axial Velocity Contours

----- 51 X 51 X 27 Grid
——— 51 X 51 X 53 Grid

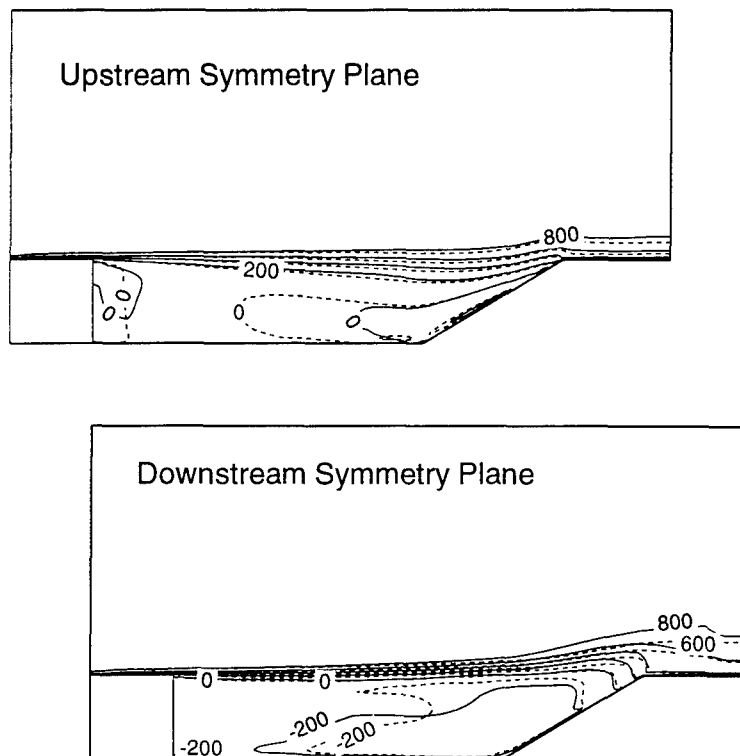


Figure 84. Axial Velocity Contours for the Symmetry Planes.

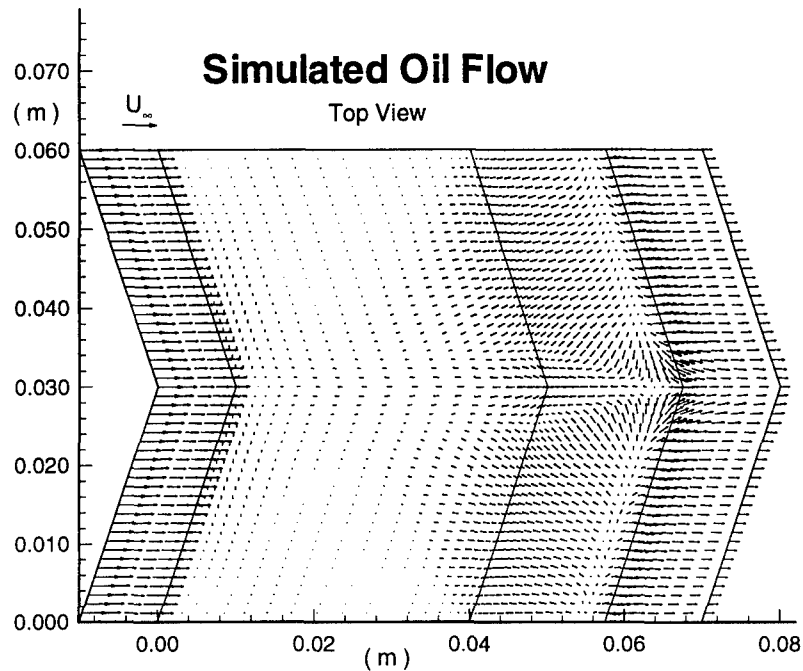


Figure 85. Velocity Vectors Off the Cavity Surface for the Swept Cavity Configuration.

the cavity at the downstream vertex. Because the flow features did not indicate significant flame spreading improvement reacting calculations were not performed on this geometry.

6.2.2 Variable Aspect Ratio Swept Cavity. In an attempt to reduce the upstream flow, the angle of the downstream cavity wall was decreased. Thus, the new cavity had a variable aspect ratio in addition to sweep. The cavity length for the upstream symmetry plane was also reduced in order to increase the sweep of the downstream surface as

shown in Figure 81. The axial velocity contours of Figure 86 show that upstream flow still occurs on the symmetry plane. However, reacting simulations on this configuration were computed to examine the increase in flame spreading.

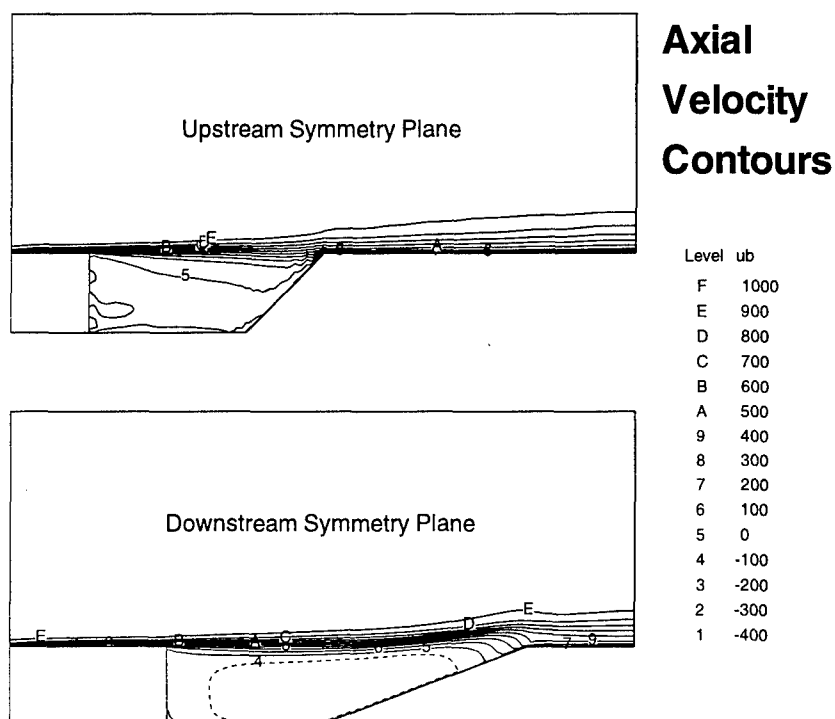


Figure 86. Axial Velocities on the Symmetry Planes of the Variable Aspect Ratio Cavity Using a 51 X 51 X 53 Grid.

6.2.3 Three-Dimensional Reacting Flow Simulations. Three-dimensional simulations using the global chemical kinetics model were performed with the value of ϕ set to 1.0. Again, this was the calibration point for the global chemical kinetic rate equation. As in the two-dimensional simulations, the integrated water mass within the cavity was used as an indication of solution convergence. Figure 87 shows the time

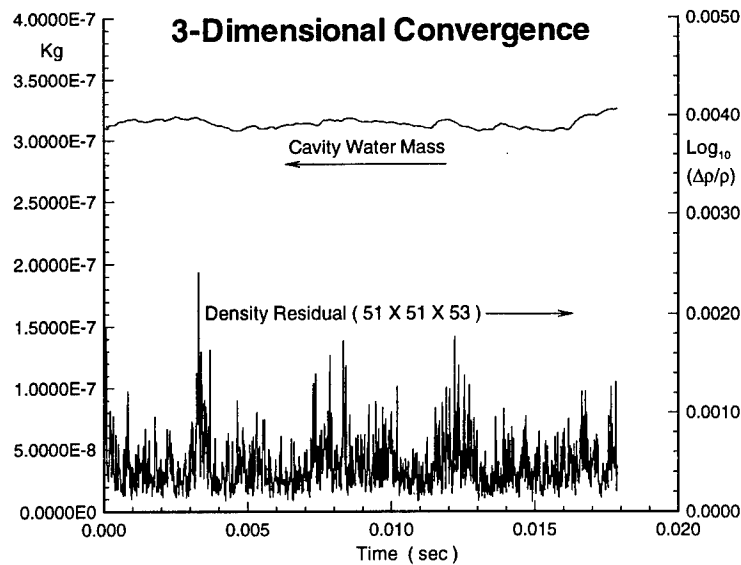


Figure 87. Time History of Integrated Cavity Water Mass for Three Dimensional Calculation.

history of the integrated water mass within the cavity. The integrated water mass was less steady than the two-dimensional cases.

The water mass fraction contours at the exit of the domain shown in Figure 88 illustrates that a slight increase in flame spreading was produced on the centerline. The cross plane velocity vectors show two axial vortices exiting the domain. These vortices would also further enhance the downstream mixing. Thus, the combustor performance would be improved with the three dimensional cavity. A slight asymmetry formed on the centerline due to sensitivity to small disturbances on the reattachment plane.

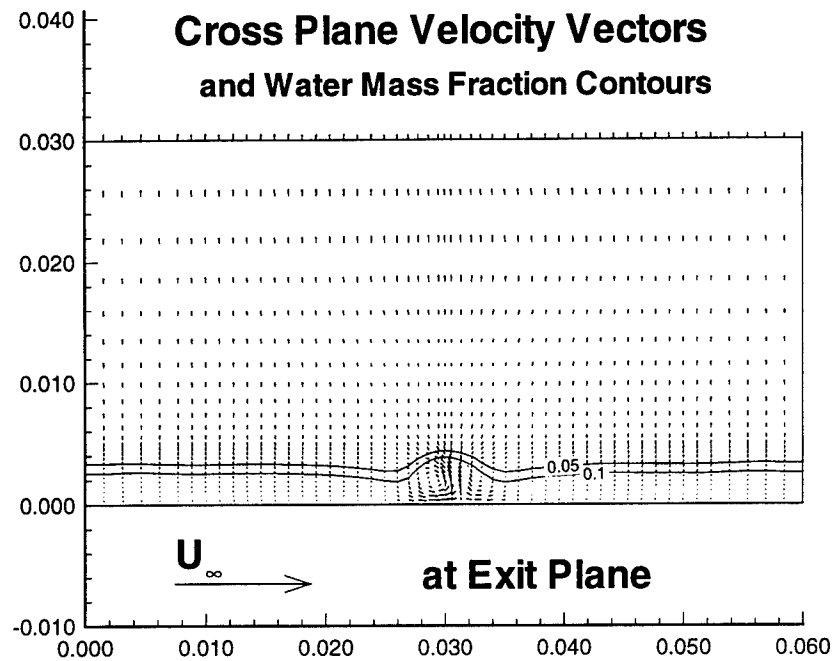


Figure 88. Cross Plane Velocity Vectors and Water Mass Fraction Contours at the Domain Exit.

6.3. Summary of Three-Dimensional Results

The three-dimensional simulations showed that axial vorticity can be generated by cavity sweep. The flow into the cavity at the downstream vertex generated a reversed flow along the central plane. The reversed flow reduced the amount of axial vorticity leaving the cavity. The reacting simulations showed that a swept variable aspect ratio cavity could enhance flame spreading.

7. Conclusions

The flame holding properties of recessed cavities in supersonic flow were numerically investigated. Several numerical models were applied, including perfectly stirred reactor models and multi-dimensional computational fluid dynamics (CFD). The perfectly stirred reactor models were used to calibrate global reaction rates for use in the CFD models, investigate chemical kinetic effects, and size the cavity for flame holding. The two-dimensional CFD model confirmed the applicability of the perfectly stirred reactor models in the analysis of the flammability limits of cavity flame holders. The CFD analysis provided residence time and detailed flow information. This research showed that cavity flame holders can provide flame holding for hydrocarbon scramjet applications and provided design methods for determining the size of the flame holder required.

7.1. Perfectly Stirred Reactor Results

With a simplified perfectly stirred reactor analysis, a range of residence times where multiple solutions exist was identified. This range was shown to depend on the inflow temperature, reaction heat release and activation energy. The lower residence time was defined as the lower bound of the multiple solution range. The upper bound was defined as the upper residence time. Between the lower and upper residence times, the reactor could have multiple states. One state with nearly complete reaction, and the other state with very little reaction, are possible. The upper residence time represents the minimum residence time where the mixture in the cavity would auto-ignite. The lower residence time represents the minimum residence time required to sustain combustion

within the reactor, where some ignition method may be required to start the combustion process within the cavity.

A numerical methodology was developed for calculating the upper and lower residence times using more complex reaction mechanisms. For calculating the lower residence time, the steady state PSR model was applied for a long residence time with complete combustion. Then, successively shorter residence times were modeled until the temperature drop indicated the lower residence time. Also, the ignition delay time was calculated using complex reaction rate sets. Using this methodology, reaction rate coefficients for a global reaction were tuned to match the lower residence time and ignition delay time of more complex reaction sets. The global reaction rate was then used in multi-dimensional simulations. Also, the thermodynamic data for the product species were adjusted so that the equilibrium flame temperature of the global reaction matched the complex reaction rate set results.

The perfectly stirred reactor analysis was used to show the orders of magnitude variations among chemical kinetic rate sets. The PSR analysis also demonstrated the lower residence time dependence on temperature and fuel-to-air ratio. The ignition delay time and upper residence time increase as temperature decreases for hydrogen and propane reaction models. The lower residence time was shown to be less sensitive to temperature decrease than the ignition delay or upper residence times. The ignition delay time and upper residence times increased rapidly when the temperature was below 900 K for hydrogen fuel or below 1000 K for propane fuel. Also, the PSR shear layer mixing simulations showed that trace species diffusion enhances flame spreading rates. Heat loss was also shown to increase lower residence times, hence decreasing the flammability limits.

7.2. Multi-Dimensional Results

For supersonic cavity flows, the Baldwin Lomax turbulence model in the SPARK code was shown to give reasonable results. The velocity and shear stress profiles matched experimental laser Doppler velocimetry data for a similar configuration. The baseline grid was shown to be adequate for resolving the flame holding properties of cavity flame holders.

Non-reacting two-dimensional simulations were used to determine the residence time of a cavity. This residence time was consistently about twice the residence time estimated by a simple model that was based on only the free stream velocity and cavity depth. The simple model was calibrated with the two-dimensional blowout results to give an estimate of the required cavity size based on PSR lower residence time calculations.

For most cases, the perfectly stirred analysis gave slightly wider flammability limits than the two-dimensional analysis. The largest uncertainty was shown to be the kinetic rate set. The regression of the flame front, from the shear layer into the cavity, was the same for both rich and lean blowouts. Near blowout, the flame occupied most of the cavity, indicating that the perfectly stirred assumption was appropriate near blowout. Therefore, the perfectly stirred reactor assumption was shown to be well suited to determining the blowout limits. Also, the lower residence time analysis could be used to translate experimental results to true flight conditions.

The combustion within the cavity was not observed to couple with the fluid dynamic instabilities of the cavity configuration to create large amplitude oscillations. The heat release in the cavity acted like a mass addition to push the shear layer above the

cavity trailing edge, which reduced the coupling of the shear layer with the cavity pressure. Thus, with combustion, the oscillation levels were typically reduced.

Heat loss to the cavity walls was shown to reduce flammability limits. Also, a lower temperature inflow boundary layer was shown to reduce flammability. The heat transfer estimation model used in the perfectly stirred reactor analysis predicted about one third the heat transfer rate calculated in the two-dimensional simulation. Therefore, a factor of five on the estimation model should give conservative results for flammability analysis.

The lower residence time was also shown to be a good indicator of flammability for the propane reaction. Ignition delay times for propane are orders of magnitude longer than for hydrogen at the same condition. However, the lower residence times differ by only a factor of three. The propane simulation showed that the flame spreading into the core flow was reduced as compared to the hydrogen levels. The flame was still sustained by the cavity as the lower residence time analysis indicated. This analysis indicated that a cavity with a depth of 1 cm would provide flame holding with propane as a fuel.

Three-dimensional simulations investigating cavity sweep and variable aspect ratio, have shown that longitudinal vorticity can be transferred into axial vorticity. However, the geometries analyzed here had a large reversed flow near the cavity vertex, where the vorticity exits the cavity. This reversed flow tends to pull the vorticity into the cavity. Modifications to the cavity of varying the aspect ratio and aft ramp angle were simulated with similar results. The reacting flow simulations showed that the flame spreading was slightly enhanced by the three-dimensional cavity geometry.

7.3. Recommendations

Based on the excellent comparison between the perfectly stirred reactor model and the multi-dimensional simulations, the following recommendations are made. The perfectly stirred reactor model is well suited for chemical kinetic evaluations. Use the lower residence time for evaluating chemical kinetics models. Calibrate reduced kinetic sets using the lower residence time methodology applied herein.

For an initial cavity size estimate, calculate the lower residence time using a perfectly stirred reactor model. Then, compute the cavity depth from $D = \tau_r \cdot U / 4040$. This equation accounts for the slightly reduced flammability limits from the two-dimensional calculations.

A cavity depth of 1.0 cm appears to be adequate for flame holding of hydrocarbon fuel with the baseline cavity shape. The cavity depth should not scale with combustor size because it is limited by chemical kinetics. Thermally insulate the cavity and upstream wall for improved flammability limits.

Further investigations into three dimensional cavities for better flame spreading are recommended. The use of upstream protuberances to lower the momentum of the flow above the cavity is recommended. This would allow the flow to exit the cavity more easily, thus reducing the reversed flow problem. Other mixing enhancement methods, for example a curved combustor, may be used in conjunction with a cavity flame holder for improved scramjet performance.

Appendix A. Numerical Integration Methods for Perfectly Stirred Reactor Model.

This section summarizes the numerical integration methods used within the perfectly stirred reactor program. The methods are an arbitrary order Runge-Kutta, a third order Adams-Moulton, and Euler Implicit. These are applied to a general system of differential equations which can be combined into vector form as

$$\left| \frac{\partial U_1}{\partial t}, \frac{\partial U_2}{\partial t}, \dots, \frac{\partial U_n}{\partial t} \right|^T = \left| F_1, F_2, \dots, F_n \right|^T$$

or $\frac{\partial \mathbf{U}}{\partial t} = \mathbf{f}(\mathbf{U}, t)$. Since, for unforced chemical kinetic systems, \mathbf{f} has no explicit dependence on time, time can be removed from the vector function to give $\frac{\partial \mathbf{U}}{\partial t} = \mathbf{f}(\mathbf{U})$.

A.1. Arbitrary Order Runge-Kutta.

The arbitrary order Runge-Kutta method was derived as follows. The Taylor Series expansion of $\mathbf{U}(t+\Delta t)$ about $\mathbf{U}(t)$ gives

$$\mathbf{U}(t+\Delta t) = \mathbf{U}(t) + \Delta t \cdot \frac{\partial \mathbf{U}(t)}{\partial t} + \frac{(\Delta t)^2}{2!} \cdot \frac{\partial^2 \mathbf{U}(t)}{\partial t^2} + \frac{(\Delta t)^3}{3!} \cdot \frac{\partial^3 \mathbf{U}(t)}{\partial t^3} + \dots$$

Since the derivative operator is a linear operator this series can be factored into

$$\mathbf{U}(t+\Delta t) = \mathbf{U}(t) + \Delta t \cdot \frac{\partial}{\partial t} \left(\mathbf{U}(t) \right) + \frac{\Delta t}{2} \cdot \frac{\partial}{\partial t} \left(\frac{\partial}{\partial t} \mathbf{U}(t) \right) + \frac{\Delta t}{3} \cdot \frac{\partial}{\partial t} \left(\frac{\partial^2}{\partial t^2} \mathbf{U}(t) \right) + \frac{\Delta t}{4} \cdot \frac{\partial}{\partial t} \left(\frac{\partial^3}{\partial t^3} \mathbf{U}(t) \right) + \dots$$

Then substitution of $f()$ for $\partial/\partial t$ gives

$$U(t+\Delta t) = U(t) + \Delta t \cdot f(U(t)) + \frac{\Delta t}{2} \cdot f(U(t)) + \frac{\Delta t}{3} \cdot f(U(t)) + \frac{\Delta t}{4} \cdot f(U(t)) + \dots$$

The above substitution is valid only for linear systems where $f()$ is a linear operator about $f(U)$ on U , that is $f(U + \Delta + \Gamma) - f(U) = f(U + \Delta) + f(U + \Gamma) - 2f(U)$. However for continuous systems, the operator $f()$ can be replaced by $f(U + \Delta) = f(U) + \frac{df}{dU} \cdot \Delta$ in the limit as Δ approaches zero. This new operator is linear about $f(U)$.

The above series can be truncated at any order, *ord*, then solved with the recurrence relation

$$\begin{aligned} U_{ord} &= U(t) + \frac{\Delta t}{ord} \cdot f(U(t)) \\ U_{ord-1} &= U(t) + \frac{\Delta t}{ord-1} \cdot f(U_{ord}) \\ U_{ord-2} &= U(t) + \frac{\Delta t}{ord-2} \cdot f(U_{ord-1}) \\ &\vdots \\ U_1 &= U(t) + \Delta t \cdot f(U_2) \\ U(t+\Delta t) &= U_1 \end{aligned}$$

In this way the solution can be advanced one time level at a time. Each time step requires *ord* evaluations of the function and for this method the time step was limited by stability constraints.

If the function operator, $f()$, can be approximated as a diagonalizable linear operator, the system can be split into a set of scalar equations. The function operator can

then be put into the form of a complex number, the eigenvalue, times the operand for each scalar equation. This makes the scalar equation $du/dt = a \cdot u$ suitable for stability analysis. The method was unstable if a small error, ϵ , added to u would increase in magnitude as the solution continues.

Expressing the numerical method as a linear operator, $u(t + \Delta t) = L(u)$, then adding a small error gives,

$$u(t + \Delta t) + \epsilon(t + \Delta t) = L(u + \epsilon) = L(u) + L(\epsilon) \quad .$$

This implied that $\epsilon(t + \Delta t) = L(\epsilon)$. Then at time, $t + n\Delta t$, with repeated applications of the operator the error becomes

$$\epsilon(t + n\Delta t) = L(\epsilon(t + (n-1)\Delta t)) = L(L(\epsilon(t + (n-2)\Delta t))) = \dots = L^n(\epsilon)$$

If the magnitude of the largest eigenvalue of the operator is less than one, the error decreases to zero but if the magnitude of the largest eigenvalue is greater than one, any error would grow in magnitude making the method unstable.

For the model equation the fourth order Runge-Kutta method gave

$$L = 1 + a \cdot \Delta t + \frac{(a \Delta t)^2}{2!} + \frac{(a \Delta t)^3}{3!} + \frac{(a \Delta t)^4}{4!}$$

. The magnitude of the operator for complex values of $a\Delta t$ is plotted in Figure 89. The method was stable inside the contour of value one. This indicates that if a was real and negative then Δt must be less than $2.78 / (-a)$ for stability.

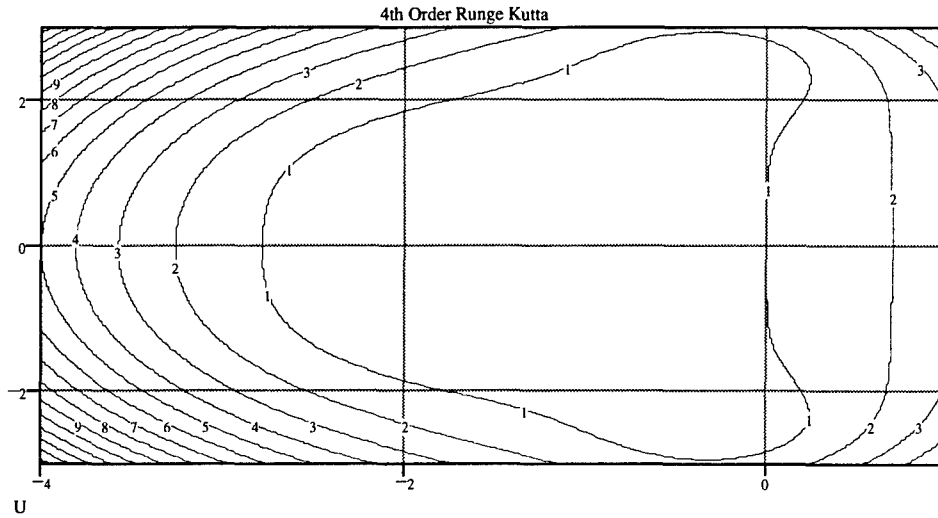


Figure 89. Operator Magnitude for Fourth Order Runge-Kutta Integration for Complex Values of $a\Delta t$.

A.2. Third Order Adams-Moulton Method.

Another approach to the time integration was to express the function as a polynomial in time giving

$$\begin{aligned}
 U(t + \Delta t) &= U(t) + \int_t^{t+\Delta t} f(U) d\tau \\
 &= U(t) + \int_t^{t+\Delta t} \left(\sum_{i=0}^I a_i \cdot \tau^i + Error \right) d\tau
 \end{aligned}$$

Fitting the polynomial through the value of the functional at $t - \Delta t$, t and $t + \Delta t$ gives

$$f(U) = f_0 + \frac{\tau - t}{2 \cdot \Delta t} \cdot (f_+ - f_-) + \frac{(\tau - t)^2}{2 \cdot \Delta t^2} \cdot (f_+ - 2 \cdot f_0 + f_-) + Error$$

where f_+ , f_0 and f_- are the function evaluated at $t + \Delta t$, t and $t - \Delta t$ respectively.

Performing the integration and rearranging terms then gave

$$U(t + \Delta t) = U(t) + \Delta t \cdot \left(\frac{5}{12} \cdot f_+ + \frac{4}{3} \cdot f_0 - \frac{1}{12} \cdot f_- \right) + \int_t^{t + \Delta t} Error \, d\tau \quad (16)$$

In this method f_+ was not known until $U(t + \Delta t)$ was evaluated. To overcome this problem a predictor step was used where a linear polynomial fit through f_0 and f_- was integrated to give

$$\begin{aligned} \bar{U} &= U_0 + \Delta t \cdot \left(\frac{3}{2} \cdot f_0 - \frac{1}{2} \cdot f_- \right) + \int_t^{t + \Delta t} Error_p \, d\tau \\ \bar{f}_+ &= f(\bar{U}) \end{aligned}$$

The error term, E_p , for the polynomial (83:4) is

$$Error_p(\tau) = \frac{(\tau - t) \cdot (\tau - (t - \Delta t))}{3!} \cdot f^{(3)}(\xi) \quad , \quad \xi \in (t - \Delta t, t + \Delta t)$$

where ξ varies with τ . If $f^{(3)}$ is bounded on the interval $(t - \Delta t, t + \Delta t)$, then let

$M_p \geq |f^{(3)}(\xi)| \quad \forall \quad \xi \in (t - \Delta t, t + \Delta t)$. Then after integration the error on \bar{U} is bounded as

$$\left| \int_t^{t + \Delta t} Error_p \, d\tau \right| \leq \frac{M_p}{3!} \cdot \frac{5}{6} \cdot \Delta t^3 \quad .$$

Assuming f to be Lipschitz continuous,

$$\left| \frac{f(U+\Delta) - f(U)}{U+\Delta - U} \right| \leq L, \quad \forall \Delta \text{ such that } (U+\Delta) \in \text{the Domain of } f, \text{ the magnitude}$$

of the error on \bar{f}_+ is bounded by $\frac{M_p \cdot L}{3!} \cdot \frac{5}{6} \cdot \Delta t^3$.

A similar analysis on the error of equation (16) gives

$$\left| \int_t^{t+\Delta t} \text{Error } d\tau \right| \leq \frac{M_c}{4!} \cdot \frac{1}{4} \cdot \Delta t^4$$

where $M_c \geq |f^{(4)}(\xi)| \quad \forall \xi \in (t-\Delta t, t+\Delta t)$. The effect of the error on the predictor, must be included to determine the total error. At $t+\Delta t$, the predictor error is $\bar{f}_+ - f_+$.

From equation (16), the predictor integration of the error is $5/12 \cdot \Delta t \cdot (\bar{f}_+ - f_+)$. The total error is then bounded by

$$\left(\frac{M_c}{16} + \frac{5 \cdot M_p \cdot L}{3} \right) \cdot \frac{\Delta t^4}{12}.$$

After substitution of the predictor into the corrector step this sequence gives

$$U_+ = U_0 + \frac{a \cdot \Delta t}{24} \left((26 + 3 \cdot a \cdot \Delta t) U_0 - (2 + a \cdot \Delta t) U_- \right)$$

for the model equation. Substitution of the operator L , with $U_+ = L(U_0)$ and

$U_0 = L(U_-)$, gives the quadratic equation

$$L^2 + \left(1 + \frac{26 \cdot a \cdot \Delta t}{24} + \frac{(a \cdot \Delta t)^2}{8} \right) \cdot L + \frac{a \cdot \Delta t}{24} (2 + a \cdot \Delta t) = 0$$

For stability the maximum value of the operator must be less than or equal to one. Figure 90 shows the largest of the two magnitudes of the operator for complex values of $a \Delta t$. For stability with a negative a value the time step would need to be less than $2.4 / (-a)$, which is more restrictive than the fourth order Runge-Kutta method. However, this method requires only two evaluations of the function for each time step.

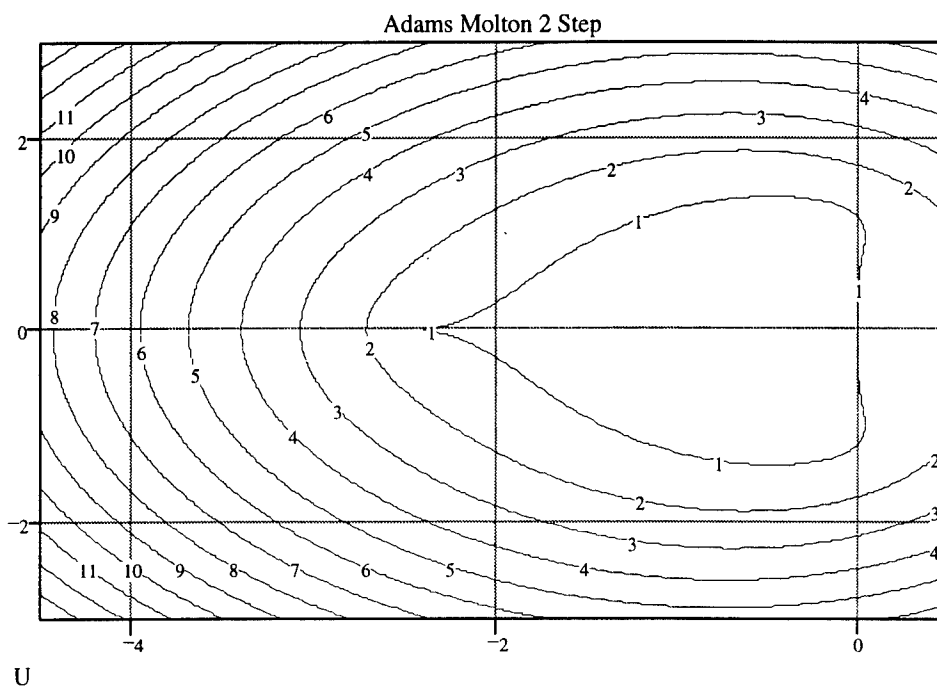


Figure 90. Largest Operator Magnitude for Third Order Adams-Moulton Predictor Corrector Method.

A.3. Euler Implicit Method.

The Euler implicit method can be derived from the time integration

$$\begin{aligned}
U(t+\Delta t) &= U(t) + \int_t^{t+\Delta t} f(U) d\tau \\
&= U(t) + \int_t^{t+\Delta t} (f_+ + \text{Error}_1) d\tau
\end{aligned}$$

where the symbols are the same as in Section A.2. As in Sect. A.2 the Error is bounded by $M \cdot \Delta t / 2$ where $|M| \geq \left| \frac{\partial f(\tau)}{\partial t} \right| \forall \tau \in (t, t + \Delta t)$ (83). However, f_+ is not known until U_+ has been evaluated. To overcome this problem, a first order Taylor series approximation of f_+ is used $f_+ = f + \Delta t \cdot \frac{\partial f}{\partial t} + \frac{\Delta t^2}{2} \cdot \frac{\partial^2 f(\zeta)}{\partial t^2}$ where ζ is some value between t and $t+\Delta t$. Applying the chain rule,

$$\begin{aligned}
\frac{\partial f}{\partial t} &= \begin{pmatrix} \frac{\partial f_1}{\partial t} \\ \frac{\partial f_2}{\partial t} \\ \vdots \\ \vdots \end{pmatrix} = \begin{pmatrix} \frac{\partial f_1}{\partial U_1} \cdot \frac{\partial U_1}{\partial t} + \frac{\partial f_1}{\partial U_2} \cdot \frac{\partial U_2}{\partial t} + \dots \\ \frac{\partial f_2}{\partial U_1} \cdot \frac{\partial U_1}{\partial t} + \frac{\partial f_2}{\partial U_2} \cdot \frac{\partial U_2}{\partial t} + \dots \\ \vdots \\ \vdots \end{pmatrix} \\
&= \begin{pmatrix} \frac{\partial f_1}{\partial U_1}, \frac{\partial f_1}{\partial U_2}, \dots \\ \frac{\partial f_2}{\partial U_1}, \frac{\partial f_2}{\partial U_2}, \dots \\ \vdots \\ \vdots \end{pmatrix} \cdot \begin{pmatrix} \frac{\partial U_1}{\partial t} \\ \frac{\partial U_2}{\partial t} \\ \vdots \\ \vdots \end{pmatrix} = \mathbf{A} \cdot \frac{\partial \mathbf{U}}{\partial t}
\end{aligned}$$

Then using a first order approximation to $\frac{\partial U}{\partial t} = \frac{U_+ - U_0}{\Delta t} + Error_2$ the integration equation becomes

$$U_+ = U_0 + \Delta t \cdot (f_0 + A \cdot (U_+ - U_0) + Error_1 + A \cdot Error_2)$$

where $Error_2$ is bounded by $M_2 \cdot \Delta t / 2$ with $|M_2| \geq \left| \frac{\partial U(\tau)}{\partial t} \right| \forall \tau \in (t, t + \Delta t)$. Both error terms are order Δt so the total error is order Δt^2 . This can be rearranged to

$$U_+ - U_0 = \Delta U = \Delta t \cdot (f_0 + A \cdot \Delta U)$$

ΔU can be calculated from

$$(I - \Delta t \cdot A) \cdot \Delta U = \Delta t \cdot f_0 \quad (17)$$

Then U_+ is calculated from $U_+ = U_0 + \Delta U$.

The term $Error_2$ can be reduced by applying a Newton iteration at the time level $t + \Delta t$ on the error term, $Err = \Delta U - \Delta t f(U_+)$. The resulting iteration equations are

$$\begin{aligned} (I - \Delta t \cdot A) \cdot \delta &= Err = \Delta U_{old} - \Delta t \cdot f(U_{+old}) \\ U_{+new} &= U_{+old} - \delta \end{aligned} \quad (18)$$

Since the matrix on the left hand side of equations (17) and (18) are the same an efficient LU decomposition could be used for the solution of (18).

This method is stable for all $a\Delta t$ with a real part less than zero in the model equation. The stable range is shown by the operator magnitude contours in Figure 91.

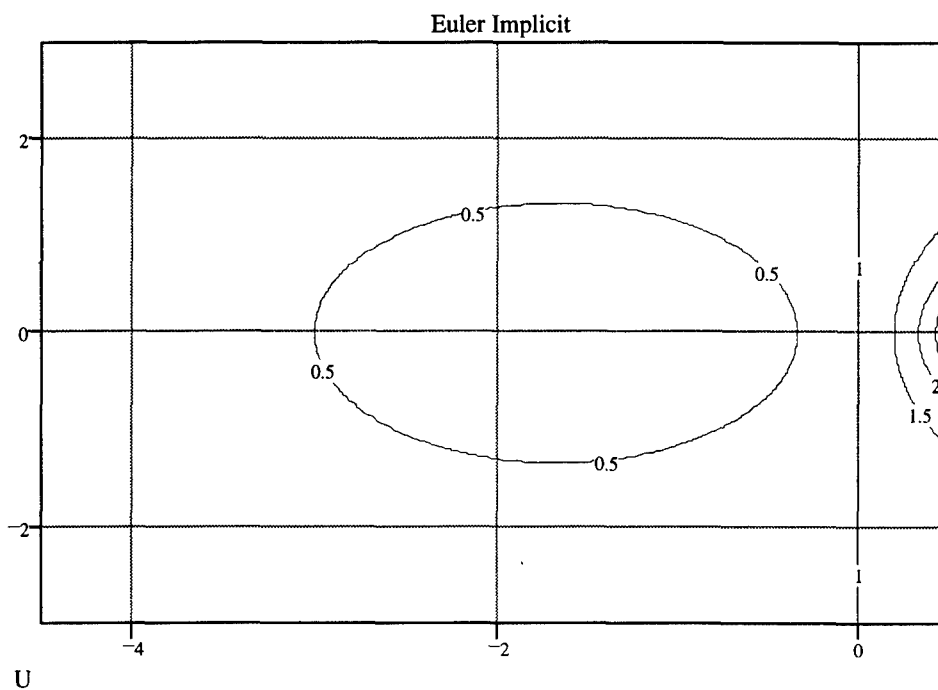


Figure 91. Operator Magnitude for Euler Implicit Method.

A.4. Comparison of Methods

Because of the small time step required for stability all of the methods gave nearly identical results. Figure 98 shows an ignition delay calculation using full hydrogen-oxygen kinetics model. The time scale of this figure was highly expanded to show the differences in the results. The first order methods gave slightly different ignition times. The second and higher order methods gave nearly identical results. The slight apparent difference in the higher order methods are due to the different time values of the data points. For most PSR time integrations the Euler implicit method was used because it took the least amount of computational time. Other integration methods were periodically used to check the Euler integration results with comparisons similar to those in Figure 92.

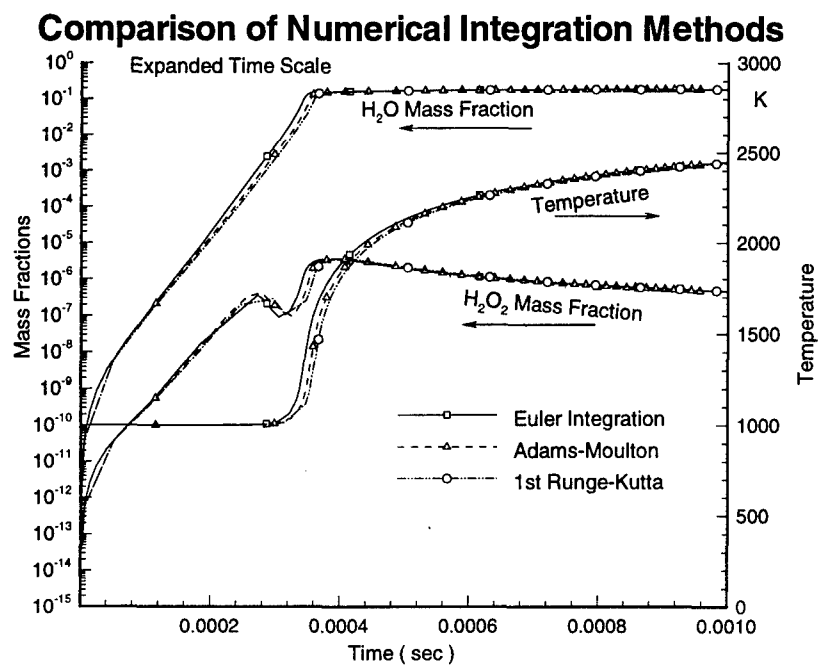


Figure 92. Comparison of Integration Methods for a Full Set H-O Ignition Calculation on an Expanded Scale.

Appendix B. Summary of Reaction Rate Sets.

This section contains the chemical kinetic rate set, input files used for the perfectly stirred reactor model. A description of the file format is followed by the hydrogen-oxygen rate sets. Then a sampling of hydrocarbon rate sets input files is given.

The first line of the input file consist of a file description. The second line contains three integers and a floating point number. The integers are the number of species, the number of third body catalysts, and the number of reaction rate equations. The floating point number is an input value of the universal gas constant, R_u , for use in the exponent of the rate constants.

The next line contains the names of the species. Following this line are the catalytic efficiencies for the species, given in the same order as the species names. In the reactions the catalyst are specified as M, M1, M2, M3, The first catalyst may optionally be specified as M0.

After the catalyst are specified, each line contains a reaction rate equation. First, the reactant species with optional stoichiometry coefficient are given. Any number of reactants may be specified. The reactants are separated by a "+" sign. After the reactants an "=" sign starts the products list. The products are specified in the same maner as the reactants until a semicollon ends the product list. Next, the forward Arrhenius rate coefficients are given in the order A_f , p_f , E_f . The forward rate constant used is

$$k_f = A_f \cdot T^{p_f} \cdot e^{-E_f / (R_u \cdot T)} .$$

After the forward rate coefficients, the reverse rate coefficients are given. The reverse rate constant A_b is used as a flag for the type of reverse rate calculation. If A_b is zero, then

Gibb's energy is used to calculate the reverse rate. If A_b is negative, the reverse rate is set to zero. Specific negative values for A_b are used for flags to set specific reaction rates in reduced set formulations. Table 16 summarizes the input format with spaces used to separate input variables.

Table 16. Rate Set Input File Format.

Line No.	Line Contents
1	File Description
2	# Species, # Catalysts, # Reaction Equations, Ru
3	Species Chemical Symbols
One Line Each Catalist	Third Body Weights for Each Species used to Form Each Catalyst. Specified in Same Order as Line 3.
One Line Each Reaction Equation	Reactants "=" Products ";" A_f , p_f , E_f , A_b , p_b , E_b Reactants = v'_{i1} Symbol _{i1} "+" v'_{i2} Symbol _{i2} "+" ... v' not included implies $v' = 1.0$, Spaces must be between v' , Symbol, and + . $A_b = 0.0$ indicates use Gibb's reverse rate. $A_b < 0.0$ indicates no reverse rate.

For the full hydrogen-oxygen reactions the following input files were used.

The Warnatz Rate Set :

Warnatz Reaction Set from Combustion Chemistry ed. Gardiner, Jr., W.C. pp.

199,336-337

9 1 17 1.0

O2 H2 H2O OH O H HO2 H2O2 N2

0.4 2.5 16.25 1.0 1.0 1.0 1.0 1.0 0.4	
O2 + H = OH + O ;	1.2e17 -91 8311 1.8e13 0.0 0.0
H2 + O = OH + H ;	1.5E04 2.00 3801 0.0
H2 + OH = H2O + H ;	1.0E08 1.6 1660 4.6e08 1.6 9345
2 OH = H2O + O ;	1.5E09 1.14 0 1.5e10 1.14 8684
2 H + M = H2 + M ;	3.88e16 -0.6 0 3.52e14 0.0 48350
OH + H + M = H2O + M ;	8.62e21 -2.0 0 9.85e15 0.0 57491
2 O + M = O2 + M ;	2.86E17 -1.0 0 3.43e14 0.0 54244
H + O2 + M = HO2 + M ;	8.0e17 -0.8 0 0.0
H + HO2 = 2 OH ;	1.5e14 0.0 505 0.0
H + HO2 = H2 + O2 ;	2.5e13 0.0 349 0.0
O + HO2 = OH + O2 ;	2.0e13 0.0 0 0.0
OH + HO2 = H2O + O2 ;	2.0e13 0.0 0 0.0
2 OH + M = H2O2 + M ;	3.25e22 -2.0 0 3.0e17 0.0 22852
H + H2O2 = H2 + HO2 ;	1.7e12 0.0 1888 7.3e11 0.0 9393
H + H2O2 = H2O + OH ;	1.0e13 0.0 1804 0.0
O + H2O2 = OH + HO2 ;	2.8e13 0.0 3223 0.0
OH + H2O2 = H2O + HO2 ;	7.0e12 0.0 722 0.0

Radhakrishnan Rate Set File :

H-O Reaction Set from Propane Set Pg.82 Vol II K. Radhakrishnan

9 5 18 1.987

H2 O2 H2O OH O H HO2 H2O2 N2

1.0 1.0 1.0 1.0 1.0 1.0 1.0 1.0 1.0

2.3 .78 6.0 1.0 1.0 1.0 1.0 6.6 1.0

1.0 1.3 21.3 1.0 1.0 1.0 1.0 1.0 1.3

4.0 1.5 20. 1.0 1.0 1.0 1.0 1.0 1.5

4.1 2.0 15. 1.0 1.0 1.0 1.0 1.0 2.0

O	+	H2O	=	OH	+	OH	;	6.8E+13	0.	18365.	0.0
H	+	O2	=	OH	+	O	;	1.89E+14	0.	16400.	0.0
O	+	H2	=	OH	+	H	;	4.20E+14	0.	13750.	0.0
H	+	HO2	=	H2	+	O2	;	7.28E+13	0.	2126.	0.0
O	+	HO2	=	OH	+	O2	;	5.0E+13	0.	1000.	0.0
HO2	+	OH	=	H2O	+	O2	;	8.0E+12	0.	0.	0.0
H	+	HO2	=	2 OH			;	1.34E+14	0.	1070.	0.0
H2	+	HO2	=	H2O2	+	H	;	7.91E+13	0.	25000.	0.0
OH	+	H2O2	=	H2O	+	HO2	;	6.1E+12	0.	1430.	0.0
HO2	+	HO2	=	H2O2	+	O2	;	1.8E+12	0.	0.	0.0
H	+	H2O2	=	OH	+	H2O	;	7.8E+11	0.	0.	0.0
M1	+	H2O2	=	M1	+	2 OH	;	1.44E+17	0.	45510.	0.0
H2	+	OH	=	H2O	+	H	;	4.74E+13	0.	6098.	0.0
H	+	M2 + O2	=	HO2	+	M2	;	1.46E+15	0.	-1000.	0.0
M3	+	H2O	=	M3 + H	+	OH	;	1.30E+15	0.	105140.	0.0
H	+	M + O	=	OH	+	M	;	7.1E+18	-1.0	0.	0.0
M4	+	H2	=	M4 + H	+	H	;	2.2E+14	0.	96000.	0.0
M	+	O2	=	M + O	+	O	;	1.8E+18	-1.0	118020.	0.0

Glassman Rate Set File :

Glassman Rates 1-20 pp.448-449

9 1 21 1.0

O2 H2 H2O OH O H HO2 H2O2 N2

1.0 1.0 1.0 1.0 1.0 1.0 1.0 1.0 1.0

O2 + H	=	OH + O	;	5.13e16	-.816	8314	0.0
H2 + O	=	OH + H	;	1.82e10	1.00	4482	0.0
H2 + OH	=	H2O + H	;	2.19e13	0.00	2593	0.0
O + H2O	=	2 OH	;	6.76e13	0.0	9245	0.0
2 H + M	=	H2 + M	;	3.02e15	0.0	0	0.0

$2\text{O} + \text{M} = \text{O}_2 + \text{M} ;$	1.91e13	0.0	-901	0.0
$\text{H} + \text{O} + \text{M} = \text{OH} + \text{M} ;$	1.00e16	0.0	0	0.0
$\text{OH} + \text{H} + \text{M} = \text{H}_2\text{O} + \text{M} ;$	1.41e23	-2.0	0	0.0
$\text{O}_2 + \text{H} + \text{M} = \text{HO}_2 + \text{M} ;$	1.51e15	0.0	-504	0.0
$\text{H} + \text{HO}_2 = \text{H}_2 + \text{O}_2 ;$	2.51e13	0.0	352	0.0
$\text{H} + \text{HO}_2 = 2\text{OH} ;$	2.51e14	0.0	956	0.0
$\text{H} + \text{HO}_2 = \text{H}_2\text{O} + \text{O} ;$	5.01e13	0.0	504	0.0
$\text{HO}_2 + \text{OH} = \text{H}_2\text{O} + \text{O}_2 ;$	5.01e13	0.0	504	0.0
$\text{HO}_2 + \text{O} = \text{OH} + \text{O}_2 ;$	5.01e13	0.0	504	0.0
$\text{HO}_2 + \text{HO}_2 = \text{H}_2\text{O}_2 + \text{O}_2 ;$	1.00e13	0.0	504	0.0
$\text{H}_2\text{O}_2 + \text{OH} = \text{H}_2\text{O} + \text{HO}_2 ;$	1.00e13	0.0	906	0.0
$\text{H}_2\text{O}_2 + \text{H} = \text{H}_2\text{O} + \text{OH} ;$	3.16e14	0.0	4502	0.0
$\text{H}_2\text{O}_2 + \text{H} = \text{HO}_2 + \text{H}_2 ;$	1.70e12	0.0	1888	0.0
$\text{H}_2\text{O}_2 + \text{M} = 2\text{OH} + \text{M} ;$	1.20e17	0.0	22912	0.0
$\text{O} + \text{OH} + \text{M} = \text{HO}_2 + \text{M} ;$	1.00e17	0.0	0	0.0
$\text{H}_2 + \text{O}_2 = 2\text{OH} ;$	2.51e12	0.0	19613	0.0

Drummond Rate Set File:

H-O Reaction Set (Ref. Num. Appr. to Comb. Modeling, Eds. Oran + Boris pg. 374)

9 1 18 1.9859

H2 O2 H2O OH O H HO2 H2O2 N2

1.0 1.0 1.0 1.0 1.0 1.0 1.0 1.0 1.0

$\text{H}_2 + \text{O}_2 = 2\text{OH} ;$.170e14	.0	48150.	0.0
$\text{O}_2 + \text{H} = \text{OH} + \text{O} ;$.142e15	.0	16400.	0.0
$\text{H}_2 + \text{OH} = \text{H}_2\text{O} + \text{H} ;$.316e08	1.8	3030.	0.0
$\text{H}_2 + \text{O} = \text{H} + \text{OH} ;$.207e15	.0	13750.	0.0
$2\text{OH} = \text{H}_2\text{O} + \text{O} ;$.550e14	.0	7000.	0.0
$\text{OH} + \text{H} + \text{M} = \text{H}_2\text{O} + \text{M} ;$.221e23	-2.0	0.	0.0
$2\text{H} + \text{M} = \text{H}_2 + \text{M} ;$.653e18	-1.0	0.	0.0

O2 + H + M = HO2 + M ;	.320e19	-1.0	0.	0.0
OH + HO2 = O2 + H2O ;	.500e14	.0	1000.	0.0
H + HO2 = H2 + O2 ;	.253e14	.0	700.	0.0
H + HO2 = 2 OH ;	.199e15	.0	1800.	0.0
O + HO2 = O2 + OH ;	.500e14	.0	1000.	0.0
2 HO2 = O2 + H2O2 ;	.199e13	.0	0.	0.0
H2 + HO2 = H + H2O2 ;	.301e12	.0	18700.	0.0
OH + H2O2 = H2O + HO2 ;	.102e14	.0	1900.	0.0
H + H2O2 = H2O + OH ;	.500e15	.0	10000.	0.0
O + H2O2 = OH + HO2 ;	.199e14	.0	5900.	0.0
H2O2 + M = 2 OH + M ;	.121e18	.0	45500.	0.0

A Rate Set That Includes Hydrogen - Oxygen and Nitrogen Reactions:

H-O-N Reaction Set Pg.82 Vol II K. Radhakrishnan Delete C Compounds

18 6 37 1.987

H2 O2 H2O OH O H HO2 H2O2 N2 N NO N2O NO2 NH HNO HNO2 HNO3 AR

1.0 1.0 1.0 1.0 1.0 1.0 1.0 1.0 1.0 1.0 1.0 1.0 1.0 1.0 1.0 1.0 1.0 1.0

2.3 .78 6.0 1.0 1.0 1.0 1.0 6.6 1.0 1.0 1.0 1.0 1.0 1.0 1.0 1.0 1.0 1.0

1.0 1.3 21.3 1. 1.0 1.0 1.0 1.0 1.3 1.0 1.0 1.0 1.0 1.0 1.0 1.0 1.0 1.0

4.0 1.5 20. 1.0 1.0 1.0 1.0 1.0 1.5 1.0 1.0 1.0 1.0 1.0 1.0 1.0 1.0 1.0

4.1 2.0 15. 1.0 1.0 1.0 1.0 1.0 2.0 1.0 1.0 1.0 1.0 1.0 1.0 1.0 1.0 1.0

1.4 0.7 1.0 1.0 1.0 1.0 1.0 1.0 1.0 1.0 1.0 1.0 1.0 1.0 1.0 1.0 1.0 1.0

O	+	H2O	=	OH	+	OH	;	6.8E+13	0.	18365.	0.0
H	+	O2	=	OH	+	O	;	1.89E+14	0.	16400.	0.0
O	+	H2	=	OH	+	H	;	4.20E+14	0.	13750.	0.0
H	+	HO2	=	H2	+	O2	;	7.28E+13	0.	2126.	0.0
O	+	HO2	=	OH	+	O2	;	5.0E+13	0.	1000.	0.0
HO2	+	OH	=	H2O	+	O2	;	8.0E+12	0.	0.	0.0

H	+	HO2	=	2 OH		; 1.34E+14	0.	1070.	0.0
H2	+	HO2	=	H2O2 +	H	; 7.91E+13	0.	25000.	0.0
OH	+	H2O2	=	H2O +	HO2	; 6.1E+12	0.	1430.	0.0
HO2	+	HO2	=	H2O2 +	O2	; 1.8E+12	0.	0.	0.0
H	+	H2O2	=	OH +	H2O	; 7.8E+11	0.	0.	0.0
M1	+	H2O2	=	M1 +	2 OH	; 1.44E+17	0.	45510.	0.0
H2	+	OH	=	H2O +	H	; 4.74E+13	0.	6098.	0.0
H + M2 + O2			=	HO2 +	M2	; 1.46E+15	0.	-1000.	0.0
M3	+	H2O	=	M3 + H +	OH	; 1.30E+15	0.	105140.	0.0
H	+	M + O	=	OH +	M	; 7.1E+18	-1.0	0.	0.0
M4	+	H2	=	M4 + H +	H	; 2.2E+14	0.	96000.	0.0
M	+	O2	=	M + O +	O	; 1.8E+18	-1.0	118020.	0.0
NH	+	OH	=	N +	H2O	; 5.0E+11	0.5	2000.	0.0
HO2	+	NO	=	NO2 +	OH	; 2.09E+12	0.	-477.	0.0
O	+	NO2	=	NO +	O2	; 1.0E+13	0.	596.	0.0
NO	+	M + O	=	NO2 +	M	; 5.62E+15	0.	-1160.	0.0
NO2	+	H	=	NO +	OH	; 3.47E+14	0.	1470.	0.0
NO	+	H	=	N +	OH	; 2.63E+14	0.	50410.	0.0
NO	+	O	=	N +	O2	; 3.8E+9	1.	41370.	0.0
O	+	N2	=	NO +	N	; 1.80E+14	0.	76250.	0.0
N	+	NO2	=	2 NO		; 4.0E+12	0.	0.	0.0
M	+	N2O	=	M + N2 +	O	; 6.92E+23	-2.5	65000.	0.0
O	+	N2O	=	N2 +	O2	; 1.0E+14	0.	28020.	0.0
O	+	N2O	=	2 NO		; 6.92E+13	0.	26630.	0.0
N2O	+	H	=	N2 +	OH	; 7.59E+13	0.	15100.	0.0
NO2	+	H2	=	HNO2 +	H	; 2.4E+13	0.	29000.	0.0
OH	+	M5 + NO2	=	HNO3 +	M5	; 3.0E+15	0.	-3800.	0.0
OH	+	M NO	=	HNO2 +	M	; 5.6E+15	0.	-1700.	0.0
HNO	+	H	=	H2 +	NO	; 5.0E+12	0.	0.	0.0
H	+	M + NO	=	HNO +	M	; 5.4E+15	0.	-600.	0.0

HNO + OH = H2O + NO ; 3.6E+13 0. 0. 0.0

Another Rate Set for Hydrogen-Oxygen from Radhakrishnan:

H-O Set from H-O-N set, K. Radhakrishnan pg. 326 Vol I.

9 4 18 1.0

O2 H2 H2O OH O H HO2 H2O2 N2

1.0 1.0 1.0 1.0 1.0 1.0 1.0 1.0 1.0

1.0 1.0 20. 1.0 1.0 1.0 1.0 1.0 1.0

1.0 3.0 6.0 1.0 1.0 2.0 1.0 1.0 1.0

0.0 3.3 21. 1.0 1.0 1.0 1.0 1.0 1.5

O2 + H = OH + O ;	5.1e16	-0.82	8313.6	0.0
H2 + O = OH + H ;	1.8e10	1.00	4446.3	0.0
H2 + OH = H2O + H ;	1.2e09	1.30	1827.9	0.0
OH + OH = O + H2O ;	6.0e08	1.30	0	0.0
OH + H + M1 = H2O + M1 ;	7.5e23	-2.60	0 0.0	
O2 + M = 2 O + M ;	1.9e11	0.5	48119.2	0.0
H2 + M2 = 2 H + M2 ;	2.2e12	0.5	46628.7	0.0
H2 + O2 = 2 OH ;	1.7e13	0.0	24059.6	0.0
H + O2 + M3 = HO2 + M3 ;	2.1e18	-1.0	0.0 0.0	
H + 2 O2 = HO2 + O2 ;	6.7e19	-1.42	0.0 0.0	
H + HO2 = H2 + O2 ;	2.5E13	0.0	352.5	0.0
H + HO2 = 2 OH ;	2.5E14	0.0	956.7	0.0
O + HO2 = O2 + OH ;	4.8E13	0.0	503.6	0.0
OH + HO2 = O2 + H2O ;	5.0E13	0.0	503.6	0.0
2 HO2 = H2O2 + O2 ;	2.0e12	0.0	0.0	0.0
H2O2 + M = 2 OH + M ;	1.2e17	0.0	22911.5	0.0
H2O2 + H = HO2 + H2 ;	1.7e12	0.0	1888.3	0.0
H2O2 + OH = H2O + HO2 ;	1.0e13	0.0	906.4	0.0

Hydrogen-Oxygen Rate Set File with H2O2 Removed.

H-O (- H2O2) Reaction Set from Propane Set Pg.82 Vol II K. Rad.

8 4 13 1.9859

H2 O2 H2O OH O H HO2 N2

1.0 1.0 1.0 1.0 1.0 1.0 1.0 1.0 1.0

1.0 1.3 21.3 1. 1.0 1.0 1.0 1.0 1.3

4.0 1.5 20. 1.0 1.0 1.0 1.0 1.0 1.5

4.1 2.0 15. 1.0 1.0 1.0 1.0 1.0 2.0

O	+	H2O	=	OH	+	OH	;	6.8E+13	0.	18365.	0.0
H	+	O2	=	OH	+	O	;	1.89E+14	0.	16400.	0.0
O	+	H2	=	OH	+	H	;	4.20E+14	0.	13750.	0.0
H	+	HO2	=	H2	+	O2	;	7.28E+13	0.	2126.	0.0
O	+	HO2	=	OH	+	O2	;	5.0E+13	0.	1000.	0.0
HO2	+	OH	=	H2O	+	O2	;	8.0E+12	0.	0.	0.0
H	+	HO2	=	2 OH			;	1.34E+14	0.	1070.	0.0
H2	+	OH	=	H2O	+	H	;	4.74E+13	0.	6098.	0.0
H	+	M1 + O2	=	HO2	+	M1	;	1.46E+15	0.	-1000.	0.0
M2	+	H2O	=	M2 + H	+	OH	;	1.30E+15	0.	105140.	0.0
H	+	M + O	=	OH	+	M	;	7.1E+18	-1.0	0.	0.0
M3	+	H2	=	M3 + H	+	H	;	2.2E+14	0.	96000.	0.0
M	+	O2	=	M + O	+	O	;	1.8E+18	-1.0	118020.	0.0

Hydrogen- Oxygen Rate Set with H2O2 and HO2 Removed:

H-O (- HO2 -H2O2) from Propane Set Reaction Set Pg.82 Vol II K. Rad.

7 3 8 1.9859

H2 O2 H2O OH O H N2

1.0 1.0 1.0 1.0 1.0 1.0 1.0 1.0

4.0 1.5 20. 1.0 1.0 1.0 1.0 1.5

4.1 2.0 15. 1.0 1.0 1.0 1.0 2.0

O	+	H2O	=	OH	+	OH	;	6.8E+13	0.	18365.0.0
H	+	O2	=	OH	+	O	;	1.89E+14	0.	16400.0.0
O	+	H2	=	OH	+	H	;	4.20E+14	0.	13750.0.0
H2	+	OH	=	H2O	+	H	;	4.74E+13	0.	6098.0.0
M1	+	H2O	=	M1 + H	+	OH	;	1.30E+15	0.	105140.0.0
H	+	M + O	=	OH	+	M	;	7.1E+18	-1.0	0.0.0
M2	+	H2	=	M2 + H	+	H	;	2.2E+14	0.	96000.0.0
M	+	O2	=	M + O	+	O	;	1.8E+18	-1.0	118020.0.0

For hydrocarbon reactions the following rate set files were used.

Full Propane Reaction Set Input File:

Propane Reaction Set Pg.82 K. Radhakrishnan

42 6 136 1.987

H2 O2 H2O OH O H HO2 H2O2 N2 N NO N2O NO2 NH2 NH HNO HNO2
HNO3 CO CO2 CH CH2 CH3 CH4 HCO CH2O CH3O C2H C2H2 C2H3 C2H4 C2H5
C2H6 C2HO C2H2O NCO HNCO C3H8 C3H7 HCN CN AR
1.0
1.0 1.0 1.0 1.0 1.0 1.0 1.0 1.0 1.0 1.0 1.0 1.0 1.0 1.0 1.0 1.0 1.0 1.0 1.0
2.3 .78 6.0 1.0 1.0 1.0 1.0 6.6 1.0 1.0 1.0 1.0 1.0 1.0 1.0 1.0 1.0 1.0 1.0 1.0
1.0 1.0 1.0 1.0 1.0 1.0 1.0 1.0 1.0 1.0 1.0 1.0 1.0 1.0 1.0 1.0 1.0 1.0 1.0

1.0 1.3 21.3 1. 1.0 1.0 1.0 1.0 1.3 1.0 1.0 1.0 1.0 1.0 1.0 1.0 1.0 1.0 1.0 1.0 1.0 1.0 7.0 1.0 1.0 1.0
 1.0
 4.0 1.5 20. 1.0 1.0 1.0 1.0 1.0 1.5 1.0 1.0 1.0 1.0 1.0 1.0 1.0 1.0 1.0 1.0 1.0 1.0 4.0 1.0 1.0 1.0
 1.0
 4.1 2.0 15. 1.0 1.0 1.0 1.0 1.0 2.0 1.0 1.0 1.0 1.0 1.0 1.0 1.0 1.0 1.0 1.0 1.0 1.0 1.0 1.0 1.0 1.0
 1.0
 1.4 0.7 1.0
 1.0

		C3H8 =	C2H5 +	CH3 ;	5.0E+15	0.	83500. 0.0
CH3	+	C3H8 =	CH4 +	C3H7 ;	3.55E+12	0.	10300. 0.0
		C3H7 =	C2H4 +	CH3 ;	3.0E+14	0.	33200. 0.0
M	+	CH4 =	M + CH3 +	H ;	2.0E+17	0.	88000. 0.0
H	+	CH4 =	CH3 +	H2 ;	1.26E+14	0.	11900. 0.0
CH4	+	O2 =	CH3 +	HO2 ;	7.94E+13	0.	56000. 0.0
O	+	CH4 =	CH3 +	OH ;	1.9E+14	0.	11720. 0.0
OH	+	CH4 =	CH3 +	H2O ;	2.5E+13	0.	5010. 0.0
CH3	+	O2 =	CH3O +	O ;	2.4E+13	0.	28680. 0.0
CH3	+	OH =	CH3O +	H ;	6.3E+12	0.	0. 0.0
M	+	CH3O =	M + CH2O +	H ;	5.0E+13	0.	21000. 0.0
CH3	+	CH3 =	C2H6		2.4E+14	-.4	0. 0.0
H	+	C2H6 =	C2H5 +	H2 ;	1.32E+14	0.	9700. 0.0
O	+	C2H6 =	C2H5 +	OH ;	1.13E+14	0.	7850. 0.0
OH	+	C2H6 =	C2H5 +	H2O ;	8.7E+13	0.	3520. 0.0
M	+	C2H5 =	M + C2H4 +	H ;	1.0E+17	0.	31000. 0.0
C2H5	+	O2 =	C2H4 +	HO2 ;	2.0E+12	0.	5000. 0.0
H	+	C2H5 =	C2H4 +	H2 ;	4.8E+13	0.	0. 0.0
CH3	+	CH2 =	C2H4 +	H ;	2.0E+13	0.	0. 0.0
H	+	C2H4 =	H2	C2H3 ;	1.5E+14	0.	10200. 0.0
M	+	C2H4 =	M + C2H2 +	H2 ;	2.6E+17	0.	79300. 0.0
C2H4	+	OH =	C2H3 +	H2O ;	4.8E+12	0.	1230. 0.0

C2H4	+	OH	=	CH3	+	CH2O	;	2.0E+12	0.	960.	0.0
C2H4	+	O	=	CH3	+	HCO	;	3.3E+12	0.	1130.	0.0
C2H4	+	O	=	CH2O	+	CH2	;	2.5E+13	0.	5000.	0.0
M	+	C2H3	=	M + C2H2	+	H	;	3.0E+15	0.	32000.	0.0
C2H3	+	O2	=	CH2O	+	HCO	;	3.98E+12	0.	-250.	0.0
C2H3	+	H	=	C2H2	+	H2	;	6.0E+12	0.	0.	0.0
C2H3	+	O	=	C2H2O	+	H	;	3.3E+13	0.	0.	0.0
C2H3	+	OH	=	C2H2	+	H2O	;	5.0E+12	0.	0.	0.0
C2H3	+	CH2	=	C2H2	+	CH3	;	3.0E+13	0.	0.	0.0
C2H3	+	C2H	=	2 C2H2			;	3.0E+13	0.	0.	0.0
M	+	C2H2	=	M + C2H	+	H	;	4.2E+16	0.	107000.	0.0
C2H2	+	O	=	CH2	+	CO	;	1.6E+14	0.	9890.	0.0
C2H2	+	O	=	C2HO	+	H	;	4.0E+14	0.	10660.	0.0
C2H2	+	OH	=	C2H	+	H2O	;	6.3E+12	0.	7000.	0.0
C2H2	+	OH	=	C2H2O	+	H	;	3.3E+11	0.	200.	0.0
C2H	+	O2	=	C2HO	+	O	;	5.00E+13	0.	1500.	0.0
C2H	+	OH	=	C2HO	+	H	;	2.0E+13	0.	0.	0.0
C2HO	+	O2	=	2 CO	+	OH	;	1.46E+12	0.	2500.	0.0
C2HO	+	O	=	2 CO	+	H	;	1.202E+12	0.	0.	0.0
C2HO	+	OH	=	2 HCO			;	1.0E+13	0.	0.	0.0
C2HO	+	H	=	CH2	+	CO	;	5.0E+13	0.	0.	0.0
C2HO	+	CH2	=	C2H3	+	CO	;	3.0E+13	0.	0.	0.0
C2HO	+	CH2	=	CH2O	+	C2H	;	1.0E+13	0.	2000.	0.0
		2 C2HO	=	C2H2	+	2 CO	;	1.0E+13	0.	0.	0.0
C2H2O	+	OH	=	CH2O	+	HCO	;	2.8E+13	0.	0.	0.0
C2H2O	+	OH	=	C2HO	+	H2O	;	7.5E+12	0.	3000.	0.0
C2H2O	+	H	=	CH3	+	CO	;	1.13E+13	0.	3428.	0.0
C2H2O	+	H	=	C2HO	+	H2	;	7.5E+13	0.	8000.	0.0
C2H2O	+	O	=	C2HO	+	OH	;	5.0E+13	0.	8000.	0.0
C2H2O	+	O	=	CH2O	+	CO	;	2.0E+13	0.	0.	0.0

M	+	C2H2O	=	M + CH2	+	CO	;	2.0E+16	0.	60000.	0.0
C2H	+	O	=	CO	+	CH	;	5.0E+13	0.	0.	0.0
CH3O	+	O2	=	CH2O	+	HO2	;	1.0E+13	0.	7170.	0.0
CH3O	+	H	=	CH2O	+	H2	;	2.0E+13	0.	0.	0.0
M	+	CH2O	=	M + HCO	+	H	;	5.0E+16	0.	81000.	0.0
CH2O	+	OH	=	HCO	+	H2O	;	3.0E+13	0.	1200.	0.0
CH2O	+	H	=	HCO	+	H2	;	2.5E+13	0.	3990.	0.0
CH2O	+	O	=	HCO	+	OH	;	3.5E+13	0.	3510.	0.0
CH3	+	CH2O	=	CH4	+	HCO	;	1.0E+10	0.5	6000.	0.0
CH3	+	HCO	=	CH4	+	CO	;	3.0E+11	.5	0.	0.0
CH3	+	HO2	=	CH3O	+	OH	;	2.0E+13	0.	0.	0.0
M	+	CH3	=	M + CH2	+	H	;	1.95E+16	0.	91600.	0.0
H	+	CH3	=	H2	+	CH2	;	2.7E+11	.67	25700.	0.0
O	+	CH3	=	OH	+	CH2	;	1.9E+11	.68	25700.	0.0
OH	+	CH3	=	H2O	+	CH2	;	2.7E+11	.67	25700.	0.0
CH	+	CO2	=	HCO	+	CO	;	3.7E+12	0.	0.	0.0
CH	+	O2	=	HCO	+	O	;	1.0E+13	0.	0.	0.0
CH2	+	O2	=	CH2O	+	O	;	5.0E+11	0.5	6960.	0.0
CH2	+	O	=	CH	+	OH	;	2.0E+11	.7	25800.	0.0
CH2	+	OH	=	CH	+	H2O	;	5.0E+11	.5	5900.	0.0
CH2	+	H	=	CH	+	H2	;	3.2E+11	0.7	4970.	0.0
CH2	+	CH2	=	C2H3	+	H	;	5.0E+12	0.	0.	0.0
CH2	+	CH2	=	C2H2	+	H2	;	4.0E+13	0.	0.	0.0
HCO	+	O2	=	CO	+	HO2	;	3.0E+13	0.	0.	0.0
HCO	+	O	=	CO	+	OH	;	3.0E+13	0.	0.	0.0
HCO	+	OH	=	CO	+	H2O	;	3.0E+13	0.	0.	0.0
HCO	+	H	=	CO	+	H2	;	2.0E+13	0.	0.	0.0
M	+	HCO	=	M + H	+	CO	;	2.9E+14	0.	15570.	0.0
CO	+	M + O	=	CO2	+	M	;	2.4E+15	0.	4100.	0.0
CO	+	O2	=	CO2	+	O	;	2.5E+12	0.	47690.	0.0

CO	+	OH	=	CO2	+	H	;	4.17E+11	0.	1000.	0.0
CO	+	HO2	=	CO2	+	OH	;	5.75E+13	0.	22930.	0.0
O	+	H2O	=	OH	+	OH	;	6.8E+13	0.	18365.	0.0
H	+	O2	=	OH	+	O	;	1.89E+14	0.	16400.	0.0
O	+	H2	=	OH	+	H	;	4.20E+14	0.	13750.	0.0
H	+	HO2	=	H2	+	O2	;	7.28E+13	0.	2126.	0.0
O	+	HO2	=	OH	+	O2	;	5.0E+13	0.	1000.	0.0
HO2	+	OH	=	H2O	+	O2	;	8.0E+12	0.	0.	0.0
H	+	HO2	=	2 OH			;	1.34E+14	0.	1070.	0.0
H2	+	HO2	=	H2O2	+	H	;	7.91E+13	0.	25000.	0.0
OH	+	H2O2	=	H2O	+	HO2	;	6.1E+12	0.	1430.	0.0
HO2	+	HO2	=	H2O2	+	O2	;	1.8E+12	0.	0.	0.0
H	+	H2O2	=	OH	+	H2O	;	7.8E+11	0.	0.	0.0
M1	+	H2O2	=	M1 + 2 OH			;	1.44E+17	0.	45510.	0.0
H2	+	OH	=	H2O	+	H	;	4.74E+13	0.	6098.	0.0
H	+	M2 + O2	=	HO2	+	M2	;	1.46E+15	0.	-1000.	0.0
M3	+	H2O	=	M3 + H	+	OH	;	1.30E+15	0.	105140.	0.0
H	+	M + O	=	OH	+	M	;	7.1E+18	-1.0	0.	0.0
M4	+	H2	=	M4 + H	+	H	;	2.2E+14	0.	96000.	0.0
M	+	O2	=	M + O	+	O	;	1.8E+18	-1.0	118020.	0.0
CH	+	N2	=	HCN	+	N	;	1.0E+11	0.	19000.	0.0
CN	+	H2	=	HCN	+	H	;	6.0E+13	0.	5300.	0.0
O	+	HCN	=	OH	+	CN	;	1.4E+11	.68	16900.	0.0
OH	+	HCN	=	HNCO	+	H	;	4.0E+11	0.	2800.	0.0
CN	+	O	=	CO	+	N	;	1.2E+13	0.	0.	0.0
CN	+	OH	=	NCO	+	H	;	2.5E+14	0.	6000.	0.0
H2	+	NCO	=	HNCO	+	H	;	1.0E+14	0.	9000.	0.0
HNCO	+	H	=	NH2	+	CO	;	1.0E+14	0.	8500.	0.0
CN	+	O2	=	NCO	+	O	;	3.2E+13	0.	1000.	0.0
CN	+	CO2	=	NCO	+	CO	;	3.7E+12	0.	0.	0.0

O	+	NCO	=	NO	+	CO	;	2.0E+13	0.	0.	0.0
N	+	NCO	=	N2	+	CO	;	1.0E+13	0.	0.	0.0
H	+	NCO	=	NH	+	CO	;	2.0E+13	0.	0.	0.0
CH	+	NO	=	N	+	HCO	;	1.6E+13	0.	9940.	0.0
CH	+	NO	=	O	+	HCN	;	2.0E+12	0.	0.	0.0
NH	+	OH	=	N	+	H2O	;	5.0E+11	0.5	2000.	0.0
HO2	+	NO	=	NO2	+	OH	;	2.09E+12	0.	-477.	0.0
O	+	NO2	=	NO	+	O2	;	1.0E+13	0.	596.	0.0
NO	+	M + O	=	NO2	+	M	;	5.62E+15	0.	-1160.	0.0
NO2	+	H	=	NO	+	OH	;	3.47E+14	0.	1470.	0.0
NO	+	H	=	N	+	OH	;	2.63E+14	0.	50410.	0.0
NO	+	O	=	N	+	O2	;	3.8E+9	1.	41370.	0.0
O	+	N2	=	NO	+	N	;	1.80E+14	0.	76250.	0.0
N	+	NO2	=	2 NO			;	4.0E+12	0.	0.	0.0
M	+	N2O	=	M + N2	+	O	;	6.92E+23	-2.5	65000.	0.0
O	+	N2O	=	N2	+	O2	;	1.0E+14	0.	28020.	0.0
O	+	N2O	=	2 NO			;	6.92E+13	0.	26630.	0.0
N2O	+	H	=	N2	+	OH	;	7.59E+13	0.	15100.	0.0
NO2	+	H2	=	HNO2	+	H	;	2.4E+13	0.	29000.	0.0
OH	+	M5 + NO2	=	HNO3	+	M5	;	3.0E+15	0.	-3800.	0.0
OH	+	M + NO	=	HNO2	+	M	;	5.6E+15	0.	-1700.	0.0
HNO	+	H	=	H2	+	NO	;	5.0E+12	0.	0.	0.0
H	+	M + NO	=	HNO	+	M	;	5.4E+15	0.	-600.	0.0
HNO	+	OH	=	H2O	+	NO	;	3.6E+13	0.	0.	0.0

Reduced Propane Reaction Rate Set:

Lewis Propane

model,ALLSPD-3D,Ver.1.0a,<West&Dry,Comb.Sci.&Tech,27,pp31-43,1981

6 0 2 1.0

O2 H2O N2 CO CO2 C3H8

C3H8 + 3.5 O2 = 3 CO + 4 H2O ; 5.62E+09 0.0 15098.1 -3.

CO + 0.5 O2 = CO2 ; 2.24E+12 0.0 20140 -4.

Note: The -3 for Ab indicates that the reaction rate equation is

$$rr_1 = [C_3H_8]^{0.1} \cdot [O_2]^{1.65} \cdot A_f \cdot e^{-E_f / (Ru \cdot T)}$$

and the -4 indicates that the reaction rate for the second equation is

$$rr_2 = [H_2O]^{0.5} \cdot [O_2]^{0.25} \cdot [CO] \cdot A_f \cdot e^{-E_f / (Ru \cdot T)} \\ - [CO_2] \cdot 5.0 \cdot 10^8 \cdot e^{-20140 / (Ru \cdot T)}$$

The Full Methane Reaction Set Input File was :

Full Methane from Propane Reaction Set Pg.82 K. Radhakrishnan

31 6 88 1.987

H2 O2 H2O OH O H HO2 H2O2 N2 N NO N2O NO2 NH2 NH HNO HNO2

HNO3 CO CO2 CH CH2 CH3 CH4 HCO CH2O CH3O NCO HNCO HCN CN

1.0
 1.0
 2.3 78 6.0 1.0 1.0 1.0 1.0 6.6 1.0 1.0 1.0 1.0 1.0 1.0 1.0 1.0 1.0 1.0 1.0 1.0
 1.0
 1.0 1.3 21.3 1. 1.0 1.0 1.0 1.0 1.3 1.0 1.0 1.0 1.0 1.0 1.0 1.0 1.0 1.0 1.0 1.0
 1.0
 4.0 1.5 20. 1.0 1.0 1.0 1.0 1.0 1.5 1.0 1.0 1.0 1.0 1.0 1.0 1.0 1.0 1.0 1.0 1.0 1.0
 1.0
 4.1 2.0 15. 1.0 1.0 1.0 1.0 1.0 2.0 1.0 1.0 1.0 1.0 1.0 1.0 1.0 1.0 1.0 1.0 1.0 1.0
 1.0
 1.4 0.7 1.0 1.0 1.0 1.0 1.0 1.0 1.0 1.0 1.0 1.0 1.0 1.0 1.0 1.0 1.0 1.0 1.0 1.0
 1.0

M	+	CH4	=	M + CH3	+	H	;	2.0E+17	0.	88000.0.0
H	+	CH4	=	CH3	+	H2	;	1.26E+14	0.	11900.0.0
CH4	+	O2	=	CH3	+	HO2	;	7.94E+13	0.	56000.0.0
O	+	CH4	=	CH3	+	OH	;	1.9E+14	0.	11720.0.0
OH	+	CH4	=	CH3	+	H2O	;	2.5E+13	0.	5010. 0.0
CH3	+	O2	=	CH3O	+	O	;	2.4E+13	0.	28680.0.0
CH3	+	OH	=	CH3O	+	H	;	6.3E+12	0.	0. 0.0
M	+	CH3O	=	M + CH2O	+	H	;	5.0E+13	0.	21000.0.0
CH3O	+	O2	=	CH2O	+	HO2	;	1.0E+13	0.	7170. 0.0
CH3O	+	H	=	CH2O	+	H2	;	2.0E+13	0.	0. 0.0
M	+	CH2O	=	M + HCO	+	H	;	5.0E+16	0.	81000.0.0
CH2O	+	OH	=	HCO	+	H2O	;	3.0E+13	0.	1200. 0.0
CH2O	+	H	=	HCO	+	H2	;	2.5E+13	0.	3990. 0.0
CH2O	+	O	=	HCO	+	OH	;	3.5E+13	0.	3510. 0.0
CH3	+	CH2O	=	CH4	+	HCO	;	1.0E+10	0.5	6000. 0.0
CH3	+	HCO	=	CH4	+	CO	;	3.0E+11	.5	0. 0.0
CH3	+	HO2	=	CH3O	+	OH	;	2.0E+13	0.	0. 0.0
M	+	CH3	=	M + CH2	+	H	;	1.95E+16	0.	91600.0.0

H	+	CH3	=	H2	+	CH2	;	2.7E+11	.67	25700.	0.0
O	+	CH3	=	OH	+	CH2	;	1.9E+11	.68	25700.	0.0
OH	+	CH3	=	H2O	+	CH2	;	2.7E+11	.67	25700.	0.0
CH	+	CO2	=	HCO	+	CO	;	3.7E+12	0.	0.	0.0
CH	+	O2	=	HCO	+	O	;	1.0E+13	0.	0.	0.0
CH2	+	O2	=	CH2O	+	O	;	5.0E+11	0.5	6960.	0.0
CH2	+	O	=	CH	+	OH	;	2.0E+11	.7	25800.	0.0
CH2	+	OH	=	CH	+	H2O	;	5.0E+11	.5	5900.	0.0
CH2	+	H	=	CH	+	H2	;	3.2E+11	0.7	4970.	0.0
HCO	+	O2	=	CO	+	HO2	;	3.0E+13	0.	0.	0.0
HCO	+	O	=	CO	+	OH	;	3.0E+13	0.	0.	0.0
HCO	+	OH	=	CO	+	H2O	;	3.0E+13	0.	0.	0.0
HCO	+	H	=	CO	+	H2	;	2.0E+13	0.	0.	0.0
M	+	HCO	=	M + H	+	CO	;	2.9E+14	0.	15570.	0.0
CO	+	M + O	=	CO2	+	M	;	2.4E+15	0.	4100.	0.0
CO	+	O2	=	CO2	+	O	;	2.5E+12	0.	47690.	0.0
CO	+	OH	=	CO2	+	H	;	4.17E+11	0.	1000.	0.0
CO	+	HO2	=	CO2	+	OH	;	5.75E+13	0.	22930.	0.0
O	+	H2O	=	OH	+	OH	;	6.8E+13	0.	18365.	0.0
H	+	O2	=	OH	+	O	;	1.89E+14	0.	16400.	0.0
O	+	H2	=	OH	+	H	;	4.20E+14	0.	13750.	0.0
H	+	HO2	=	H2	+	O2	;	7.28E+13	0.	2126.	0.0
O	+	HO2	=	OH	+	O2	;	5.0E+13	0.	1000.	0.0
HO2	+	OH	=	H2O	+	O2	;	8.0E+12	0.	0.	0.0
H	+	HO2	=	2 OH			;	1.34E+14	0.	1070.	0.0
H2	+	HO2	=	H2O2	+	H	;	7.91E+13	0.	25000.	0.0
OH	+	H2O2	=	H2O	+	HO2	;	6.1E+12	0.	1430.	0.0
HO2	+	HO2	=	H2O2	+	O2	;	1.8E+12	0.	0.	0.0
H	+	H2O2	=	OH	+	H2O	;	7.8E+11	0.	0.	0.0
M1	+	H2O2	=	M1 +	2 OH		;	1.44E+17	0.	45510.	0.0

H2	+	OH	=	H2O	+	H	;	4.74E+13	0.	6098.	0.0
H	+	M2 + O2	=	HO2	+	M2	;	1.46E+15	0.	-1000.	0.0
M3	+	H2O	=	M3 + H	+	OH	;	1.30E+15	0.	105140.	0.0
H	+	M + O	=	OH	+	M	;	7.1E+18	-1.0	0.	0.0
M4	+	H2	=	M4 + H	+	H	;	2.2E+14	0.	96000.	0.0
M	+	O2	=	M + O + O			;	1.8E+18	-1.0	118020.	0.0
CH	+	N2	=	HCN	+	N	;	1.0E+11	0.	19000.	0.0
CN	+	H2	=	HCN	+	H	;	6.0E+13	0.	5300.	0.0
O	+	HCN	=	OH	+	CN	;	1.4E+11	.68	16900.	0.0
OH	+	HCN	=	HNCO	+	H	;	4.0E+11	0.	2800.	0.0
CN	+	O	=	CO	+	N	;	1.2E+13	0.	0.	0.0
CN	+	OH	=	NCO	+	H	;	2.5E+14	0.	6000.	0.0
H2	+	NCO	=	HNCO	+	H	;	1.0E+14	0.	9000.	0.0
HNCO	+	H	=	NH2	+	CO	;	1.0E+14	0.	8500.	0.0
CN	+	O2	=	NCO	+	O	;	3.2E+13	0.	1000.	0.0
CN	+	CO2	=	NCO	+	CO	;	3.7E+12	0.	0.	0.0
O	+	NCO	=	NO	+	CO	;	2.0E+13	0.	0.	0.0
N	+	NCO	=	N2	+	CO	;	1.0E+13	0.	0.	0.0
H	+	NCO	=	NH	+	CO	;	2.0E+13	0.	0.	0.0
CH	+	NO	=	N	+	HCO	;	1.6E+13	0.	9940.	0.0
CH	+	NO	=	O	+	HCN	;	2.0E+12	0.	0.	0.0
NH	+	OH	=	N	+	H2O	;	5.0E+11	0.5	2000.	0.0
HO2	+	NO	=	NO2	+	OH	;	2.09E+12	0.	-477.	0.0
O	+	NO2	=	NO	+	O2	;	1.0E+13	0.	596.	0.0
NO	+	M + O	=	NO2	+	M	;	5.62E+15	0.	-1160.	0.0
NO2	+	H	=	NO	+	OH	;	3.47E+14	0.	1470.	0.0
NO	+	H	=	N	+	OH	;	2.63E+14	0.	50410.	0.0
NO	+	O	=	N	+	O2	;	3.8E+9	1.	41370.	0.0
O	+	N2	=	NO	+	N	;	1.80E+14	0.	76250.	0.0
N	+	NO2	=	2 NO			;	4.0E+12	0.	0.	0.0

M	+	N2O	=	M + N2	+	O	;	6.92E+23	-2.5	65000.	0.0
O	+	N2O	=	N2	+	O2	;	1.0E+14	0.	28020.	0.0
O	+	N2O	=	2 NO			;	6.92E+13	0.	26630.	0.0
N2O	+	H	=	N2	+	OH	;	7.59E+13	0.	15100.	0.0
NO2	+	H2	=	HNO2	+	H	;	2.4E+13	0.	29000.	0.0
OH	+	M5 + NO2	=	HNO3	+	M5	;	3.0E+15	0.	-3800.	0.0
OH	+	M + NO	=	HNO2	+	M	;	5.6E+15	0.	-1700.	0.0
HNO	+	H	=	H2	+	NO	;	5.0E+12	0.	0.	0.0
H	+	M + NO	=	HNO	+	M	;	5.4E+15	0.	-600.	0.0
HNO	+	OH	=	H2O	+	NO	;	3.6E+13	0.	0.	0.0

The Reduced Methane Reaction Rate File:

Lewis reduced methane model

12 0 10 1.9859

H2 O2 H2O OH O H N2 N NO CO CO2 CH4

3 O2	+	2 CH4	=	2 CO	+	4 H2O	;	3.29E+12	0.	30000.	-2.
N2	+	O	=	N	+	NO	;	1.00E+14	0.	75010.	0.0
N	+	O2	=	NO	+	O	;	6.30E+09	1.1	6280.	0.0
N	+	OH	=	NO	+	H	;	3.00E+11	0.	0.	0.0
H2	+	O2	=	H2O	+	O	;	5.00E+12	1.0	48000.	0.0
H2	+	O	=	H	+	OH	;	2.50E+14	0.	6000.	0.0
H	+	O2	=	O	+	OH	;	4.00E+14	0.0	18000.	0.0
H2O	+	O2	=	2 O	+	H2O	;	5.00E+18	0.0	112239.	0.0
CO	+	OH	=	CO2	+	H	;	1.51E+07	1.3	-758.	0.0
CO	+	H2O	=	CO2	+	H2	;	5.50E+04	1.3	-1000.	0.0

Note: The -2 for A_b indicates that the reaction rate for the first reaction is

$$rr_1 = [CH_4]^{0.1} \cdot [O_2]^{1.6} \cdot A_f \cdot e^{-E_f / (R_u \cdot T)}$$

The Full Ethylene Reaction Set File:

Full Ethylene reduced from Propane Reaction Set Pg.82 K. Radhakrishnan

37 6 126 1.987

H2 O2 H2O OH O H HO2 H2O2 N2 N NO N2O NO2 NH2 NH HNO HNO2
HNO3 CO CO2 CH CH2 CH3 CH4 HCO CH2O CH3O C2H C2H2 C2H3 C2H4 C2HO
C2H2O NCO HNCO HCN CN

1.0
1.0
2.3 78 6.0 1.0 1.0 1.0 1.0 6.6 1.0 1.0 1.0 1.0 1.0 1.0 1.0 1.0 1.0 1.0 1.0 1.0
1.0 1.0 1.0 1.0 1.0 1.0 1.0 1.0 1.0 1.0 1.0 1.0 1.0 1.0 1.0 1.0 1.0 1.0 1.0
1.0 1.3 21.3 1. 1.0 1.0 1.0 1.0 1.3 1.0 1.0 1.0 1.0 1.0 1.0 1.0 1.0 1.0 1.0 1.0
1.0 1.0 1.0 1.0 1.0 1.0 1.0 1.0 1.0 1.0 1.0 1.0 1.0 1.0 1.0 1.0 1.0 1.0 1.0
4.0 1.5 20. 1.0 1.0 1.0 1.0 1.0 1.5 1.0 1.0 1.0 1.0 1.0 1.0 1.0 1.0 1.0 1.0 1.0
1.0 1.0 1.0 1.0 1.0 1.0 1.0 1.0 1.0 1.0 1.0 1.0 1.0 1.0 1.0 1.0 1.0 1.0 1.0
4.1 2.0 15. 1.0 1.0 1.0 1.0 1.0 2.0 1.0 1.0 1.0 1.0 1.0 1.0 1.0 1.0 1.0 1.0 1.0
1.0 1.0 1.0 1.0 1.0 1.0 1.0 1.0 1.0 1.0 1.0 1.0 1.0 1.0 1.0 1.0 1.0 1.0 1.0
1.4 0.7 1.0 1.0 1.0 1.0 1.0 1.0 1.0 1.0 1.0 1.0 1.0 1.0 1.0 1.0 1.0 1.0 1.0
1.0 1.0 1.0 1.0 1.0 1.0 1.0 1.0 1.0 1.0 1.0 1.0 1.0 1.0 1.0 1.0 1.0 1.0 1.0

M	+	CH4	=	M + CH3	+	H	;	2.0E+17	0.	88000. 0.0
H	+	CH4	=	CH3	+	H2	;	1.26E+14	0.	11900. 0.0
CH4	+	O2	=	CH3	+	HO2	;	7.94E+13	0.	56000. 0.0
O	+	CH4	=	CH3	+	OH	;	1.9E+14	0.	11720. 0.0
OH	+	CH4	=	CH3	+	H2O	;	2.5E+13	0.	5010. 0.0

CH3	+	O2	=	CH3O	+	O	;	2.4E+13	0.	28680.	0.0		
CH3	+	OH	=	CH3O	+	H	;	6.3E+12	0.	0.	0.0		
M	+	CH3O	=	M	+	CH2O	+	H	;	5.0E+13	0.	21000.	0.0
CH3	+	CH2	=	C2H4	+	H	;	2.0E+13	0.	0.	0.0		
H	+	C2H4	=	H2	+	C2H3	;	1.5E+14	0.	10200.	0.0		
M	+	C2H4	=	M	+	C2H2	+	H2	;	2.6E+17	0.	79300.	0.0
C2H4	+	OH	=	C2H3	+	H2O	;	4.8E+12	0.	1230.	0.0		
C2H4	+	OH	=	CH3	+	CH2O	;	2.0E+12	0.	960.	0.0		
C2H4	+	O	=	CH3	+	HCO	;	3.3E+12	0.	1130.	0.0		
C2H4	+	O	=	CH2O	+	CH2	;	2.5E+13	0.	5000.	0.0		
M	+	C2H3	=	M	+	C2H2	+	H	;	3.0E+15	0.	32000.	0.0
C2H3	+	O2	=	CH2O	+	HCO	;	3.98E+12	0.	-250.	0.0		
C2H3	+	H	=	C2H2	+	H2	;	6.0E+12	0.	0.	0.0		
C2H3	+	O	=	C2H2O	+	H	;	3.3E+13	0.	0.	0.0		
C2H3	+	OH	=	C2H2	+	H2O	;	5.0E+12	0.	0.	0.0		
C2H3	+	CH2	=	C2H2	+	CH3	;	3.0E+13	0.	0.	0.0		
C2H3	+	C2H	=	2 C2H2			;	3.0E+13	0.	0.	0.0		
M	+	C2H2	=	M	+	C2H	+	H	;	4.2E+16	0.	107000.	0.0
C2H2	+	O	=	CH2	+	CO	;	1.6E+14	0.	9890.	0.0		
C2H2	+	O	=	C2HO	+	H	;	4.0E+14	0.	10660.	0.0		
C2H2	+	OH	=	C2H	+	H2O	;	6.3E+12	0.	7000.	0.0		
C2H2	+	OH	=	C2H2O	+	H	;	3.3E+11	0.	200.	0.0		
C2H	+	O2	=	C2HO	+	O	;	5.00E+13	0.	1500.	0.0		
C2H	+	OH	=	C2HO	+	H	;	2.0E+13	0.	0.	0.0		
C2HO	+	O2	=	2 CO	+	OH	;	1.46E+12	0.	2500.	0.0		
C2HO	+	O	=	2 CO	+	H	;	1.202E+12	0.	0.	0.0		
C2HO	+	OH	=	2 HCO			;	1.0E+13	0.	0.	0.0		
C2HO	+	H	=	CH2	+	CO	;	5.0E+13	0.	0.	0.0		
C2HO	+	CH2	=	C2H3	+	CO	;	3.0E+13	0.	0.	0.0		
C2HO	+	CH2	=	CH2O	+	C2H	;	1.0E+13	0.	2000.	0.0		

	2 C2HO	=	C2H2	+	2 CO	; 1.0E+13	0.	0.	0.0
C2H2O	+ OH	=	CH2O	+	HCO	; 2.8E+13	0.	0.	0.0
C2H2O	+ OH	=	C2HO	+	H2O	; 7.5E+12	0.	3000.	0.0
C2H2O	+ H	=	CH3	+	CO	; 1.13E+13	0.	3428.	0.0
C2H2O	+ H	=	C2HO	+	H2	; 7.5E+13	0.	8000.	0.0
C2H2O	+ O	=	C2HO	+	OH	; 5.0E+13	0.	8000.	0.0
C2H2O	+ O	=	CH2O	+	CO	; 2.0E+13	0.	0.	0.0
M	+ C2H2O	= M + CH2	+	CO	; 2.0E+16	0.	60000.	0.0	
C2H	+ O	=	CO	+	CH	; 5.0E+13	0.	0.	0.0
CH3O	+ O2	=	CH2O	+	HO2	; 1.0E+13	0.	7170.	0.0
CH3O	+ H	=	CH2O	+	H2	; 2.0E+13	0.	0.	0.0
M	+ CH2O	= M + HCO	+	H	; 5.0E+16	0.	81000.	0.0	
CH2O	+ OH	=	HCO	+	H2O	; 3.0E+13	0.	1200.	0.0
CH2O	+ H	=	HCO	+	H2	; 2.5E+13	0.	3990.	0.0
CH2O	+ O	=	HCO	+	OH	; 3.5E+13	0.	3510.	0.0
CH3	+ CH2O	=	CH4	+	HCO	; 1.0E+10	0.5	6000.	0.0
CH3	+ HCO	=	CH4	+	CO	; 3.0E+11	.5	0.	0.0
CH3	+ HO2	=	CH3O	+	OH	; 2.0E+13	0.	0.	0.0
M	+ CH3	= M + CH2	+	H	; 1.95E+16	0.	91600.	0.0	
H	+ CH3	=	H2	+	CH2	; 2.7E+11	.67	25700.	0.0
O	+ CH3	=	OH	+	CH2	; 1.9E+11	.68	25700.	0.0
OH	+ CH3	=	H2O	+	CH2	; 2.7E+11	.67	25700.	0.0
CH	+ CO2	=	HCO	+	CO	; 3.7E+12	0.	0.	0.0
CH	+ O2	=	HCO	+	O	; 1.0E+13	0.	0.	0.0
CH2	+ O2	=	CH2O	+	O	; 5.0E+11	0.5	6960.	0.0
CH2	+ O	=	CH	+	OH	; 2.0E+11	.7	25800.	0.0
CH2	+ OH	=	CH	+	H2O	; 5.0E+11	.5	5900.	0.0
CH2	+ H	=	CH	+	H2	; 3.2E+11	0.7	4970.	0.0
CH2	+ CH2	=	C2H3	+	H	; 5.0E+12	0.	0.	0.0
CH2	+ CH2	=	C2H2	+	H2	; 4.0E+13	0.	0.	0.0

HCO	+	O2	=	CO	+	HO2	;	3.0E+13	0.	0.	0.0
HCO	+	O	=	CO	+	OH	;	3.0E+13	0.	0.	0.0
HCO	+	OH	=	CO	+	H2O	;	3.0E+13	0.	0.	0.0
HCO	+	H	=	CO	+	H2	;	2.0E+13	0.	0.	0.0
M	+	HCO	=	M + H	+	CO	;	2.9E+14	0.	15570.	0.0
CO	+	M + O	=	CO2	+	M	;	2.4E+15	0.	4100.	0.0
CO	+	O2	=	CO2	+	O	;	2.5E+12	0.	47690.	0.0
CO	+	OH	=	CO2	+	H	;	4.17E+11	0.	1000.	0.0
CO	+	HO2	=	CO2	+	OH	;	5.75E+13	0.	22930.	0.0
O	+	H2O	=	OH	+	OH	;	6.8E+13	0.	18365.	0.0
H	+	O2	=	OH	+	O	;	1.89E+14	0.	16400.	0.0
O	+	H2	=	OH	+	H	;	4.20E+14	0.	13750.	0.0
H	+	HO2	=	H2	+	O2	;	7.28E+13	0.	2126.	0.0
O	+	HO2	=	OH	+	O2	;	5.0E+13	0.	1000.	0.0
HO2	+	OH	=	H2O	+	O2	;	8.0E+12	0.	0.	0.0
H	+	HO2	=	2 OH			;	1.34E+14	0.	1070.	0.0
H2	+	HO2	=	H2O2	+	H	;	7.91E+13	0.	25000.	0.0
OH	+	H2O2	=	H2O	+	HO2	;	6.1E+12	0.	1430.	0.0
HO2	+	HO2	=	H2O2	+	O2	;	1.8E+12	0.	0.	0.0
H	+	H2O2	=	OH	+	H2O	;	7.8E+11	0.	0.	0.0
M1	+	H2O2	=	M1 +	2 OH		;	1.44E+17	0.	45510.	0.0
H2	+	OH	=	H2O	+	H	;	4.74E+13	0.	6098.	0.0
H	+	M2 + O2	=	HO2	+	M2	;	1.46E+15	0.	-1000.	0.0
M3	+	H2O	=	M3 + H	+	OH	;	1.30E+15	0.	105140.	0.0
H	+	M + O	=	OH	+	M	;	7.1E+18	-1.0	0.	0.0
M4	+	H2	=	M4 + H	+	H	;	2.2E+14	0.	96000.	0.0
M	+	O2	=	M + O	+	O	;	1.8E+18	-1.0	118020.	0.0
CH	+	N2	=	HCN	+	N	;	1.0E+11	0.	19000.	0.0
CN	+	H2	=	HCN	+	H	;	6.0E+13	0.	5300.	0.0
O	+	HCN	=	OH	+	CN	;	1.4E+11	.68	16900.	0.0

OH	+	HCN	=	HNCO	+	H	;	4.0E+11	0.	2800.	0.0
CN	+	O	=	CO	+	N	;	1.2E+13	0.	0.	0.0
CN	+	OH	=	NCO	+	H	;	2.5E+14	0.	6000.	0.0
H2	+	NCO	=	HNCO	+	H	;	1.0E+14	0.	9000.	0.0
HNCO	+	H	=	NH2	+	CO	;	1.0E+14	0.	8500.	0.0
CN	+	O2	=	NCO	+	O	;	3.2E+13	0.	1000.	0.0
CN	+	CO2	=	NCO	+	CO	;	3.7E+12	0.	0.	0.0
O	+	NCO	=	NO	+	CO	;	2.0E+13	0.	0.	0.0
N	+	NCO	=	N2	+	CO	;	1.0E+13	0.	0.	0.0
H	+	NCO	=	NH	+	CO	;	2.0E+13	0.	0.	0.0
CH	+	NO	=	N	+	HCO	;	1.6E+13	0.	9940.	0.0
CH	+	NO	=	O	+	HCN	;	2.0E+12	0.	0.	0.0
NH	+	OH	=	N	+	H2O	;	5.0E+11	0.5	2000.	0.0
HO2	+	NO	=	NO2	+	OH	;	2.09E+12	0.	-477.	0.0
O	+	NO2	=	NO	+	O2	;	1.0E+13	0.	596.	0.0
NO	+	M + O	=	NO2	+	M	;	5.62E+15	0.	-1160.	0.0
NO2	+	H	=	NO	+	OH	;	3.47E+14	0.	1470.	0.0
NO	+	H	=	N	+	OH	;	2.63E+14	0.	50410.	0.0
NO	+	O	=	N	+	O2	;	3.8E+9	1.	41370.	0.0
O	+	N2	=	NO	+	N	;	1.80E+14	0.	76250.	0.0
N	+	NO2	=	2 NO			;	4.0E+12	0.	0.	0.0
M	+	N2O	= M +	N2	+	O	;	6.92E+23	-2.5	65000.	0.0
O	+	N2O	=	N2	+	O2	;	1.0E+14	0.	28020.	0.0
O	+	N2O	=	2 NO			;	6.92E+13	0.	26630.	0.0
N2O	+	H	=	N2	+	OH	;	7.59E+13	0.	15100.	0.0
NO2	+	H2	=	HNO2	+	H	;	2.4E+13	0.	29000.	0.0
OH	+	M5 + NO2	=	HNO3	+	M5	;	3.0E+15	0.	-3800.	0.0
OH	+	M + NO	=	HNO2	+	M	;	5.6E+15	0.	-1700.	0.0
HNO	+	H	=	H2	+	NO	;	5.0E+12	0.	0.	0.0
H	+	M + NO	=	HNO	+	M	;	5.4E+15	0.	-600.	0.0

HNO + OH = H2O + NO ; 3.6E+13 0. 0. 0.0

Reduced Ethylene Rate Set File:

LaRC ethylene model, AIAA Journal, Vol. 32, No. 1 Jan. 94

10 1 10 1.9859

H2 O2 H2O OH O H N2 CO CO2 C2H4

2.5 1.0 16.0 1.0 1.0 1.0 1.0 1.0 1.0 1.0

C2H4 + O2 = 2 CO + 2 H2 ; 1.80e+14 0. 35500. 0.0

CO + M + O = CO2 + M ; 5.30E+13 0. -4540. 0.0

CO + OH = CO2 + H ; 4.40E+06 1.5 -740. 0.0

H2 + O2 = 2 OH ; 1.70E+13 0. 48000. 0.0

H + O2 = OH + O ; 2.60E+14 0. 16800. 0.0

OH + H2 = H2O + H ; 2.20E+13 0. 5150. 0.0

O + H2 = OH + H ; 1.80e+10 1.0 8900. 0.0

2 OH = H2O + O ; 6.30E+13 0. 1090. 0.0

2 H + M = M + H2 ; 6.40E+17 -1.0 0. 0.0

H + M + OH = M + H2O ; 2.20E+22 -2.0 0. 0.0

References

1. Bushnell, D.M., "Mixing and Combustion Issues in Hypersonic Air-breathing Propulsion," in *Combustion in High-Speed Flows*, eds. Buckmaster, J., Jackson, T.L., and Kumar, A., Kluwer Academic Publishers, Norwell, MA, 1994.
2. Huellmantel L.W., Ziemer R.W. and Cambel A.B., "Stabilization of Premixed Propane-Air Flames in Recessed Ducts," *ARS Journal*, pp. 31-43, Jan 1957.
3. Glassman I., *Combustion*, 2nd ed., Academic Press, Inc., Orlando, FL, 1987.
4. Kerrebrock, J.L., *Aircraft Engines and Gas Turbines*, MIT Press, Cambridge, Mass (1992)
5. Gutmark, E., Schadow, K.C., Parr, T.P., Parr, D.M. and Wilson, K.J., "Combustor Enhancement by Axial Vortices," *AIAA Journal of Propulsion and Power*, Vol. 5, No. 5, Sept-Oct., 1989, pp 555-563.
6. Kumar, A., Bushnell, D.M. and Hussaini, M. Y., "Mixing Augmentation Technique for Hypervelocity Scramjets," *AIAA Journal of Propulsion and Power* Vol. 5, No. 5, Sept-Oct., 1989, pp 514-522.
7. Riggins, D.W., Mekkes, G.L., McClinton, C.R., and Drummond, J.P., "A Numerical Study of Mixing Enhancement in a Supersonic Combustor", AIAA paper 90-0203, 1990.
8. Waitz, I.A., Marble, F.E. and Zukowski, E.E., "Investigation of a Contoured Wall Injector for Hypervelocity Mixing Augmentation", *AIAA Journal*, Vol. 31, No. 6, pp 1014-1021, June, 1993.
9. Tillman, T.G., Patrick, W.P. and Paterson, R.W., "Enhanced Mixing of Supersonic Jets", AIAA paper 88-3002, 1988.
10. Hartfield, R.J., Hollo, S.D. and McDaniel, J.C., "Experimental Investigation of a Supersonic Swept Ramp Injector Using Laser-Induced Iodine Florescence", AIAA paper 90-1518, June 1990.
11. Northam, G.B., Greenberg, I. and Byington, C.S., "Evaluation of Parallel Injector Configurations for Supersonic Combustion", AIAA paper 89-2525, 1989.
12. Zaman, K.B.M.Q., Reeder, M.F. and Samimy, M., "Supersonic Jet Mixing Enhancement by 'Delta-Tabs'," AIAA paper 92-3548, 1992.
13. Davis, D.L., "Numerical Analysis of Techniques for Efficient Generation of Vorticity in Supersonic Flows," AIAA paper 92-0828. Jan. 1992.

14. Davis,D.L., "Scramjet Fuel Mixing Enhancement by Cross-Stream Pressure Gradients", AIAA paper 93-2139, 1993.
15. Pauley, W.R., Eaton, J.K., "Experimental Study of the Development of Longitudinal Vortex Pairs Embedded in a Turbulent Boundary Layer," *AIAA Journal*, Vol.26, No.7, pp816-823, 1988.
16. Avrashkov V., Baranovsky S., Levin V., "Gasdynamic Features of Supersonic Kerosene Combustion in a Model Combustion Chamber," AIAA paper 90-5268, 1990.
17. Vinogradov, V., Kobigsky, S. and Petrov, M., "Experimental Investigation of Liquid Carbohydrogen Fuel Combustion in Channel at Supersonic Velocities", AIAA paper 92-3429, July 1992.
18. Vinogradov V., "Russian Hydrogen Fueled Scramjet Engine Technology," Report No. 700-606023-0-1, Contract N606023-0(JHU/Applied Physics Laboratory, Lurel, Md.) Moscow, 1994.
19. Ortwerth P., Mather A., Vinogradov V., Grin V., Goldfeld M. and Starov A., "Experimental and Numerical Investigation of Hydrogen and Ethylene Combustion in a Mach 3-5 Channel with a Single Injector," AIAA paper 96-3245, July 1996.
20. Billig F.S., Waltrup P.J., and Stockbridge R.D., "Integral-Rocket Dual-Combustion Ramjets: A New Propulsion Concept," *AIAA Journal of Spacecraft and Rockets*, Vol 17, No. 5, Sept-Oct 1980.
21. Kay I.W., "Scramjet Component Technology Program, Phase II- Task 1 Combustor Technology Tests," UTRC Rpt. R94-970246-21, Contract F33615-90-C-2093, Feb. 1994.
22. Reed, R.J., *North American Combustion Handbook, Third Edition, Volume I*, North American Mfg. Co., Cleveland, OH, 1986.
23. Romankov O.N., Starostin F.I., "Design and Investigation of the Stand and Flying Scramjet Models Conceptions and Results of Experiments," AIAA paper 93 - 2447, June 1993.
24. Curran, E.T., "An Investigation of Flame Stability in a Coaxial Dump Combustor", Dissertation, AFIT/AE/DS79-1, 1979.
25. Zukoski, E.E. and Marble, F.E., "Experiments Concerning the Mechanism of Flame Blowoff from Bluff Bodies," *Proceedings of the Gas Dynamics Symposium on Aerothermochemistry*, Northwestern University 1956.

26. Stull, F.D., Craig, R.R., and Hojnacki, J.T., "Dump Combustor Parametric Investigation," AFAPL-TR-74-90, U.S. Air Force, Jan. 1975.
27. Povinelli, L.A., "The Ignition Delay Concept for Recessed Flameholders," *Combustion and Flame*, Vol. 4, No. 4, Dec 1960.
28. Hsu, K. Y., Goss, L.P., Trump, D.D., and Roquemore, W.M., "Performance of a Trapped-Vortex Combustor," AIAA-95-0810, Jan. 1995.
29. Niioka, T., Terada, K., Kobayashi, H., and Hasegawa, S., "Flame Stabilization Characteristics of a Strut Divided into Two Parts in Supersonic Airflow," *Journal of Propulsion and Power*, Vol. 11, No. 1, Jan-Feb 1995 pp 112-116
30. Heller, H.H., and Bliss, D.B., "Aerodynamically Induced Pressure Oscillations in Cavities- Physical Mechanisms and Suppression Concepts," AFFDL-TR-74-133, 1975.
31. Rockwell, D., and Naudascher, E., "Review - Self-Sustaining Oscillations of Flow Past Cavities," *Transactions of the ASME, Journal of Fluids Engineering*, Vol. 100, pp 152-165, June 1978.
32. Tam, C.K.W. and Block, P.J.W., "On the Tones and Pressure Oscillations Induced by Flows Over Rectangular Cavities," *Journal of Fluid Mechanics*, Vol. 89, Part 2, pp 3 - 399, 1978.
33. Komerath, W.M., Ahuja, K.K., and Chambers, F.W., "Prediction and Measurement of Flows Over Cavities - A Survey," AIAA-87-0166, Jan. 1987.
34. Hankey, W.L., and Shang, J.S., "Analysis of Pressure Oscillations in an Open Cavity," *AIAA Journal*, Vol 18, No. 9, pp 892-898.
35. Borland, C.J., "Numerical Prediction of the Unsteady Flowfield in an Open Cavity", AIAA-77-673, June 1977.
36. Gorski, J.J., Ota, D.K. and Chakravarthy, S.R., "Calculation of Three Dimensional Cavity Flow Fields," AIAA-87-0117, Jan. 1987.
37. Suhs, N.E., "Computations of Three-Dimensional Cavity Flow at Subsonic and Supersonic Mach Numbers," AIAA-87-1208, June 1987.
38. Baysal, O., Srinivasan, S., and Stallings Jr., R.L., "Unsteady Viscose Calculations of Supersonic Flows Past Deep and Shallow Three-Dimensional Cavities," AIAA-88-0101, Jan 1988.

52. Tam,C.-J.,Orkwis,P.D., and Disimile,P.J., "Supersonic Open Cavity Flow Physics Ascertained from Algebraic Turbulence Model Simulations," AIAA-96-0075, Jan. 1996.
53. Franke,M.E.,and Carr,D.L., "Effect of Geometry on Open Cavity Flow-Induced Pressure Oscillations," AIAA-75-492,2nd Aero-Acoustics Conf.,Hampton, Va.,March 1975.
54. Sarno,R.L.,and Franke,M.E., "Suppression of Flow-Induced Pressure Oscillations in Cavities," *Journal of Aircraft*, Vol.31, No.1, Jan-Feb. 1994.
55. Oppenheim,A.K., "The Beauty of Combustion Fields and Their Aerothermodynamic Significance", in *Dynamics of Reactive Systems, Part I: Flames and Configurations*, AIAA Prog. in Astro. and Aero., Vol 105, AIAA, Washington, D.C.,1986.
56. Giovannini,A. "Residence Time in Flow Combustor," in *Dynamics of Reactive Systems, Part I: Flames and Configurations*, Eds. Bowen,J.R., Leyer J.-C., and Soloukhin,R.I., Vol. 105 of *Progress in Astronautics and Aeronautics*, Summerfield,M. Editor-in-Chief, AIAA, Washington DC, 1986.
57. Maull,D.J. and East,L.F., "Three-dimensional Flow in Cavities," *Journal of Fluid Mechanics*, Vol. 16, part 4, 1963, pp620-632.
58. Settles,G.S., Williams,D.R., Baca,B.K.,Bogdonoff,S.M., "Reattachment of a Compressible Turbulent Free Shear Layer," *AIAA Journal*, Vol.20, No. 1 , Jan 1982, pp60-67.
59. Petrie,H.L.,Samimy,M.,and Addy,A.L., "A Study of Compressible Turbulent Free Shear Layers Using Laser Doppler Velocimetry," AIAA-85-0177, Jan. 1985.
60. Torda,T.P. and Patel,B.R., "Investigation of Flows in Triangular Cavities," *AIAA Journal*, Vol. 7, No.12, Dec. 1969, pp 2365-2367.
61. Samimy,M.,Petrie,H.L., and Addy,A.L., "A Study of Compressible Turbulent Reattaching Free Shear Layers," *AIAA Journal*, Vol.24, No.2. Feb 1986.
62. Hayakawa,K.,Smits,A.J., and Bogdonoff,S.M., "Turbulence Measurements in a Compressible Reattaching Shear Layer", AIAA-83-0299, Jan. 1983.
63. Horstman,C.C.,Settles,G.S.,Williams,D.R., and Bogdonoff,S.M., "A Reattaching Free Shear Layer in Compressible Turbulent Flow - A Comparison of Numerical and Experimental Results," AIAA-81-0333, Jan. 1981.
64. King R.A.,Creel,Jr.,T.R., and Bushnell,D.M., "Experimental Study of Free-Shear Layer Transition Above a Cavity at Mach 3.5," AIAA-89-1813.

65. McGregor, O.W., and White, R.A., "Drag of Rectangular Cavities in Supersonic and Transonic Flow Including the Effects of Cavity Resonance," *AIAA Journal*, Vol.4, No.11, Nov. 1970, pp 1959-1964.
66. Little Jr, B.H., and Whipkey, R.R., "Locked Vortex Afterbodies," *Journal of Aircraft*, Vol.16, No.5, May 1979, pp 296-302.
67. Tanner, M., "Base Cavity at Angles of Incidence," *AIAA Journal*, Vol.26, No.3, March 1988, pp 376-377.
68. Warnatz, J., "Rate Coefficients in the C/H/O System" in *Combustion Chemistry* ed. Gardiner, W.C., Jr., Springer-Verlag, New York NY, 1984.
69. White, F.M., *Viscous Fluid Flow, 2nd. Ed.*, McGraw-Hill, Inc. New York, 1991.
70. Radhakrishnan, K. and Bittker, D.A., "LSENS, A General Chemical Kinetics and Sensitivity Analysis Code for Homogeneous Gas-Phase Reactions, Part II. Code Description and Usage," NASA Reference Publication 1329, Feb. 1994.
71. Drummond, J.P., "Supersonic Reacting Internal Flow Fields," *Numerical Approaches to Combustion Modeling*, Eds. Oran, E.S., and Boris, J.P., Progress in Astronautics and Aeronautics, AIAA Washington, D.C., 1991.
72. Walters, R.W., Cinnella, P., and Slack, D.C., "Characteristic Based Algorithms for Flows in Thermochemical Nonequilibrium," *AIAA Journal* Vol.30, No.5, pp1304-1313, 1992.
73. Carpenter, M.H., "Three Dimensional Computations of Cross-Flow Injection and Combustion in a Supersonic Flow," AIAA paper 89-1870, June 1989.
74. McBride, B.J., Gordon, S., and Reno, M.A., "Coefficients for Calculating Thermodynamic and Transport Properties of Individual Species," NASA TM 4513, Oct. 1993.
75. Andrussov, L., "Diffusion, Viscosity and Conductivity of Gases" in *Progress in International Research on Thermodynamic and Transport Properties* Eds. Masi, J.F. and Tsai, D.H., ASME, Academic Press, Inc., New York, New York, 1962.
76. Wilcox, D.C., *Turbulence Modeling for CFD*, DCW Industries, Inc., La Cañada, California, 1993.
77. Baldwin, B.S. and Lomax, H., "Thin Layer Approximation and Algebraic Model for Separated Turbulent Flows," AIAA-78-257, Washington D.C., 1978.

78. MacCormac, R.W., "The Effect of Viscosity in Hypervelocity Impact Cratering," AIAA-69-354, April 1969.
79. MacCormack, R.W., and Baldwin, B.S., "A Numerical Method for Solving the Navier-Stokes Equations with Application to Shock-Boundary Layer Interactions," AIAA-75-1, Jan 1975.
80. Bowersox, R.D.W., and Schetz, J.A., "Model for Compressible Turbulence in Hypersonic Wall Boundary and High-Speed Mixing Layers," AIAA Journal, Vol. 32, No. 7, July 1994, pp 1531-1533.
81. Risha, D.J., "Numerical Analysis of Mixing Phenomena of Supersonic Shear Layers", Dissertation, Univ. of Dayton, 1994.
82. Ziemer, R.W., and Cambel, A.B., "Flame Stabilization in the Boundary Layer of Heated Plates," *ARS Jet Propulsion Journal*, Sept. 1958, pp. 592-599.
83. Ekland, D.R., Fletcher, D.G., Hartfield Jr., R.J., McDaniel, J/C., Northam, G.B., Dancey, C.L., and Wang, J.A., "Computational/Experimental Investigation of Staged Injection into a Mach 2 Flow," AIAA Journal, Vol. 32, No. 5, May 1994, pp 907-916.
84. Fatunla, S.O., *Numerical Methods for Initial Value Problems in Ordinary Differential Equations*, Academic Press, Inc, New York, 1988.

Vita

Douglas L. Davis was [REDACTED] He graduated from Milton-Union High School in 1974 and entered undergraduate studies at Rose-Hulman Institute of Technology in Terre Haute, Indiana. He graduated with a Bachelor of Science degree in Mechanical Engineering in May 1978. Upon graduation, he started to work for the Ramjet Combustor Technology Branch of the Air Force Aero Propulsion Laboratory. While conducting experimental combustor research, he earned a Master of Science degree in Systems Engineering at Wright State University in Fairborn, Ohio. In September 1993, he began full time study in the Department of Aeronautics and Astronautics of the Air Force Institute of Technology.

Permanent Address: [REDACTED]
[REDACTED]

REPORT DOCUMENTATION PAGE			Form Approved OMB No. 0704-0188	
Public reporting burden for this collection of information is estimated to average 1 hour per response, including the time for reviewing instructions, searching existing data sources, gathering and maintaining the data needed, and completing and reviewing the collection of information. Send comments regarding this burden estimate or any other aspect of this collection of information, including suggestions for reducing this burden, to Washington Headquarters Services, Directorate for Information Operations and Reports, 1215 Jefferson Davis Highway, Suite 1204, Arlington, VA 22202-4302, and to the Office of Management and Budget, Paperwork Reduction Project (0704-0188), Washington, DC 20503.				
1. AGENCY USE ONLY (Leave blank)		2. REPORT DATE September 1996		3. REPORT TYPE AND DATES COVERED Doctoral Dissertation
4. TITLE AND SUBTITLE Numerical Analysis of Two and Three Dimensional Recessed Flame Holders for Scramjet Applications			5. FUNDING NUMBERS	
6. AUTHOR(S) D. L. Davis				
7. PERFORMING ORGANIZATION NAME(S) AND ADDRESS(ES) Air Force Institute of Technology 2750 P Street WPAFB OH 45433-7765			8. PERFORMING ORGANIZATION REPORT NUMBER	
9. SPONSORING/MONITORING AGENCY NAME(S) AND ADDRESS(ES) WL/POPS Bldg 18 1950 Fifth Street WPAFB OH 45433-7251			10. SPONSORING/MONITORING AGENCY REPORT NUMBER AFIT/DS/ENY/96-12	
11. SUPPLEMENTARY NOTES				
12a. DISTRIBUTION / AVAILABILITY STATEMENT Approved for public release; distribution unlimited.			12b. DISTRIBUTION CODE	
13. ABSTRACT (Maximum 200 words) <p>This study investigated the flame holding properties of recessed cavities in supersonic flow using numerical analysis techniques. A simplified analytical model indicated that an important property for flame holding was the lower residence time. Several chemical kinetic rate models for hydrogen and hydrocarbon combustion were compared. The perfectly stirred reactor model also indicated that trace species diffusion should increase flame spreading rate, and that heat loss reduces flame holding limits. After nonreacting calibration, two-dimensional simulations confirmed the perfectly stirred reactor results for blowout limits. Also, the effect of trace species diffusion on flame spreading was shown to be negligible, and the reduced flammability with heat loss was confirmed. Lowering the temperature of the inflow boundary layer was shown to reduce the flammability limits. Three-dimensional cavities were shown to generate axial vorticity and slightly enhance flame spreading. The methodology developed in this research provides a design guide for the size of cavity required to provide flame holding for a scramjet combustor. Also, reduction of heat losses was shown to be a method to improve flame holding performance without increasing the cavity size.</p>				
14. SUBJECT TERMS Scramjet, Flame Holder, Combustion, Stirred Reactor			15. NUMBER OF PAGES 236	
			16. PRICE CODE	
17. SECURITY CLASSIFICATION OF REPORT Unclassified	18. SECURITY CLASSIFICATION OF THIS PAGE Unclassified	19. SECURITY CLASSIFICATION OF ABSTRACT Unclassified	20. LIMITATION OF ABSTRACT UL	

GENERAL INSTRUCTIONS FOR COMPLETING SF 298

The Report Documentation Page (RDP) is used in announcing and cataloging reports. It is important that this information be consistent with the rest of the report, particularly the cover and title page. Instructions for filling in each block of the form follow. It is important to **stay within the lines** to meet **optical scanning requirements**.

Block 1. Agency Use Only (Leave blank).

Block 2. Report Date. Full publication date including day, month, and year, if available (e.g. 1 Jan 88). Must cite at least the year.

Block 3. Type of Report and Dates Covered. State whether report is interim, final, etc. If applicable, enter inclusive report dates (e.g. 10 Jun 87 - 30 Jun 88).

Block 4. Title and Subtitle. A title is taken from the part of the report that provides the most meaningful and complete information. When a report is prepared in more than one volume, repeat the primary title, add volume number, and include subtitle for the specific volume. On classified documents enter the title classification in parentheses.

Block 5. Funding Numbers. To include contract and grant numbers; may include program element number(s), project number(s), task number(s), and work unit number(s). Use the following labels:

C - Contract	PR - Project
G - Grant	TA - Task
PE - Program Element	WU - Work Unit Accession No.

Block 6. Author(s). Name(s) of person(s) responsible for writing the report, performing the research, or credited with the content of the report. If editor or compiler, this should follow the name(s).

Block 7. Performing Organization Name(s) and Address(es). Self-explanatory.

Block 8. Performing Organization Report Number. Enter the unique alphanumeric report number(s) assigned by the organization performing the report.

Block 9. Sponsoring/Monitoring Agency Name(s) and Address(es). Self-explanatory.

Block 10. Sponsoring/Monitoring Agency Report Number. (If known)

Block 11. Supplementary Notes. Enter information not included elsewhere such as: Prepared in cooperation with...; Trans. of...; To be published in.... When a report is revised, include a statement whether the new report supersedes or supplements the older report.

Block 12a. Distribution/Availability Statement.

Denotes public availability or limitations. Cite any availability to the public. Enter additional limitations or special markings in all capitals (e.g. NOFORN, REL, ITAR).

DOD - See DoDD 5230.24, "Distribution Statements on Technical Documents."

DOE - See authorities.

NASA - See Handbook NHB 2200.2.

NTIS - Leave blank.

Block 12b. Distribution Code.

DOD - Leave blank.

DOE - Enter DOE distribution categories from the Standard Distribution for Unclassified Scientific and Technical Reports.

NASA - Leave blank.

NTIS - Leave blank.

Block 13. Abstract. Include a brief (*Maximum 200 words*) factual summary of the most significant information contained in the report.

Block 14. Subject Terms. Keywords or phrases identifying major subjects in the report.

Block 15. Number of Pages. Enter the total number of pages.

Block 16. Price Code. Enter appropriate price code (*NTIS only*).

Blocks 17. - 19. Security Classifications. Self-explanatory. Enter U.S. Security Classification in accordance with U.S. Security Regulations (i.e., UNCLASSIFIED). If form contains classified information, stamp classification on the top and bottom of the page.

Block 20. Limitation of Abstract. This block must be completed to assign a limitation to the abstract. Enter either UL (unlimited) or SAR (same as report). An entry in this block is necessary if the abstract is to be limited. If blank, the abstract is assumed to be unlimited.